Rapid Response to Extraordinary Events: Transient Neutrino Sources with the IceCube Experiment

D I S S E R T A T I O N

zur Erlangung des akademischen Grades
Doctor rerum naturalium (Dr. rer. nat.)
im Fach Physik

eingereicht
an der Mathematisch-Naturwissenschaftlichen Fakultät
der Humboldt-Universität zu Berlin

von Thomas Kintscher

Gutachterinnen:
1. Prof. Dr. Elisa Bernardini
2. Dr. Anna Franckowiak
3. Prof. Dr. Anna Nelles

Tag der mündlichen Prüfung:
16.09.2020

Präsidentin der Humboldt-Universität zu Berlin:
Prof. Dr.-Ing. Dr. Sabine Kunst

Dekan der Mathematisch-Naturwissenschaftlichen Fakultät:
Prof. Dr. Elmar Kulke

Abstract

Dem IceCube-Experiment ist es im Jahr 2013 gelungen, einen Fluss von Neutrinos mit extraterrestrischem Ursprung nachzuweisen, und damit das Neutrino als weiteres kosmisches Botenteilchen zu etablieren. Damit stellt sich die Frage nach dem Ursprung der Neutrinos, die einen komplementären Blick auf die Quellen bieten und möglicherweise die alte Frage nach dem Ursprung der kosmischen Strahlung lösen können.

Bisherigen zeitunabhängigen Suchen nach punktartigen Quellen von Neutrinos ist es nicht gelungen, einzelne Kandidaten zu isolieren und veränderliche und kurzlebige Quellen kommen als Ursprung in Betracht. Solche Quellen zeigen vermutlich auch in anderen Beobachtungen, z.B. mit Gammastrahlen, veränderliches Verhalten. IceCubes Fähigkeiten, den gesamten Himmel rund um die Uhr zu beobachten, ermöglichen es, dauerhaft nach aufflackernden Neutrinoquellen zu suchen und die astronomische Gemeinschaft mit kürzestmöglicher Verzögerung darauf aufmerksam zu machen.

In dieser Arbeit wird die Echtzeitidentifikation und -rekonstruktion von Myonneutrinokandidaten mit IceCube verbessert. Dabei wird eine Sensitivität erreicht, die mit etablierten nicht-Echtzeit Analysen vergleichbar ist. Die kontinuierlich vom Experiment am Südpol übermittelten Ereignisinformationen werden sofort hinsichtlich bemerkenswerter Ereignisse analysiert. Bekannte astrophysikalische Quellen von Gammastrahlung werden auf zeitlich veränderliche Neutrinoemission hin beobachtet. Eine Verallgemeinerung dieser Methode erlaubt nun auch die Suche nach Signalen von Neutrinoquellen, ohne durch eine Liste möglicher Quellkandidaten beeinflusst zu sein. Weiterhin werden die hochenergetischsten Neutrinokandidaten, die wahrscheinlich astrophysikalischen Ursprungs sind, sofort identifiziert und der globalen astronomischen Szene bekannt gemacht.

Zu guter Letzt werden die Suchalgorithmen auf zwei Blazare, 1ES 1959+650 und TXS 0506+56, angesetzt, um ihr Potential zu demonstrieren. Zum ersten Mal konnten dabei im Fall von TXS 0506+056 Anzeichen dafür gefunden werden, dass es sich um eine Quelle hochenergetischer, kosmischer Neutrinos handelt.

Die im Rahmen dieser Arbeit entwickelte Infrastruktur erlaubt es nun, die astronomische Gemeinschaft zu benachrichtigen, sobald signifikante Neutrinoereignisse registriert werden, oder wenn sich Neutrinocluster auf der Zeitskalen zwischen Tagen und Wochen entwickeln. Die Infrastruktur ermöglicht weiterhin die zügige Suche nach Neutrinos in Reaktion auf interessante, astrophysikalische Ereignisse, wie z.B. die Beobachtung von Gravitationswellen.

Abstract

The discovery of an flux of neutrinos of astrophysical origin with the IceCube experiment in 2013 has broadened our understanding of cosmic messengers and opened a new window on the universe. By addressing the newly pertinent question about their sources, neutrinos can provide a complementary view on cosmic accelerators and may help solving the long-standing puzzle of the origin of the cosmic rays.

As traditional time-integrated searches for point-like sources of neutrinos have not been able to isolate individual astrophysical sites, variable and transient sources shift into focus. Such sources may also exhibit variable behavior in other observations, such as gamma-rays. Using IceCube's capabilities to observe the entire sky around-the-clock, it is possible to continuously search for neutrino flares, and alert the community with the lowest possible latency in the case of a detection.

This thesis improves the identification and reconstruction of muon neutrino candidates with IceCube in real-time, achieving a sensitivity which is comparable to dedicated offline analyses. The stream of neutrino candidates is analyzed in several regards, always aiming to alert partner experiments to inspire follow-up observations. Known emitters of gamma-rays are monitored for time-variable neutrino emission. A generalization of this method now monitors the entire sky for neutrino flares, unbiased and free from pre-defined source lists. In addition, the most-energetic neutrino candidates with the highest chance to be of astrophysical origin are selected for alerts and broadcasted to the global astronomical community.

In addition, the search methods are applied to two source candidates, the blazars 1ES 1959+650 and TXS 0506+056, to demonstrate their performance. In the case of TXS 0506+056 the study yielded evidence of a source of high-energetic, astrophysical neutrinos for the first time.

The infrastructure built in this work now allows to properly notify the community whenever significant neutrino events are recorded, or significant flares develop on time-scales from days to several weeks. It also allows to quickly perform neutrino follow-up searches in response to interesting astrophysical events, such as the observation of gravitational waves.

Contents

List of Figures

List of Tables

1 Introduction

Discovering the presence of a flux of high-energetic astrophysical neutrinos by the IceCube experiment in 2014 has opened a new window on the universe.

And as with any great discovery, it immediately begs new questions, the most pertinent one being about the origin of those neutrinos. Unraveling their sources would have an evenly broad impact on the field and finally provide an answer to the almost 100 year old question about the origin of the cosmic rays.

The same processes, which are expected to produce the cosmic rays, would also produce neutrinos. Therefore, identifying a source of neutrinos would provide a smoking gun signature of a source of cosmic rays. Unlike the charged particles that make up the cosmic rays, neutrinos are electrically neutral and can travel from their production site to Earth without deflection. Moreover, as opposed to photons, neutrinos interact only weakly allowing them to travel unabsorbed. These features make the neutrino a unique tool for studying the high-energy universe.

However, even 8 years after the construction of the detector was completed, no source has clearly stood out in the neutrino data collected by IceCube, motivating the need for novel search strategies beyond the capabilities of any single experiment.

The approach pursued in this work aims to leverage the unique properties of the different messenger particles, such as neutrinos and photons. In an unintended coincidence, this idea has been explored in the wake of the detection of supernova SN1987A, when a signal of low-energetic neutrinos was found to have arrived ahead the optical detection. However, two ground-breaking events in the last three years truly launched the era of multi-messenger astronomy.

The first one was the observation of gravitational waves by the LIGO and VIRGO collaborations, in particular from the merger of two neutron stars in August 2017, which was followed by a gamma-ray burst 2 seconds later. Automated notices to the astronomical community allowed for timely follow-up observations over a broad range of wavelengths, which benefitted the understanding and classification of that event. Similarly, one month later in September 2017, the IceCube experiment detected a very energetic neutrino, which was likely to be of astrophysical origin. Again, an automated alert to many telescopes world-wide revealed that the potential counterpart, the blazar TXS 0506+056, was showing enhanced emission in both high and very high energy gamma-rays. This association would have gone unnoticed, had it not been for the automated alert systems.

These events mark just the beginning of multi-messenger astronomy and highlight the importance of timely collaborative observations.

In this work, the concept of immediate, online data analysis for the IceCube experiment is improved and expanded. Following a summary of the multi-messenger

concept (Chap. 2) the operating principle of the IceCube neutrino observatory (Chap. 3) is explained.

A central ingredient to this work was the improvement of the identification and reconstruction of neutrino candidates in real-time at the South Pole (Chap. 4). For every identified event, a short summarizing report is sent to the north immediately where it can be analyzed further. Three applications of this event stream are developed: First, it allows monitoring known gamma-ray emitters for time-variable neutrino emission (Sec. 6.1). Second, it is also used to monitor the entire sky for neutrino flares, unbiased of pre-conceived source hypotheses (Sec. 6.2). Third, it contains events which have a large probability of being of signal-like origin and are therefore interesting by themselves (Sec. 6.4).

The work concludes with the study of two promising source candidates: 1ES 1959+650 is a blazar, which is famous for a gamma-ray flare in 2002, during which a neutrino may have been detected by IceCube's predecessor experiment AMANDA. The recent flaring activity in gamma-rays warrants another look at this object (Sec. 6.5).

Finally, the aforementioned blazar TXS 0506+056 is of interest beyond the coincidence of a high energetic neutrino and a gamma-ray flare. It has also been investigated for historical activity using IceCube's large sample of historically recorded data (Sec. 6.6).

2 Multi-Messenger Astronomy

The discovery of cosmic rays by Pacini and Hess in 1912 [1, 2] has greatly boosted particle physics and opened up the new field of astro-particle physics. This chapter summarizes the relation between the cosmic rays, their potential sources and the use of the different particles in the context of neutrino astronomy.

The main question of this work concerns the origin of high-energetic neutrinos, which can be produced in two channels: The photohadronic channel, in which a proton interacts with an ambient photon,

$$p(\bar{p}) + \gamma \rightarrow \Delta^+ \rightarrow \begin{cases} p + \pi^0 \\ n + \pi^\pm \end{cases} , \tag{2.1}$$

and the hadronuclear channel,

$$p + p \rightarrow \text{hadrons} \rightarrow \pi^{0,\pm} + X , \tag{2.2}$$

in which two protons interact. Photohadron production requires more energetic protons, while hadronuclear production is also possible for low-energetic protons. In both cases, the pions decay, giving rise to (among other particles) neutrinos and photons:

$$\pi^0 \rightarrow \gamma + \gamma , \tag{2.3}$$

and

$$\begin{aligned} \pi^\pm &\rightarrow \mu^\pm + \nu_\mu(\bar{\nu}_\mu) \\ &\quad \hookrightarrow e^\pm + \nu_e(\bar{\nu}_e) + \bar{\nu}_\mu(\nu_\mu) . \end{aligned} \tag{2.4}$$

A source of energetic protons, which is possibly surrounded by radiation and photon fields, should therefore produce both photons and neutrinos. Detecting these messenger particles allows to probe this model.

The protons (and other charged nuclei) in this scenario are the particles which also make up the cosmic rays, described in Sec. 2.1. Afterwards, the acceleration and potential source classes, which provide favorable environments, are discussed in Sec. 2.2. After a review of the features of the cosmic messenger particles in Sec. 2.3, the chapter concludes with the current state of neutrino astronomy 2.4.

2.1 Cosmic Rays

100 years after its discovery, the origin of this extra-terrestrial radiation is still unclear. Cosmic rays are charged ions arriving at Earth with energies reaching up to 300 EeV.

Their energy spectrum, which is shown in Fig. 2.1, spans 11 decades in energy. It can be described by a power-law flux of $d\phi/dE \propto E^{-\gamma}$, where the spectral index γ changes in different places of the spectrum, which are labelled the "knee", the "2nd knee" and the ankle.

Around 3 PeV, the knee marks the change of the spectral index from 2.7 to 3.1. The origin of the knee is suggested to correlate with the transition from galactic to extragalactic cosmic rays, as more energetic particles may not be confined by the galaxy's magnetic field anymore. In addition, the composition tends towards heavier nuclei above the knee. The spectrum softens again at the second knee from 3.1 to 3.3. The nature of the ankle at 5 EeV, where the spectral index flattens to 2.5, still debated. Particles in the energy range above 1 EeV are commonly referred to as the ultra-high energy cosmic rays (UHECR).

A strong suppression of the flux above 100 EeV is observed, but it is unclear whether this is simply the maximal energy of the most powerful accelerators, or the upper bound on the energy of extra-galactic protons proposed by Greisen, Zatespin and Kizmin (GZK) [4, 5]. During their travel from the source, cosmic rays of ultra-high energy would interact with photons from the cosmic microwave background,

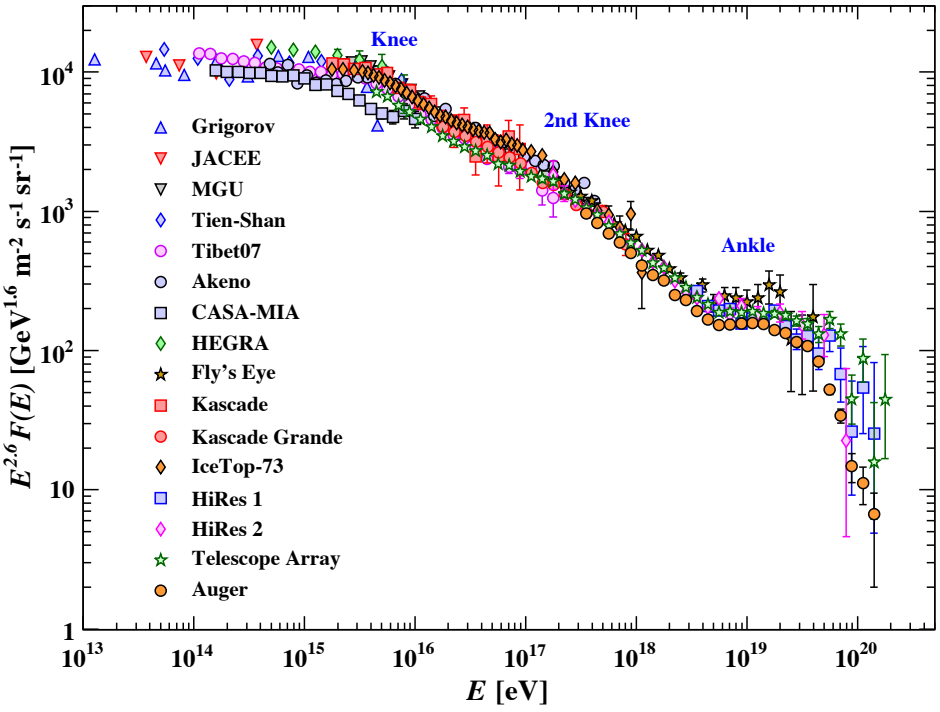

Figure 2.1: All-particle energy spectrum of cosmic rays, shown as a function of energy per nucleus (taken from [3]). The flux is multiplied with $E^{2.6}$ in order to highlight the features of the spectrum.

producing a Δ resonance via

$$p + \gamma \rightarrow \Delta^+ \rightarrow p + \pi^0 \,, \tag{2.5}$$

$$\text{and} \quad p + \gamma \rightarrow \Delta^+ \rightarrow n + \pi^+ \,. \tag{2.6}$$

Pions subsequently decay. Protons can undergo the process again until their energy falls below the threshold of $5 \cdot 10^{19}$ eV. In the context of neutrino observations, this process is relevant as neutrinos are a product of the decaying pions.

The power-law shape of the flux greatly reduces the event rate towards higher energies. While the rate of particles at the knee is around 1 $m^{-2}\,s^{-1}$, it is down to 1 particle per km^2 per century at the highest energies. Consequently, their observation requires the instrumentation of large areas, which is only possible with ground-based detectors. They observe the cosmic-rays indirectly from the particle showers, which develop after the interaction of a high-energetic particle with a nucleus in the atmosphere.

Hence, the primary particle is not directly observed and the composition of this flux is uncertain, with measurements by the Pierre Auger collaboration suggesting a heavier, mixed composition containing elements up to iron [6, 7], whereas the Telescope Array (TA) collaboration reports a light composition of protons and Helium in the range of 1 EeV to 10 EeV. Both results are however subject to large systematic errors, and compatible within their uncertainties. A leptonic component, such as electrons, accounts for less than one percent of the cosmic ray flux [8], and in consequence is neglected when referring to cosmic rays in the following.

In any case, inter- and intra-galactic magnetic fields deflect these charged particles as they travel from their production sites to Earth. Thus, the arrival direction of a particle does not point at its origin complicating the identification of individual sources. Galactic supernova remnants (SNR) have been proposed as early as 1934 [9]. More recently, the Fermi-LAT collaboration did find signatures of neutral pion decays in the gamma-ray spectrum of two SNRs, providing direct evidence that they at least partly supply the galactic cosmic rays [10]. The Pierre Auger collaboration has discovered a large-scale anisotropy in the arrival directions, where a deficit at the galactic center points towards an extra-galactic origin [11]. Furthermore, it has been suspected that the deflection at the highest energies is small enough to allow the identification of sources with a sufficiently large sample of observations. While the Pierre Auger observatory initially found evidence for a correlation of ultra-high energy cosmic-rays with active galactic nuclei (AGN), it could not be confirmed in recent analyses [12].

Once a cosmic ray particle reaches the Earth's atmosphere and interacts with a nucleus, a number of secondary particles is produced. These particles themselves interact again or decay, until their energies are below interaction thresholds and decay is the only remaining option. As a result, a particle shower develops. Most important in the context of this work are pions and kaons which are produced in the shower

and decay into muons and neutrinos:

$$\begin{aligned}\pi^{\pm} \,/\, K^{\pm} &\to \mu^{\pm} + \nu_{\mu}(\bar{\nu}_{\mu}) \\ &\quad \searrow e^{\pm} + \nu_e(\bar{\nu}_e) + \bar{\nu}_{\mu}(\nu_{\mu}) \,. \end{aligned} \tag{2.7}$$

Among the secondary shower particles, muons and neutrinos are the most long-lived or least-interacting particles, which allows them to reach the ground, and even underground detectors such as IceCube. These decays of kaons and pions give rise to the so-called "conventional" atmospheric neutrino flux [13]. In addition, the production of charmed mesons contributes additional neutrinos [14]:

$$p + X \to c + \bar{c} + X' \to \overset{\text{hadronize}}{\cdots} \to D^{0,\pm} \to \nu_{e,\mu} + X'' \,. \tag{2.8}$$

The predicted flux is subject to uncertainties from the hadronic interaction cross-sections, which have been measured in collider experiments, such as the LHC, and need to be extrapolated to the higher energies of the cosmic rays. So far, IceCube has not found evidence of this so-called "prompt" atmospheric flux [15].

2.2 Cosmic Accelerators

While observations established the existence of cosmic rays up to ultra high energies, it is unclear how those energies are achieved.

Following the suggestion of Zwicky that supernova remnants might be source of the galactic cosmic rays, Fermi developed models to reconcile the suggestions with the observed energies. Two types of are distinguished [16]: First-order Fermi acceleration (also known as diffusive shock acceleration) is thought to occur at the boundary of moving magnetic shock fronts, where the shock wave locally propagates like a plane wave. The particles ahead (downstream) of the shock wave has the initial energy E_0 and hits the shock front, which travels at velocity β. Turbulent magnetic fields cause it to scatter several times, yet it has a finite probability to exit the shock, having gained energy. While the energy gain at each scatter depends on the incoming and outgoing angles between particle velocity and shock front, it can be shown that the energy spectrum in this simple model follows

$$\frac{dN}{dE} \propto \left(\frac{E}{E_0}\right)^{\gamma} \tag{2.9}$$

The spectral index γ is related to the escape probability and the energy gain per scatter, it is found to be around -2. Due to interactions of the accelerated particles on their way to Earth, the observed spectrum is softer.

Second-order Fermi acceleration can take place at the boundary of moving, magnetized interstellar clouds. In case of the shock front not being an approximately plane wave, the particle is scattered randomly, causing a lower energy gain per scatter and making this process muss less efficient than the first-order acceleration.

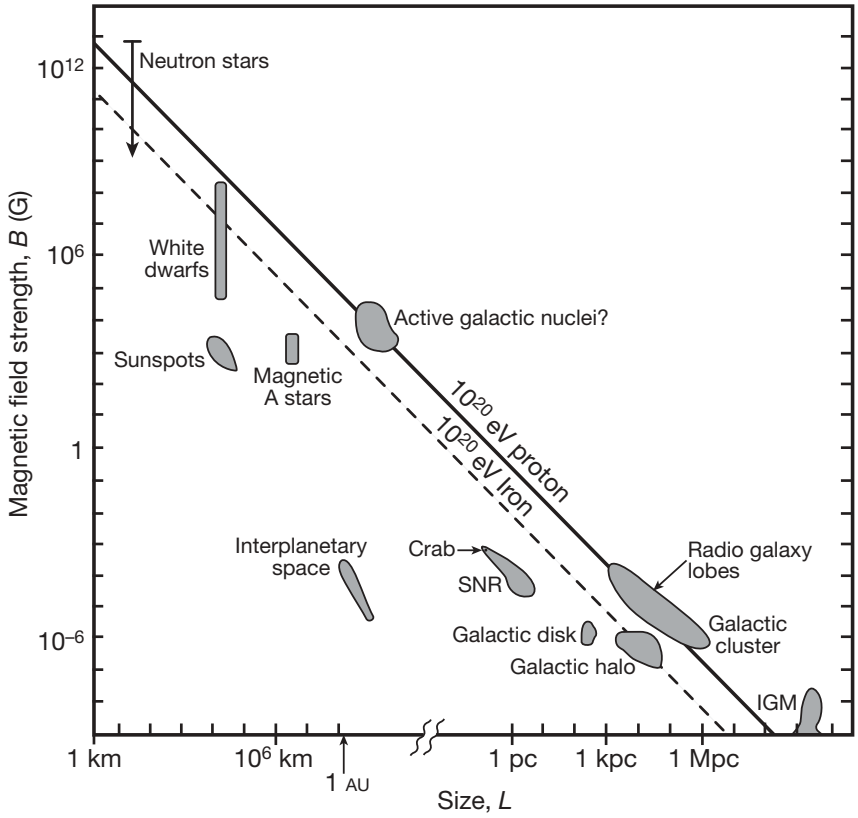

Figure 2.2: Hillas diagram (taken from [17]). Particles can only be accelerated as long as they are confined by the magnetic field B in the acceleration region of size L. The solid (dashed) line marks the GZK cut-off for protons (irons). (SNR: supernova remnants. IGM: intergalactic magnetic field).

In a magnetic field of finite radius R, a particle will eventually reach an energy large enough, such that it will not be contained by the magnetic field anymore. Assuming a particle of charge q with momentum p moving perpendicular to the magnetic field B, then its Larmor radius R is given by

$$R = \frac{p}{|q|\,B} \,. \tag{2.10}$$

Once the energy reaches E_{max} (and $E \approx p$), the radius will exceed the size of the magnetic field, allowing the particle to escape the accelerating environment. Therefore

$$E_{max} = |q|\,B\,R \,. \tag{2.11}$$

Increasing particle energies require either stronger magnetic fields or larger radii. This relation illustrates the limit of particle acceleration in earth-bound, human-made accelerators, which are limited by the practical constraints of large accelerator radii.

Possible astrophysical acceleration sites are shown with respect to Eq. 2.11 in Fig. 2.2. This approach only constrains the maximum attainable energy, in order to reach it an acceleration mechanism must be present.

Active Galactic Nuclei

Active galactic nuclei (AGN) are central regions of galaxies, where matter is accreted around a supermassive black hole, i.e. a black hole's mass M_{BH} is in the range of $10^6 - -10^{10}$ solar masses ($M_\odot$). Matter accreted and falling into the black hole produces activity in the form of emission across the entire electromagnetic spectrum. In equilibrium conditions, where the inward gravitational pull equals the outward radiation pressure, the attainable luminosity is given by the Eddington luminosity:

$$L_{edd} = 1.3 \cdot 10^{38} \left(\frac{M_{BH}}{M_\odot} \right) \text{erg s}^{-1} \ . \quad (2.12)$$

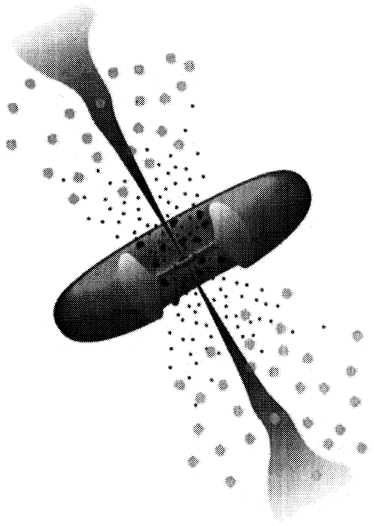

Figure 2.3: Sketch of an active galactic nucleus (taken from [18]).

Conservation of angular momentum causes matter to form an accretion disk around the black hole. In 10% of the AGN, infalling matter is accelerated and forms two collimated jets perpendicular to the accretion disk, as sketched in Fig. 2.3. The jet radiates along its axis, and those AGN where the jet is pointed towards Earth define the sub-class of blazars.

Blazars which show broad emission lines in their spectrum are classified as flat-spectrum radio quasars (FSRQ), while those without broad emission lines fall into the category of BL Lacertae objects (BL Lacs). Although the formation mechanism of the jet is not entirely understood, the matter and radiation in the jet are thought to provide an astrophysical beam dump, which gives rise to different particle physics processes. In gamma-rays, the spectral energy distribution (SED) generally exhibits two humps, as shown in Fig. 2.4. Leptonic models attempt to explain the low-energy hump by synchrotron emission from electrons, and the high-energy hump by inverse Compton scattering of the radiation fields. Alternatively, hadronic models employ decays of charged mesons, in particular

$$\text{charged pions, } \pi^\pm \to \mu^\pm + \nu_\mu(\bar{\nu}_\mu) \ , \quad (2.13)$$
$$\hookrightarrow e^\pm + \nu_e(\bar{\nu}_e) + \bar{\nu}_\mu(\nu_\mu) \ ,$$
$$\text{and neutral pions, } \pi^0 \to \gamma\gamma \ . \quad (2.14)$$

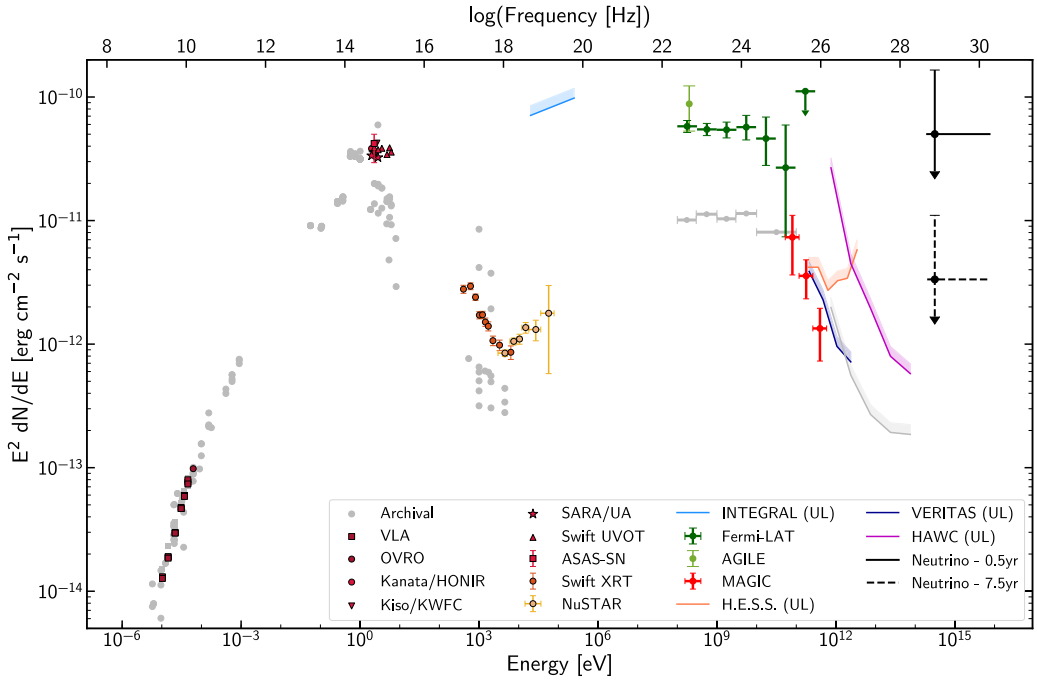

Figure 2.4: Spectral energy distribution (SED) of the blazar TXS 0506+056 (taken from [19]). The multi-wavelength observation campaign following an IceCube high-energy neutrino alert in 2017 yielded the observation of the SED in the flaring state, while grey data points were taken during a past, quiescent phase.

The decay in Eq. 2.13 yields a flavor ratio of $(\nu_e : \nu_\mu : \nu_\tau)$ of $(1 : 2 : 0)$. Oscillations on the journey to Earth would average out the flavors yielding a ratio of $(1 : 1 : 1)$ [20]. (Not) Observing those neutrinos would therefore allow a distinction of leptonic and hadronic scenarios. The possibility of hadronic emission makes blazars a prime target in the search for the sources of extra-galactic neutrinos. Another distinction between the models is through flux variability: In a leptonic scenario, both humps would originate from the same environment and show correlated variability, whereas hadronic scenarios suggest that flares could appear only in the high-energy regime, without correlated low-energy variability (an "orphan" flare) [21].

The location of the synchrotron peak and the flux ratio between both humps allow a classification along the "blazar sequence", from FSRQ, over low-frequency peaked BL Lacs (LBL), to high-frequency peaked BL Lacs (HBL).

Supernovae and Gamma Ray Bursts

Another source class that is expected to produce neutrinos are supernovae. In fact, the supernova 1987A was the first case of a multi-messenger observation, which

allowed the first glimpse at extra-galactic neutrinos at MeV energies. Three hours prior to the optical discovery of what is the closest supernova in the last 400 years, bursts of neutrinos were recorded by three neutrino experiments: Baksan, IMB and Kamiokande II [22–25]. The shock which develops in the exploding supernova expands into the interstellar space and can accelerate particles using first-order Fermi acceleration [9, 16]. Nearby molecular clouds can provide a target for the relativistic particles, such that pions are produced in nuclear interactions. Fermi-LAT has recently observed the gamma-rays from π^0 decays in two supernova remnants (SNR), thereby confirming SNRs as acceleration sites for galactic cosmic rays up to a few GeV [10].

Even more energetic processes are gamma-ray bursts (GRB), which release up to 10^{54} erg in beamed gamma-ray emission over a time scale of seconds to minutes. Bursts lasting for more than two seconds are considered long GRBs and linked to the aforementioned core-collapse supernovae [26]. Short GRBs on the other hand have recently been correlated with the merger of neutron stars [27].

2.3 Cosmic Messengers

Particle physics culminated in the very successful "Standard Model", which comprises three generations of matter, separated into quarks and leptons and interacting through electromagnetic, weak and strong forces.

Those elementary particles, and composites thereof, serve as unique cosmic messengers. Protons and charged nuclei have already been introduced as the main component of the cosmic rays. Their charged nature makes them susceptible to deflection in (inter-)galactic magnetic fields. In turn, directly pin-pointing individual sources is prohibited by their near-isotropic flux.

Photons have been the tool to study potential sources for many decades. Their electrically neutral nature allows them to point back at their origin. Different energy regimes are distinguished and a large variety of telescopes and instruments has been designed for the study of their wavelengths, such as the Fermi-LAT satellite for the high-energy regime (50 MeV – 300 GeV) [28], and the Imaging Air Cherenkov Telescopes (IACT) MAGIC [29, 30], VERITAS [31], and HESS [32] for the very high-energy regime (VHE, above 50 GeV). However, in the VHE gamma-ray regime, extragalactic background light (EBL) limits the exploration of extra-galactic sources [33, 34]. It is the product of all stellar emission in the universe, between infrared and ultraviolet wavelengths [35]. Pair production between VHE photons and EBL photons attenuates the VHE gamma-rays. Thus, the furthest observed source of VHE gamma-rays is the blazar QSO B0218+357 at a redshift of 0.944 [36].

Nevertheless, gamma-ray observations in the high- and very high-energy regime can resolve sources with arcminute precision. Fermi-LAT is able to survey the entire sky every three hours, providing a large sample of near-continuous observations in the high-energy range. Ground-based telescopes, such as MAGIC, can access the VHE regime, with a smaller field of view of 4 deg^2, and requiring dark conditions. These constraints allow taking snapshots of the VHE emission, following pre-planned observation schedules, or external triggers.

Neutrinos

Similar to photons, neutrinos are not electrically charged. Therefore they can reach observatories undeflected and in principle point back to their source. Their weakly-interacting nature and correspondingly small cross-section allows them to travel greater distances than photons. In addition, they may escape dense environments, which would otherwise trap or absorb photons. Their greatest strength is also their greatest weakness. The small cross-section and the low flux at the highest energies requires large-scale detectors, such as IceCube.

However, as mentioned before, the production of neutrinos is tied to hadronic interactions (Eq. 2.13), and goes along with the production of high-energy gamma-rays. Therefore, the observation of a cosmic source of high-energetic neutrinos would provide valuable input to theoretical models. Pion decay also occurs in the atmosphere in cosmic ray-induced showers, posing an additional challenge to experiments.

2.4 Neutrino Astronomy

Only three sources of extra-terrestrial neutrinos have been discovered so far: the sun, the supernova 1987A, and a diffuse flux of astrophysical neutrinos. While neutrinos from both the sun and the supernova have been detected in the MeV range, the diffuse flux measured by IceCube consists of TeV to PeV energies.

With the IceCube detector at the South Pole, it can be measured on two ways. A sample of through-going muons which originate from muon-neutrino interactions provides a large number of events. Most of them originate from atmospheric neutrinos. Looking through the Earth at the hemisphere opposite of the detector provide a natural shielding against atmospheric muons. The current best-fit flux is

$$d\phi/dE = 1.44^{+0.25}_{-0.24} \cdot (E/100\,\mathrm{TeV})^{-2.28^{+0.08}_{-0.09}} \cdot 10^{-18}\,\mathrm{GeV}^{-1}\,\mathrm{cm}^{-2}\,\mathrm{s}^{-1}\,\mathrm{sr}^{-1}[40]\,. \qquad (2.15)$$

Starting events require the neutrino interaction vertex to be inside the detector. This a self-veto technique provides an efficient suppression of both atmospheric muons and neutrinos. Therefore, it is not limited to one hemisphere, allowing a measurement over the entire sky. The best-fit flux is

$$d\phi/dE = 6.45^{1.46}_{-0.46} \cdot (E/100\,\mathrm{TeV})^{-2.89^{+0.20}_{-0.19}} \cdot 10^{-18}\,\mathrm{GeV}^{-1}\,\mathrm{cm}^{-2}\,\mathrm{s}^{-1}\,\mathrm{sr}^{-1}[41]\,. \qquad (2.16)$$

Both analyses select different event topologies and access different parts of the spectrum, hence the difference between Eq. 2.15 and 2.16 could point at a break in the spectrum, although there is no evidence for a break in either analysis. The ANTARES experiment located in the Mediterranean sea offers a complementary view. Due to its smaller instrumented volume, it has not been able to discover the astrophysical flux, but yielded limits compatible with the IceCube results [42].

The observed fluxes are derived from a statistical average, it is not possible to distinguish astrophysical from atmospheric neutrinos on a per-event basis. However, from the measured flux, several hundred astrophysical neutrinos are expected per

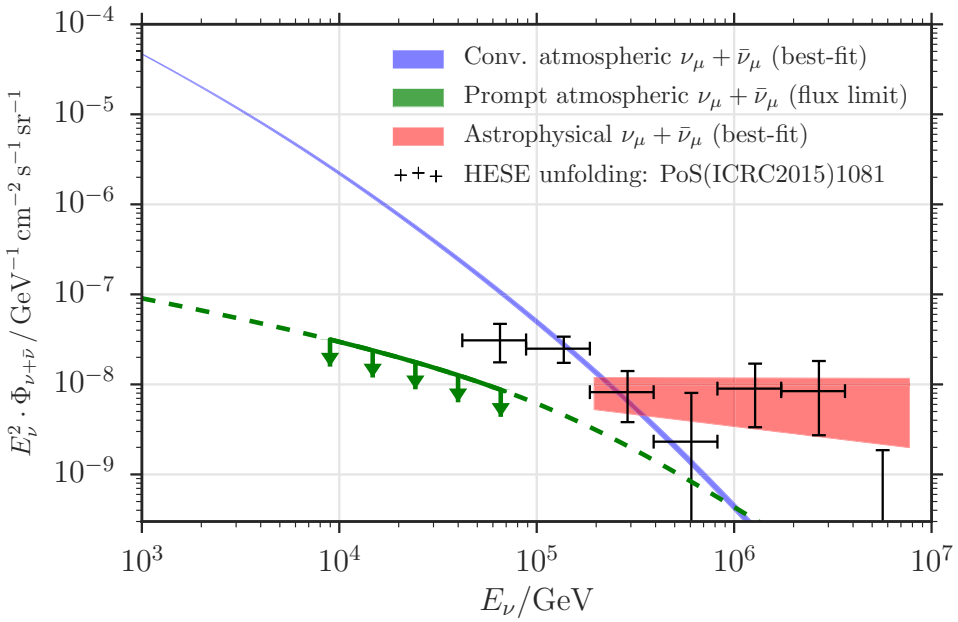

Figure 2.5: Best-fit neutrino spectra for the unbroken power-law model. The width of the line corresponding to conventional atmospheric neutrinos (blue) represents the one sigma error on the measured spectrum. The width of the line corresponding to astrophysical neutrinos (red) shows the effect of varying both astrophysical parameters within one sigma of the best fit values, without accounting for correlation. The green line represents the upper limit on the prompt model [37]. The horizontal width of the red band denotes the energy range of neutrino energies which contribute 90% to the total likelihood ratio between the best-fit and the conventional atmospheric-only hypothesis. The black crosses show the unfolded spectrum published in [38] (Figure and caption taken from [39]).

year. Thus, the strongest sources of neutrinos might yield more than one event and appear as a cluster of events. In addition to separating signal from background, searching for clusters also benefits from the improved directional pointing of multiple events. While for individual muon-neutrinos typical angular errors of 0.5° to 1° can be achieved, the point spread function of multiple signal events reduces to ≈ 0.3° (as shown later in Sec. 6.2).

So far, the history of high-energy point-source searches is mostly a history of non-detections. From the high-energy starting events, which have a high-chance of being of astrophysical origin, no clustering has been observed, as shown in Fig. 2.6a. A likelihood-based search method has been employed, yielding a p-value of 77 % compatibility with the null hypothesis [43]. The situation with the sample of through-going muons is similar: the likelihood analysis has yielded a p-value of 29 % in the northern sky and 17% in the southern sky [44]. Including a prior on the energy

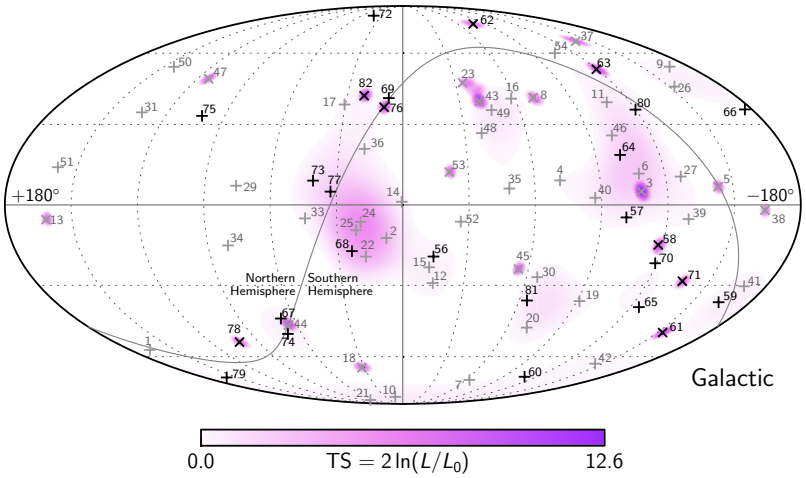

(a) Skymap of high-energy starting events [43].

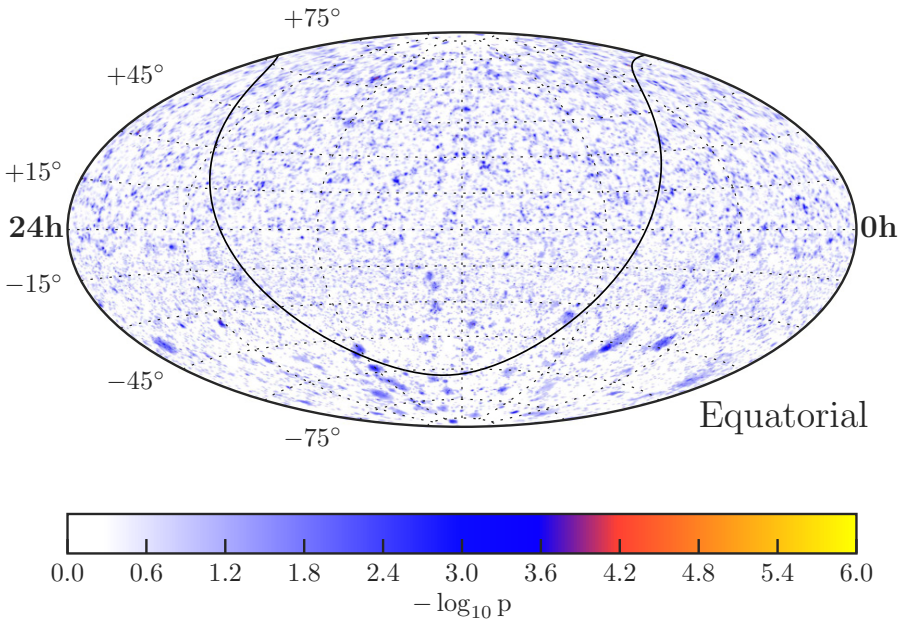

(b) Skymap of likelihood analysis using through-going muon-neutrino candidates [44].

Figure 2.6: Two recent skymaps from searches for neutrino point sources with IceCube. In both cases, no significant excess of events was observed.

spectrum, requiring it to be close to that of the measured astrophysical flux in the northern hemisphere has also not shown any evidence for sources [40]. In addition, a generic model for time-dependent emission has been tested, as well as correlation with the gamma-ray flux of sources monitored by Fermi-LAT [45]. The combined data samples of IceCube and ANTARES have been searched for an excess of neutrinos correlated with the Galactic plane. No significant excess was found, and the sensitivity

of the combined data set starts to constrain models for Galactic cosmic ray production and transport [46].

In summary, with a large sample of neutrino candidates recorded by existing neutrino detectors no evidence for neutrino sources could be found in time-integrated searches. After 10 years, continuing to operate the experiments for another year only improves the sensitivity by a few percent.

Alternative approaches are required: by combining the neutrino observations with those of gamma-rays and searching for correlated emission on short time-scales, the background can be suppressed effectively. The combined significance of a contemporaneous observation can unravel sources, which would otherwise not stand out in a stand-alone IceCube analysis. As such, this work aims to increase the amount of contemporaneous observations through a real-time analysis of the neutrino data, which can provide timely triggers to gamma-ray observatories.

3 Neutrino Detection with IceCube

In order to probe high-energetic phenomena in the universe, IceCube aims to detect neutrinos in the energy range of TeV to PeV.

While solar neutrinos in the MeV range were detected in radiochemical detectors in underground laboratories, the power-law scaling of the astrophysical flux at the highest energies and the small interaction cross-section requires a large scale detector. Detector projects, former and current, proposed or realized, such as DUMAND [47], Baikal [48], ANTARES [49] and AMANDA [50], have explored the possibility of using a large, naturally occurring detection medium.

High-energy neutrino interactions yield charged particles, which traverse the medium, water or ice, faster than the phase velocity of light in that medium. Optical sensors are placed in the medium in order to record the Cherenkov photons, which are emitted during superluminal motion [51]. Collecting enough photons for a precise reconstruction with a sparsely instrumented detector requires a detection medium with large absorption and scattering lengths. Large bodies of such clear media can be found in remote lakes, the deep ocean, and glaciers.

3.1 The IceCube Concept

The IceCube neutrino observatory is located at the geographic South Pole. 5160 digital optical modules (DOMs) are deployed in the Antarctic glacier at depths between 1450 m and 2450 m, as can be seen in Fig. 3.1.

The modules are aligned and connected through 86 vertical strings. Each string consists of 60 DOMs and a cable, which connects the optical modules to the counting house ("IceCube Lab") on the surface, supplies power and enables communications. 78 of the strings are aligned in a hexagonal grid with 125 m spacing, which makes up the primary detector. DOMs are placed at intervals of 17 m along the strings, starting from the bottom end. The remaining 8 strings form the more densely instrumented sub-detector "DeepCore", with a string spacing between 41 m and 105 m, and a DOM spacing between 7 m and 10 m. Six of DeepCore's strings feature DOMs with 35% higher quantum efficiency. In turn, while the larger IceCube detector's energy threshold is around 100 GeV, it is lowered to 10 GeV in the DeepCore region.

In addition, an array of 162 ice-filled tanks is located at the surface, located in pairs above the IceCube strings. Each tank is filled with ice and contains two IceCube DOMs. This "IceTop" detector is sensitive to cosmic-ray induced air showers in the energy range from PeV to EeV [53].

The deep Antarctic glacier, where the IceCube detector is located, provides suitable

conditions for the detection of Cherenkov light. Pressure of the glacier on top causes the deep ice to be free of air bubbles. Yet, photons still undergo scattering and absorption processes, which affect the detection efficiency and the reconstruction accuracy. Proper understanding of the ice is therefore a crucial ingredient and subject to past and ongoing studies [54]. In situ measurements have found the South Pole ice to be clearer than laboratory or lake ice [55]. At the depths of IceCube, scattering is mainly caused by dust particles, like mineral grains and sea salt crystals. Similarly, the absorption length in the South Pole ice is dominated by impurities in the form of insoluble dust [56]. A map of the scattering and absorption coefficients as a function of depth and wavelength is shown in Fig. 3.2. Starting at 1400 m and deeper, scattering and absorption are minimal, although four peaks are visible. The most prominent peak is located at a depth of 2000 m could be traced to dust concentration which accumulated $\approx 65,000$ years ago [57]. The description of the ice has been refined in many iterations over time by aggregating measurements, such as calibration using light sources deployed along with AMANDA [56]., ice core measurements from different places in Antarctica [58, 59], to in situ measurements obtained with the LEDs mounted in the IceCube DOMs [54]. New measurements also allowed refinements to the modelling itself, starting a uniform and homogenous model, to the inclusion of the depth-layered structure, the parametrization of the increased scattering in the refrozen drill holes, the tilt of the layers, and the anisotropy [60].

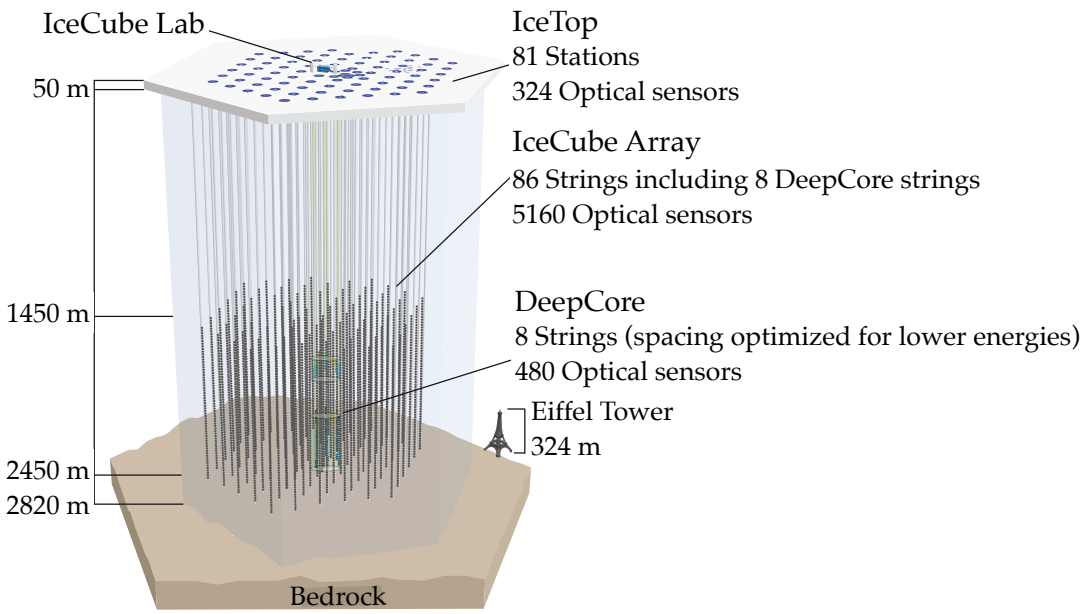

Figure 3.1: Sketch of the IceCube Detector, which is located at the South Pole (taken from [52]). Holes were drilled into the ice, reaching depths of ≈ 2.5 km. A string hosting 60 optical sensors was lowered into each of the 86 holes, thus instrumenting approximately 1 km^3 in the clearest ice of the Antarctic glacier.

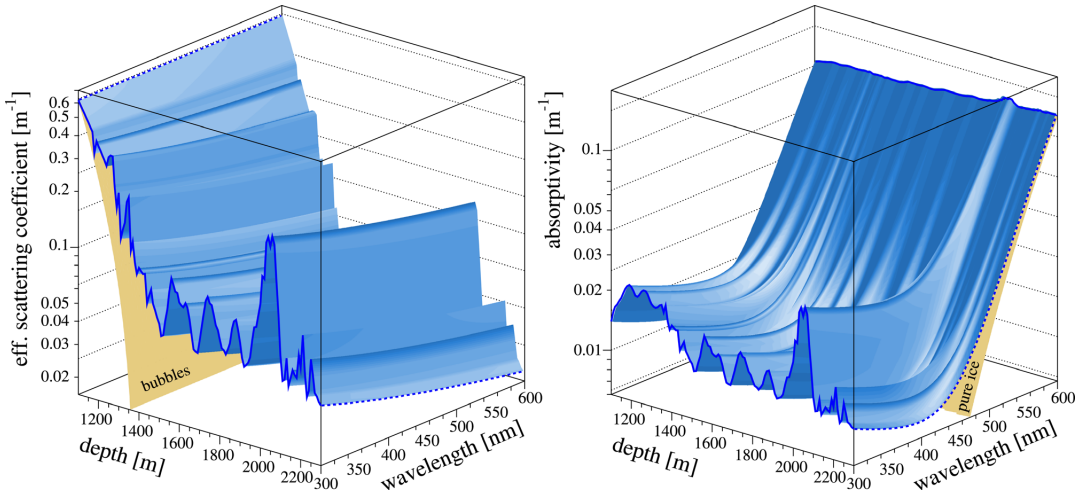

Figure 3.2: Map of the optical scattering and absorption in the South Pole ice (taken from [56]). The effective scattering coefficient (absorptivity) is the inverse of the mean free path with respect to scattering (absorption). Yellow surfaces indicate the sole contribution of air bubbles to scattering, and the contribution from pure ice to absorption. Blue surfaces show the features of the South Pole ice with all its impurities.

IceCube is sensitive to neutrinos interacting in deep inelastic scattering with an atomic nucleus in or near the detector. Different types of interactions yield different signatures in the detector:

- Neutral-current interactions:

$$\nu_l + X \xrightarrow{Z} \nu_l + X' \,. \tag{3.1}$$

  While the neutrino escapes undetected, the nucleus X is broken up and its remnants X′ yield a hadronic particle shower.

- Charged-current interactions:

$$\nu_l + X \xrightarrow{W} l + X' \,. \tag{3.2}$$

  If the lepton l is a muon above GeV energies, it will travel far enough to be detectable through a "track-like" signature. An electron or tau neutrino will instead trigger an electromagnetic shower. In addition, the fragmented nucleus X′ yields a hadronic shower.

  In the case of a tau neutrino, the tau lepton has a median range of $\approx 50\,\mathrm{m}/1\,\mathrm{PeV}$, allowing the identification of tau neutrino-induced events at PeV energies.

In addition, downward-going muons produced in cosmic-ray induced air showers above the detector can reach and pass through the detector.

The electromagnetic or hadronic showers produced in the neutrino interactions have lengths of several meters. They are therefore almost point-like when compared to the sensor spacing of IceCube. Cherenkov light from their decay products forms a spherical light pattern. On the one hand, the directional reconstruction of the primary neutrino is challenging, yielding a median resolution of 10° at 100 TeV. On the other hand, contained showers allow for a precise determination of the energy with an uncertainty of approximately 10% [61].

Muon tracks leave an elongated light signature that is distinct from the spherical shape of showers. The long lever arm greatly benefits the angular reconstruction, providing an angular resolutions of 0.3° at 1 TeV (Fig. 3.7). Traversing the entire detector prohibits a calorimetric measurement and limits the energy resolution to a factor of 2 (Sec. 3.4.3).

An assortment of IceCube event signatures is shown in Fig. 3.3. This work focuses on the identification and reconstruction of muon tracks, leveraging their pointing capabilities for astrophysical purposes. Muons produced in atmospheric showers tend to mimic the signature of neutrino-induced muon tracks, as can be seen by comparing Fig. 3.3a and 3.3d. Thus a large part of this work is devoted to removing them.

3.2 Digital Optical Modules

The principal sensor components of the detector are contained in the DOMs. A spherical glass sphere of 13" in diameter houses the components sketched in Fig. 3.5.

The main component is a downward-facing 10" photomultiplier tube (PMT). It is complemented by circuit boards responsible for the power supply, data acquisition, communication, and calibration.

Two halves make up the glass sphere, which is split at the equator and joined and sealed as the last step of the module production. A 16 mm hole allows the cable to leave the module. The entire structure of the DOM, the cable penetrator assembly, and the suspension from the main cable (all of which can be seen in Fig. 3.4) are designed to withstand the refreezing process and maintain the vertical alignment of the DOMs along the string.

The photomultiplier is sensitive to wavelengths between 300 nm and 650 nm with a quantum efficiency of 25% at 390 nm. DeepCore's DOMs have a higher quantum efficiency of 34%. A wire mesh grid surrounds the PMT and shields it from the magnetic field at the South Pole, which would otherwise degrade the collection efficiency and the single photoelectron resolution.

For calibration purposes, the "Flasher board" contains 12 LEDs which can emit light with a wavelength of 400 nm on most DOMs, and other wavelengths between 340 nm and 505 nm on 16 special DOMs. The light output can be adjusted by controlling the driving voltage and current, the latter is also monitored by a digitzer for later analysis.

Waveforms recorded by the PMT can vary widely, with amplitudes ranging from 1 mV to 2 V, and widths from 12 ns to 1500 ns, depending on the energy of the observed particle and the distance to the DOM.

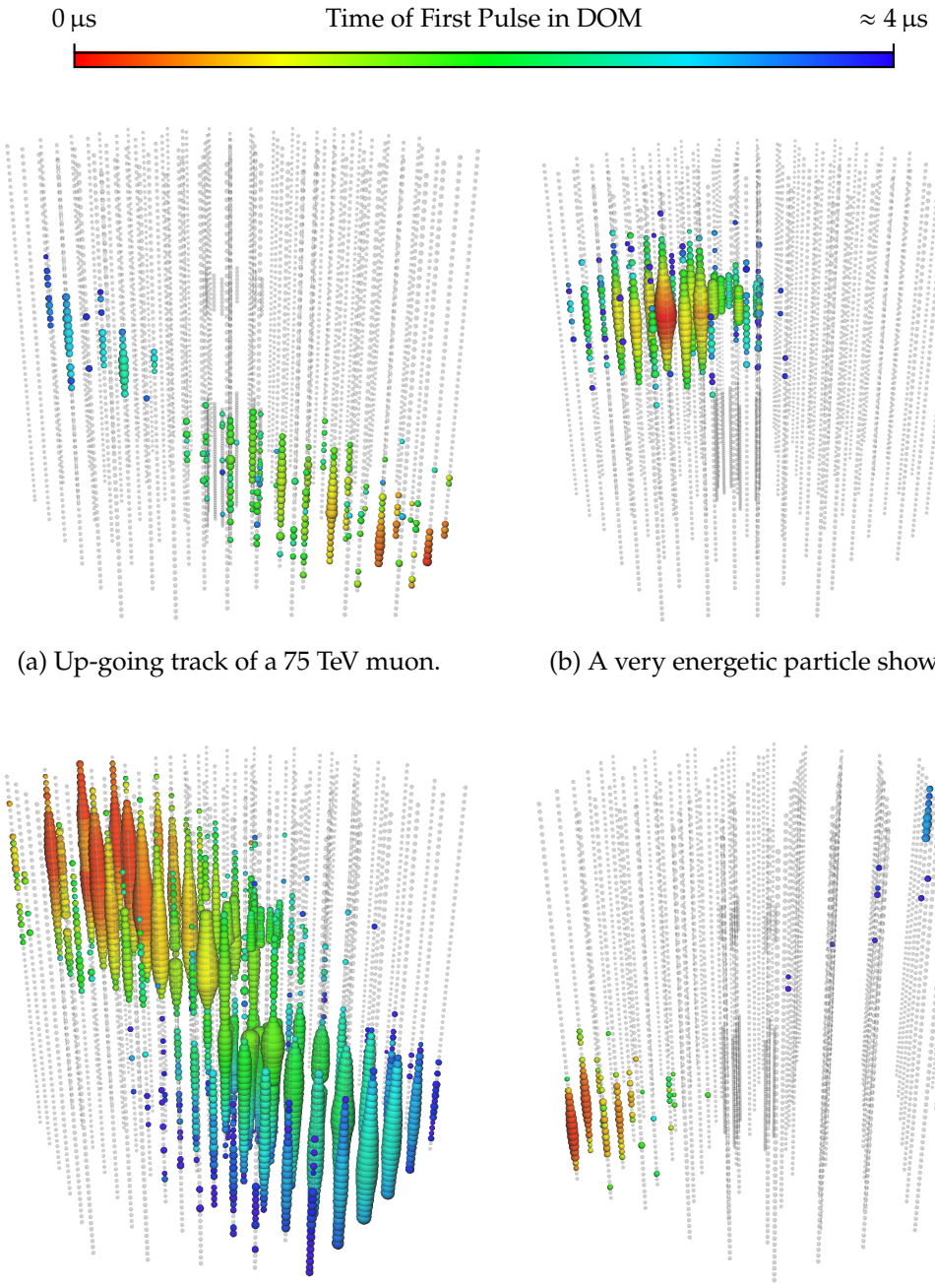

(a) Up-going track of a 75 TeV muon.

(b) A very energetic particle shower.

(c) Muons from an air shower, induced by a 100 EeV cosmic-ray proton.

(d) Two coincident atmospheric muons.

Figure 3.3: IceCube event signatures. Bubble colors are proportional to the time of the first photon recorded in a DOM (red: earliest, blue: latest). Bubble sizes are proportional to the logarithm of the observed charge.

A discriminator triggers the recording of the waveform (called a "launch") once the voltage threshold corresponding to 0.25 photoelectrons is crossed. Routing the PMT signal through the "Delay board" allows recording the waveform starting already 75 ns before the trigger. Analog transient waveform digitizers (ATWD) and a fast analog-to-digital (fADC) converter capture and digitize the PMT signal [62].

The first 427 ns are captured by the ATWD. It provides three channels, which operate at different amplifier gains in order cover the entire dynamic range of the PMT output. Signals are sampled at 300 Msps and digitized with 10-bit resolution. In addition to the ATWD, the fADC continuously samples at a lower rate of 40 Msps, and digitizes with a resolution of 10-bit.

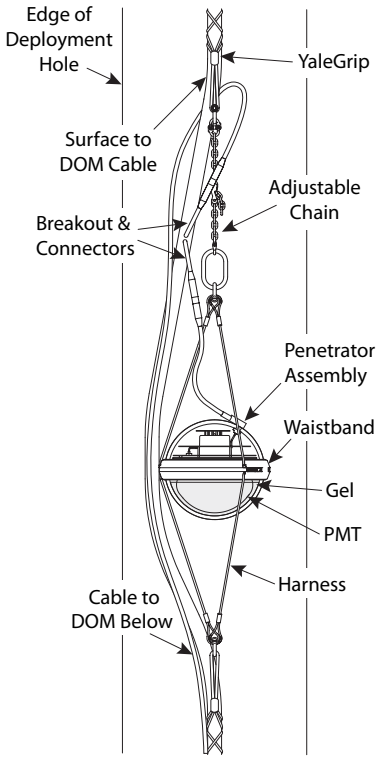

Figure 3.4: DOM suspension and cable routing (taken from [52]).

In summary, for the case of a single photon, the digitized waveform is available from 75 ns before the discriminator threshold until 6.4 µs afterwards. The digitized waveforms follow characteristic shapes of the amplifiers and are proportional to the charge collected by the PMT. In the case of IceCube, a single photon typically deposits $\approx$ 1.6 picocoulombs, which is defined to be 1 photoelectron (PE). Using shape templates of single photon pulses, which were recorded in laboratory and in-ice studies, the output of the four channels from the ATWD and fADC is simultaneously unfolded in a non-negative least squares fitting [63]. It provides a series of pulses, each defined by a time, charge and width. This format is sufficiently compact, such that it is included in the daily satellite transmission of all filtered events. A goodness-of-fit test decides whether the unfolding was successful, otherwise the full digitized waveform is included for offline studies.

3.3 Trigger and Event Filtering

The fundamental handling of the detector data is common to all analyses and runs directly at the South Pole. The main goals are:

- defining the triggering criteria, which cause the detector to be read out,

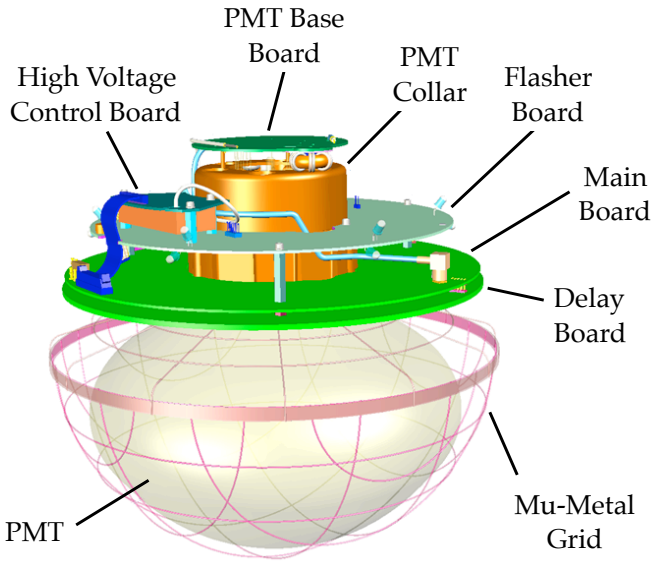

Figure 3.5: Sketch of a Digital Optical Module (taken from [52]). The entire assembly of the PMT and the support electronics are placed in a spherical glass pressure housing (not shown), designed to withstand the pressure of the surrounding glacier.

- splitting the readout into separate physics events,
- cleaning noise hits,
- and selecting potential track-like event candidates.

The end result is a stream of events, each containing a cleaned set of pulses, ready for higher-level analyses such as the one described in Chapter 4.

The next paragraphs will describe each of these steps.

Trigger: As explained in Sec. 3.2, the Digital Optical Modules can observe individual photons and digitize the waveforms from the photomultiplier tube. In order to Next, a trigger system aims to ignore stray noise hits and identify potential signals.

A part of this workload already takes place in the DOM. Once a hit is observed by a DOM, the software on the DOM checks neighboring or next-to-neighboring DOM on the same string for hits coincident within $\pm 1\,\mu s$. For these so called "hard local coincidence" (HLC) hits, the full digitized waveform is stored. If no hits were observed by (next-to-)neighboring DOMs, this is called a "soft local coincidence" (SLC) hit and only the amplitude information is stored, since it is more likely to originate from noise.

Hit information is stored in memory on the DOM mainboard and requested once per second by computers on the surface. HLC hit information is passed to the trigger software to decide which time periods contain potentially interesting hits.

The "simple multiplicity trigger" (SMT-8) requires at least 8 HLC hits during a sliding time window of 5 μs. The threshold is adjusted to match the sensitivity of the detector and varies for the DeepCore and IceTop sub-detectors. Other triggers exist, e.g. for the purpose of taking calibration or minimum bias data.

Realizing the SMT-8 condition marks the start of the trigger time window. It ends once the sliding time window does not contain any more HLC hits. The trigger windows from this and other triggers are merged into a global trigger window. All HLC and SLC hits recorded during this global trigger window are sent to the event builder and written to disk, where it is picked up by the Processing and Filtering (PnF) system for the next steps.

At this point, the data streams consists of "DAQ events", each of which may still contain several particles and will be split into "physics events" in the next step. The median trigger rate is 2.7 kHz, corresponding to 1 TB/day [52]. It is saved to hard disks at the South Pole and shipped to Madison, WI once per year for storage.

Event Splitting: The trigger conditions in the previous paragraph are designed to capture the hits related to particle interactions inside a conservatively padded time window. Hence one DAQ event may be caused by several overlapping triggers and consist of several distinct physics events which need to be split.

Only the SMT-8 is considered in this analysis, and the DAQ event is searched for contiguous time windows during which this trigger condition is fulfilled. Along with 4 μs before and 6 μs afterwards these time window define physics events.

The method is called "trigger splitting" and is the only form of event splitting which is performed in this analysis. It is able to split e.g. two muons which arrive slightly separated in time. However, truly time-coincident muons which are only spatially separated and pass through the detector simultaneously will not be split into separate events. Subsequent reconstruction algorithms, which expect exactly one muon per event, will generally fail on this class of events. Hence they are considered an undesired background to the analysis and further event selection stages will attempt to remove these coincident events.

Other offline analyses employ a form of topological event splitting, which attempts to disentangle spatially-separated particles [64]. Such an approach risks splitting the track of one muon into two parts, e.g. when a dim track traverses the dust layer without depositing any light. The remaining parts of the track would be reconstructed as two muons from similar directions, artificially increasing the significance of a point-source analysis. As the development of this approach has stalled and the aforementioned issue has not been resolved, it is not being used in this analysis.

Pulse Cleaning: The event produced by the splitting procedure contains all pulses recorded during the event time window. A cleaning algorithm is applied to remove pulses which are unlikely to originate from signal: At first, only HLC pulses are kept as a seed. Next, any other (SLC) pulses around each of these DOMs are also kept if they are closer than 150 m and recorded within 1 μs. This process is repeated three

times.

Using the time-ordered series of the surviving pulses, one 6 μs-wide time window is selected which contains the largest number of pulses.

Those steps are intended to identify a bright clusters of pulses which are spatially and causally connected, and remove single DOMs whose pulses stem from either noise or very dim atmospheric muons. The map of surviving pulses is used as the input to all following reconstructions.

Muon Filter: So far, the data stream provides candidates for physics events, each consisting of a set of potential signal hits. Different kinds of particles are observable by IceCube, and a filtering stage aims at an early, quick classification in order to reduce the event rate for more sophisticated analyses.

One of these filters, the "muon filter", aims to reject all events unlikely to be muon candidates, which reduces the event rate from the 2.7 kHz at the trigger level to ≈ 40 Hz.

It attempts a coarse track reconstruction using the "LineFit" and the single-photoelectron likelihood fit (which will be described in detail in Sec. 3.4). For up-going muon event candidates, the likelihood value is used as a measure of the fit quality to reject shower-like event topologies.

For down-going candidates, the event rate is still very large due to the contribution of muons from air showers next to neutrino-induced muons. As the astrophysical neutrino spectrum is expected to be much harder ($\sim E^{-2}$) than the the energy spectrum of atmospheric muons ($\sim E^{-3.7}$), a minimum integrated charge (Q_{tot}) is required for down-going events. The following cut is adopted:

$$\begin{aligned} \frac{\log \mathcal{L}}{N_{ch} - 3} &\leq 8.7 && \text{for} \quad -1.0 < \cos\theta \leq 0.2\,, \\ \log Q_{tot} &> 3.9 \cdot \cos\theta + 0.65 && \text{for} \quad 0.2 < \cos\theta \leq 0.5\,, \\ \log Q_{tot} &> 0.6 \cdot \cos\theta + 2.3 && \text{for} \quad 0.5 < \cos\theta \leq 1.0\,. \end{aligned} \tag{3.3}$$

At 40 Hz the rate of events passing the muon filter is small enough for daily satellite transfer, which is important for offline analyses, and allows running more advanced reconstructions for the subsequent online analysis.

In case of an event passing at least any one filter the extracted set of pulses is sent through a satellite link (with a bandwidth allocation of ~ 100 GB/day) to the data warehouse in Madison, WI. As an additional safeguard against bugs in the processing, the raw waveforms for every triggered event are stored on hard disks at the South Pole and shipped to Madison once a year.

3.4 Muon Event Reconstruction

Particle interactions in (or near) the IceCube detector yield one of several different event topologies. While muons (and highly energetic tau neutrinos) traversing the

detector produce elongated track-like events, neutral-current interactions inside the detector volume show a spherical signature. Specific reconstructions have been tailored for these event topologies – this work however focuses on the reconstruction of track-like events produced by through-going muons. Their long lever arm provides the best handle on their direction (and that of the original neutrino), which is a key ingredient in the search for point-like sources.

Typically, a muon neutrino will undergo a charged-current interaction outside of the detector and the resulting muon traverses the detector. As only the segment of the track contained inside the instrumented volume is observed, the energy of the primary neutrino can only be weakly constrained.

In other analyses [65, 66] a distinction is made with respect to whether the neutrino interaction takes place inside or outside the detector volume. While the inclusion of such knowledge in the reconstruction improves the estimates of both the direction and energy, the algorithms are quite time consuming: At a runtime of 1 h per event they lend themselves to provide a refined estimate of the direction in the wake of the initial alert.

Due to the time constraints and the sparseness of muon tracks starting in the detector, this feature is neglected in the following and all events are treated under the hypothesis of a through-going muon.

3.4.1 Angular Reconstruction

The determination of the original direction of a neutrino candidate is a vital ingredient in searches for point sources. Passing through the filtering chain, several directional reconstructions are performed. The underlying hypothesis for all of them is a track-like signature of a muon passing through the detector.

LineFit: This first, basic reconstruction method assumes that a plane wave of light passes through the detector (disregarding the Cherenkov cone) and produces the observed first pulses in each DOM.

A muon is considered to be traveling along a straight line at a constant velocity $\vec{v}$. Passing through some point $\vec{r}_0$ at time t_0, its position $\vec{r}$ at any time t is given by:

$$\vec{r}(t) = \vec{r}_0(t_0) + (t - t_0)\,\vec{v}\ . \tag{3.4}$$

The line fit minimizes the squared distance between the track hypothesis and the positions of the DOMs $\vec{x}_i$ that recorded a pulse at time t_i,

$$\min_{\vec{v},\vec{r}_0} \sum_{i=1}^{N} ||\,\vec{r}(t_i) - \vec{x}_i\,||_2\ , \tag{3.5}$$

with N being the total number of hit DOMs.

Equation 3.5 can be solved analytically [67] without the need for a time-consuming minimizer, lending itself to a first guess method. An additional hit cleaning improves

this method [68] by excluding hits from likely scattered photons, as scattering properties of the ice are neglected in the fit. Furthermore, additional robustness to noise hits is achieved by replacing the square in Eq. 3.5 with a Huber penalty function [**huber_1964**] which reduces the weight given to hits far away from the track.

Eventually, this method provides both a coarse estimate of the direction as a seed for the following maximum-likelihood fit, as well as an estimate of the velocity $|\vec{v}|$ which is used as a parameter in the final event selection.

Single Photoelectron (SPE) Fit: A more realistic model of the light emission along the muon track can be employed to obtain a refined estimate of the muon direction.

A high-energy muon traveling faster than the phase velocity of light in ice produces a cone of Cherenkov light [51]. Its wavefront is emitted with respect to the muon track under the Cherenkov angle

$$\cos\theta_c = (n\,\beta)^{-1}\,, \tag{3.6}$$

where n is the refractive index and β is the velocity of the muon. The present scenario of relativistic particles ($\beta \simeq 1$) in ice ($n \simeq 1.32$) yields a Cherenkov angle of $\theta_c \approx 41°$ [69].

A muon track expressed in the geometry of Fig. 3.6, traveling in the normalized direction $\vec{v}$ and passing an arbitrary point $\vec{r}_0$ at time t_0, emits a Cherenkov light front which arrives at a DOM located at $\vec{x}_i$ with a distance d from the track. In the absence of scattering the expected photon arrival time t_{geo} is then given by

$$t_{geo} = t_0 + \frac{\vec{v}(\vec{x}_i - \vec{r}_0) + d\,\tan\theta_c}{c_{vac}}\,, \tag{3.7}$$

where c_{vac} is the speed of light in vacuum. The difference to the observed arrival time t_{obs} is called the time residual

$$t_{res} = t_{obs} - t_{geo}\,. \tag{3.8}$$

The probability distribution p_1 for the time residual of a single photon can be used to express the likelihood of observing the all time residuals under a given track hypothesis:

$$\mathcal{L} = \prod_{i=1}^{N_{Ch}} p_1(t_{res,i}|\vec{r}_0, \theta, \varphi)\,. \tag{3.9}$$

Here the muon track has been expressed in terms of a supporting vector $\vec{r}_0$, the zenith angle θ and the azimuth angle φ. For each of the hit DOMs (N_{Ch}) the likelihood considers the first observed photon, respectively, as it is expected have been scattered the least. Hence, Eq. 3.9 is called the single photoelectron (SPE) likelihood.

When performing a maximum-likelihood this method requires a seed, which is provided by the previous LineFit (Eq. 3.5). Aside from the direction the likelihood value itself also yields a quality parameter to judge the hypothesis of an event actually

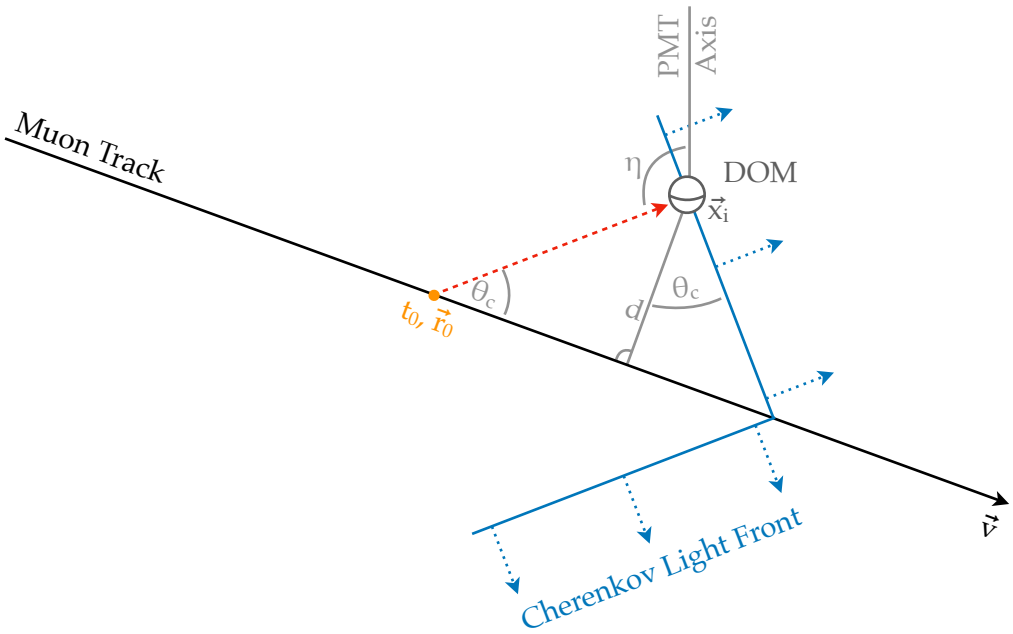

Figure 3.6: Sketch of the Cherenkov light front emitted from a muon track, with the quantities used in the directional reconstruction. The geometric photon arrival time is defined by the time it takes a photon emitted at $\vec{r}_0$ to reach the optical module at $\vec{x}_i$, while traveling unscattered along the path highlighted in red. Adapted from [69].

being a muon with a track-like signature. Compared to the LineFit this method provides a refined estimate of the direction, the precision which depends on the knowledge about the time residual PDF p_1.

Calibration using a laser light source with the Baikal experiment [70] led to the analytic expression (called "Pandel" function)

$$p_1(t_{res}) = \frac{1}{N(d)} \frac{\tau^{-(d/\lambda)} \cdot t_{res}^{d/\lambda-1}}{\Gamma(d/\lambda)} \cdot \exp\left[-t_{res} \cdot \left(\frac{1}{\tau} + \frac{c_{vac}}{n \cdot \lambda_a}\right) - \frac{d}{\lambda_a}\right] \tag{3.10}$$

$$\text{with} \quad N(d) = \exp\left[-\frac{d}{\lambda_a}\right] \cdot \left(1 + \frac{c_{vac} \cdot \tau}{n \cdot \lambda_a}\right)^{-d/\lambda} , \tag{3.11}$$

where λ_a is the absorption length, and λ and τ are fit parameters determined from a photon propagation Monte Carlo simulation.

The AMANDA collaboration fit this function to a model of the South Pole ice, and extended it to account for additional effects such as PMT jitter and the delay in case of backwards illumination of the PMT [69].

Due to detector symmetries or unexpected hits caused by noise or scattering the likelihood space may exhibit several local minima. They can be mitigated using an

iterative approach: After the first iteration yields a direction $\vec{v}_0$, n random directions $\vec{v}_i$ are chosen such that each fulfills $\sphericalangle(\vec{v}_0, \vec{v}_i) = 180°/n$. Those directions are used as seeds in repeated fits. eventually selecting the result with the best likelihood value. In practice, $n = 2$ is chosen for online applications.

MPE Likelihood Fit: In case of muons with an energy larger than 1 TeV it becomes increasingly likely to detect more than one photon in each DOM. Thus, Eq. 3.9 can be modified to express the probability of the first out of N_i photons observed in DOM i at the time residual $t_{res,i}$:

$$\mathcal{L} = \prod_{i=1}^{N_{Ch}} \left[N_i \cdot p_1(t_{res,i}) \cdot \left(\int_{t_{res,i}}^{\infty} p_1(t_{res,i}) \right)^{N_i - 1} \right] , \tag{3.12}$$

forming the multi photoelectron (MPE) likelihood.

Compared to the SPE likelihood, this method provides an improved angular resolution at higher energies at the cost of increased computing time. In order to achieve a fast convergence, this fit is typically seeded with the result of the SPE likelihood fit.

SplineMPE Fit: Instead of using the analytic Pandel function in the MPE likelihood, the parameter p_1 in Eq. 3.12 can be determined more accurately using a simulation of the photon propagation. Such simulations have been performed for various configurations of the light source (muon) and the receiver (DOM), specifically varying the distance between the muon and the DOM, as well as the angle between the track and the PMT axis, and the depth in the ice.

The results of this simulation are available in large multi-dimensional look-up tables [71] and, more recently, in the form of interpolating splines [72, 73]. The latter improve the evaluation time over the look-up tables, reduce the memory footprint, and allow for online use of this algorithm.

The MPE likelihood in connection with a spline-fitted time residual function is called "SplineMPE". It substitutes the homogenous ice model of the Pandel function with a more realistic model that considers the depth-dependent absorption and scattering properties. For the reconstruction of *cascades* recent progress also allowed the inclusion of the anisotropic properties of the ice [74], for which a suitable parameterization with respect to muon tracks has not yet been developed.

A number of improvements to the SplineMPE algorithm have been conceived since its inception [75]. They attempt to model the stochastic energy losses of high energy muons (only the continuous Cherenkov emission has been considered so far), PMT noise, and the inter-DOM timing jitter. It has been tested which of those improvements can be applied in online event reconstructions – while most modifications reduce the angular error at the expense of additional computing time, the following two modifications were included in the online system:

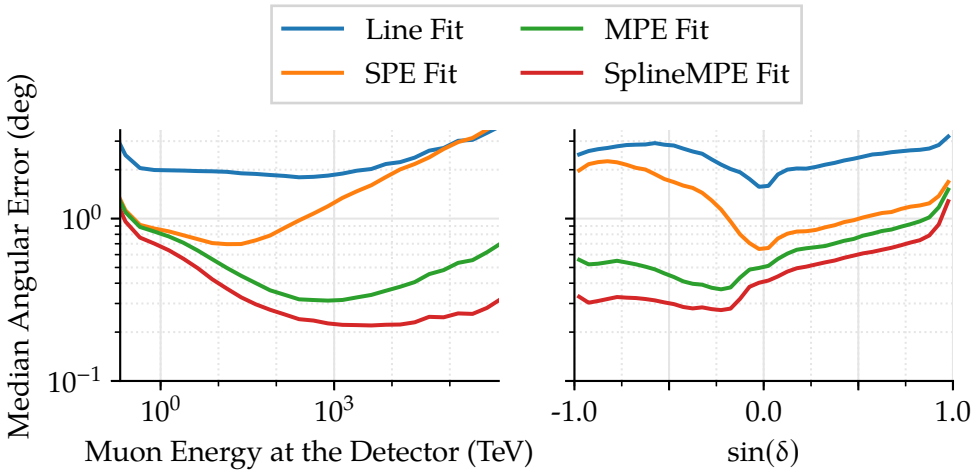

Figure 3.7: Comparison of the median angular resolution for muons, using different reconstruction algorithms at the final event selection level. Left: The angular resolution is shown as a function of the true muon energy at the detector, averaged over all declinations. Right: The angular resolution is shown as a function of the declination averaged over all energies.

- Additional energy losses from the muon in the form of stochastic processes can produce additional, late pulses at the DOMs. Such pulses influence the observed distribution of time residuals, as well as the number of recorded photons N_i in Eq. 3.12. The convergence of the fit can be improved by removing photons which are unlikely to be related to the continuous light emission: The cumulative distribution of the observed time residuals in each DOM is compared to the cumulative distribution of the expected time residuals $\int_0^{t_{res}} p_1(t)dt$ in a Kolmogorov-Smirnov test [76, 77]. If the test fails (a significance level of 20%), the last pulse in a DOM is removed until either the test passes, or only one pulse is left. Only the pulses passing the test are eventually used in the maximum likelihood fit.

- The SPE and MPE likelihood of Eq. 3.9 and 3.12 are combined into $\mathcal{L}_{SPE}^{(1-m)} \cdot \mathcal{L}_{MPE}^{m}$, with the parameter m being a function of the muon energy. It blends between the SPE and MPE likelihoods and has been optimized using simulations. For muons below 1 TeV $m = 0.4$ suppresses the contribution from the MPE likelihood, whereas for muons above 300 TeV the full MPE likelihood is restored with $m = 1$. Although this behavior is not entirely understood, it was found to improve the angular resolution of muon with energies below 1 TeV.

These modifications slightly improve the angular error, but more importantly they speed up the likelihood evaluation and fitting, providing additional headroom to include other costly reconstructions mentioned in the following chapters.

Figure 3.7 shows the median angular resolution for the aforementioned methods at the final level of the event selection. The benefits of the MPE likelihood are clearly visible for high-energetic events, as well as the improvements from the improved ice model used in the SplineMPE fit. The best angular resolution is achieved for horizontal events. For inclined, up-going events the resolution worsens as fewer high-energy muons with high photon counts reach the detector due to earth's absorption, and the detector geometry with its different lateral and vertical DOM spacing suiting horizontal events. For inclined, down-going events the worsening angular resolution is caused by the event selection mostly permitting high-energetic events, whose stochastic light emission is not modeled in the likelihood, and the detector geometry.

A simulation-independent test of the angular reconstruction using the sun and moon shadows has validated the cited angular resolution to a precision of 0.2° [78].

3.4.2 Angular Error Estimation

The search for point sources does not just hinge on a good direction reconstruction but also on the knowledge about the per-event *error* of that reconstruction. It directly influences the probability of of a signal event being reconstructed at a certain direction as described in Sec. 5.

In the most simple form the angular resolution can be determined from a set of simulated events by evaluating the median difference between true and reconstructed directions. However, the accuracy of the reconstruction depends strongly on the circumstances of each event, such as the number of photons recorded, the track length inside the detector, the depth in the ice, or the zenith angle. As such, a per-event estimate of the resolution is preferable.

The following paragraphs describe the methods used to provide a per-event estimate of the angular error. While offline analyses are able to choose the most accurate one, this may come with a computational complexity which the online event reconstruction cannot afford. After studies of the execution time, the best algorithm that can be accomodated within the computational constraints at the South Pole will be chosen based on per-event properties as described later in Sec. 4.4.

Cramér-Rao Estimation: An estimate of the angular resolution can be derived using the Cramér-Rao inequality [79, 80]: It states that the best attainable variance of an unbiased estimator is bounded by the inverse of the Fisher information. Expressed in terms of IceCube's muon track reconstruction a track is described by the five parameters $\vec{x} = (\vec{r}_0, \theta, \varphi)$ and the elements of its covariance matrix are bounded by:

$$\mathrm{Cov}(\vec{x}_i, \vec{x}_k) \geq \frac{1}{I(\vec{x})_{ik}} \,. \tag{3.13}$$

Here, I is the Fisher information matrix defined as:

$$I(\vec{x})_{ik} = -\left\langle \frac{\partial^2}{\partial x_i \, \partial x_k} \log \mathcal{L}(\vec{x}|t_{res}) \right\rangle_{t_{res}} \,. \tag{3.14}$$

The square root of the diagonal elements of the covariance matrix yields an estimate for the variances in azimuth, σ^2_φ, and zenith, σ^2_θ. They can be combined into an estimate of the circularized error [81]

$$\sigma = \sqrt{\frac{\sigma^2_\theta + \sigma^2_\varphi \, \sin^2\theta}{2}} \, . \tag{3.15}$$

Eventual analytical expressions for the covariance matrix were derived and can be found in [82]. The availability of closed-form expressions and the lack of a numerical minimization make this the fastest and most stable approach. With execution times generally below 1 µs it is applied to all events passing the online filter.

Paraboloid Method: The directional reconstruction is performed through a likelihood fit where the shape of the likelihood minimum is expected to relate to the angular resolution. In the case of Gaussian-distributed measurement errors of time residuals in the likelihood, or a large number of measurements, the likelihood function will converge towards a Gaussian shape itself and the standard deviation σ_x with respect to a parameter x can be determined from

$$-\log \mathcal{L}(x \pm \sigma_x) = -\log \mathcal{L}(x) + 0.5 \, . \tag{3.16}$$

In the case of muon track reconstruction, the likelihood function has several fit parameters of which only the azimuth and zenith are of interest, and the region around the minimum is expected to be of a paraboloid (2-dimensional Gaussian) shape.

In practice, 24 sampling points are defined around the minimum – 3 different choices in zenith with 8 equally spaced points in azimuth. In order to evaluate the profile likelihood landscape the azimuth and zenith values are fixed at each sampling point and the likelihood is optimized in the remaining parameters of the supporting vector $\vec{r}_0$. A 2-dimensional parabola is fitted to the sampling points from which the size of the ellipse corresponding to Eq. 3.16 can be determined [83].

Previous analyses [81] found best sensitivity when averaging the semiaxes σ_x and σ_y of the ellipse, yielding the angular error

$$\sigma = \sqrt{\frac{\sigma^2_x + \sigma^2_y}{2}} \, . \tag{3.17}$$

The need for additional numerical minimization steps makes this approach much slower than the Cramér-Rao-based estimate, but it has been shown to yield the best estimate of the angular resolution. Hence, it is the standard method in offline analyses [44, 84] at the time of writing.

Bootstrapping: Another statistical method to estimate distributions of statistics in cases where the underlying theoretical distribution is unknown is the "bootstrapping"

approach, which applies a random resampling with replacement to the available set of observations.

A sample of observations $X_0 = (x_1, \ldots, x_k)$ defines the empirical distribution function $\hat{F}$ to the (unknown) theoretical distribution F. Now, the approach generates the bootstrap samples $X_b = (x_1^*, \ldots, x_k^*), b = 1 \ldots n$ by randomly drawing with replacement n random samples according to $\hat{F}$. Finally, the distribution of the statistical measure of interest T is not determined from the theoretical distribution, $T(F)$; instead it is approximated from the empirical distribution function using the bootstrapped samples $T_b = T(X_b, \hat{F})$ [85].

In the case of IceCube, this method can be used to obtain an estimate for the angular error of a track reconstruction. In the language used before, F corresponds to the direction of the track and x can be understood as the pulses seen in the detector from a given track. A bootstrapped event is created by randomly sampling pulses from the charge-weighted set of pulses in original event, until the total charge in the resampled event equal to the total charge in the original event. In practice, this step is repeated 6 times in the online analysis (this work) or 8 times in offline analyses [44]). After the track reconstruction has been applied to each bootstrapped event, the average direction and the median angular difference of the bootstrapped events can be calculated as a measure of the angular uncertainty.

3.4.3 Energy Reconstruction

Aside from its direction the energy of an observed muon and its parent neutrino are of interest to this analysis as well. It can provide additional separation power leveraging the different spectra of atmospheric and astrophysical neutrinos, and it allows to determine the energy spectrum of a neutrino source candidate.

This analysis focuses on muons around 1 TeV which can travel several kilometers in ice. The IceCube detector comprises one cubic kilometer of ice, much smaller than the surrounding glacier. Hence, interactions are most likely to take place outside of the detector and only the section of the muon track passing through can be observed. Having undergone unobserved energy losses impeded the precise reconstruction of the muon, or even the neutrino, at the interaction vertex. It is however possible to estimate the muon energy at the detector, which provides a lower bound on the neutrino energy.

This is in contrast to events starting or contained in the instrumented volume, where the detector would serve as a calorimeter.

A charged lepton, e.g. the muon and any secondary leptons produced by it, traversing the ice at a speed greater than the Cherenkov threshold will emit Cherenkov radiation along its path [51]. The number of photons produced is proportional to the track length, which in turn is found to be proportional to the energy of these particles [86].

At energies above the critical energy ($\sim$ 1 TeV) the energy loss rate is dominated by bremsstrahlung and pair production processes resulting in electromagnetic showers, as well as hadronic showers following photonuclear interactions. The sparsely

instrumented detector does not allow to resolve the development of these showers and each can be approximated as point-like with a spherical light emission pattern [63].

Since the light yield scales linearly with the energy, the reconstruction methods aim to scale the template of the expected photon count simulated at a reference energy (typically 1 GeV) to the observed photon count. Hence, the number of observed photons is expected to follow a Poisson distribution and the likelihood of an energy E, given k observed photons is given by

$$\mathcal{L} = \frac{\lambda^k}{k!} \exp(-\lambda) \,, \tag{3.18}$$

where $\lambda = \Lambda E + \rho$ is the mean expected number of photons given the template Λ, and ρ considers additional contributions such as noise [63].

The template Λ will generally depend on the location of the emitting track, the location of the observing DOM, and the DOM's orientation with respect to the track. In the context of online analyses' constraints regarding computation time, two reconstruction methods are used with parametrize the light yield template.

MuEX: A first approximation [87] considers the muon emitting Cherenkov light uniformly along its track. The expected number of photons then depends on the distance between the track and the DOM. In close proximity the effect of scattering is negligible and a $1/r$ dependence in the photon density results from absorption. At larger distances the diffusive behavior is approximated. Both regimes are connected with an expression found empirically and verified in simulation [63]. The average local absorption and scattering lengths between track and DOM are tabulated and consider the layered structure of the ice.

The accuracy of this this model is vastly improved by accounting for not just the uniform emission from minimum-ionizing muons, but also the stochastic emissions by convolving Eq. 3.18 with a skewed probability distribution which allows for large over-fluctuations in the tails.

TruncatedEnergy: A different approach deals with the stochastic energy losses by spatially splitting the track and apply Eq. 3.18 while considering each segment as an individual detector.

The segment size is either fixed to 120 m, comparable to the inter-string distance, or dynamically chosen such that each segment includes exactly one DOM. Additionally, a cylindrical cut only includes DOMs not closer than 10 m and not further than 80 m from the track, as the behavior of bright DOMs close to the track not well understood yet and photons in DOMs far away are unlikely to be causally connected to the track.

The energy is evaluated in each segment, with the expectation in Eq. 3.18 obtained from the same spline-fitted parametrization of the ice which is used by the directional reconstruction in Sec. 3.4.1. Then, half of the segments with the highest estimate of dE/dx are excluded. The average of the remaining segments can be calibrated to yield an estimate of the muon energy, which is robust with respect to the large event-to-event variations in the stochastic processes [88].

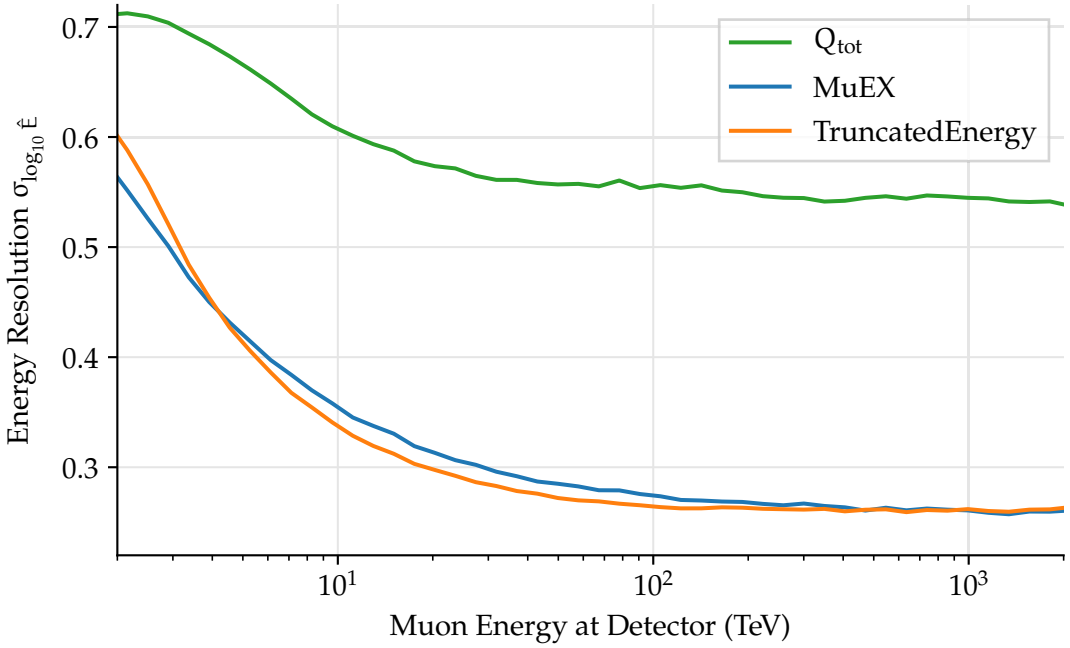

Figure 3.8: Energy resolution for the reconstruction algorithms MuEX and TruncatedEnergy at the final level of the event selection. For comparison, also the total deposited charge (Q_{tot}) is tested as an energy estimator. The resolution is calculated following [63], assuming a primary neutrino spectrum $\propto E_\nu^{-2}$.

The resolution of both energy estimators is tested using the prescription in [63] and shown in Fig. 3.8. At the final level of the event selection, which essentially comprises track-like events, both reconstructions exhibit similar performance. At low energies, the energy resolution is limited by the low number of photons observed in an event and the almost energy-independent energy loss rate of minimum-ionizing muons. The segmented approach (TruncatedEnergy) is better calibrated and offers slightly higher energy resolution between 5 and 500 TeV, hence it was chosen in Sec. 6.4 to identify high-energy muons.

TruncatedEnergy requires at least ~300 m of track length to calculate a reliable average of its segments, while the skewed PDF (MuEX) is not subject to such constraints. Thus, MuEX was chosen for the point-source search in Sec. 5 to maximize the effective area and provide best sensitivity.

3.5 Simulation

In order to test the event selection and reconstruction steps, as well as the final point-source analysis, simulations of different event classes are used.

Signal (neutrino) events are simulated using a version of the ANIS neutrino generator, that has been modified for use inside the IceCube software framework [89].

Starting from a uniform flux of neutrinos at the Earth's surface, neutrinos are propagated towards the detector considering their interaction cross section and the matter density in the Earth [90]. In or close to the detector volume, the simulated neutrinos are forced to interact, and an interaction probability weight is stored along with the event. The neutrinos are generated with a power-law energy spectrum, which can be re-weighted later to an arbitrary energy spectrum, e.g. following models of the astrophysical or atmospheric fluxes.

Background events consisting of muons from cosmic-ray induced air showers are simulated using CORSIKA [91, 92]. Following the shower development, the muons reaching the detector volume are stored. Similar to the signal simulation, the events are simulated following a generic flux model and can be re-weighted later to more refined models. Muons from atmospheric showers are also mixed into the signal event simulation at a natural rate (about one muon in 10 events) to account for multiple coincident particles passing through the detector simultaneously.

In both the signal and the background case, the Muon Monte Carlo (MMC, [93, 94]) propagates the muons and records continuous and stochastic energy losses, storing the track segments and their light yield. Photons from the muon track are propagated towards the DOMs. In the case of low-energetic particles, individual photons are tracked, which provides very good precision and allows to easily incorporate the latest ice models, at the cost of computational complexity [95]. For high-energetic particles, pre-tabulated photon expectations at the DOMs (Sec. 3.4.1) are used to speed up the simulation. Eventually, an IceCube-internal software called "DOMLauncher" simulated the response of the photomultiplier tube and the DOM mainboard up to the fADC and ATWD digitization. The output is fed into the triggering and filtering software, which also runs at the South Pole.

In this work, the neutrino signal is estimated from simulations of neutrinos in the energy range between 100 GeV and 1 EeV. The atmospheric muon background is estimated from CORSIKA simulations with primary energies ranging from 600 GeV to 100 EeV.

3.6 Online Detector Monitoring

While IceCube aims at providing continuous data taking, occasionally planned and unplanned interruptions occur. Typical planned interruptions to stable data taking happen mainly during software upgrades, or during calibration, when artificial light may be produced by the LEDs on the DOMs or the in-ice calibration lasers. Unplanned interruptions may occur in the case of external power outages, but also when single DOMs or entire strings stop working. In the latter case the DAQ will automatically remove the failed components and attempt to continue data-taking with a partial detector configuration.

For final level analyses it is important to identify the periods of time during which the detector was operating in a stable and consistent manner. For offline analyses completed 8-hour segments are centrally vetted by a combination of automatic checks

and manual inspection.

Online analyses need to make an informed decision in an instant to avoid emitting false alerts based on detector artefacts. They also need to be able to determine the actual good detector uptime in a given time window. This is achieved by a combination of static and dynamic safeguards [96–98].

Static safeguards cover known or expected abnormalities: A list of DOMs known to be faulty is maintained, and they are automatically excluded from data-taking made known to reconstructions. During the operation of in-ice LEDs or lasers the real-time event stream is disabled automatically. The same applies to software upgrades and taking of calibration data.

To identify periods of inadequate data quality three quantities are monitored in particular:

- the rate of the simple multiplicity trigger,
- the event rate passing the muon filter,
- and the rate of events passing the OnlineL2 event selection cuts.

The trigger rate is a very simple and low level quantity with few external dependencies and can spot issues that affect a small number of DOMs. The filter rates also include early reconstructions and reconstructed event properties are monitored for sudden changes. At this early selection level the event rate is still large enough to provide adequate statistics and detect deviations from expected behavior.

The three quantities are counted in 10 minute bins and a rate is calculated in each bin. The last bin in a run may be shorter than 10 minutes when accounting for the actual detector stop time. Abnormal deviations are detected by comparing to an exponential, moving average of past data. Where a simple moving average will give equal weight to all past measurements, the exponential average will give more weight to more recent measurements and gradually decrease the weight given to measurements made further in the past. This approach is chosen to deal with the gradually changing conditions at the South Pole:

The low level event rate in IceCube is dominated by muons which originate from cosmic-ray induced particle showers in the atmosphere. The air temperature changed throughout the year, leading to change in the density profile. The temperature ranges roughly from $-80\,^{\circ}\mathrm{C}$ in January to $-40\,^{\circ}\mathrm{C}$ in August, with a corresponding variation in the observed muon rate by $\pm 10\,\%$ [99].

Given a series of measurements $\{x_1, \ldots, x_n\}$, the exponential moving average at a time i is defined as

$$\overline{x}_i = \alpha\, x_i + (1-\alpha)\cdot \overline{x}_{i-1} \tag{3.19}$$
$$\text{with } \overline{x}_0 = x_0\ ,$$

along with its standard deviation

$$\sigma_i = \overline{x^2}_i - \overline{x}_i^2\ . \tag{3.20}$$
$$\tag{3.21}$$

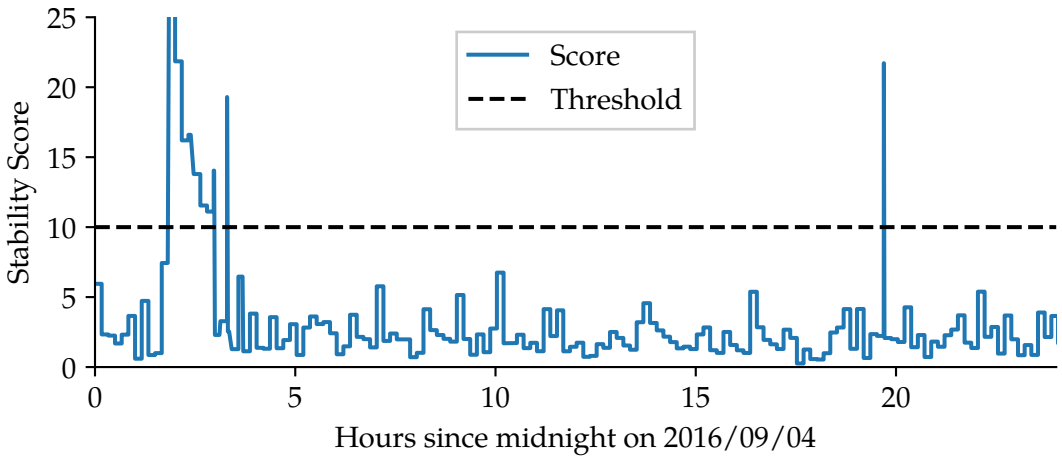

Figure 3.9: Example of the stability score which quantifies the quality of the online data taking. In this example a faulty power supply (on the left) and a full restart of the detector (on the right) cause some downtime during otherwise stable operations and are correctly identified (Published in [96]).

The weight parameter alpha has been tuned to 0.01 in the past to accommodate these large scale variations, as well as intra-day variations due to sudden changes in weather [97].

Summing the relative deviations of the k aforementioned trigger and filter rates and comparing them to the previous moving average yields a measure for the detector stability:

$$S_i = \sum_{k=1}^{3} \frac{|x_i^k - \overline{x^k}_{i-1}|}{\sigma_{i-1}^k} \,. \tag{3.22}$$

The quantity S_i is called the stability score which is calculated in every time bin. An empirically determined cut is placed and time bins with a score larger than 10 are discarded from the analysis. The total good uptime in a given period is then

An example of the behavior of the stability score is shown in Fig. 3.9. On the chosen day the data taking suffered two brief interruptions: First, a broken uninterruptible power supply caused a string to stop delivering data. Later, a full detector restart was performed.

Past comparisons between online and offline monitoring methods have shown good agreement and differences in good detector uptime are smaller than 1 % [96, 97]. Typically the online monitoring system excludes a little more periods, due to the resolution of the time-binned trigger and filter rates, due to the conservative cut on the stability score erring on the side of caution.

Once a new time bin was recorded and the associated trigger and filter rates have been received in the northern hemisphere, the stability score is calculated and stored in the I3Live database, where it can be queried by all analyses.

4 The Real-Time Alert System

The real-time alert system consists of several components, which will be described in this chapter: Section 4.1 presents an introductory overview of the architecture of the realtime alert system. It outlines the flow from the event selection at the South Pole to the analyses running on computers in the northern hemisphere.

Before defining the event selection, the characteristic signal and background properties are reviewed in Sec. 4.2. The details of the event selection are split into two sections. The first reconstructions and data reductions cuts which are a common starting point for several analyses in IceCube and take place early in the processing pipeline are summarized in Sec. 4.3. The final level event selection and its implementation with the help of boosted decision trees (BDTs) is a key component of this work and is described in detail in Sec. 4.4.

Having selected a suitable set of events and reconstructed each event's most important properties, the analysis strategies in the search for neutrino point sources are introduced in Sec. 5.

4.1 System Architecture

A first real-time analysis of neutrino data and subsequent follow-up observations with a partner telescope was implemented in 2006 for the AMANDA-II and MAGIC experiments [100]. It then evolved into the gamma-ray follow-up (GFU) program between the IceCube, MAGIC and VERITAS observatories [101]. In 2008 an optical and X-ray follow-up (OFU [102]) program was launched between IceCube, the Robotic Optical Transient Search Experiment (ROTSE, [103]) the optical Palomar Transient Factory (PTF, [104]) and the Swift satellite [105]. While these programs were looking for clusters of neutrino candidates, efforts were also made within IceCube to identify single neutrino candidates with a high probability of being of astrophysical origin. Eventually, these efforts culminated in the current setup of the real-time alert system [96], which will be described in the following.

The waveforms recorded by each in-ice photo-multiplier are digitized and sent to the surface, where they are received by the string hubs and passed to the data acquisition system (DAQ). Next, the processing and filtering (PnF) system tests for the trigger conditions, and applies the reconstructions, which are necessary to make filter decisions. Various filters exist for different physics analyses; the relevant ones for this work are the so-called „Muon Filter", the „OnlineL2 Filter" and the „GFU Filter", which are applied in this order and will be described in Sec. 4.4.

These filters aim to identify track-like muon neutrino candidates, and reconstruct

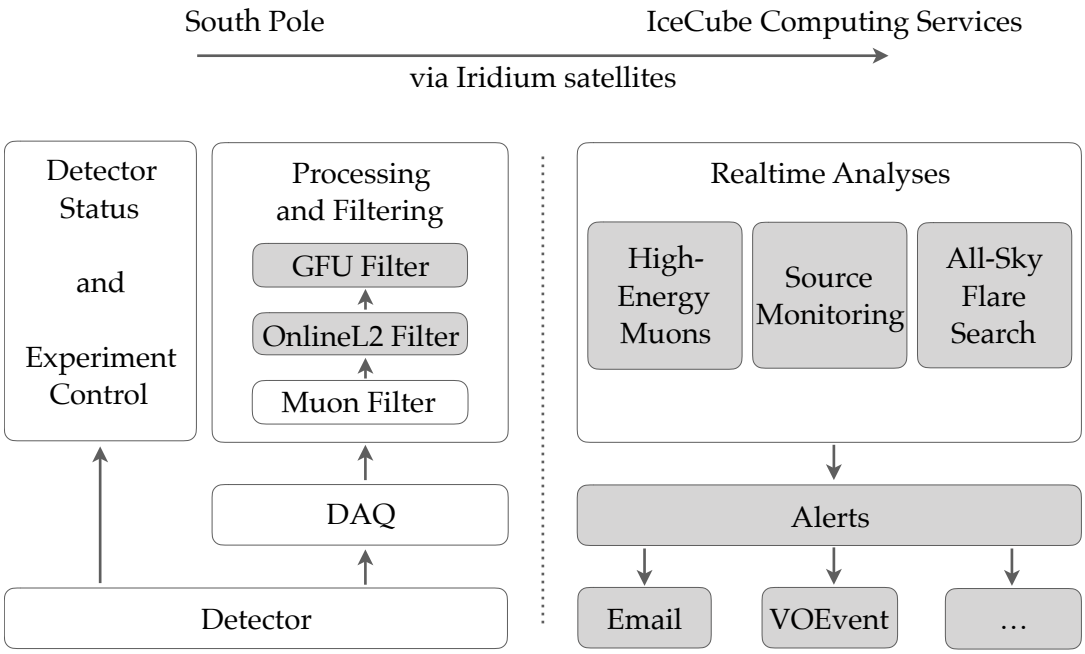

Figure 4.1: Overview of the real-time infrastructure of the IceCube experiment. The shaded boxes highlight the parts which have been built or were contributed to in the course of this work.

the properties which are relevant for point source searches. Special attention is paid to the runtime of the entire process. The PnF system needs to evaluate every filter on every event, and even though it does so in a parallelized fashion, long processing times for individual events will create a backlog of events. In order to avoid filling up the event queues, the runtime for the combination of the OnlineL2 and GFU filters must not exceed 15 seconds, even for the most rare events. This constraint influences the choices of the reconstruction algorithms (see Sec. 4.4).

An event which passes all filter levels is most likely a well-reconstructed muon track. It is characterized by the following (reconstructed) properties, which are sent via Iridium:

- Run and event number,
- event time,
- reconstructed direction,
- estimated angular uncertainty,
- and estimated muon energy.

Those quantities represent the input for the analyses described in Sec. 6. They are serialized for transmission to the computing center in the Northern Hemisphere using

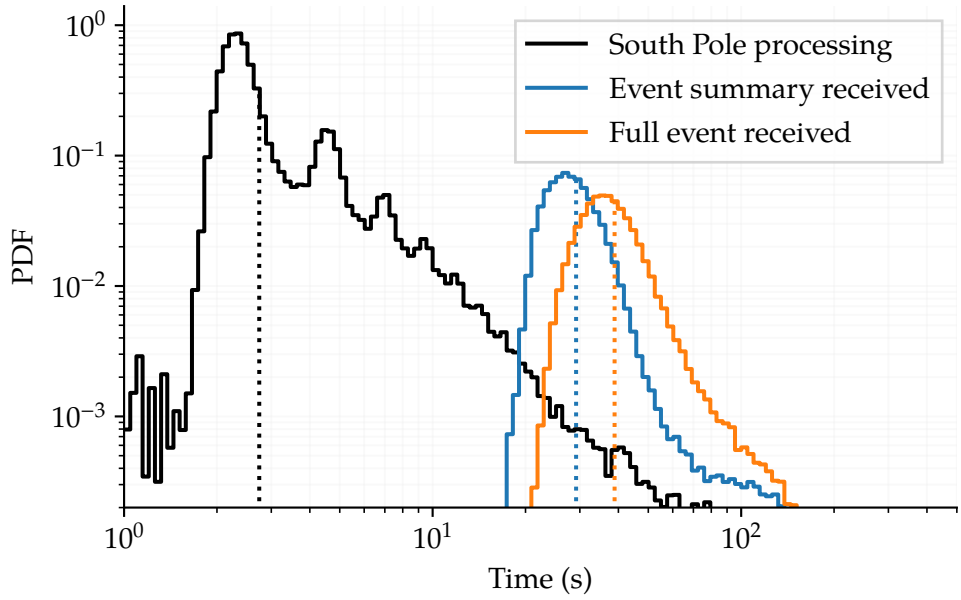

Figure 4.2: Latency of the event transmission through the Iridium system from Oct. 1 until Dec. 31, 2018. The time is measured with respect to the DAQ trigger time at the South Pole until the data has been received and stored in the database in the Northern Hemisphere. The median latency for the short messages summarizing a few key quantities of an event is 29 s, whereas the full event data containing information about all PMT pulses has a median latency of 39 s. For comparison, the time taken for the entire event filtering and reconstruction at the South Pole is shown in black.

the Javascript Object Notation (JSON) format [106], which produces text messages that are both human readable and still compact: typical event summaries take up around 1.3 KB per event and can be compressed by 20-50 %. They are sent with the highest priority along with other detector status messages. In contrast, the full event data which contains a compressed representation of the raw waveforms takes up between 150 and 250 KiB per event depending on the number of pulses, and is sent at a lower priority so as not to interfere with the regular experiment monitoring and control.

Figure 4.2 shows the total latency between an event triggering the DAQ at the South Pole and the availability of the event summary and full event data in a computing center in the Northern Hemisphere. Even for the short messages there is a minimal latency of around 20 seconds introduced by the readout, processing and filtering chain at the South Pole. The median latency for event summary data of half a minute is the dominant latency in the entire real-time analysis chain.

Communication is handled by IceCube's experiment control system „I3Live" [52]. Linking the South Pole and the main computing center in Madison, WI, it provides tools to control the detector from the Northern Hemisphere and a data channel to

exchange control and status messages. The data connectivity is provided round the clock through the Iridium satellite network [107, 108], with a bandwidth of 2.4 kbit/s per modem. Messages can be exchanged between various endpoints on both ends through the ZeroMQ message distribution framework [109]. Operating in a publisher-subscriber mode, it allows publishers to send messages to the network under a chosen topic, and (one or more) clients subscribing to (one or more) topics. This setup is used to transmit both the short event data and the full event information for the events selected by the real-time filtering and reconstruction to the Northern Hemisphere.

Additionally, the Iridium link is used to transmit information such as current trigger and filter rates, which allow for a classification of periods of stable data-taking conditions. This information is stored in „I3Live" and used by the analysis code to conservatively exclude data which was recorded during unstable periods and calculate the good uptime as described in Sec. 3.6.

Once the event data is received, it is stored in a database and sent via ZeroMQ to the analysis software, which runs on a dedicated machine. Several of IceCube's alert systems (such as high-energy starting events, extreme high energy events [96], and this work) are implemented as individual clients, which share a common library. This library called „realtime-tools" and developed in the context of this work provides frequently used tools such as: subscribing to an event stream, accessing archival events from the database, querying the detector status, sending status reports via text messages, and emitting alerts through different mediums.

The clients for each analysis run as separate processes in order to maximize stability and uptime as well as facilitate new, parallel developments. These analysis clients typically listen to the event stream, keep an archive of previous events, apply data quality cuts and execute the analyses described in Sec. 6. In case that a pre-defined significance threshold is exceeded, alerts are generated in pre-defined formats and sent either directly to partner experiments (such as H.E.S.S) or to alert distribution networks (such as GCN). The information released along with is agreed upon by the participating experiments and will be shared either in human-readable formats such as email, or through machine-readable formats like VOEvent [110], which enable automated follow-up observations cutting the human-in-the-loop. The generated alerts are also fed back into the experiment control software I3Live for purposes of archiving and easy future access by collaboration members.

Different clones of the follow-up machine exist in order to test new versions of the analysis code on the real event stream, while inhibiting alerts, before the code gets eventually deployed and switched on.

4.2 Event Selection Goals

The reconstruction and filtering of neutrino candidate events is a key component of the analysis. For the reasons presented in the previous section the event reconstruction and filtering is performed in the computing center at the South Pole.

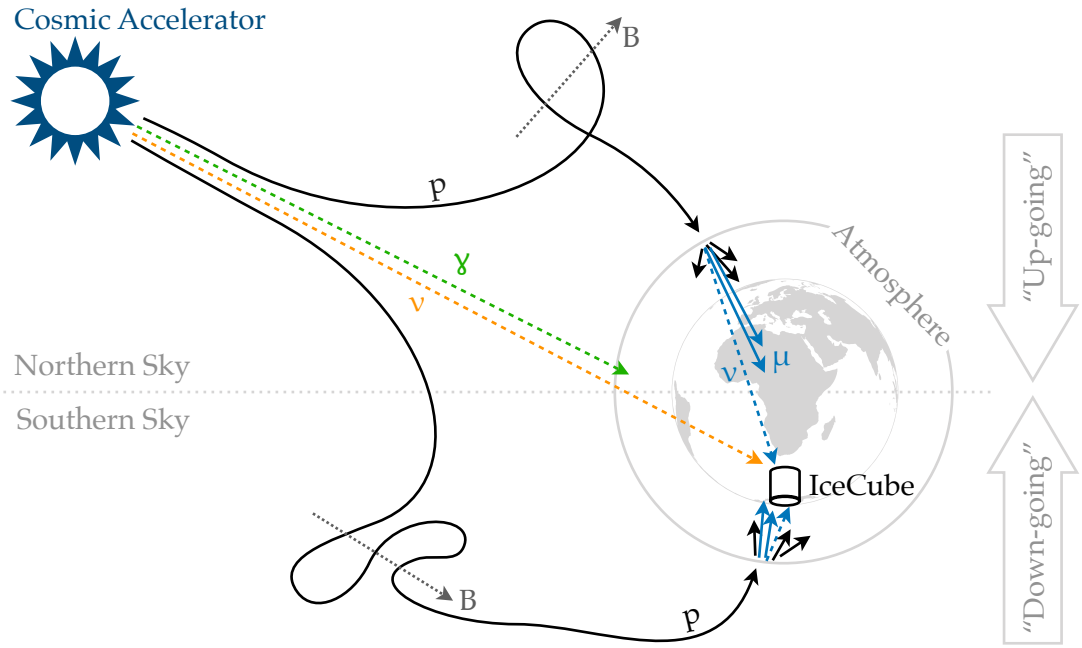

Figure 4.3: Not-to-scale sketch of observable particles forming signal (orange) and background (blue) events in the detector. Neutral particles (e.g. neutrinos) point back to their origin, while charged particles (e.g. protons) are deflected by magnetic fields. Neutrinos produced in atmospheric showers can reach IceCube, whereas the remainder of *northern* hemisphere showers gets absorbed by Earth.

Both computing power and the bandwidth of the low-latency data link are scarce resources, it is important to reduce the amount data as much as possible by removing events unlikely to be part of the signal.

The events encountered in the detector can be grouped in several regards. The *shape* of the event can be either spherical or track-like. The event may be caused by different *particles*, e.g. muons, but also other leptons or hadrons. The *origin* can be astrophysical in the sense that the event was caused by the interaction of an astrophysical neutrino, or atmospheric, meaning that the observed particle or one of its parent particles was produced in a cosmic-ray induced atmospheric particle shower.

Accurate directional information is necessary in order to resolve point-like neutrino sources. The best angular resolution is provided by muons, whose track-like shape provides a long lever arm, constrains the direction well, and allows for a fast reconstruction[1].

Thus, the overall signal objective is defined as well-reconstructed, track-like events which were caused by a muon from an astrophysical neutrino interaction in or near the

[1] Improving the angular resolution of other flavors is about to make substantial progress [111].

detector. Since the actual neutrino cannot be observed and the event is formed by the muon, these events are indistinguishable from muons produced in the atmosphere, which can be muons produced in showers and reaching the ground or muon neutrinos interacting in the ice. A distinction is not possible at the stage of the event selection and is deferred to the analysis stage searching either for clustering of events (Sec. 5) or for the most energetic, individual events (Sec. 6.4).

Thus, the goal of the event selection is set as follows: identify single muons whose track is well-reconstructed and yield a sample of track-like events with high purity and efficiency. Background events (i.e. events not fulfilling these criteria) fall into different classes, depending on the region of the sky (see Fig. 4.3).

Muons produced in atmospheric showers in the northern hemisphere will be absorbed while traversing the Earth; only the neutrinos produced the showers will be able to reach the South Pole, interact and be observed in IceCube. Yet, it is not sufficient to select solely tracks which are reconstructed as going upwards through the detector: Downward-going muons produced in airshowers directly above the detector may end up misreconstructed due to ambiguous event topologies, e.g. when the interaction takes place near the edge of the detector, or the muon passes through a corner. This is the dominant background component to truly up-going events for two reasons. The atmospheric muon flux is much larger than the atmospheric muon neutrino flux, and geometrically the most of the fiducial volume of the detector is found around the outer edges. The challenge posed to the event selection for the northern sky is to remove those events, without removing the signal events with similar topologies.

Atmospheric showers in the southern hemisphere produce neutrinos and muons, both of which can reach the detector and define the background in this part of the sky. They produce the same down-going, track-like signature as signal events, but at a much larger abundance than the signal. In addition, a single atmospheric shower may produce several muons traveling in parallel, whose spatial separation is much smaller than the inter-string distance of IceCube. Hence, they appear as one bright muon track, which may actually consist of several, much less energetic muons. Rejecting this class of events is the main challenge in the southern sky.

The two background regimes motivate the application of zenith- (or declination-) dependent selections. The boundary is not sharply defined, and different values were used in past analyses. Typically, the background rate from atmospheric muons changes very little until a few degrees from the horizon, where path length through the ice overburden get shorter. Eventually, a value of 82° in zenith (−8° in declination) is used in this work, unless otherwise noted. Aside from the aforementioned argument, it was also chosen to be compatible with the existing, early event selection in order to ensure a smooth distribution in zenith for the final event sample.

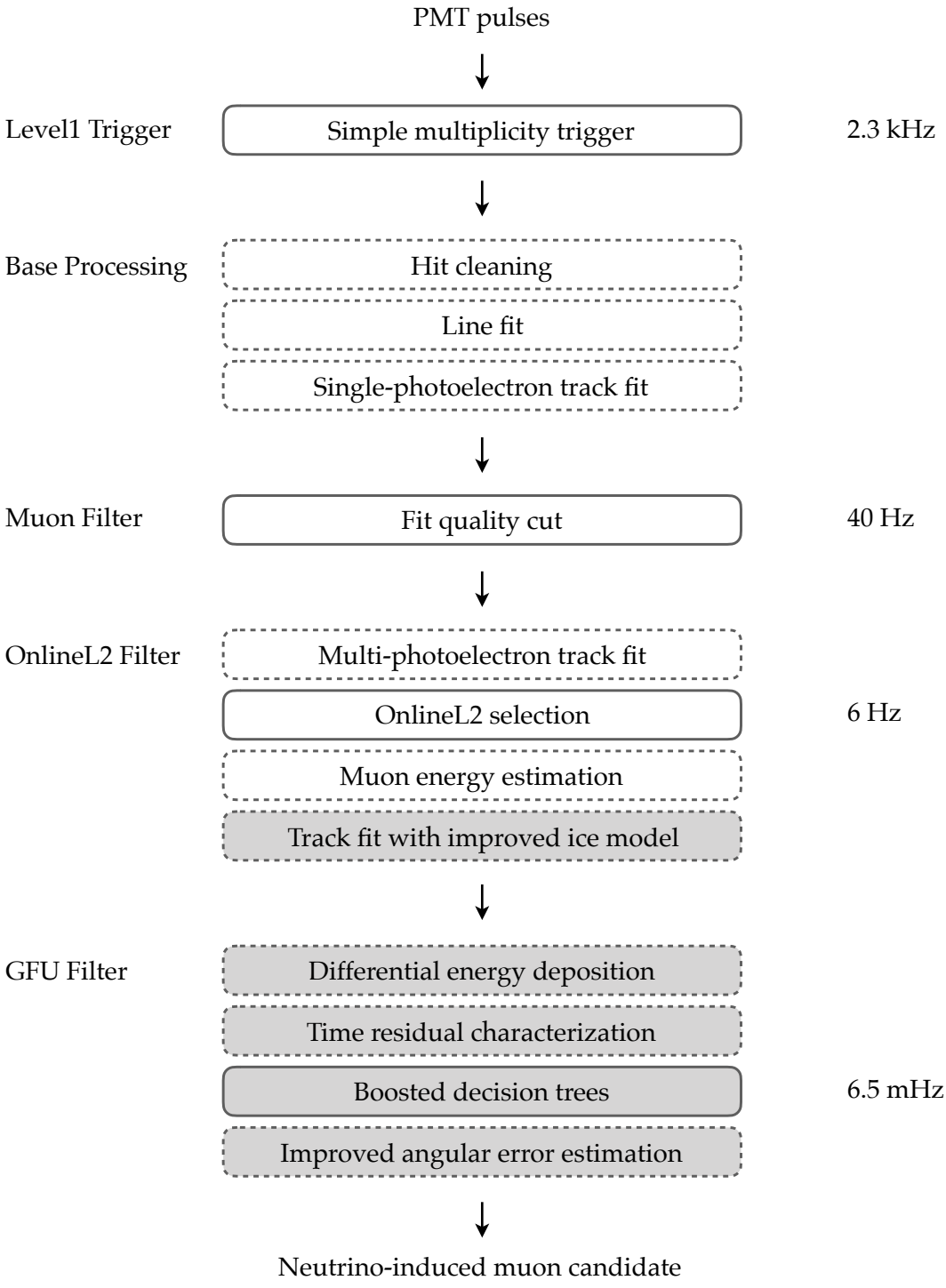

Figure 4.4: Overview of the real-time event selection and reconstruction. The various stages of events processing done at the South Pole are shown from top to bottom. Dashed boxes list steps in the reconstruction, while solid boxes indicate cuts to reduce the data rate and increase the purity. At each cut level the approximate event rate is given on the right. Shaded boxes have been added or improved for this work.

4.3 Online Event Processing

In general, fast and simple reconstructions are performed at an early stage in the process, where the event rate is still high. Then, data reduction cuts based on the reconstruction results are made in order to reduce the event and allow for applying another round of more sophisticated but slower reconstructions.

Such a chain of reconstructions and cuts is outlined in Fig. 4.4, which presents an overview of the reconstruction and filtering chain employed in this analysis. Dashed boxes indicate the cuts which reduce the event rate, while solid boxes list the different reconstruction techniques, which were introduced in Sec. 3.4.

All events are passing through the trigger and base processing, followed by the Muon filter (Sec. 3.3), reducing the data rate to 40 Hz by rejecting background which does not match the reconstruction's hypothesis of a track-like shape. Next, the Online Level 2 (OnlineL2) filter runs additional reconstructions of direction and energy and finally the GFU filter[2] applies a multi-variate selection based on the output of these reconstructions. For the events passing this last selection the uncertainty on the direction is estimated.

OnlineL2 Filter

The OnlineL2 filter and is designed to provide a common starting point for several online or near-realtime searches for transients and variable point sources [102, 113, 114].

It starts by refining the directional reconstruction. The single-photoelection (SPE) likelihood fit performed earlier by the muon filter works well for bright muons which traverse the entire detector, but is challenged by more ambiguous topologies such as corner-clipping muons with only a very short part of the track inside the detector, or tracks running down a lane of DOMs along one of the detector's symmetry axes. Multiple local extrema can exist in the the likelihood function (Eq. 3.9) in these cases, such that the minimizer may not yield the global minimum. As a mitigation, the fit is repeated with 2 different, random seed directions at 120° from the original fit solution.

Afterwards, the multi-photoelectron (MPE) fit (Eq. 3.12) is seeded with the direction from the SPE fit and provides a more realistic hypothesis for higher energy events, thus improving the fit quality especially for muons above 1 TeV (see Fig. 3.7). While the SPE fit only considers the first pulse in each DOM, the MPE fit also takes the total deposited charge into account, providing a more reliable reconstruction and allowing proper identification of previously mis-reconstructed down-going events.

Based on the results of these fits, cuts [113] reduce the event rate from 40 Hz further down to 6 Hz. As was the case in the muon filter at the previous level, the cuts still combine the fit quality (as determined by the likelihood value) and the integrated charge in the event. The sky is split into four different regions with different signal and background properties.

[2] Historically named after the Gamma-ray Follow-Up program; and the name stuck [97, 112].

The cuts follow the same motivation as those of the previously described muon filter. Being based on the improved MPE fit, signal and background are better separated allowing for tighter cuts and the six-times reduction in event rate. All the while, >99% of the signal for up-going events and >80% of the signal for down-going events are preserved (assuming a primary neutrino spectrum $\propto E^{-2}$). Trimming the event sample at this point will also speed up the final machine learning step.

The specific form of the cut at its justification is explained in depth in [113]. Up to this point, the input variables to the cuts are still constrained by the computing power available at the South Pole, which has not changed since the original inception of the OnlineL2 filter, hence they were not changed for this work.

The event rate is now low enough to run more computationally demanding algorithms, which are required as an input in the final neutrino-pure selection step developed for this work.

The direction will be reconstructed by the SplineMPE reconstruction (Sec. 3.4.1). It is applied on a subset of pulses that have been cleaned of late pulses, reducing the number of table lookups associated with the evaluation of the time residuals, and improving the convergence of the minimizer. Other more sophisticated options, such as additional convolutions of the likelihood function in order to treat noise or stochastic energy losses, were found in the course of this work to increase the runtime especially for very bright (interesting) events, hence they are omitted. It was found that in addition to the runtime benefits, this configuration provides even a slightly more accurate reconstruction than the default settings used in the previous offline point-source search [111].

As an additional input for the next selection step, the energy estimation methods "MuEX" and "TruncatedEnergy" (Sec. 3.4.3) are applied using the SplineMPE track hypothesis.

This provides the input for the last selection step, the "GFU filter", which was redesigned for this work and will be described in more detail in Sec. 4.4. It aims at providing a sample of events with the best possible neutrino purity, by using a machine-learning classifier. Rejecting most of the remaining mis-reconstructed down-going events, and introducing some rejection power against down-going muon bundles, it reduces the event rate to 6.5 mHz. This corresponds to 200.000 events per year in the final data sample, of which roughly two thirds are up-going and one third is down-going.

Angular Error Estimation

The last ingredient to the subsequent searches for point sources is an estimate of the angular error of each event. It is crucial for the sensitivity to point sources and different methods have been described in Sec. 3.4.2, with anti-correlated complexity and precision.

The fastest, but least precise method is the estimator based on the Cramér-Rao inequality. It features a fast, analytic solution which makes evaluation on all events feasible. Thus it provides a fallback estimate in case the other methods cannot be run.

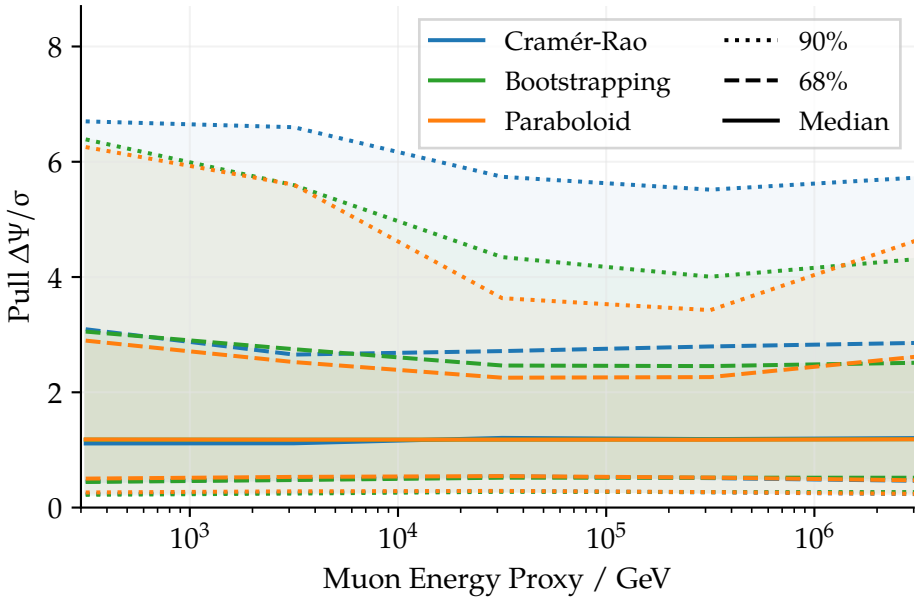

(a) Pull of angular error estimators as a function of muon energy.

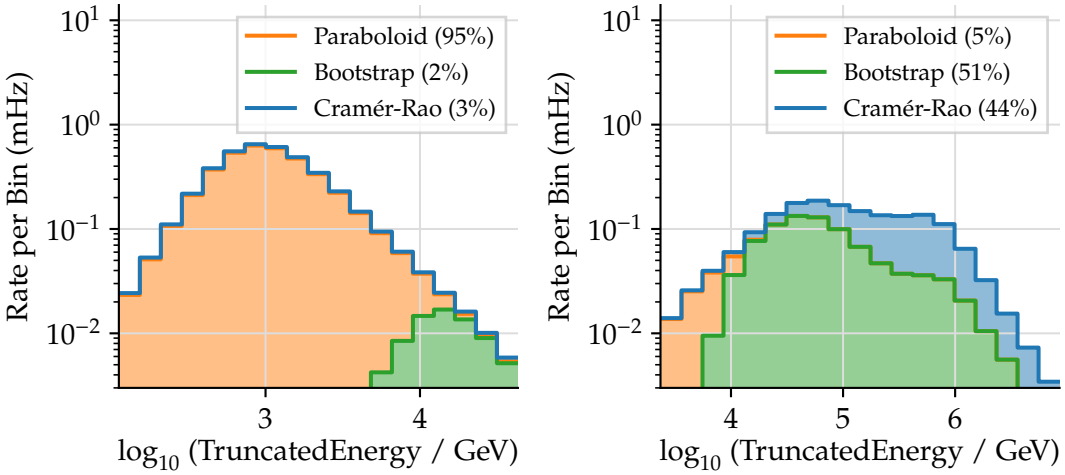

(b) Energy distribution (up-going events). (c) Energy distribution (down-going events).

Figure 4.5: Angular error estimators, which are available online. Panel (a) shows the median, as well as the central 50% and 90% intervals of the pull distribution as a function of muon energy proxy.
Panels (b) and (c) show the distribution of the muon energy proxy for events at the final level, highlighting three classes of events, which differ by the applied angular error estimator. Running the estimators is one of the most time-consuming steps, with the runtime scaling linearly with event energy or the number of hit DOMs. The paraboloid and bootstrapping methods are superior to the Cramér-Rao approach, but computing resources at the South Pole limit the availability as depicted.

Offline analyses have achieved the best sensitivity using the Paraboloid method, i.e. sampling the profile likelihood around the best-fit position and fitting it with a paraboloid shape. For this to work, the profile likelihood needs to be evaluated on three equidistant rings around the best fit, with eight sampling points per ring. These 24 additional likelihood minimizations and the table lookups involved to determine the local time residuals make this time consuming, more so as events get more energetic.

Alternatively the bootstrapping approach draws random samples from the observed distribution of charges in the event and applies the likelihood fit to those. The variance of the bootstrapped distribution serves as an estimator of the angular uncertainty. While an eight-fold resampling of the events provides a performance on par with the Paraboloid method, it is also equally slow. As a compromise, the number of iterations was reduced to six, yet the runtime is still proportional to the number of hit DOMs (N_{Ch}).

The performance of the estimators can be quantified by the distribution of the pull, i.e. the ratio between the true and the estimated angular error. Figure 4.5a shows the central 50% and 90% quantiles for each of the three methods as a function of the muon energy proxy. The large 90% quantile of the Cramér-Rao method is evident and indicative for a tail towards large pulls, i.e. events with severely underestimated angular errors. Thus, Paraboloid and Bootstrapping are the preferred methods.

The South Pole test setup, a duplicate of the South Pole computing resources located in Madison, was used to measure the runtime of the different algorithms. As events are processed on a first-in-first-out basis, and there is only a fixed size buffer for incoming events during the processing of an earlier event, the maximum runtime is limited to 15 s. Should the processing of an event exceed maximum runtime limit, it will be aborted, no filter decision will be taken, and the event will be tagged and stored for offline investigation. Using a sample of archival events, even the slowest event must be completely processed during this time. From this study the following choice was made regarding which algorithm to run:

	MuEX < 4 TeV	MuEX ≥ 4 TeV
$N_{Ch} < 300$	Paraboloid	Bootstrapping
$N_{Ch} \geq 300$	Paraboloid	Cramér-Rao

As shown in Fig. 4.5 this setup provides improved angular error estimators (i.e. better than the Cramér-Rao method) for 97% of upgoing and 60% of downgoing events. While the sensitivity to neutrino clusters from point sources is improved to almost the level of offline analyses (Sec. 5.4), the uncertainty of the most-interesting, energetic single muons still cannot be determined accurately.

Figure 4.6 shows the time spent on the most time-consuming reconstructions at the second-to-last and at the final selection level. Eventually the total chain of reconstructions is roughly 10 times faster compared to offline analyses, while encountering only percent-level differences in sensitivity (as will be shown later).

Table 4.1 also lists each reconstruction along with its median execution time, and the longest execution time observed.

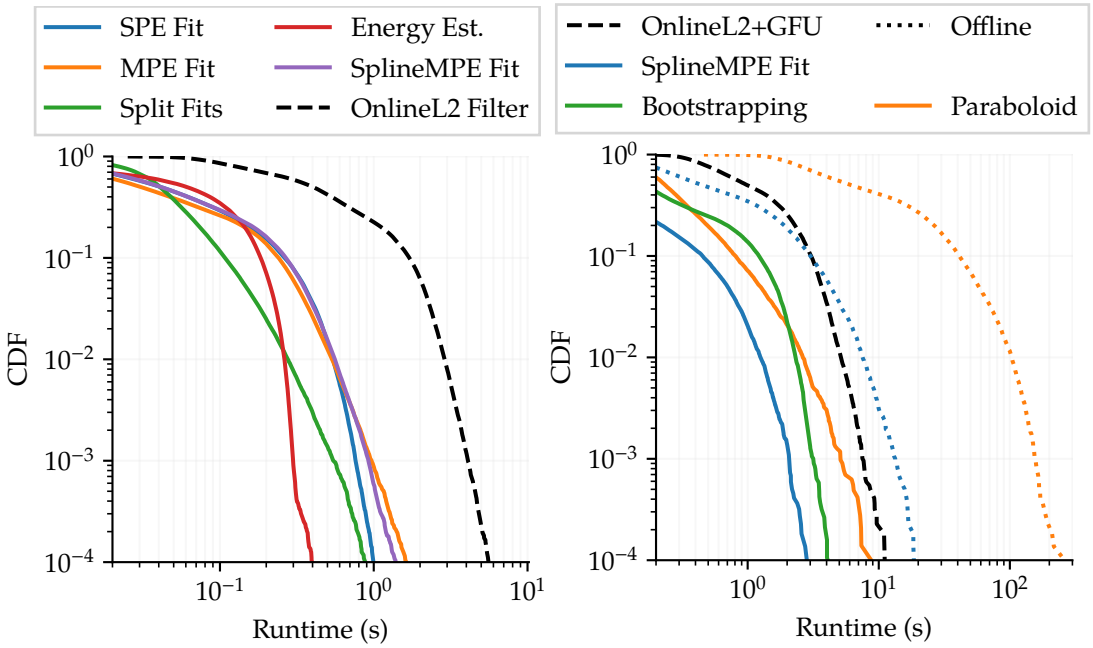

(a) at OnlineL2 filter level

(b) at GFU filter level

Figure 4.6: Cumulative distribution of the execution time for the most time-consuming reconstructions. The left panel is built from events at the intermediate selection level, whereas the right panel shows the time needed for events passing the final event selection. At each filter stage, solid lines show individual reconstructions and dashed lines show the sum of all reconstructions. For comparison, the dotted lines in the right panel indicate the time needed for the most sophisticated reconstructions commonly used in offline analyses.

All estimators of the angular uncertainty exhibit a bias between the estimated and the true angular error, for two reasons: The kinematic angle in between the neutrino and the muon of about 1° at an energy of 1 TeV is invisible to the detector as only the muon is visible and reconstructible. This systematic deviation can be well determined from simulations and corrected for. In addition, the likelihood (Eq. 3.12) models an infinite muon track with a continuous Cherenkov light yield. Stochastic losses are not taken into account in the configuration used online. While corrections to the likelihood have been developed [75] or are under investigation [115], their computational complexity makes them unsuitable for online use. For energies above 10 TeV the likelihood model is increasingly unrealistic and the shape around the global maximum does not accurately describe the reconstruction's uncertainty. Both effects justify an energy-dependent correction of the estimator by calibrating the pull, i.e. the ratio between the true angular error $\Delta\Psi$ and the estimate σ, with respect to the direction of the neutrino.

Reconstruction Name	Type	Execution Time (seconds) Median		Max	
SPE Fit	Direction	0.04		1.25	
Bayesian Fit	Direction	0.01		0.33	
Split Fits	Direction	0.04		1.28	
MPE Fit	Direction	0.03		2.71	
MuEX	Energy	0.06		0.53	
SplineMPE (fast)	Direction	0.04		2.68	
Cramér-Rao	Angular Error	0.01		0.03	
TruncatedEnergy	Energy	0.01		0.04	
OnlineL2 Filter Total		0.40		7.76	
Paraboloid	Angular Error	0.24	(0.43)	10.6	(54.52)
Bootstrapping	Angular Error	0.17	(0.21)	4.7	(22.52)
GFU Filter Total		0.40		13.18	
Online Total		0.99		14.83	
SplineMPE (offline)	Direction	0.45		31.81	
Paraboloid (offline)	Angular Error	6.15		410.33	
Offline Total		7.59		451.79	

Table 4.1: Per-event execution time of selected online reconstructions. The estimates were obtained on a system equivalent to those used at the South Pole. For online use, the angular error estimates are only evaluated on a subset of events. Their execution time considering *all* events at the final filter level is given in brackets. For comparison, the times from the same reconstructions but configured with the settings typically used in offline analyses are shown.

In further analyses the angular error is modeled using a two-dimensional, circularized Gaussian distribution. Within one standard deviation a 39 % containment is provided, hence the median pull is expected at 1.1774 standard deviations. Calculating the pull in different bins of the muon energy proxy MuEX, a correction factor can be determined in each bin, and a spline fit provides a smooth correction to the pull. Since different estimators are used depending on certain event properties, the procedure is applied to each estimator separately, before the results are combined. Figure 4.7 shows an example of the pull distribution using the online angular error estimators. The steps in the distribution occur due to the energy-dependent use of different estimators. While the median can be calibrated well, the width of the central 68% containment band is limited by the variance of these estimators.

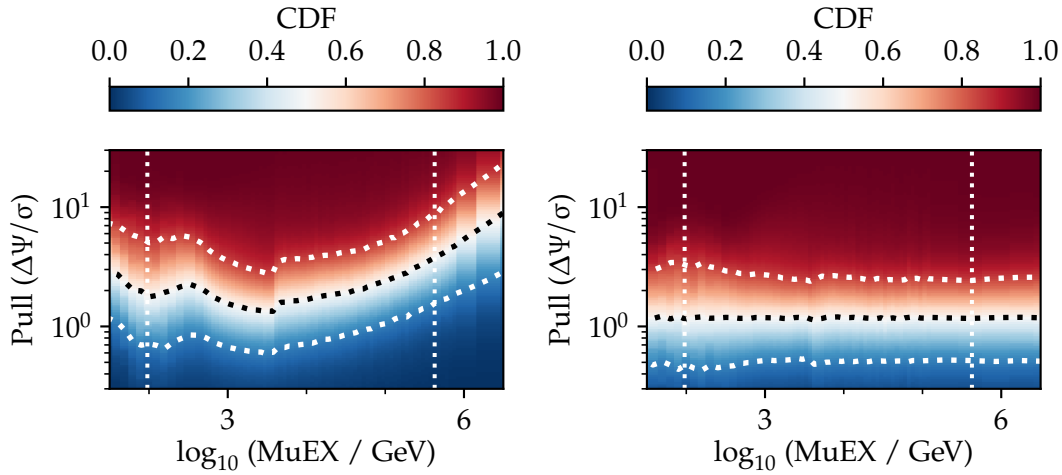

(a) Before correction

(b) After correction

Figure 4.7: Pull correction for angular errors. The pull between the true ($\Delta\Psi$) and reconstructed error (σ) with respect to the neutrino direction is corrected as a function of the muon energy proxy (MuEX). The left (right) panel shows the original (corrected) distribution. The dotted, horizontal lines show the median (black) and the surrounding 68% containment (white), whereas the vertical lines indicate the central 99-percentile found in the data. The seemingly discontinuous distribution in the left panel is due to different estimation methods being used depending on the muon energy.

4.4 Neutrino Event Selection

At this stage, the sample of events still consists mostly of mis-reconstructed events from down-going particles produced in air showers. Yet, the event rate is low enough to be able to evaluate sophisticated reconstruction methods in terms of direction and energy of the events. The final filter step now aims at selecting only properly reconstructed events, while maintaining the largest possible signal efficiency.

Besides the time it takes to reconstruct events, a reduction of the event rate is also necessary to accommodate the stream of event information within the available satellite bandwidth.

Since the dominant kind of background is different in the two hemispheres, two separate classifiers will be developed using an individual set of variables in each hemisphere. The details for the northern and southern sky are given in Sec. 4.4.1 and 4.4.2, respectively, following a description of the general principle.

Boosted Decision Trees

At this point, several reconstructions have been applied, whose observables provide means to further down-select the number of events and reject the background.

Cuts on single observables essentially split the data sample in two parts, which is rarely efficient or effective. Cuts based on multiple observables select a hypercube out of the data. While this can provide a more efficient selection, the adjustment of the cuts becomes tedious due to the large number of possible combinations of observables and their correlations. Thus, an automated way of building such a multi-variate classifier is desirable. While this work uses decision trees, other means of events classification have been studied in recent works with similar results [116].

A decision tree is a set of binary decisions, which can be several levels deep. Each node is defined by an observable and a cut value. Depending on which side of the cut an event ends up on, it is passed on to one or another node. After passing the last node, and event assigned to a signal- or background-dominated leaf.

The purity p of each leaf is defined as

$$p = \frac{w_s}{w_s + w_b} , \tag{4.1}$$

where w_s and w_b are the sums of signal and background event weights, respectively, in the leaf. The output of the nodes is connected to further nodes which split the content of the leaf again, in order to increase the purity in the leaves. Each cut splits the events into sub-samples with the summed event weights w_L and w_R and the purities p_L and p_R, respectively, to the left (L) and right (R) of the cut value. The training process evaluates the observables and their possible cut values at each node. A choice of observable and cut is made which maximizes the separation gain

$$\Delta S = w \cdot S(p) - w_L \cdot S(p_L) - w_R \cdot S(p_R) , \tag{4.2}$$

where S is the Gini separation criterion:

$$S(p) = p \cdot (1 - p) . \tag{4.3}$$

The process is repeated and the decision tree grows until a stopping criterion is reached, such as the maximal depth of the tree.

After a tree is assembled, it is applied to the sample of training events, and event weights will be adjusted depending on whether the event was classified correctly, i.e. increasing the weight of mis-classified events (a process called "boosting"). Constructing another tree and repeating the entire procedure yields a set of "Boosted Decision Trees".

A variation is to introduce a random element to the training process: A small number out of all observables are selected randomly at each node and the one which maximizes Eq. 4.2 is picked for the tree. Building up many trees in that way yields a "Random Forest".

The software used in this work combines both strategies, boosting the event weights in between training steps and randomizing the choice of observables at each node.

Care must be taken to limit the training and avoid it picking up on the peculiarities of the finite sample of training events, instead of finding the broader patterns in the data. This phenomenon is known as "overfitting" or "overtraining" and is mitigated

through several mechanisms, e.g. the random choice of observables, limiting the number of trees and the depth of the trees, and demanding that at least a certain number of events remain in the final leaves.

Implementations of the algorithm are found in the publicly available "scikit-learn" package [117], as well as IceCube's internal "pyBDT" implementation[3]. The scikit-learn toolkit was used for the training, as its decision trees provided the best separation power. However, in practice, the classification is done uses pyBDT, as it is a reviewed IceCube software project which had already been successfully deployed at the South Pole.

4.4.1 Northern Sky

This filter is based on the output of the OnlineL2 filter, which employs different cuts in different zenith regions and defines up-going events as having a reconstructed zenith of $\theta > 82^\circ$. In order to produce smooth variable distributions and avoid sudden changes in the event rate, this definition of the threshold is kept and used now to train separate classifiers for the northern and southern parts of the sky.

Decision Tree Variables

As explained in Sec. 4.2 the background events in the northern sky consist of mis-reconstructed down-going muons and mis-identified cascades, as well as atmospheric neutrinos. The latter's signature is indistinguishable from the astrophysical neutrinos, which form the signal sample. Hence, the filter strives achieve a sample of (muon-) neutrinos with high purity by removing the the mis-reconstructed muons and cascades. This focus suggests the use of training variables which can be grouped in three categories: quality of the reconstruction, robustness of the recons truction, and event topology.

Reconstruction Quality

Track Likelihood: The likelihood value of the directional reconstruction (Sec. 3.4.1) provides an immediate handle on the match between the observed event properties and the hypothesis of a muon track. Comparable values between different events are obtained by normalizing the likelihood with the number of degrees of freedom. A track fit aims to optimize time residuals at each DOM, using five free parameters, suggesting

$$\frac{\log \mathcal{L}}{N_{Ch} - 5}$$

as a proxy for the fit quality. It was however found in previous analyses that an energy-dependent behavior remains which is better controlled with a different re-scaling

[3] http://software.icecube.wisc.edu/documentation/projects/pybdt/index.html

of

$$\frac{\log \mathcal{L}}{N_{Ch} - 3.5} .$$

Note that for technical reasons the optimization algorithms minimize the negative of the likelihood.

Angular Error: Aside from the actual, optimized likelihood value also the shape of the likelihood landscape around the optimum is of interest. In this analysis, the Cramér-Rao method (Sec. 3.4.1) is used to derive the second order derivative (i.e. the curvature) of the likelihood function at the direction of the best fit value. A slight curvature suggests a broad optimum, which is only loosely defined, whereas a strong curvature would indicate a narrow optimum, which is well constrained and representative of a good reconstruction. In principle, the paraboloid method (Sec. 3.4.1) would provide an even better view, as it samples the likelihood landscape at several points around the optimum. Unfortunately it requires too much computing time which prohibits its use at this stage and it is only applied later on a subset of all events.

LineFit Speed: The simplest directional reconstruction, the LineFit (Sec. 3.4.1), models the PMT pulses with a plane wave passing through the detector. While not very physical, this approach provides an estimate of the velocity of the particle. For actual, high-energetic muons with a successful reconstruction, this value is expected around the speed of light, whereas the distribution is smeared out for background events, which do not fit the hypothesis.

Reconstruction Robustness

Angle between SplineMPE and LineFit: Even though the LineFit method does not accurately model the geometry of the light emission or the local ice properties, it should provide a rough estimate of the direction if the event is actually shaped like a track. The advanced likelihood-based reconstruction, using a refined model of the ice properties, should yield a similar result. If both reconstruction results differ strongly, this could indicate an unreliable fit result, as in the case of mis-identified cascades.

Split Fits: One class of mis-identified events are coincident events, i.e. two particles interacting in different parts of the detector (almost) simultaneously. The event splitting procedure (see Sec. 3.3) can only disentangle such interactions if they occur at least 10 microseconds apart. Otherwise, the directional reconstruction will try to reconcile the pulses from two unrelated particles with a common track, which is destined to fail. In order to catch those cases, the pulse series is split into two halves and both sub-sets of pulses are reconstructed individually. The splitting is done either

in at the median pulse time, or at a plane perpendicular to the track through the center of gravity, creating a total of four sub-events.

For events which only consist of one muon, all reconstructions of sub-sets of pulses should point in a similar direction as the original fit. A training variable is constructed as

$$\cos \min_{\text{Split}} \theta_{\text{Split}} - \cos \theta_{\text{SplineMPE}} \ .$$

This construction of the variable selects the sub-reconstruction with the smallest zenith angle, making it most sensitive to the down-going, atmospheric muons which provide the dominant coincident background.

Bayesian Likelihood: The expectation of down-going, atmospheric muons can be incorporated into the likelihood model by multiplying Eqn. 3.12 with a Bayesian prior [118] given by

$$\mathcal{P}(\theta) = a_0 \cdot (\cos\theta)^{a_1} \cdot \exp(-a_2/\cos\theta) \ ,$$

where the constants a are determined by the atmospheric muon flux measured by the AMANDA experiment [118, 119]. In the case of down-going muons that were reconstructed as up-going due to a local extremum in the likelihood space, this factor can increase the likelihood value of the down-going fit solution and reveal the global minimum. Thus, the difference in the fitted likelihood value with respect to the unbiased reconstruction can provide rejection power against mis-reconstructed down-going muons.

Event Topology

Center of Gravity: Muons traversing a large part of the detector are likely to be well reconstructed. However, muons skimming the outer surfaces or even just the corner of the detector can produce ambiguous light deposition patterns with a much larger chance of mis-reconstruction. The center of gravity of the hits

$$\overrightarrow{CoG} = \frac{1}{Q_{\text{tot}}} \sum_{i}^{\text{DOMs}} q_i \cdot \vec{x}_i \ ,$$

with q_i and $\vec{x}_i$ being the total charge and location of DOM i, allows the filter to determine how close an event was to the border of the detector. Following IceCube's roughly cylindrical outline, the radial component (CoG_ρ) and the depth component (CoG_z) are used in the decision trees.

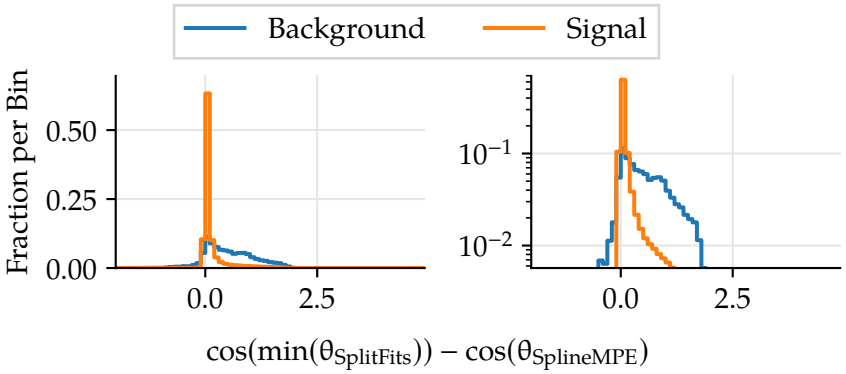

(a) Difference between the best fit of the entire set of pulses, and the most down-going fit on the split sets of pulses.

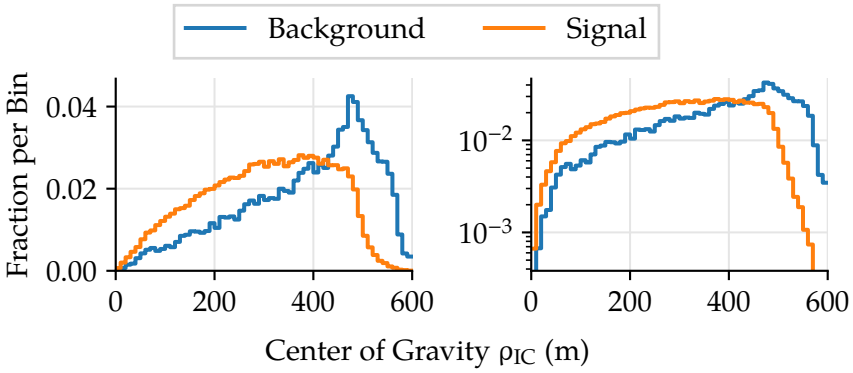

(b) Center of gravity, radial component.

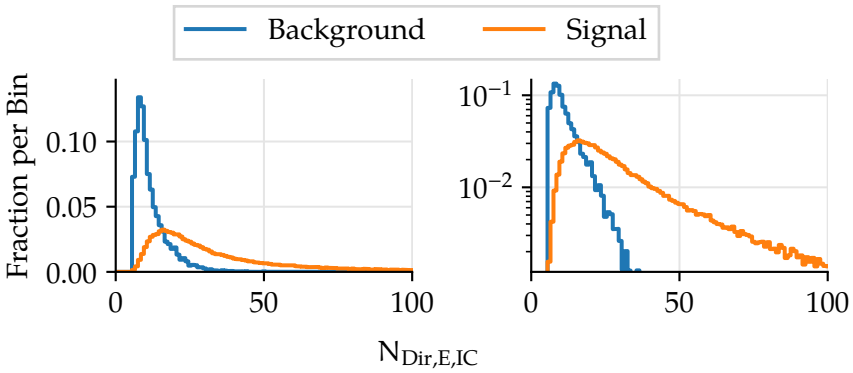

(c) Number of direct hits.

Figure 4.8: Examples of BDT input variables. Shown are the normalized distributions of variables, which are used in the training of the BDT, for the signal and background event samples. Left (right) panel show the distribution on a linear (logarithmic) scale.

Direct Hits: During the event reconstruction the concept of a time residual (Eq. 3.8) was introduced. The difference between the expected and observed photon arrival times at the DOM provides a handle of the quality of the reconstruction. Due the potential of the photon being scattered on its way through the ice, and finite timing resolution on the detector side, narrow time windows are defined around the expected arrival time during which hits are still considered "direct". The commonly used definitions are $-15\,\text{ns} \leq t_{res} \leq 75\,\text{ns}$ (time window C) and $-15\,\text{ns} \leq t_{res} \leq 250\,\text{ns}$ (time window E).

The number of direct hits N_{Dir} provides a discriminator for potentially mis-reconstructed events with few direct hits.

Searching for through-going muons, the direct hits should also be distributed along the track with a corresponding direct length L_{Dir} being defined as the distance between the first and last direct hit. Due to the large weight contributed by the time residual PDF of the first (direct) pulse to the likelihood, the direct length provides a measure of the lever arm that constrains the reconstruction.

In the case of well-reconstructed tracks the direct hits should also be distributed equally along the length of the track. The "smoothness" S measures the maximum relative deviation of the direct hits from a uniform distribution

$$S_{dir} = \max_{i \in \text{Direct Hits}} \left| \frac{i}{N_{Dir}} - \frac{l_i}{L_{Dir}} \right| ,$$

where l_i is the distance of the i-th direct hit along the track.

Distribution of Hits: The distribution of hits along the track hypothesis can also provide discrimination between actual up-going tracks and mis-reconstructed down-going muons and cascades.

The separation length L_{Sep} is defined as the distance between the center of gravity of the first and last quarter of hits. For a track-like shape this distance should be much longer than for a mis-reconstructed event.

In order to improve the rejection of coincident events, the empty track length L_{Empty} is introduced. It measures the maximum distance along the track, during which no hits were observed within a radius of 150 m around the track. Large empty track lengths can indicate that one event comprises two muons in different parts of the detector, which the reconstruction tries to combine.

Finally, the light profile around the track should be such that the DOMs with the most charge should be located close to the track, with DOMs further away from the track observing less light. The average charge-weighted track-to-DOM distance encodes this:

$$\text{AvgDistQtotDOM} = \frac{1}{Q_{tot}} \sum_{i}^{\text{DOMs}} q_i \cdot d_i ,$$

where q_i is the charge in the i-th DOM and d_i is the distance of the projection of the DOM onto the track. Well-reconstructed events show a distribution centered around

50 m, whereas the distribution of mis-reconstructed events shows a tail towards larger values where even DOMs far from the track observed a large amount of light.

Training

All variables used in the selection of up-going events are listed in Tab. 4.2. Figure 4.8 shows a few examples for the distributions of the training variables for signal and background events. In order to facilitate the BDT training and ensure that all the input variables have a well-defined, finite range of values pre-cuts are defined to clip the tails of the distributions. In addition, further processing only considers events for which the previous reconstructions have converged successfully and returned values in a meaningful range. This concerns in particular the SplineMPE directional reconstruction, its uncertainty estimation using the Cramér-Rao method, the forced down-going Bayesian likelihood fit, and the MuEX energy estimation which must yield at least 10 GeV.

Several of the variables directly relate to the number of (direct) hit DOMs. The IceCube detector is roughly homogeneously instrumented, with the exception of the DeepCore sub-array in the lower half. Here, the instrumentation density is higher and a track passing through DeepCore will yield more hits than the same track passing next to DeepCore. As the DeepCore sub-array is concentrated in one small spot (compared to the size of the surrounding detector) its hits contribute to the reconstruction with only a very short lever arm. While this does not noticeably affect the angular resolution, it can cause undesirable spikes in the distribution of related variables such as N_{Dir}. Therefore, some variables are calculated excluding the hits observed on the DeepCore DOMs, providing a more homogenized view of the detector. These variables are highlighted in italics in Tab. 4.2.

The training sample of signal events consists of simulated muon neutrino interactions (Sec. 3.5). The simulated truth is used to select a subset of events with a successful reconstruction and the desirable properties that should appear in the final sample: Only events with charged-current muon-neutrino interactions are selected, and the outgoing muon track must intersect with the instrumented volume (approximated as a cylindric volume of 1 km^3). There must be no coincident atmospheric muon simulated in the same event. Most importantly, the reconstructed track has to agree with the true direction of the *muon* to within 3°. The direction of the original neutrino is not observable and can deviate from the muon direction due to the kinematic scattering angle. Thus, the last criterium solely focuses on the reconstructing the muon as good as possible, in order to avoid an energy-dependent bias towards more energetic events.

Regarding the composition of the training sample of background events several approaches have been followed in previous analyses. Point source searches (such as [44]) have used 10% of available data events, whereas analyses of the diffuse neutrino flux (such as [39]) have used a simulated air showers for the training. It was found that the latter approach yields a more efficient selection with a larger effective area, higher purity, as well as better sensitivity to point sources [120]. This

Name	Pre-cut	Description
CoG_ρ	—	Center of gravity, radial distance
CoG_z	< 500 m	Center of gravity, z-component
L_{Sep}	> 50 m	Track hits separation length
$\log \mathcal{L}_{\text{Bayesian}} - \log \mathcal{L}_{\text{SPE2it}}$	> 20	Forced down-going likelihood fit
$\cos\theta$	> 82°	Reconstructed zenith
$\log \mathcal{L}_{\text{SplineMPE}} / (N_{\text{Ch}} - 3.5)$	< 10	Goodness of track fit
$L_{\text{Dir,C}}$	> 75 m	Direct hits track length
$N_{\text{Dir,E}}$	≥ 6	Number of direct hits
$\sigma_{\text{Cramér–Rao}}$	< 25°	Cramér-Rao error estimate
$\lvert S_{\text{Dir,E}}\rvert$	—	Smoothness of direct hits
AvgDistQtotDOM	< 250 m	Weighted track-to-DOM distance
L_{Empty}	< 600 m	Empty track length
$\cos \measuredangle(\text{SplineMPE}, \text{LineFit})$	< 60°	Angle between SplineMPE and LineFit
$\lvert\vec{v}\rvert$	< 3	Velocity estimate
$\log N_{\text{Ch}}$	≥ 6 DOMs	Number of hit DOMs
$\cos \min \theta_{\text{Split}} - \cos\theta$	—	Zenith fit of splitted event

Table 4.2: Variables used in the BDT for up-going events. The central column indicates a cut that is applied before the training (if any). Variables marked in *italics* are evaluated excluding the DeepCore DOMs, other variables are evaluated using all DOMs.

is attributed to the contamination of the data with actual signal events. Thus, the training process will not be able to determine the most efficient set of cuts once the training is effective enough that simulated signal events compete with signal events in the background sample. By construction, using simulated air showers avoids this situation.

After the training on a background event sample of down-going muons was completed, it was found that a residual contribution of mis-identified cascades from electron neutrino and neutral-current interactions remained, which was also seen in earlier offline analyses [39]. Instead of training another set of decision trees to remove those events (as in [39]), in this work the background training set was modified to include this event topology: Neutral-current interactions from the muon neutrino simulation were added to the training as an additional set of background events. The contribution to the background from atmospheric muons was weighted according to a theoretical model [13], and the background from neutrino-induced cascades was weighted according to previous measurements [39]. Since the contribution of neutrino-induced cascades is too small (compared to atmospheric muons) to be efficiently picked up in the training, the sum of both background contributions was normalized to 1, respectively, in order to reflect that both are equally undesirable in the final event sample.

Training the classifier requires a choice of meta-parameters. They were found

Parameter	Value
Number of trees	300
Maximum depth of trees	5
Minimal number of events in a leaf	1000
Random variables considered at each node	3
Boosting strength (β)	0.1
Use purity weights	Yes

Table 4.3: Meta-parameters used in the training of the BDT for up-going events. Several choices for each variable were scanned to find the configuration providing the best background rejection.

by scanning several choices for each parameter and compared in their background rejection power at a signal efficiency of 99%. Table 4.3 lists the settings that were eventually used. In order to avoid over-training the maximum depth of the trees as well as the number of events that must remain in leaf before introducing an additional split were limited. In addition, boosted training with a small boosting strength of 0.1 was combined with the randomization approach: At each node, three variables are picked at random and the one providing the best separation gain out of only those three variables is finally chosen.

Figure 4.9 shows the distribution of the BDT scores after the training. The trees are able to clearly separate the mis-reconstructed atmospheric muons from the muon-neutrino induced events. Agreement between data and simulation depends on the BDT score. It is rather poor for the lowest scores which are solely dominated by atmospheric background. The agreement improves towards the more signal-rich region, where it is very good once the sample reaches a high purity, i.e. for BDT scores larger than 0.

The available simulation was split in half, with one half used for the training and the other half for verification. An over-trained BDT, which picked up artefacts of the training sample, would perform different on the verification sample. By comparing the distributions of the BDT score for both sets of events it was verified that the learning did not over-train. The match of the distribution of BDT scores between training and verification data was successfully tested with a Kolmogorov-Smirnov test, yielding a p-value of 32% for the background and 13% for the signal event samples.

The overall set of variables was optimized for background rejection and many sets of decision trees were trained and compared in that regard. The importance of the variables that were chosen eventually is shown in Fig. 4.10 and can be judged in two ways: On the one hand, weighting each node at which a variable appears with the separation gain and the weight of the tree favors variables which appear at the early splits (where the separation gain is large) or in early trees (where the tree weight is large). Thus, these variables provide a classification of the majority of a good portion of events. On the other hand, the unweighted importance equally considers variables further down in trees or in later trees, where they provide classification for small

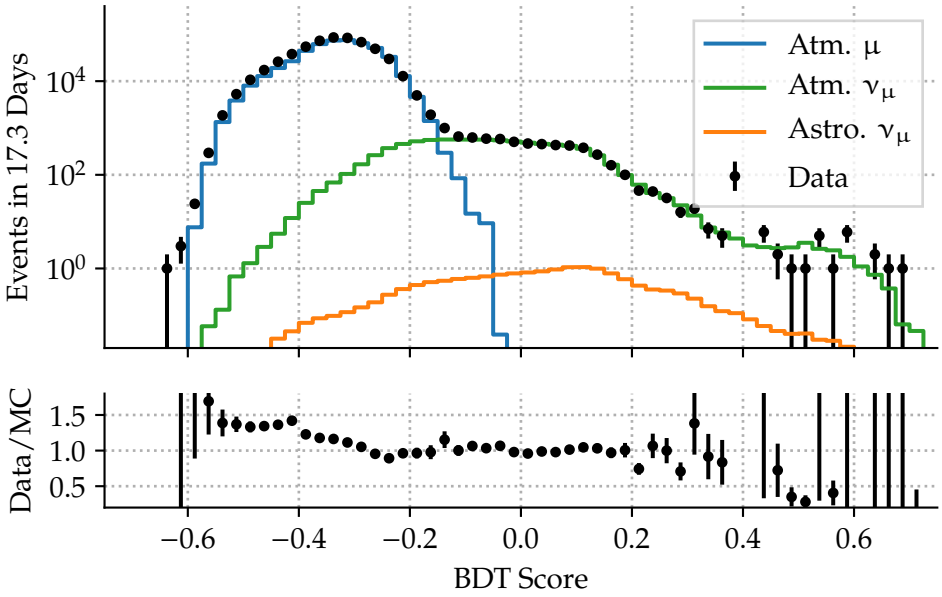

Figure 4.9: BDT scores for up-going events. The trees are able to separate the background of mis-reconstructed atmospheric muons (blue) from the muon neutrino-induced tracks (green and orange). The agreement between data and simulation is shown in the lower panel.

subsets of challenging event topologies.

The final task of choosing a BDT cut is deferred to Sec. 5.3. It needs to be optimized for the best point source discovery potential, but also provide a smooth transition at the horizon from the selection of up-going events to the selection of down-going events, which will be described in the next section.

4.4.2 Southern Sky

Whereas the background in the northern sky consisted largely of mis-reconstructed events which were expected to be almost completely rejected, the situation in the southern sky is different. Muons produced in cosmic-ray induced air showers are not shielded by the Earth and can reach the detector, producing the same signatures as neutrino-induced muons. In addition, in the context of this work, a muon bundle refers to any group of muons which were produced in an air shower and travel collinear, but may be slightly offset. The individual particles in the bundle cannot be resolved by the comparatively sparse instrumentation. Hence, a bundle of several low-energetic muons will yield a signature in the detector which is almost identical to that of a single high-energetic muon.

One way to deal with this class of events are veto techniques: By reducing the fiducial volume of the detector and mandating that no light be deposited in the

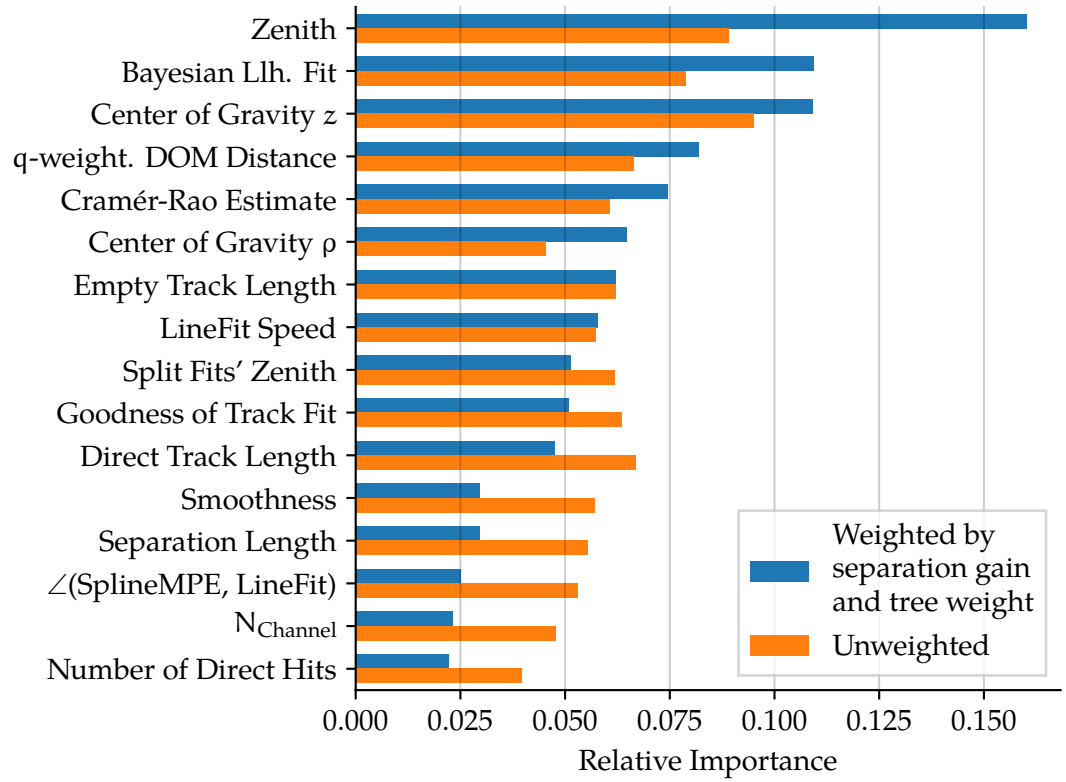

Figure 4.10: Importance of BDT variables for up-going events. The blue bars are obtained when weighting the occurrence of each variable by the separation gain at the node and the weight of the tree. The orange bars are based on the unweighted count of the nodes where the variable is used.

outer layer of strings it is possible to select only muon tracks which start inside the detector [65, 121]. Atmospheric muons (and atmospheric neutrinos accompanied by muons) would already be visible on the detector edges as they enter from outside, whereas the observation of the neutrino interaction vertex inside the detector provides a hint of a neutrino with a high chance of being of astrophysical origin. The rate of events from the southern sky starting inside the detector ($\approx 180/\text{yr}$) is constrained by the fiducial volume of the detector and is much lower than that of through-going events ($\approx 50.000/\text{yr}$), whose interaction vertex can be located anywhere in the vast surrounding glacier.

Another complication for online searches is that veto-based selections rely on the veto DOMs working properly. For example, it cannot be instantaneously determined whether a DOM saw no hits because there were no photons or because of a malfunction, which might allow atmospheric muons to sneak through the veto. Hence, while this analysis is still sensitive to starting events, it does not specifically target them.

The same reasoning applies to using the IceTop detector as a veto for air showers. It

introduces another dependency with a potentially negative effect on the uptime. Due to the area covered by the IceTop tanks, an improvement in sensitivity could only be expected for very inclined events with zenith angles below 15° [44].

Decision Tree Variables

Mis-reconstructed events are only a small concern and can be covered by the same variables that were presented in the previous Sec. 4.4.1. In order to separate single muons from multiple muons leftover from an atmospheric shower, additional variables are introduced to deal with this part of the sky.

Time Residuals The time residuals obtained from the track reconstruction have been used in pervious works to determine the quality of the reconstruction. While the direction of muon bundles can be reconstructed in the same way as that of single muons, subtle differences in the individual time residuals are expected [44].

The muons in the bundle may travel collinear, but they will be slightly offset as they originate from different interactions in the air shower. In addition, the individual muons have a lateral offset, thus the difference between muon track and DOM is different for each muon. Hence, compared to a single muon the bundle will cause pulses in the DOMs which are earlier or later than expected, i.e. they have non-zero time residuals (Eq. 3.8).

Figure 4.11 shows the observed time residuals t_{res} as a function of the track-to-DOM distance d, estimating the background distribution from data and the signal distribution from the simulation of muon neutrinos. The distributions are sampled in bins of the muon energy proxy E, as stochastic energy loss processes appear depending on the muon energy, and they are normalized in slices of the track-to-DOM distance, providing the signal or background probability $p_{s|b}(t_{res}|d, E)$ for each hit.

The signal-to-background ratio in the lower row shows that early hits are a likely indication of a background event. Late hits hint at a signal-like muon, but are also caused by scattered photons, especially here in the case of down-going events where the Cherenkov light may not directly illuminate the PMT. In order to reduce the weight of late pulses appearing due to scattered photons only the first pulse in each DOM is used.

Combining the information from all hit DOMs in an event, a likelihood ratio can be constructed as follows:

$$\log \mathcal{L}_{t_{res}} = \log \left(\prod_{i}^{N_{Ch}} \frac{p_s(t_{res,i}|d_i, E)}{p_b(t_{res,i}|d_i, E)} \right) = \sum_{i}^{N_{Ch}} \log \frac{p_s(t_{res,i}|d_i, E)}{p_b(t_{res,i}|d_i, E)} \,. \tag{4.4}$$

Additionally, a reduced log likelihood ratio is defined as $\log \mathcal{L}_{t_{res}} / N_{Ch}$.

DDDDR Another difference between single muons and muon bundles can be found in the light deposition profile. In contrast to bundles of low-energetic muons,

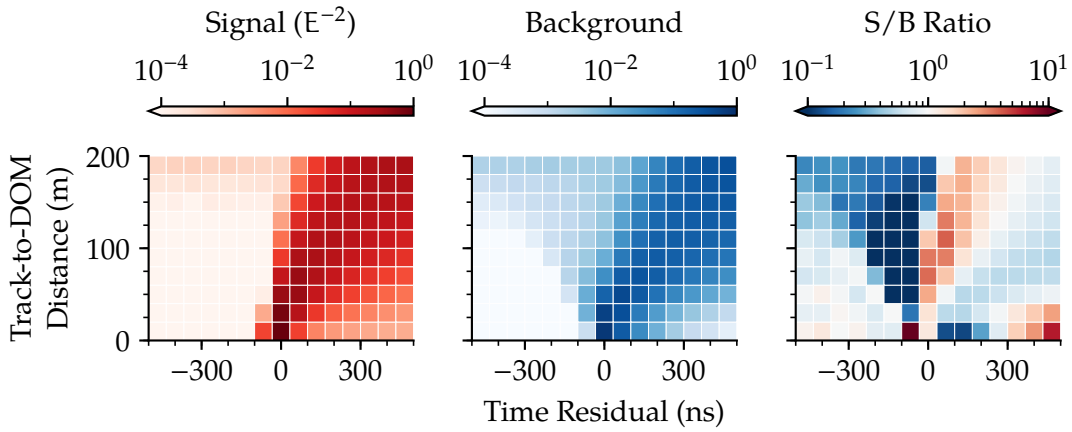

Figure 4.11: Time residual distributions for events with a muon energy proxy (MuEX) between 32 and 320 TeV. The left (middle) panel shows the distribution of the time residuals of pulses observed in signal (background) events. Background events are obtained from 3 days of archival data before the BDT cut, sampled throughout the year. The distributions are normalized in slices of the track-to-DOM distance. The right panel shows the ratio between signal and background.

single high-energetic muons will undergo occasional stochastic energy losses in addition to the near constant radiation of Cherenkov light (Sec. 3.4.3).

Identifying these stochastic losses provides additional discrimination power against bundles of multiple low-energetic muons, which may deposit the same total amount of light in the detector as a single high-energetic muon, but only show a constant Cherenkov emission.

In offline analyses an algorithm is used to unfold the individual energy depositions along the track. It fits a variable series of energy losses in order to describe the observed charge in each DOM [63]. While this method is accurate, its demands on computation time scale linearly with the number of pulses in an event, making it unfeasible to run online for the brightest, most interesting events.

Here, a faster approach is used to extract similar information: the data-derived deterministic differential deposition reconstruction (DDDDR) [122]. As with other energy reconstruction methods, the number of photons N_γ per track length Δx is assumed proportional to the energy loss ΔE. For an infinitely long track the number of observed photons falls off with $1/d_i$, where d_i is the distance between the DOM and its projection on the track. In practice, absorption and scattering in the ice cause additional light attenuation of $\exp(d_i/\lambda_{att})$. The effective attenuation length λ_{att} depends on the local ice properties and is assumed to depend on the depth. It has been determined in a previous analysis from a sample of bright, down-going muons. Taking the relative quantum efficiencies of the DOMs ϵ_i into account as well, the

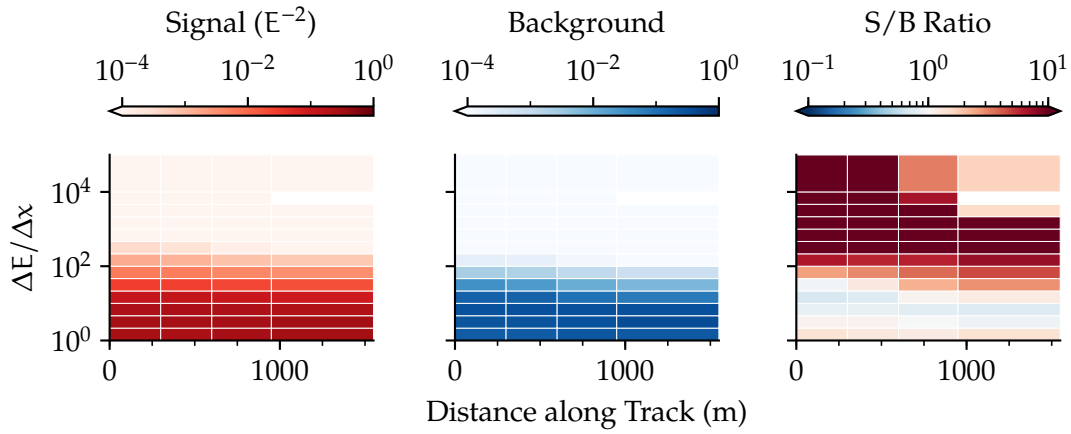

Figure 4.12: Differential energy loss distribution for events with a muon energy proxy (MuEX) between 10 and 25 TeV. The left (middle) panel shows the distribution of energy losses observed in signal (background) events. Background events are obtained from 3 days of archival data, sampled throughout the year. The right panel shows the ratio between signal and background.

differential energy loss can be expressed as:

$$\frac{\Delta E}{\Delta x} = \beta \cdot N_\gamma = \beta \cdot \frac{q_i \cdot d_i \cdot \exp(d_i/\lambda_{att}(z))}{\epsilon_i} \,. \tag{4.5}$$

Simulations were used to determine the scaling factor β and calibrate it to the true muon energy loss [122].

In order to deal with the variations in the energy losses, the track is segmented in bins of 50 m, similar to the approach outlined in Sec. 3.4.3. In each segment, Eq. 4.5 is applied to each DOM inside a cylinder of 150 m radius around the track; then the results are averaged.

Similar to Eq. 4.4 a likelihood variable is constructed from the estimated energy losses along the track. The distributions in Fig. 4.12 show the expected energy losses along the track. Stochastic, large energy losses separated by dim segments hint at a single, high-energetic muon, whereas a smooth energy loss pattern would be attributed to a bright bundle of low-energetic muons. This method of accounting of combining the signal and background probabilities of all energy losses into one variable was found to provide better separation power than previously used approaches of only looking at the ratio between the peak and the median reconstructed loss [122]. It should be noted however, that even in muon bundles of atmospheric origin the majority of the energy may be carried by one leading muon, which will undergo stochastic losses. Such events are harder to disentangle from the desired single muon events and are left as a residual background that can be tackled with the time residual likelihood from the previous chapter.

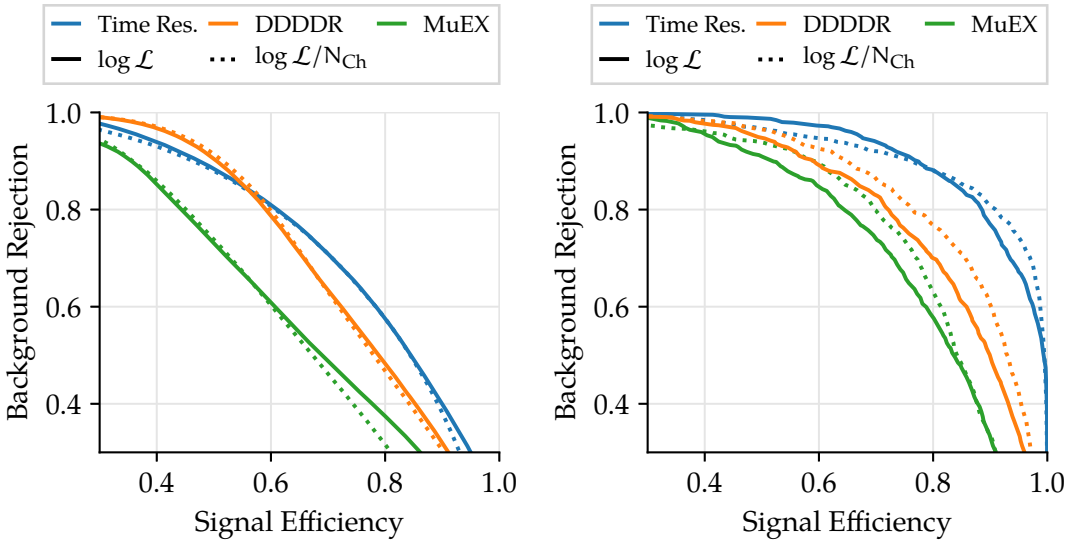

(a) All events

(b) Muon Energy Proxy > 200 TeV

Figure 4.13: Efficiency of the likelihood variables for muon bundle rejection. The solid lines are obtained using the likelihood, the dotted lines show the likelihood normalized by the number of DOMs involved. Both the time residuals and differential energy losses from DDDDR are used in the final event selection. An alternative to using DDDDR is the MuEX reconstruction, shown here for comparison.

Figure 4.13 shows the signal efficiency and background rejection curves of the methods described so far. An additional comparison is shown applying the same method to the energy loss pattern reconstructed with the MuEX energy reconstruction (Sec. 3.4.3), which is ultimately still less efficiency than using DDDDR. All methods perform increasingly better with energy, which is to be expected as the increasing stochastic energy losses allow for a better separation.

Training

All variables used in the selection of down-going events are listed in Tab. 4.4. Pre-cuts are defined to clip the tails of the distributions which facilitates the BDT training and ensures that all the input variables have a well-defined, finite range of values. In addition, further processing only considers events for which the previous reconstructions have converged successfully and returned values in a meaningful range. This concerns in particular the SplineMPE directional reconstruction, its uncertainty estimation using the Cramér-Rao method, and the MuEX energy estimation which must yield at least 316 GeV.

Additional requirements are given in Tab. 4.4. In particular, a minimal number of strings must be hit to properly constrain almost vertical events. Also, a minimal track

Name	Pre-cut	Description
$\mathcal{L}_{TRes}$	> -11	Time residuals
$\mathcal{L}_{\mathrm{DDDDR}}/\mathrm{N}_{\mathrm{Ch}}$	> -0.14	Differential energy depositions
CoG_{ρ}	< 540 m	Center of gravity, radial distance
CoG_{z}	$\leq$ 480 m	Center of gravity, z-component
$L_{\mathrm{Dir,D}}$	—	Direct hits track length
$N_{\mathrm{Dir,E}}$	$\geq$ 12	Number of direct hits
$\sigma_{\mathrm{Cramér-Rao}}$	$< 10^{\circ}$	Cramér-Rao error estimate
$\log \mathcal{L}_{\mathrm{SplineMPE}}$ / $(\mathrm{N}_{\mathrm{Ch}}-5)$	< 10	Goodness of track fit
L_{Sep}	> 75 m	Track hits separation length
q_{early} / $q_{\mathrm{Dir,A}}$	—	Early light deposition
$\log_{10}(q_{\mathrm{max}} / q_{\mathrm{tot}})$	< -0.2	Charge in brightest DOM
MuEX obs./expect.	$\in [0.5, 1.5]$	Ratio of observed to expected charge
$\cos\theta$	$\leq 82^{\circ}$	Reconstructed zenith
$\cos\theta - \cos\max\theta_{\mathrm{Split}}$	—	Zenith fit of splitted event
Variables below are only used for pre-cuts, not in the training:		
$L_{\mathrm{Dir,E}}$	> 250 m	Direct hits track length
N_{Strings}	$\geq$ 7	Number of strings
$\log \mathrm{E}_{\mathrm{MuEX}}$	> 316 GeV	Muon energy proxy
$\cos \measuredangle$(SplineMPE, LineFit)	$< 43^{\circ}$	Angle between SplineMPE and LineFit

Table 4.4: Variables used in the BDT for down-going events. The central column indicates a cut that is applied before the training (if any). Variables marked in *italics* are evaluated excluding the DeepCore DOMs, other variables are evaluated using all DOMs.

Parameter	Value
Number of trees	400
Maximum depth of trees	5
Minimal number of events in a leaf	1000
Consider n random variables at each node	3
Boosting strength (β)	0.1
Use purity weights	No

Table 4.5: Meta-parameters used in the training of the BDT for down-going events. Several choices for each variable were scanned to find the configuration providing the best background rejection.

length of 250 m is used to ensure that the track provides enough of a lever arm for pointing, and also to ensure the segmented derivation of the energy losses.

As was the case for the selection of up-going events, some variables are calculated excluding the hits observed on the DeepCore DOMs, providing a homogenized view of the detector and avoiding spikes in the distributions of the variables. The variables concerned are highlighted in italics in Tab. 4.2.

The sample of signal events used in the training is constructed in the same way as for the northern sky, except with an inverted cut on the zenith. Events must contain a charged-current muon-neutrino interaction, where the outgoing muon track intersects the instrumented volume, no coincident atmospheric muon is present in the same event, and the muon track is reconstructed within 3° of the true direction of the muon.

The sample of background events for the training is constructed from data. The signal contamination is an order of magnitude lower than in the northern sky and less of a concern than it was for up-going events. In addition, the modeling of down-going atmospheric muons in simulations does not well describe the shape of the distributions observed in data. In particular the zenith distribution is tilted with respect to data. This effect has been noticed in previous analyses and the cause could not be resolved within this work. It is expected that better interaction models and improved description of long-lived mesons in the showers will improve the agreement,

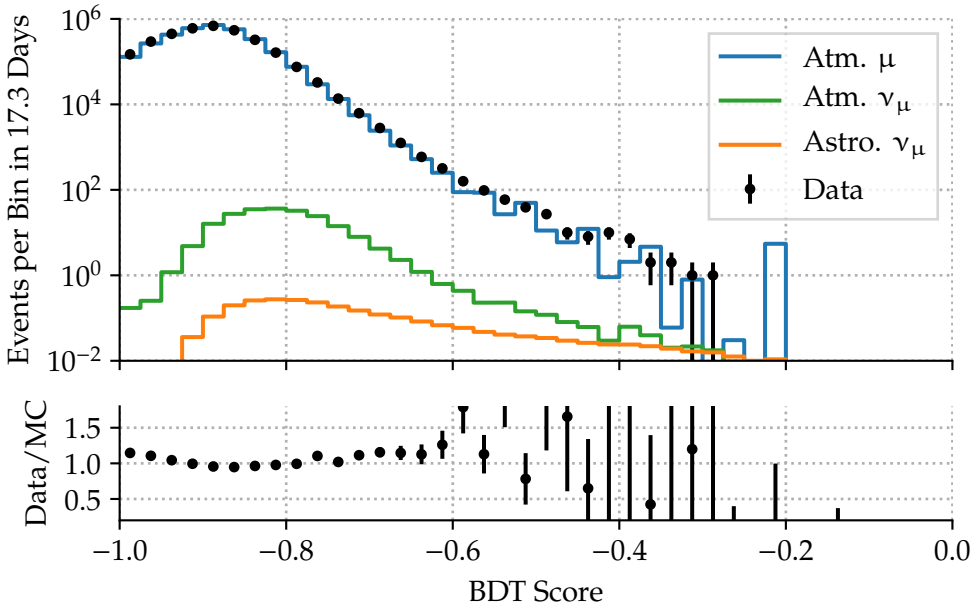

Figure 4.14: BDT scores for down-going events. No strict separation between the background of atmospheric muons (blue) from the neutrino-induced tracks of single muons (green and orange) is possible. The agreement between data and simulation is shown in the lower panel.

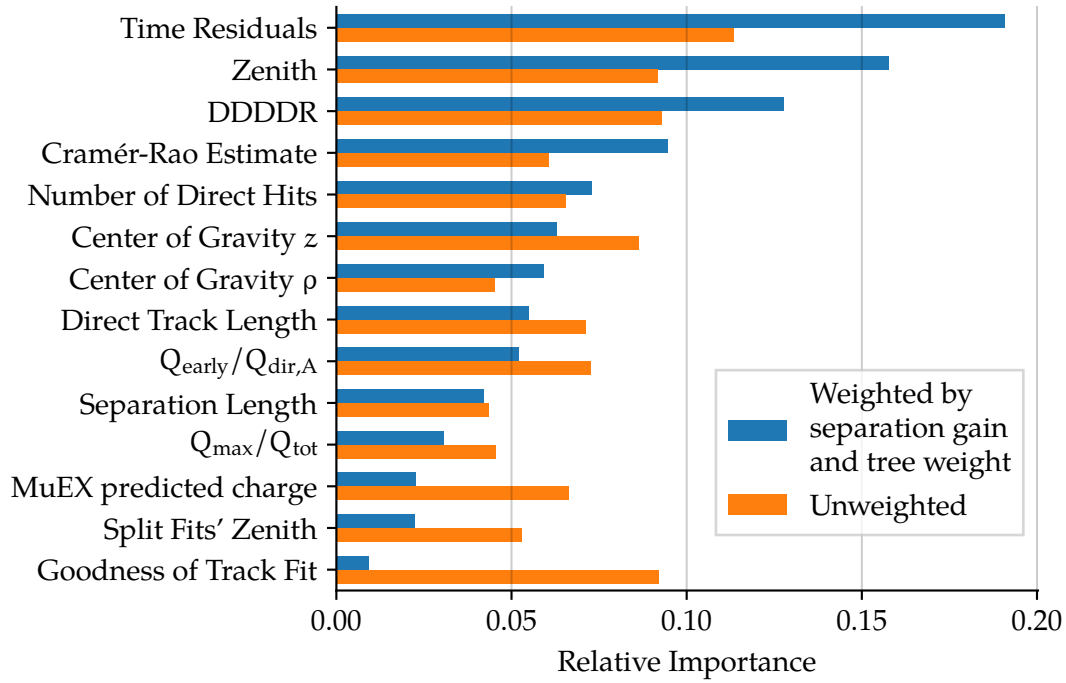

Figure 4.15: Importance of BDT variables for down-going events. The blue bars are obtained when weighting the occurrence of each variable by the separation gain at the node and the weight of the tree. The orange bars are based on the unweighted count of the nodes where the variable is used.

but they were not available at the time of writing. A sample of 10% of data recorded in 2016 serves as the background in the training. The chosen runs are evenly spread throughout the year to avoid a seasonal bias.

The meta-parameters of the classifier and the training were again found by scanning several choices for each parameter. Similar settings as in the northern sky were used and can be found in Tab. 4.5.

Figure 4.14 shows the distribution of the BDT scores for the different classes of events after the training. As opposed to the northern sky, the separation between signal and background is not clear. Eventually, the BDTs are selecting track-like events and is limited by the separation power of the variables presented in the previous section. The importance of the variables is shown in Fig. 4.15. The most powerful rejection of muon bundles is provided by the time residuals and the differential energy loss reconstruction.

5 Search Method for Time-Variable Point Sources

After selecting a sample of track-like muon neutrino candidates the next step is to localize and identify astrophysical sources. This chapter describes the statistical test, which defines the properties of event clusters. First, Sec. 5.1 introduces the likelihood method and PDFs using the example of a time-independent analysis. which is then extended to test time-dependence in Sec. 5.2. Next, the analysis method is used to optimize the BDT cut for the event selection developed in the previous chapter (Sec. 5.3). Finally, the performance of the event selection and analysis is evaluated on the final event selection, and a comparison to offline event selections is made (Sec. 5.4.

5.1 Likelihood Method and PDFs

In the following, a signal (S) and background (B) probability will be assigned to each event, considering two aspects of the reconstructed events: the direction and the energy proxy. Thus, the signal and background probability of each event i can be expressed in terms of a spatial and an energy PDF:

$$\mathcal{S}_i = P^S_{\text{spatial}}(\vec{x}_i|\vec{x}_s, \sigma_i) \cdot P^S_{\text{energy}}(E_i|\vec{x}_i, \gamma) \tag{5.1}$$

$$\text{and} \quad \mathcal{B}_i = P^B_{\text{spatial}}(\vec{x}_i) \cdot P^B_{\text{energy}}(E_i|\vec{x}_i)\,, \tag{5.2}$$

where $\vec{x}_s$ is the location of the source hypothesis, $\vec{x}_i$, σ_i and E_i are the direction, angular uncertainty and energy proxy of the event, and γ is the power-law index of the signal energy spectrum. In this analysis the separation of spatial and energy PDFs in Eqn. 5.2f is justified since the all events in the data sample feature a good directional reconstruction and a relatively coarse energy resolution and there is no correlation between the quality of the reconstruction and the energy estimate [123].

Spatial PDF

The construction of the spatial PDFs exploits that events from the atmospheric background are distributed almost uniformly over the sky, whereas signal events originating from a point-like source should cluster near the source location.

The PDF P^S_{spatial} quantifies the probability of an event being the signal of a hypo-

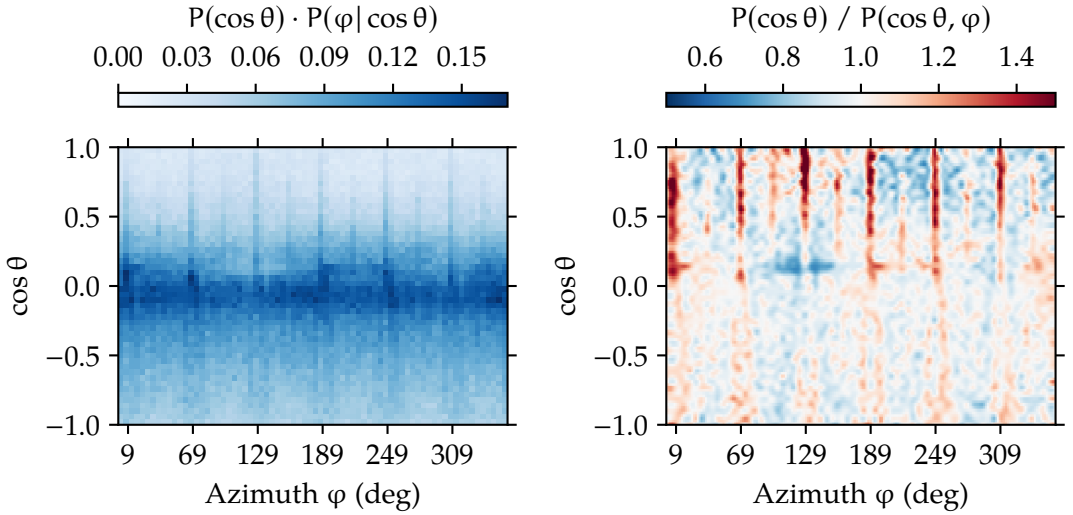

(a) Background PDF

(b) Azimuthal asymmetry

Figure 5.1: Spatial background PDF. The left panel shows the probability distribution of events in detector coordinates, azimuth φ and zenith θ, as it is obtained from archival data. The right panel illustrates the deviation of this two-dimensional distribution from a one-dimensional one, highlighting the symmetry axes of the detector.

thetical source given its location:

$$P^{S}_{\text{spatial}}(\vec{x}_i|\vec{x}_s, \sigma_i) = \frac{1}{2\pi\,\sigma_i^2}\,\exp\left(-\frac{\Delta\Psi_i(\vec{x}_i|\vec{x}_s)^2}{2\sigma_i^2}\right), \tag{5.3}$$

where $\Delta\Psi$ is the angular distance from the reconstructed direction $\vec{x}_i$ to the source location $\vec{x}_s$, and σ_i is the estimated angular uncertainty.

Not all events are reconstructed equally well, depending on the location in the detector, the track length, photon statistics, etc. Using the estimators described in Sec. 3.4.2, an individual estimate of the angular uncertainty can be assigned to each event, giving more weight to the better localized events and allowing those events to better constrain the location of a signal. A two-dimensional, circular Gaussian distribution is assumed for the point spread function – a detailed error contour is not available in online analyses and would increase the computational complexity.

Considering the background PDF, P^{B}_{spatial} is introduced to quantify the probability for an event to be found in a particular location under the background assumption. In practice, the background event rate is zenith-dependent, due to e.g. the path length in Earth that a neutrino has to traverse, the volume of ice overburden depending on the zenith angle, and varying filtering efficiency. Moreover, an azimuthal dependence exists due to symmetries of the detector geometry: The hexagonal alignment of the strings creates six preferred directions, along which a larger event rate is observed. As

the Earth's rotates, a fixed point in the sky will be exposed to a more or less sensitive detector alignment, which changes throughout a day. Although this effect is diluted over the course of several days, the analysis is designed to be suitable for all timescales and the background PDF is constructed as a function of both zenith and azimuth.

Archival data was used to create the PDF, which is shown in Fig. 5.1, along with an illustration of the magnitude of the azimuthal structure. The detector's symmetry axes are clearly visible and their effect is especially pronounced for down-going events. Here, the downward-facing DOMs require photons to be scattered and the strong cuts on reconstruction quality and time residuals tend to favor tracks along the lanes of strings with the least amount of scattering.

The orientation of the detector with respect to a fixed source can modify the acceptance by up to 40%.

Energy PDF

The energy distribution of neutrinos is expected to follow a spectrum around E^{-2} in the case of Fermi acceleration, which is close to the spectrum measured for the diffuse astrophysical neutrino flux ($E^{-2.19}$, [15]). In comparison, the spectrum of atmospheric neutrinos is much softer, following roughly a power-law of $E^{-3.7}$. Thus the per-event energy proxy can provide additional leverage for discriminating atmospheric from astrophysical neutrinos.

Figure 5.2a shows the construction of the energy PDF in detail. In order to account for the declination-dependent changes in signal and background, the construction is performed in declination bands.

The MuEX method (Sec. 3.4.3) is chosen as a proxy for the muon energy. The alternative TruncatedEnergy method requires a certain track length and a number of hit DOMs close to the track, which makes it unfeasible for low-energetic or dim tracks.

Using the energy proxy distribution from the simulation, the signal PDF is created for different spectral indices by reweighting the simulation. The chosen range for the spectrum reaches from -1, harder than the diffuse astrophysical flux, to -4, slightly softer than the spectrum of the atmospheric neutrino background.

In contrast, the background PDF is created using archival data. This distribution is contaminated by astrophysical signal events in the high-energy tail, which could be avoided by using simulations of atmospheric neutrinos and muons instead. In the southern sky, such an approach is not feasible due to the poor agreement between data and simulation. In the northern sky, the background PDF has indeed been constructed from simulation in previous works [120], under the assumption of the signal of the sources following the energy spectrum of the diffuse astrophysical flux of $E^{-2.19}$. In this work, however, no assumption is made about a common spectral index for all individual sources. Eventually, the background PDF is generated from data, allowing a conservative, but uniform treatment of the entire sky.

Figure 5.2b shows an example of the ratio between the signal and background PDFs over all declinations for a spectral index of -2. The red and blue areas highlight the signal- and background-dominated regions, respectively.

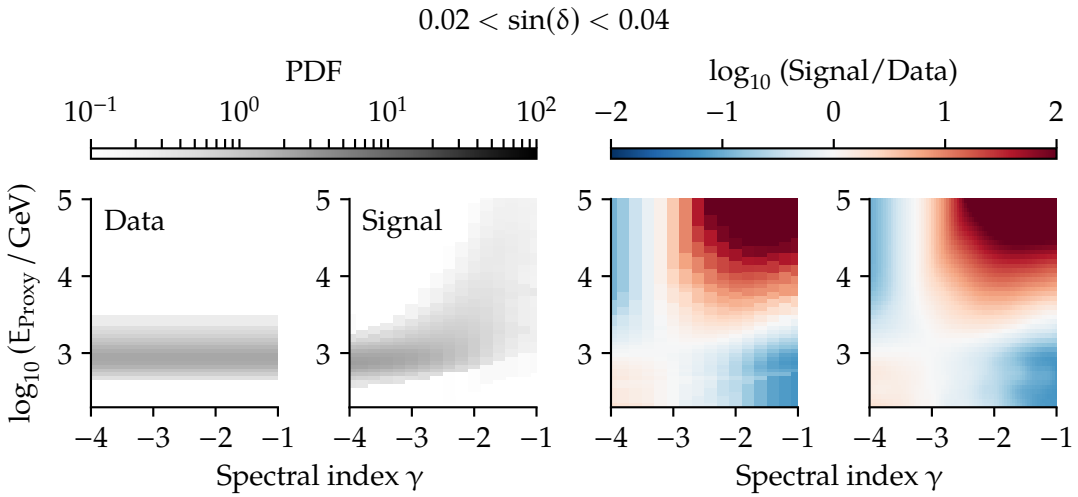

(a) Construction of the energy PDF in one declination band.

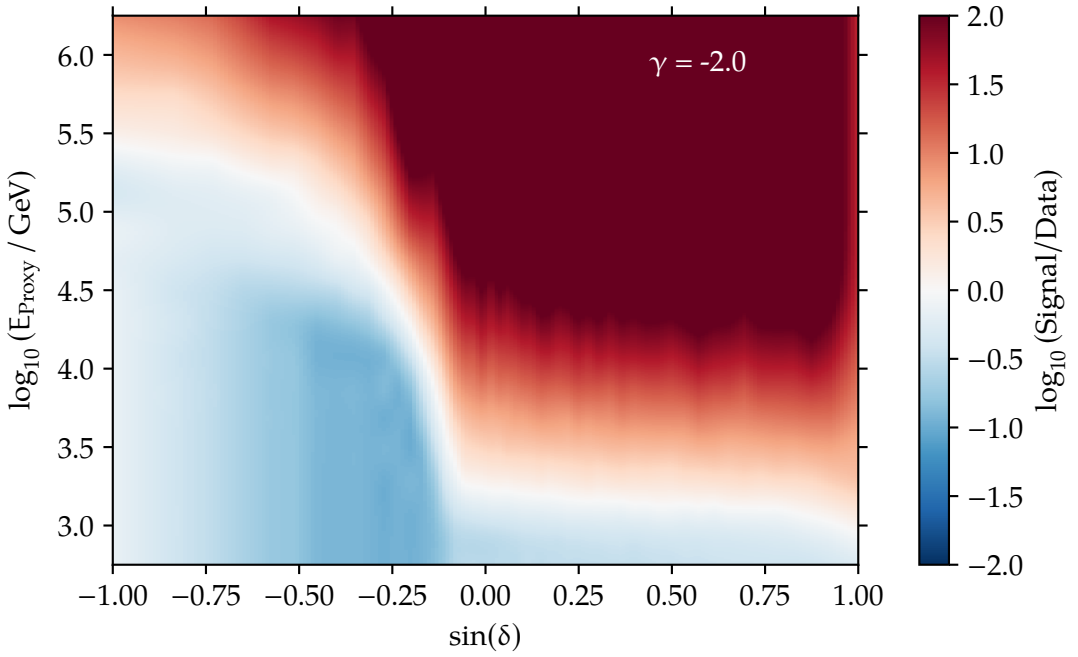

(b) All-sky energy PDF for a spectral index of -2.

Figure 5.2: Top: Construction of the energy PDF for a declination band near the horizon. The two panels on the left show the distribution of the muon energy proxy (MuEX) in data and in the signal simulation. The signal simulation is reweighted to different spectral indices. The two panels on the right show the ratio of signal to data as a histogram, which is then fitted with a two-dimensional spline.
Bottom: An example of the energy PDF for all declinations. Red (blue) areas are signal(background)-dominated.

Likelihood Formulation

The per-event signal and background PDFs (Eq. 5.1 and 5.2) can now be combined into a likelihood. Given a sample of N events, with a subset of n_s signal-like events, the likelihood is expressed as the product of the probabilities of finding each event [124]:

$$\mathcal{L}(n_s, \gamma) = \prod_{i=1}^{N} \left(\frac{n_s}{N} \cdot \mathcal{S}(\vec{\theta}_i|\gamma) + \left(1 - \frac{n_s}{N}\right) \cdot \mathcal{B}(\vec{\theta}_i) \right) , \tag{5.4}$$

where θ_i are the properties of the i-th event (direction, directional uncertainty and energy). Both the number of signal-like events n_s and their spectral index γ are free parameters, which are not known beforehand and determined by maximizing the likelihood. Bounds are placed on the parameters: n_s must be non-negative and not larger than the total number of events N. A negative n_s would correspond to an unphysical neutrino point-sink, or an underfluctuation in the data. It also complicates the numerical evaluation of the likelihood. Proper treatment of underfluctuations can yield better upper limits. Yet, the intention of this work is discovering neutrino flares with high significance. Thus, the lower bound on n_s is simply placed at 0. The allowed range for γ is chosen from -1 to -4, in agreement with the construction of the energy PDF.

Maximizing the likelihood yields the best-fitting $\hat{n}_s$ and $\hat{\gamma}$. Comparing the likelihood at this point to the background-only expectation, defines the test statistic:

$$\Lambda = 2 \log \frac{\mathcal{L}(\hat{n}_s, \hat{\gamma})}{\mathcal{L}(n_s = 0)} . \tag{5.5}$$

The background expectation is obtained by setting n_s to zero; in that case the choice of γ is irrelevant.

Since the logarithm behaves monotonically and the background expectation is constant, it is computationally favorable to directly maximize the test statistic. Plugging Eq. 5.4 into Eq. 5.5,

$$\Lambda = 2 \log \left[\frac{\prod_{i=1}^{N} \frac{n_s}{N} \mathcal{S}_i + \left(1 - \frac{n_s}{N}\right) \mathcal{B}_i}{\prod_{i=1}^{N} \mathcal{B}_i} \right] ,$$

and rewriting the expression,

$$= 2 \sum_{i=1}^{N} \left[\log \left(\frac{n_s}{N} \mathcal{S}_i + \left(1 - \frac{n_s}{N}\right) \mathcal{B}_i \right) - \log \mathcal{B}_i \right] ,$$

the test statistic can be expressed as

$$
\begin{aligned}
&= 2 \sum_{i=1}^{N} \log \left[1 + \frac{n_s}{N} \left(\frac{\mathcal{S}_i}{\mathcal{B}_i} - 1 \right) \right] \\
&= 2 \sum_{i=1}^{N} \log \left[1 + \frac{n_s}{N} \left(w_i - 1 \right) \right] \, ,
\end{aligned} \tag{5.6}
$$

where the event weight w_i is defined as the ratio of signal and background PDFs.

The muon tracks used in this work have resolutions around one degree. Therefore, events more than a few degrees away from the source hypothesis are suppressed by the spatial signal PDF (Eq. 5.3). Defining a circular bin of 5 degrees around the source hypothesis, N' events are found inside of this circle, and $N - N'$ events outside of it. Approximating $\mathcal{S}_i \approx 0$ for events outside the bin yields

$$
\Lambda = 2 \sum_{i=1}^{N'} \log \left[1 + \frac{n_s}{N} (w_i - 1) \right] + 2 \left(N - N' \right) \log \left(1 - \frac{n_s}{N} \right) \, , \tag{5.7}
$$

avoiding the computationally expensive evaluation of the signal and background PDFs for $N - N'$ events which are spatially unrelated to the source hypothesis.

The optimization algorithm "L-BFGS-B" is used to minimize the negative of the test statistic. Similar to Newton's method it searches for a stationary point by descending the gradient, while being optimized for limited memory use and supporting bound constraints [125, 126]. For efficient minimization, the partial derivatives of the test statistic can be expressed as

$$
\frac{\partial \Lambda}{\partial n_s} = 2 \sum_{i=1}^{N'} \left[\frac{w_i - 1}{N + n_s \cdot w_i} - 2 \frac{N - N'}{N - n_s} \right] . \tag{5.8}
$$

The derivative with respect to γ depends on the derivative of the energy PDF:

$$
\frac{\partial \Lambda}{\partial \gamma} = 2 \sum_{i=1}^{N'} \frac{n_s}{N + n_s w_i} \frac{\partial w_i}{\partial \gamma} \, . \tag{5.9}
$$

Parametrizing the energy PDF using cubic splines provides a well-defined, continuous derivative that can be evaluated quickly. Having sampled the weights w_i for the N' relevant events, the sums in Eqs. 5.7–5.9 can be evaluated efficiently to provide all necessary ingredients to the minimizer.

Simulated signal events are used together with background events taken from data in order to test the behavior of the likelihood fit. Figure 5.3 shows the bias in the fit parameters. The number of injected events can be recovered even for small signal strengths. In contrast, the fitted spectral index shows a large spread and can only be recovered on average for stronger signals. It is generally underestimated for

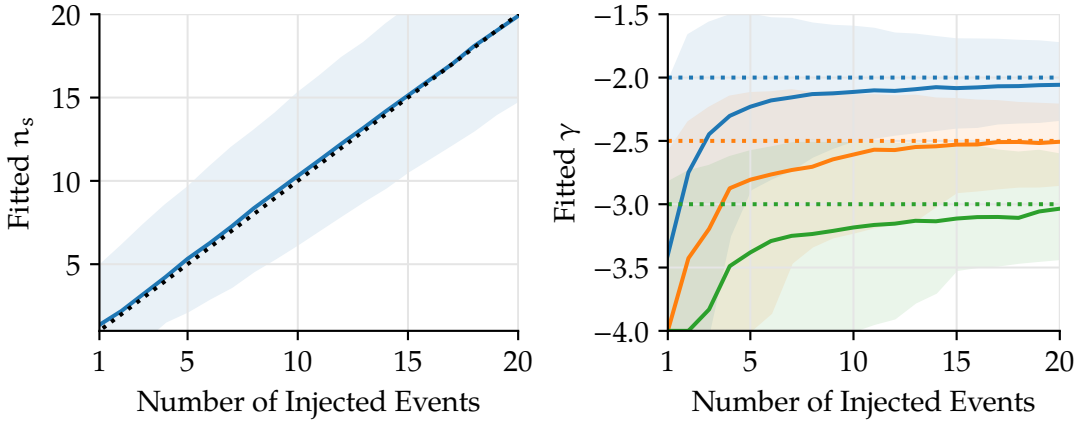

(a) Number of Signal-like Events

(b) Spectral Index

Figure 5.3: Estimated likelihood parameters for a simulated source at $\delta = 45°$. The left (right) panel shows how the number (spectral index) of injected signal events is recovered by the fit. The solid lines indicate the median, the shaded areas show the centered 68-percentile. Different simulated spectra are drawn in different colors, the dashed lines in the right plot mark the true, injected parameters.

a small number of events. This behavior is expected when fitting a steeply falling power-law to the energies of a few through-going muons which are measured with large uncertainties. In addition, the background energy PDF was constructed from data with a residual contamination from astrophysical events in the high-energy tail, which introduces a slight bias when fitting hard spectra. Also, the presence of events from the soft atmospheric background near the tested source introduces further bias towards softer spectra.

To summarize, the fitted spectral index can provide an estimate of the energy spectrum only on average, and only in the presence of a strong signal. In individual analyses it should be referenced with care due to the large uncertainties, especially in the case of low event counts.

This likelihood method outlined so far does not consider the time structure of the events, it is thus a time-integrating method. The next section will extended it towards a time-dependent analysis.

5.2 Time Clustering Algorithm

Incorporating a time dependence in the likelihood analysis is beneficial for the search of time-variable and transient sources.

Results from the search of different signals and contained events with large astrophysical probability show that cosmic neutrinos observable with IceCube are predominantly of extra-galactic origin [46]. Multi-wavelength data on extragalactic

objects show that the astrophysical sources, which are likely neutrino emitters, are variable in their neutrino emission. Assuming a correlation with neutrinos, the neutrino signal is expected to be largely time-variable.

A burst of neutrinos on a short time scale, a flare, on the time scale of days is subject to much less background than a time-integrated analysis spanning years. Thus, the purpose of the time-dependent search algorithms is to find a time window (a subset of a larger dataset), which yields the best test statistic and therefore contains the most-significant, signal-like excess.

Several methods have been proposed in the past [127, 128]. A defining feature is the assumption of the time PDF, i.e. the distribution of the signal events in time. For searching archival data, the construction could incorporate existing multi-wavelength observations under the model assumption. This is not a choice for an online analysis, or a self-triggered analysis of IceCube data only. The most generic, and model independent assumptions are either a box, defined by a start and end time, or a Gaussian distribution, defined by the central time and a width.

In this work, a box distribution is used. In contrast to the long tails of the Gaussian distribution, the box provides a well-defined flare boundary. This is important in an online analysis, where the end of the box will be aligned with the end of the dataset.

In any case, the flare duration and thus the optimal size of the time window is not known beforehand. The algorithm needs to treat the duration a free parameter and optimize for it, in order to be generally applicable to various different classes of potential neutrino sources and their emission scenarios.

Applying the time clustering algorithm to data and finding the most-significant box works as follows: Starting with an event observed at time t_k defining the end of the box, all events with $t_i < t_k$ serve as possible start times. For each possible pair of events the likelihood analysis from Sec. 5 is run using all events inside the window $[t_i, t_k]$.

Sliding this algorithm over the dataset, i.e. choosing every possible event for t_k, provides an exhaustive search over every possible time window. Two measures are taken to reduce the large amount of possible time windows, which would make this search impractical:

- The largest possible duration is limited to T_{max}. The choice of T_{max} could be based on predictions from a certain neutrino emission model to be tested. In the absence of prior knowledge about the emission time scale, the most generic choice would be the point at which the sensitivity becomes comparable to that of the time-integrated analysis.

- It can be shown that combining only events with $\mathcal{S}/\mathcal{B} < 1$ cannot yield a positive test statistic. Such low event weights may be caused by poorly localized events, events far away from the analyzed source, low-energetic events, or a combination of those factors. Thus, the number of tested time windows can be restricted by requiring $\mathcal{S}/\mathcal{B} \geq 1$ for the first and last event in the window.

A sketch of the time clustering algorithm is shown in Fig. 5.4. Starting from an

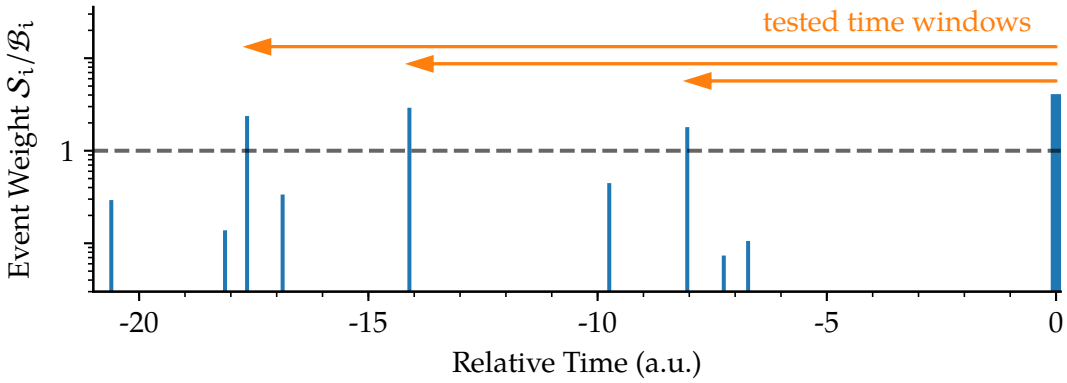

Figure 5.4: Sketch of the time clustering algorithm. Vertical bars show the weights of events, which were recorded over time. The right-most event triggers the analysis. Orange arrows denote the time windows (expanding from the trigger backwards in time), to which the point-source analysis is applied. The time windows always start with an event whose weight exceeds a defined threshold (set to 1), and end with the triggering event.

arbitrary event at time $t_k = 0$ in that example, possible clusters with earlier events (fulfilling the minimum event weight criterium) are constructed.

An algorithm testing variable flare durations should be unbiased towards the length of the time window. However, in practice, a given dataset allows for testing many more short time windows than long time windows. Thus, it will preferentially select short duration flare candidates. Modifying the test statistic mitigates this effect by introducing a penalty [127]:

$$\Lambda = 2 \log \left[\frac{\mathcal{L}(\hat{n}_s, \hat{\gamma})}{\mathcal{L}(n_s = 0)} \frac{\mathcal{U}(t_i, t_k)}{T_{max}} \right] , \tag{5.10}$$

where $\mathcal{U}$ denotes the detector uptime during the tested time window, $t_k - t_i$, i.e. the time during which the detector was operating normally and recording events (see Sec. 3.6). Equation. 5.10 is evaluated on all selected time windows, choosing the one with the largest test statistic.

This setup is equivalent to multiplying the signal and background PDFs from Eqn. 5.1 and 5.2 with a time PDF of the form

$$P^S_{time}(t) = P^B_{time}(t) = \begin{cases} \mathcal{U}(t_i, t_k)^{-1} & t_i < t < t_k \\ 0 & \text{else} \end{cases} . \tag{5.11}$$

The algorithm so far does account for two time-dependent effects. First, the detector geometry the azimuthal symmetry axes and the rotation of the Earth cause a fluctuation of up to 40 % in azimuthal acceptance, which has been included in the spatial PDF. Second, although the detector uptime is generally very stable, interruptions in data taking of up to one day have occurred in the past. This effect is relevant for flares

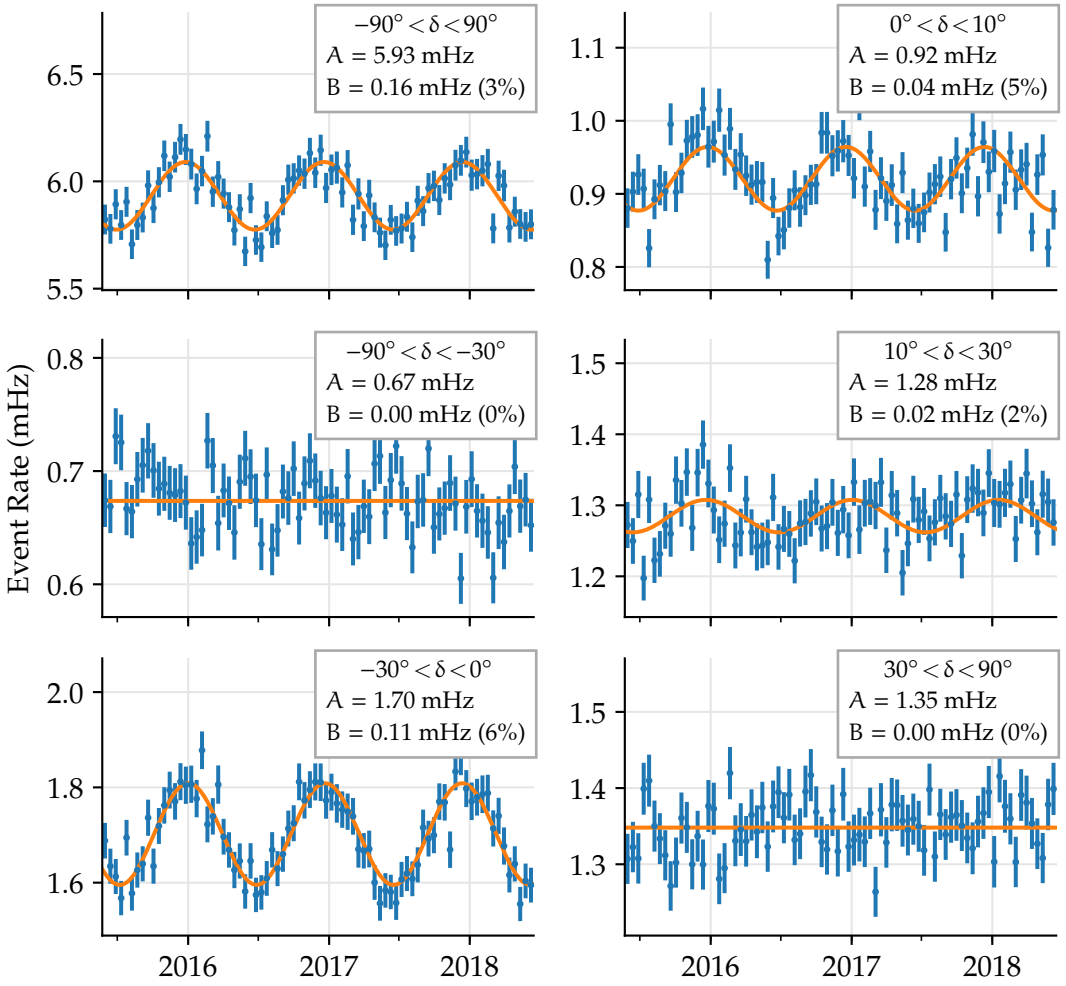

Figure 5.5: Event rate at the final selection level varying with the seasons. An average over the entire sky is shown in the top left panel, the remaining panels show different declination bands. The data (blue) is binned in 14 day intervals and fitted (orange) with $A + B \cdot \sin[\omega(t + t_0)]$. Almost no effect is seen for vertically up-going events, while seasonal variations are strongest around the horizon ($-30° < \delta < 10°$).

of comparable length and it is accounted for in Eq. 5.5. Finally, it should be noted that the background event rate arising from atmospheric showers depends on the temperature and atmospheric density profile varying over the year [99]. Figure 5.5 shows the event rate at the final event selection level over several years. Fitting the event rate with $A + B \cdot \sin[\omega(t - t_0)]$ yields the average event rate A and the amplitude B of the seasonal variations in different declination bands. Consistent with previous findings [129], the event rates varies not more than 6% over the course of half a year. Hence, this effect is neglected and the PDFs of Eq. 5.11 are considered static.

5.3 Sensitivity Optimization

Having defined the analysis methods this procedure can now be used to find the optimal BDT cut for the event selection (Sec. 4.4.1f) and evaluate the sensitivity. The next sections define the meaning of sensitivity, describe how it is calculated, and conclude with the BDT cut definition.

Definition of Sensitivity

First, the statistical test needs to be defined: The outcome of the likelihood analysis is a value of the test statistic $\hat{\Lambda}$. It is compared to the probability of observing an equal or better result by chance:

$$p(\hat{\Lambda}) = \int_{\hat{\Lambda}}^{\infty} P^B(\Lambda)\, d\Lambda = \int_{\hat{\Lambda}}^{\infty} \chi^2(\Lambda; n_{DoF})\, d\Lambda \,. \tag{5.12}$$

Here, P^B is the probability distribution of the test statistic in the absence of signal. Since the test statistic is formed from a likelihood ratio, where the null hypothesis is contained in the fit range (Eq. 5.7), the distribution of the test statistic should follow a χ^2-distribution according to Wilk's theorem [130]. The number of degrees of freedom n_{DoF} is naively expected to follow the number of free parameters, i.e. 2 in the case of the time-integrated analysis. However, the parameters are not independent (i.e. γ becomes irrelevant for $n_s \to 0$). Also, the time-dependent analysis introduces additional freedom: The number of tested time windows depends on the event rate which varies with declination, and the tested time windows overlap and share common events. These complications are mitigated by fitting the χ^2-distribution to a toy simulation.

The p-value corresponding to a result $\hat{\Lambda}$ determines the significance level and quantifies the probability of accidentally rejecting the null hypothesis. Conversely, the chance of rejecting the null hypothesis when the alternative hypothesis *is* actually true is called the power of a test, β. With these quantities, two concepts of sensitivity are commonly defined in IceCube:

- The "sensitivity" is the best possible upper limit which, in the case of a non-observation, can be set on the neutrino flux at a confidence level of 90%. That is, $p \geq 50\%$ and $\beta = 90\%$.
- The "discovery potential" is the flux, which yields a 5σ discovery in 50% of cases, i.e. $p = 2.86 \cdot 10^{-7}$ and $\beta = 50\%$. Since this can be very time consuming to evaluate, sometimes a "3σ discovery potential" is used with a corresponding, lower threshold.

Toy Simulation on Scrambled Data

The sensitivity and discovery potential fluxes are derived in two steps: First, the simulation of a background-only scenario is used to relate the test statistic to significance

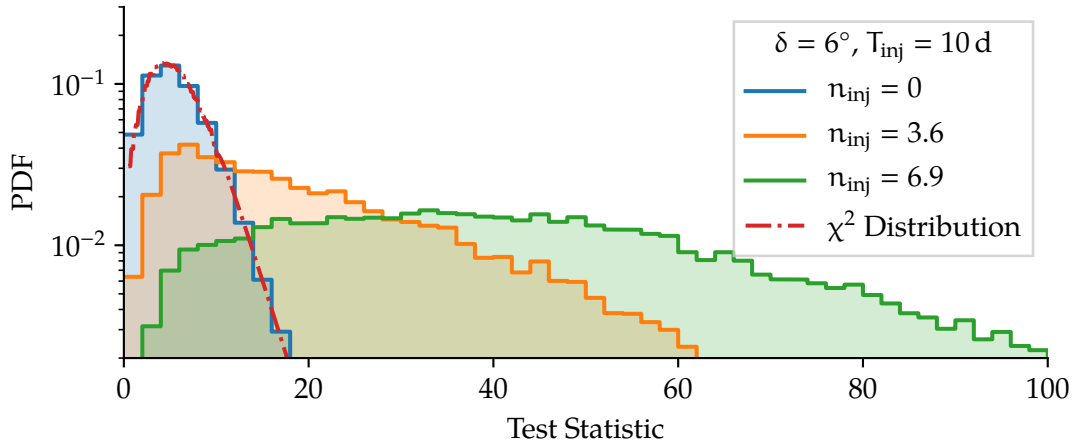

Figure 5.6: Examples of test statistic distributions for a time-dependent analysis of a source at a declination of 6° over 365 days. On top of the background (blue), a 10-day neutrino flare with a median number of signal events n_{inj} was simulated (green, orange). The case of $n_{inj} = 3.6$ represents the best possible upper limit, whereas $n_{inj} = 6.9$ yields a 5σ discovery on average.

levels, and set the discovery threshold. Second, background data will be combined with simulated signal to determine the neutrino flux which is required to cross the discovery threshold.

The toy simulations are performed using time-scrambled data. Given a set of archival events the scrambling procedure randomly shuffles the event times. Then, the transformation from local detector coordinates to equatorial coordinates, which is a function of time, is repeated using the new event times. The coordinate transformation is computationally expensive, but can be sped up by assuming the declination to be static (since IceCube is located roughly at the South Pole around which the Earth rotates), and approximating the right ascension α as follows [97]:

$$\alpha_{new} = \left(\alpha_{old} + (t_{new} - t_{old}) \cdot \frac{2\pi}{T_{sid}}\right) \mod 2\pi\,, \tag{5.13}$$

where $T_{sid} = 0.99726957\,\mathrm{d}$ is the length of a sidereal day. This shuffling of the event times destroys any possible signal in the data, while maintaining all other detector effects and the correlations between the observables. It provides a data-driven way of determining significance levels without having to rely on detector simulations. An example of a test statistic distribution in a background-only scenario is shown in blue in Fig. 5.6.

Next, the sensitivity to a given source hypothesis is tested by adding simulated events to the scrambled data. In general, simulations in IceCube are produced for a diffuse flux of neutrinos with a fixed spectral index, but can be weighted to a different spectrum. When simulating a point source, a declination band of ±5° around

the source is selected, from which events are randomly drawn according to their weights. The true declination and right ascension of each event is moved by $\Delta\delta$ and $\Delta\alpha$, respectively, to the position the simulated source. Afterwards, the reconstructed declination and right ascension are shifted by the same amount of $\Delta\delta$ and $\Delta\alpha$. This effectively turns a diffuse into a point-source simulation.

The number of injected signal events in each trial is drawn from a Poisson distribution with a mean of n_{inj}. The value of n_{inj} is adjusted until the resulting test statistic distribution meets the aforementioned criteria for sensitivity.

Figure 5.6 shows two examples of this distribution. The simulated number of events n_{inj} was determined to represent the sensitivity and discovery potentials for this particular scenario.

Neutrino Flux

In order to relate any number of events N to an incident neutrino flux ϕ, it is useful to describe the event rate as follows:

$$\frac{dN}{dt} = \int d\Omega \int_0^\infty A_{eff}(E;\delta)\, \frac{d^3\phi}{dt\, d\Omega\, dE}\, dE\ . \tag{5.14}$$

The "effective area" A_{eff} is the cross section that an ideal detector would exhibit to the neutrino flux. It is a function of the neutrino flavor, the declination δ of the source, and the neutrino energy E . Assuming an unbroken power-law, the neutrino flux ϕ can be parametrized as

$$\frac{d\phi}{dE} = \phi_0 \cdot \left(\frac{E}{E_0}\right)^{-\gamma}\ . \tag{5.15}$$

Here, ϕ_0 is the flux normalization at the energy E_0 with a typical choice of $E_0 = 1\,\text{GeV}$. In the following, sensitivities are shown as $E^\gamma\, d\Phi/dE$, where

$$E^\gamma\, \frac{d\phi}{dE} = \phi_0 \cdot E_0^\gamma = \text{const}\ . \tag{5.16}$$

The outcome of a time-dependent search is not just an overall flux, rather it is constrained to a time window. Comparisons between different time scales are facilitated by integrating the time and converting the flux ϕ to a fluence J:

$$\frac{dJ}{dE} = \int dT\, \frac{d\phi}{dE} = J_0 \cdot \left(\frac{E}{E_0}\right)^{-\gamma}\ . \tag{5.17}$$

Unless noted otherwise, effective areas are averaged over muon neutrinos and muon anti-neutrinos, and the presented flux is the sum of muon neutrino and muon anti-neutrino fluxes.

This formulation decouples the neutrino flux from the acceptance of the event selection. In the following steps, the event selection will be finalized by defining the BDT cut.

BDT Cut Optimization

The final BDT cut is chosen such that the best discovery potential to point sources is achieved. While previous analyses have used an approximation to the discovery potential for this task [44, 84, 131], here the full time-independent analysis was applied to different choices for the BDT cut at different declinations. Using the time-dependent analysis was not feasible due to the required computation time. Running the time-independent analysis on 30 days of archival data relieves the computational effort, and optimizes the discovery potential towards this time scale will afterwards also benefit the time-dependent analysis looking for flares on similar timescales. The data was evenly sampled throughout the year to mitigate the effect of seasonal variations.

Figure 5.7 shows the choice of the cut on the BDT score. Two energy spectra (E^{-2} and $E^{-2.5}$) were tested for the northern sky, where measurements of the diffuse astrophysical flux hint towards a spectral index between -2.2 and -2.5 [15, 66]. In the southern sky, where only the most energetic events are selected, E^{-2} was used. Scanning a range of BDT cuts and evaluating the corresponding sensitivity and discovery potential at each declination allows determining the best cut. It is optimized towards the discovery potential, because this work will focus on discovering neutrino flares and does not aim to set the best upper limits.

For the northern and southern sky, separate BDTs are used and a cut was chosen for each hemisphere. The BDT cut for the northern sky was chosen in between the optimal cuts for the two tested spectra. Around the horizon, both event selections needed to be joined and a polynomial cut was chosen to yield a smooth transition in the event rate between both hemispheres. In this way, a smooth transition is achieved, allowing the entire sample to be used in a uniform likelihood analysis.

5.4 Performance and Comparison to Offline Analyses

Having set the BDT cut this way finalizes the definition of the event selection. This section will summarize the properties of the selection and compare it to existing event selections.

The different atmospheric and astrophysical contributions to the final event sample are shown in Fig. 5.8 as a function of declination. Event rates of the individual backgrounds and signals are estimated from simulations. In the northern sky ($\delta > 0$), the data consists almost entirely of muon-neutrino induced events. The available simulation of down-going atmospheric muons, which would end up as mis-reconstructed events in this part of the sky, is almost entirely rejected by the online event filter.

In the southern sky ($\delta < 0$), the sample consists mostly of atmospheric muons. Due to the cuts selecting the most energetic events from this region of the sky, the contribution from atmospheric neutrinos is suppressed. For the same reason, also the expected number of astrophysical events from the southern sky is a factor of 10 lower compared to the northern sky.

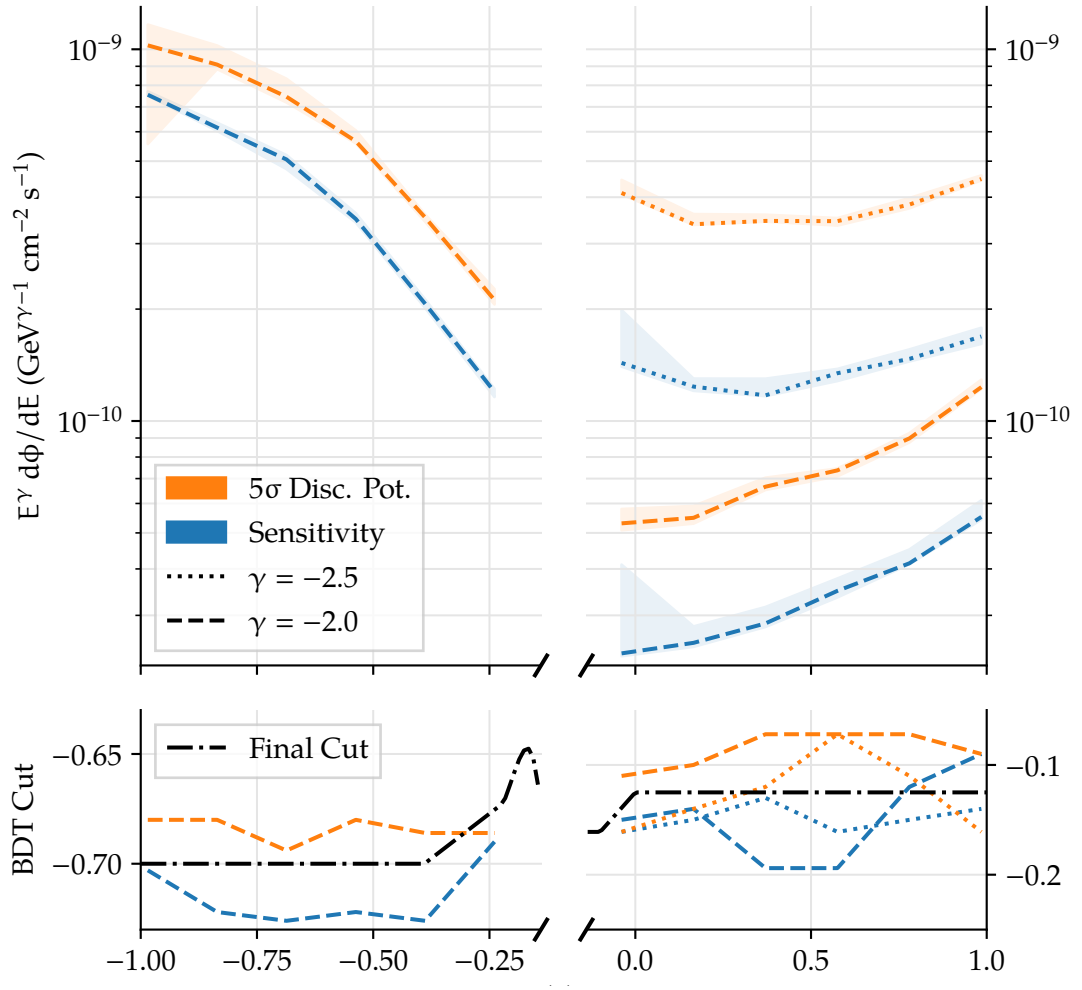

Figure 5.7: Discovery potential for different declinations. Different classifiers were trained for the northern and southern sky, with the transition at $\delta = -8°$. Upper panel: The band shows the discovery potential or sensitivity which was measured by scanning the BDT cut around the optimum. For the northern sky, two different spectra were tested. Lower panel: The colored lines show the optimal BDT cut for best sensitivity or discovery potential at different spectral indices. The black line marks the cut that is eventually used in this work.

In a previous northern sky analysis [15] the model of the atmospheric neutrino background [13] has been fitted to data, including parameters such as the absolute flux normalization and the ratio of kaons and pions. Hence, using these fitted parameters the agreement between data and simulation is very good. Such an analysis is not available for the southern sky. Here, due to the different topology of the background, consisting of down-going muons or muon bundles, only the bare predictions are

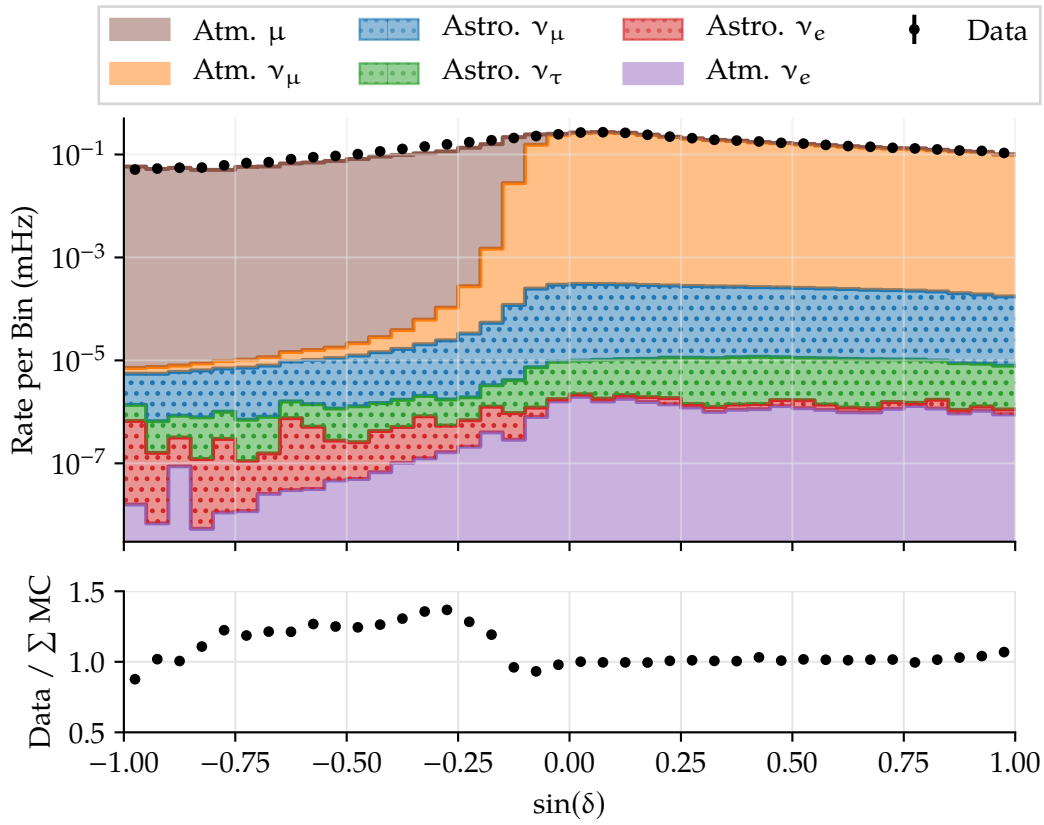

Figure 5.8: Declination distribution at the final event selection level. Data is drawn in black. The colored, stacked areas show the expected individual contributions from atmospheric (solid) and diffuse astrophysical (dotted) fluxes based on simulations.

shown [13, 132]. These simulations describe neither the event rate nor the shape very well. In addition, other experiments beyond the scope of IceCube are facing similar challenges [133, 134].

The simulation of atmospheric backgrounds is not mandatory for the next analysis steps, as the significance of point-sources is assessed using the data-driven approach described in Sec. 5.3.

In both hemispheres the contribution from the diffuse astrophysical neutrino flux is shown by extrapolating the measurement of the diffuse astrophysical flux [15] over the energy and zenith range covered by this online event selection.

In total, this event selection yields approximately 200.000 events per year, 0.1 % of which are estimated to be of astrophysical origin. A distribution of the expected number of events in terms of the neutrino energy is shown in Fig. 5.9. Two background models are shown, the dominant conventional atmospheric neutrino flux [13], as well as a prediction for the prompt atmospheric neutrino flux [14]. As the event counts

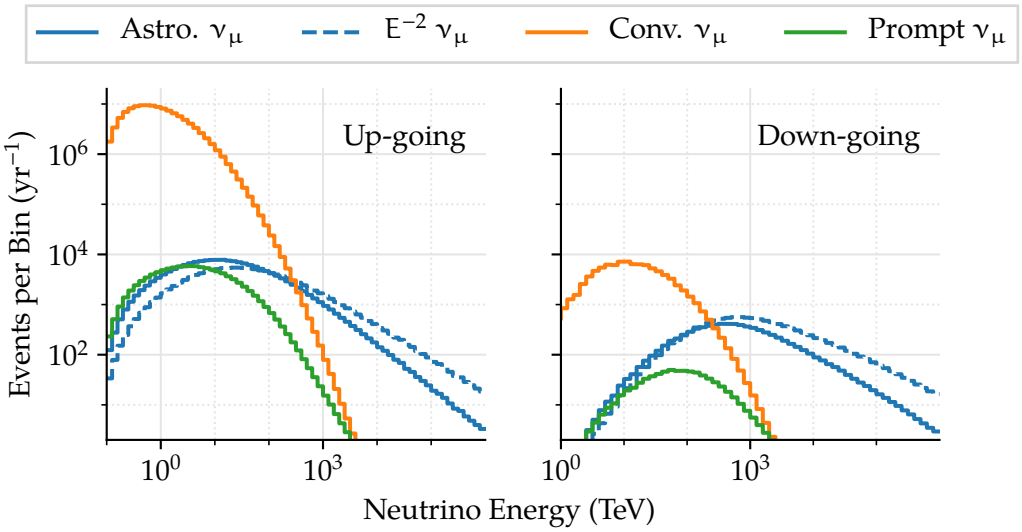

Figure 5.9: Distribution of the true neutrino energy for muon neutrino-induced events selected by the online filter. This distinction between up- and down-going events is made at $\delta = -8°$.

are shown with respect to the *neutrino* energy, the down-going panel does not cover the contribution from atmospheric *muons*. Astrophysical neutrinos only stand out at high energies, and Sec. 6.4 discusses the real-time identificatoin of those events in the online event stream. However, ≈ 150 astrophysical events are recorded at lower energies. While they cannot be distinguished from the atmospheric background on a per-event basis, Sec. 5 will discuss a search strategy for spatial clustering of events, in order to identify a signal from neutrino point-sources.

Effective Area

Figure 5.10 displays the effective area (Eq. 5.14) towards different neutrino flavors. Only events where the simulated and reconstructed neutrino direction agree within 3° are considered, in order to enable a comparison of the effective area that is useful for point-source searches. As expected, the effective area is largely dominated the selection of muons from muon-neutrino interactions, except for PeV neutrinos from the northern sky. With the interaction cross-section increasing towards higher energies, absorption becomes more likely as up-going neutrinos have to traverse more matter on their way through Earth.

Conversely, tau neutrinos contribute at or above PeV energies for several reasons: As the interaction of the tau neutrino produces a tau lepton, which decays into another tau neutrino ("regeneration"), they can traverse the Earth more likely than other flavors. Therefore, the effective area for tau neutrinos exceeds that of muon neutrinos above 10 PeV. After reaching the ice, they may interact inside the detector and the

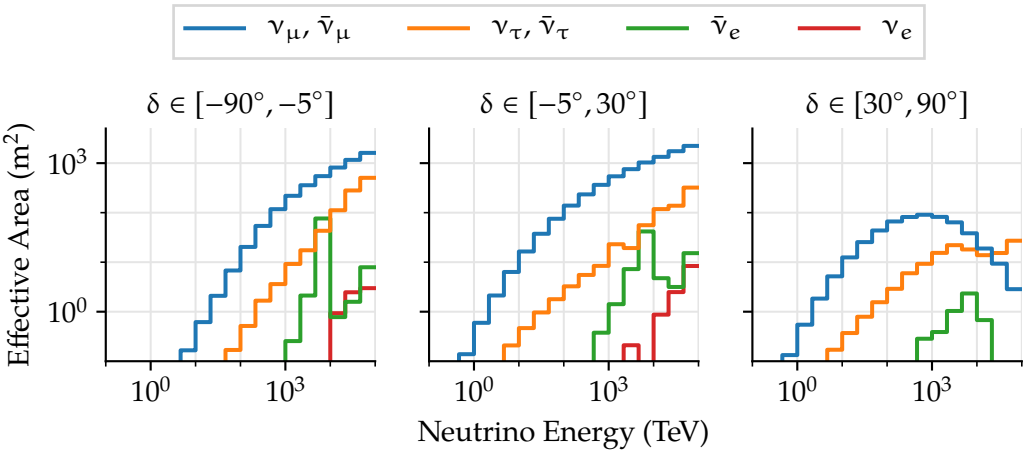

(a) Per-flavor (anti-)neutrino effective area

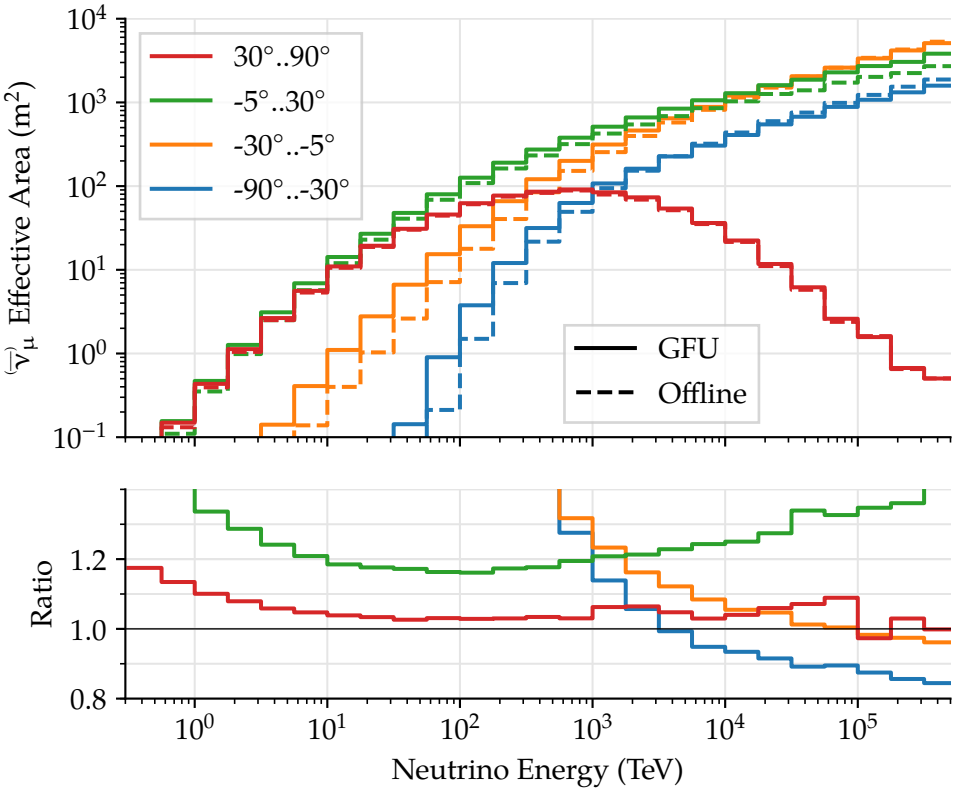

(b) Muon-(anti-)neutrino effective area, compared to the offline point-source analysis [44]

Figure 5.10: Effective area at the final event selection level in different declination bands. Only events where the true neutrino direction was reconstructed to within 3° are considered.

decay length of the tau lepton ($\approx 50\,\mathrm{m}/1\,\mathrm{PeV}$) is observed with a track-like shape in the detector. Even if the tau lepton itself cannot be resolved, a muon with energies above 200 GeV may be produced in the decay, allowing for a directional reconstruction.

The effective area towards electron neutrinos is very small in comparison. At energies around 6.3 PeV, the resonant production of a W boson ("Glashow" resonance [135]) and its subsequent decay into a muon shows up as a peak for $\bar{\nu}_e$. Similar to tau neutrinos, at or above PeV energies an electron (anti-) neutrino can also interact in the detector and produce a muon in the hadronic decay cascade. If that muon carries more than 100 GeV and escapes the decay cascade, it may be reconstructed. However, the overall contribution from electron neutrinos is negligible as the phase space for such an event topology is small, and up-going electron neutrinos are subject to enhanced oscillation due to the MSW effect [136–138].

In comparison to the offline point-source analysis, the effective area in this analysis is generally larger for up-going, and especially for horizontal directions. This behavior is likely due to the improved training, which uses simulations of the background instead of approximating it with data. It is only in the southern sky, that the offline event selection achieves a larger effective area. Here, the offline selection can make use of a more sophisticated unfolding of the energy loss pattern, which helps in the rejection of atmospheric muon bundles.

Angular Resolution

A point source search benefits from both muon effective area as well as angular resolution. In Fig. 5.11 the median angular error is shown as a function of energy, averaged over different declination bands.

The dotted lines indicate the angular error towards the true direction of the muon. At low energies the reconstruction performance is limited due to the small number of pulses available for the reconstruction. Towards higher energies, the pointing accuracy improves with increasing photon statistics. Finally, it flattens at the highest energies since the more frequent stochastic energy losses of the muon are not accounted for in the likelihood of the reconstruction.

More important for point source searches is the reconstruction with respect to the neutrino direction – shown in solid lines. It generally follows the behavior of the muon reconstruction. At low energies, the additional kinematic angle between the neutrino and the muon emerges and worsens the angular error with respect to the neutrino direction.

Sensitivity and Discovery Potential

The discovery potential is shown in Figure 5.12 using the time-integrated analysis on roughly one year of data. For comparison, two different event selections are shown in addition to this work: The previous online event selection, and the event selection from the offline point source analysis. Since different data quality decisions were made in the past, only the set of runs present in all event samples was used for this

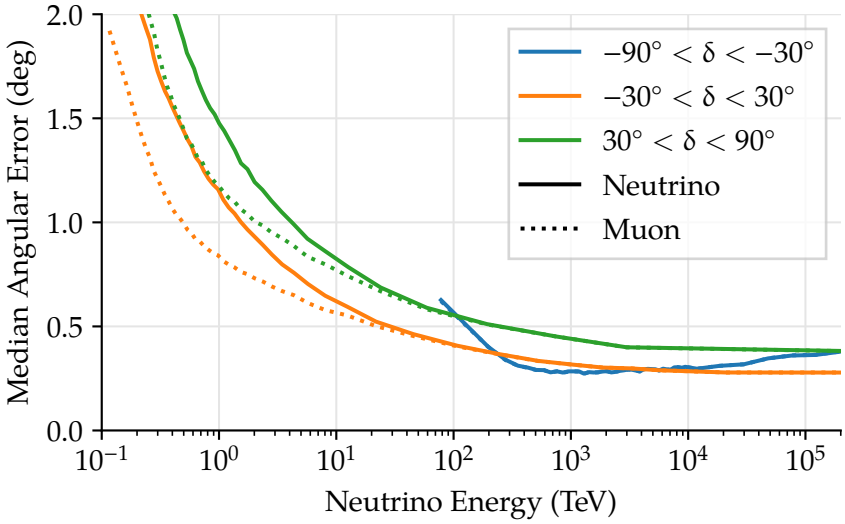

Figure 5.11: Median angular error in three declination bands. The solid (dotted) lines show the angular distance between the reconstructed direction and the true neutrino (muon) direction. Above 30 TeV, where solid and dotted lines merge, the kinematic angle becomes negligible. In the southern sky, only the most-energetic events are selected, hence the blue line starts at 100 TeV.

test. This ensures a fair comparison of the filters and reconstructions, and it is not biased by the different sample durations used in previous analyses.

In the northern sky the new selection performs $\approx 25\%$ better than the previous online selection, and $\approx 50\%$ better in the southern sky. The improvement seen here in the northern sky correlates with the enlarged effective area shown earlier. In addition, the implementation of a dedicated set of variables to reject atmospheric showers improves the discovery potential in the southern sky.

In comparison to the event selection used in the previous point source analysis, a slight improvement is also seen. This is suspected to come from the better track reconstruction where the online reconstruction uses additional pulse cleaning, that was found to improve the directional accuracy and speed up the reconstruction. The same behavior was found for a hard energy spectrum $\propto E^{-2}$ and a softer one of $\propto E^{-2.5}$, confirming that the event sample is suitable sfor searching sources over a range of possible energy spectra.

The only region where the offline analysis shows clearly better performance is for very inclined events (at declinations below $-60°$), where it uses IceTop as an additional veto.

In Fig. 5.13 the differential discovery potential is shown at three declinations and compared to the same event selections as before. This comparison shows in which energy range the sensitivity is mostly improved. The improvements here are similar those in effective area, but also consider the improved reconstructions.

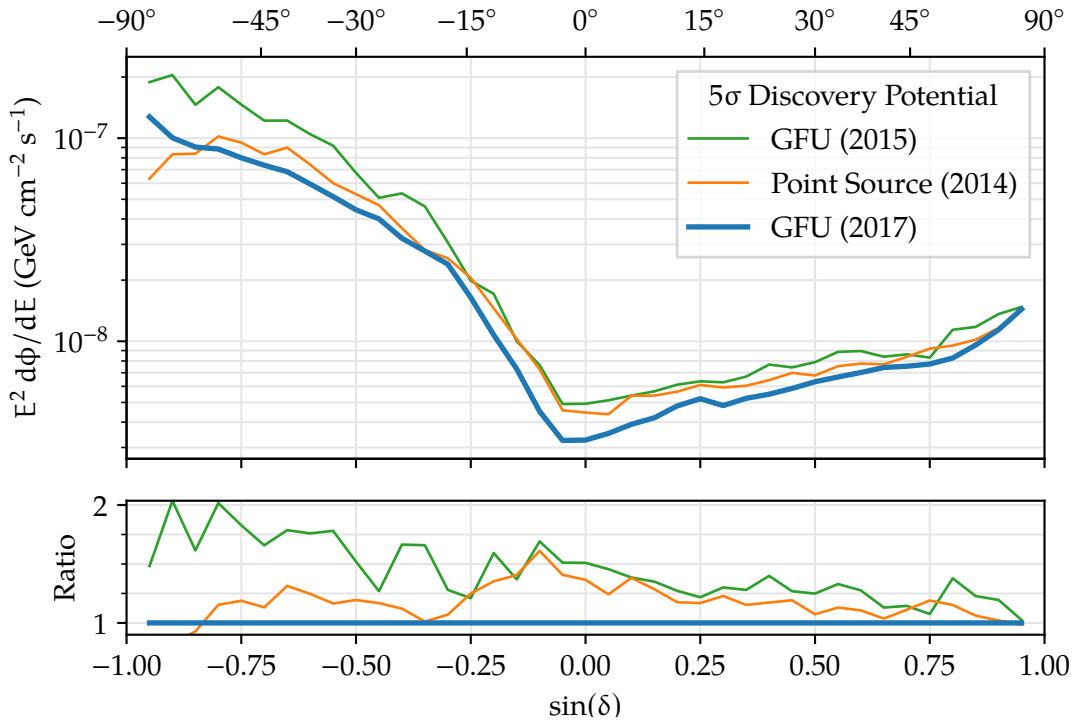

(a) Spectral index: -2.0

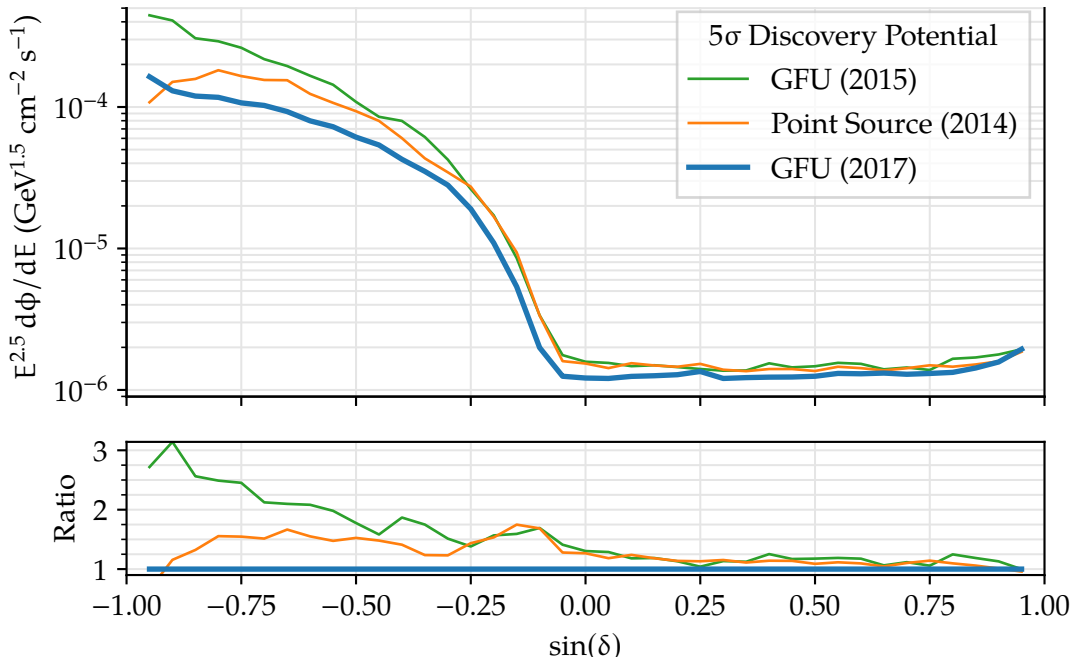

(b) Spectral index: -2.5

Figure 5.12: Sensitivity of time-integrated analysis using 357 days of data for two different energy spectra. This work is shown in blue, the previous online selection [101] in green, and the offline event selection [44] in orange.

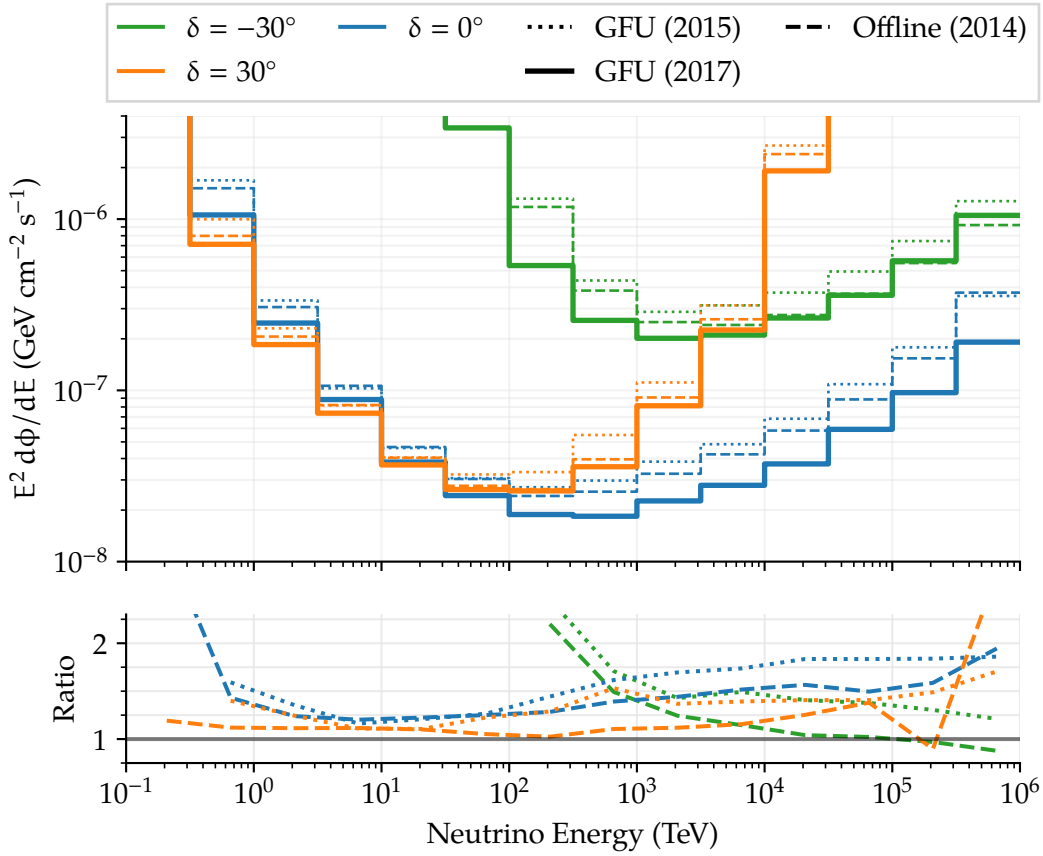

Figure 5.13: Differential discovery potential in half-decade bins at three different declinations, for a time-integrated analysis using 357 days of data. Thick solid lines: this work. Dotted lines: previous online selection [101]. Dashed lines: offline event selection [44].

6 Scientific Applications and Results

The analysis concepts in connection with the (online) event selection, can now be applied in order to actually search for neutrino point sources.

Several analyses that were implemented in the course of this work are presented in the following sections:

- The online event selection and the time-dependent likelihood analysis are used to **monitor a list of known gamma-ray emitters for potential neutrino flares**. In the case of interesting activity, an automated alert is sent to partner telescopes for follow-up observations (Sec. 6.1).

- An extension of the analysis has been developed in order to **scan the entire sky for neutrino flares**. Automated alerts are generated and sent to the global community for follow-up observations. This might discover sources which are not yet on the list of monitored sources (Sec. 6.2).

- The **most-energetic events** of the sample are interesting by themselves. They can provide an additional way to discover neutrino sources, which is not biased by a predefined source list (Sec. 6.4).

- Strong flaring activity in VHE gamma-rays was observed from the **blazar 1ES 1959+950** during the spring of 2016. The **time-dependent analysis method is used to test for corresponding activity in neutrinos** (Sec. 6.5).

- On September 19th, 2017 a very energetic neutrino event from the direction of the blazar **TXS 0506+056** triggered an automated alert. The ensuing multi-wavelength observation campaign identified flaring activity in gamma-rays and for the first time observed a potential counterpart to the neutrino in VHE gamma-rays. Triggered by this intriguing correlation, the **time-dependent analysis and the online event selection were used to check for previous flaring episodes in neutrinos** (Sec. 6.6).

In addition, due to the convenience of its immediate availability, the online event selection is now used by the IceCube collaboration for many other analyses, especially when rapid reactions are needed:

- In response to interesting observations or alerts by other observatories, the most-recent events are analyzed immediately in a search for correlated neutrino emission.

Triggered by an interesting neutrino detection by ANTARES, this strategy was followed in the course of this work, resulting IceCube's first response to an external trigger in the form of an "Astronomer's Telegram" (ATel) [139].

IceCube now routinely investigates the online event selection developed in this work for interesting excesses related to external triggers and publishes a fast response [140].

- The real-time event stream provides a **main ingredient in the search for neutrinos correlated with gravitational waves observed by the LIGO and VIRGO detectors**. This search has been performed for the binary black hole merger GW150914 and the binary neutron star merger GW170817 found in Advanced LIGO and VIRGO's first and second observation run [141, 142]. Starting with the third observation run the search has been automated [143].

6.1 Monitoring of Known Gamma-Ray Sources

While a diffuse astrophysical neutrino flux has been observed, its sources have not yet been resolved. Although many source classes have been proposed, more observations are required to constrain the parameter space.

Performing observations in gamma-rays may reveal the gamma-ray flux connected with the same hadronic processes, which also produce neutrinos. Sources such as blazars have shown highly variable behavior in gamma-rays in the past, and the neutrino flux correlated with the highest state of gamma-ray flares may be observable. Considering the time-dependence of both the neutrino and gamma-ray flux would yield a very sensitive analysis: First, the gamma-ray flares can be well observed using Imaging Atmospheric Cherenkov Telescopes (IACTs). Second, by looking at selected time windows the atmospheric neutrino background is effectively suppressed.

However, the availability of contemporaneous neutrino and gamma-ray data is scarce, even more so when considering the flaring episodes. IACTs require clear, (ideally) moon-less nights for observations. Compared to IceCube's almost 100% uptime, the duty cycle for Cherenkov telescopes is at most 20%. Moreover, while IceCube is able to observe the entire sky at once, these telescopes field of view is limited to a few square degrees and can essentially observe only one source at any given time.

In order to assemble a larger, more comprehensive set of observations, the unique properties of IceCube are used to monitor the locations of known gamma-ray emitters. Once a strong overfluctuation is registered in the neutrino sample, an alert is sent to partner IACT, which can immediately repoint and acquire gamma-ray observations from the direction of the source candidate.

Such a program was pioneered between the AMANDA and MAGIC collaborations [100]. Later it was adopted for IceCube and extended to include the VERITAS collaboration [101].

A similar program targeted towards GRBs and supernovae is called "Optical and

X-ray Follow-Up" (OFU) [102, 144]. The target are short timescale transients, which last briefly and fade within a matter of hours or days: Thus, the self-triggered search looks for at least two neutrinos arriving within 100 s not more than 3.5° apart. Significant alerts are forwarded to the Palomar Transient Factory (PTF) and to Swift for follow-up observations in the optical and X-ray regime [104, 105].

The goal of this work is the identification of flares from AGN, whose timescales range from minutes to weeks. Using the time-dependent analysis method (Sec. 5.2) provides a flexible time window and the benefits of the likelihood method, which considers per-event properties such as the energy and angular uncertainty.

6.1.1 Analysis Mode

The analysis operates on a pre-defined list of sources. Every time a new neutrino candidate arrives, the event weight w_i (the ratio of the signal and background PDFs, $\mathcal{S}$ and $\mathcal{B}$ in Eq. 5.1 and 5.2) is evaluated with respect to each source location. In the case that $w_i \geq 1$ is fulfilled for a source, the time-clustering analysis is triggered.

For this decision the event weight w_i is evaluated using a spectral index of -3. Compared to the atmospheric background following a spectrum of $\propto E^{-3.7}$, the energy term of the weight is almost flat in energy. Only little preference is given to more energetic events. Instead, the spatial term in w_i dominates and requires the source location to be within $\approx 1\sigma$ ($\approx 1°$–$2°$) of the event's angular uncertainty. This construction improves the sensitivity of the analysis to clusters of lower-energetic events.

The event which triggers the analysis defines the end of the time window, which is kept fixed. Earlier events with $w_i \geq 1$ define possible starting points for the time window. After maximizing the likelihood in each time window, the best-fitting time window is chosen. If the test statistic passes a pre-defined threshold, an alert is emitted.

The maximum allowed size of the time window T_{max} needs to be defined. In the previous implementation, the choice of 21 days was made [101]. Extending T_{max} requires testing additional time windows, which increases the number of likelihood evaluations. This is not an issue for the online analysis, where one event arrives every few minutes, but it is challenging for the toy simulation used in the calculation of the discovery potential. For this work, the algorithm was implemented in C++ (wrapped with a user-friendly Python interface), which reduces the runtime compared to the previous implementation in pure Python, allowing the investigation of larger time windows.

Figure 6.1 shows the discovery potential towards various flare lengths for different choices of T_{max}. The simulation was repeated for 9 different declinations with similar results. In general, extending the time window comes only with a small penalty for short flares. In turn, a much larger benefit concerning longer flares is found. This is for the following reasons:

- A larger T_{max} tests additional possible time windows. Thus there is a penalty due to the larger number of trials, i.e. look-elsewhere effect [145]. There are

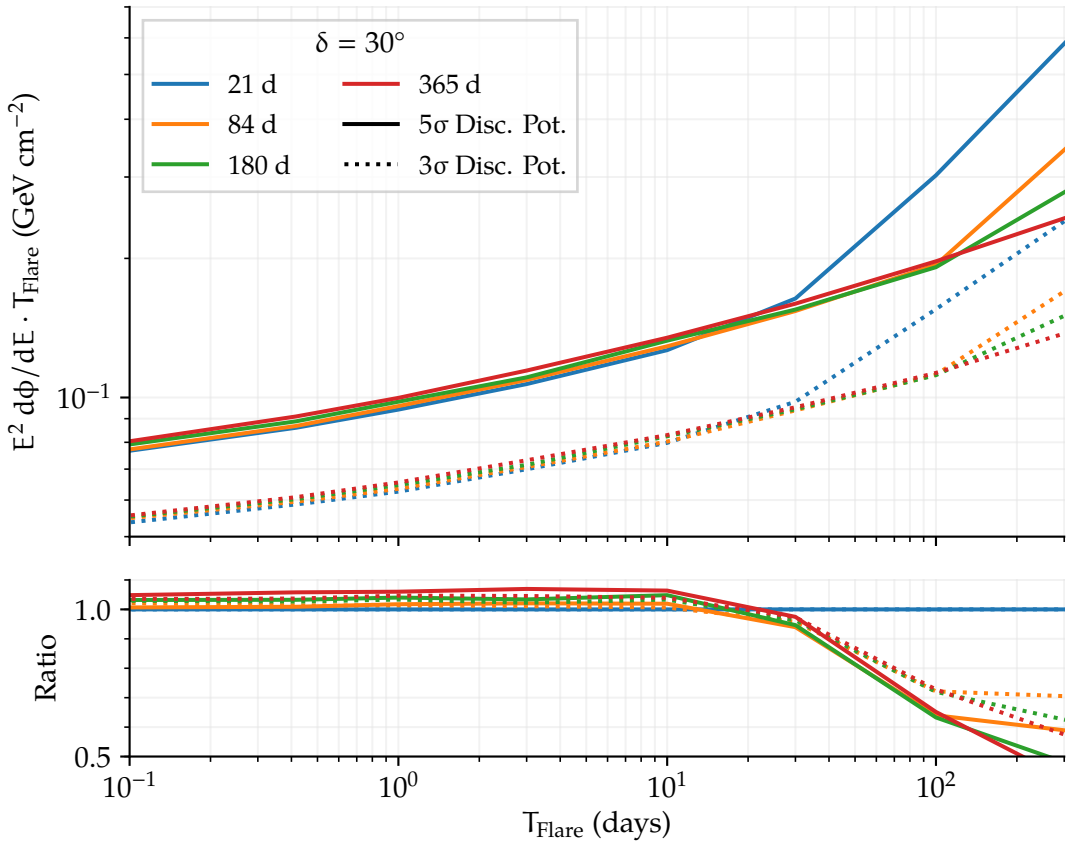

Figure 6.1: Discovery potential for different time window cuts. Four different choices for the largest allowed time window are simulated. For each choice, the discovery potential towards different simulated flare lengths (T_{Flare}) is shown. The ratio is evaluated with respect to the shortest choice (21 days).

many small time windows possible, which are tested in any case, whereas only few large time windows fit inside a given dataset. Therefore the penalty from the additional trials of testing longer time windows is small. This is also reflected by the test statistic, where the dependence on the maximal time window is $\sim \log(T_{max})$.

- For longer flares a penalty of missing an event is incurred, if T_{max} is chosen too short and it does not fit inside the box. The test statistic (Eq. 5.6) is driven by the sum of signal-like events, each of which contributes roughly $\approx n_s/N \cdot w_i$. If the event is signal-like, i.e. close to the source and possibly high energetic, it has a large weight and the test statistic will drop severly if the event is missed.

In summary, missing one event due to a too short choice of T_{max} has a more negative impact on the discovery potential than the additional trial factor incurred from testing additional event combinations. Thus, the overall choice remains rather arbitrary and

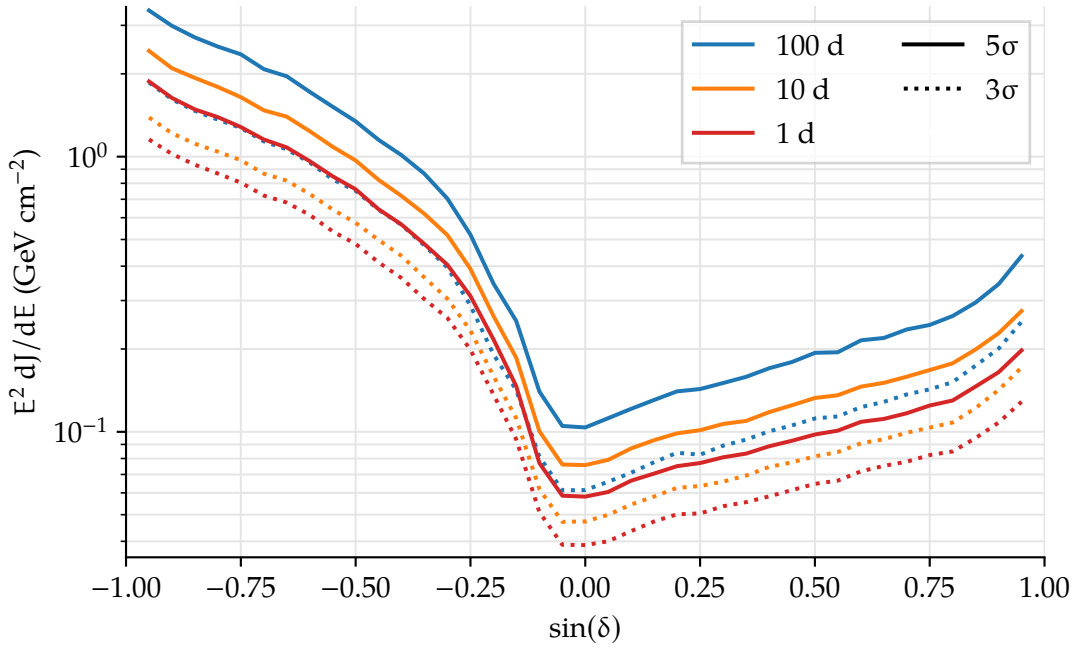

Figure 6.2: Discovery potential of the time-dependent analysis, when scanning over one year of data from the online filter.

unconstrained by the large number of model predictions. For the following online analyses, T_{max} is limited to 180 days, which is partly motivated by the result of the analysis result of TXS 0506+056 in Sec. 6.6.

Besides using this analysis method for issuing real-time alerts, it is also possible to search for the most-significant flares. in a fixed (archival) data sample. The discovery potential that can be achieved when analyzing a benchmark period of one year of data is shown in Fig. 6.2. The overall shape follows that of the time-integrated discovery potential shown in Fig. 5.12 and is determined by the event selection. Here, the absolute discovery flux additionally depends on the flare duration.

For this kind of study, the signal events are simulated uniformly during the flare (i.e. with a box-like shape), the same shape that is fitted by the analysis. Past analysis have used a Gaussian time profile both in the likelihood as well as in the signal hypothesis [127, 146]. In the absence of a discovered source, both choices are rather arbitrary. The box time profile is more suitable for a rolling, online analysis, since its start and, in particular, its end are well defined. Thus, the end of the box time profile can always be aligned with the end of the dataset, in contrast to a Gaussian profile with its infinite tail.

Simulating Gaussian-shaped flares, and reconstructing them using the box likelihood (or the other way around) allows to determine the impact of the choice of the time profile. The discovery potential is reduced by just 10% when the simulated and fitted shapes differ, while both the spectral index and the flare duration are still recovered by the fit.

6.1.2 Source Selection

Together with the improvements of the event selection developed in this work, the list of monitored sources was revised using the updated source catalogs from the Fermi-LAT collaboration. In the following, the selection criteria are outlined.

The third Fermi catalog of active galactic nuclei (3LAC, [147]) and the third Fermi catalog of hard spectrum sources (3FHL, [148]) serve as a starting point. The 3LAC contains sources detected by Fermi-LAT in the energy range between 100 MeV and 300 GeV. It contains 1951 AGN: 457 FSRQs, 632 BL Lac-type objects, 460 blazars of unknown type, and 32 non-blazar AGN. The 3FHL catalog contains sources with a hard spectrum, which are characterized between 10 GeV and 2 TeV. Out of its 1230 AGN, it adds 178 AGN to the sample that were not included in the 3LAC.

As a guiding principle of the selection, the sources should not just be potential neutrino emitters, but there should be a chance of observing the sources by the partner telescope. Hence, three lists are created, tailored to the MAGIC, VERITAS and H.E.S.S. telescopes, respectively. Based on the 3FGL and 3FHL catalogs, the following selection steps are applied:

1. The source should be visible for some time during the year. Using the latitude of the telescope, and the declination of the source, the maximum altitude (elevation above the horizon) must be larger than 50° (H.E.S.S.: 60°). The large culmination is necessary to achieve the lowest possible energy threshold.

   This cut tends to select sources from the northern hemisphere for MAGIC and VERITAS, and sources from the southern hemisphere for H.E.S.S..

2. Sources should be extra-galactic, with a measurement of the redshift z and $z \leq 1$. All FSRQs and about half of all BL Lac-type objects in the catalog have a known redshift.

   The threshold corresponds to the most-distant object that has been observed in very high energy gamma-rays [36].

3. As this analysis targets flares, sources with a history of variability are selected. In the 3LAC, a likelihood test compares the variable, monthly averaged lightcurves against the hypothesis of a steady source.

   In the 3FHL catalog, a bayesian blocks algorithm [149, 150] divides the observed flux state into blocks under the assumption of a constant flux within each block. A source with 2 or more blocks is considered variable.

   Only sources identified as being variable at 99% confidence level are considered for this analysis.

4. The flux measured by Fermi-LAT is extrapolated above 100 GeV, taking the extragalactic background light into account [33, 34]. The remaining, integrated flux above 100 GeV has to exceed the 5σ discovery potential of the telescope in 2 hours (H.E.S.S.: 5 h) of observations.

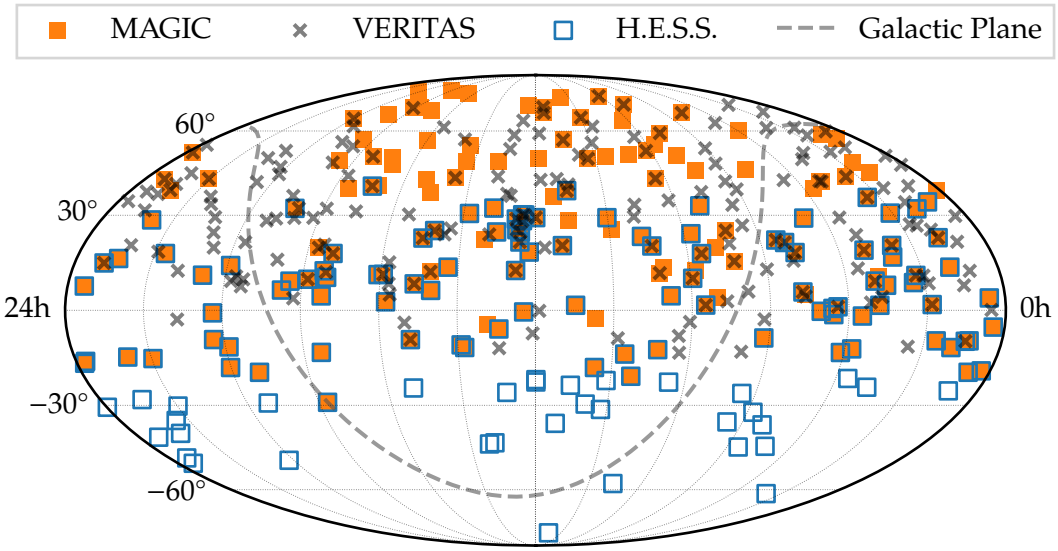

Figure 6.3: Skymap showing the locations of the monitored sources in equatorial coordinates. A different source list is created for each telescope, with the sources indicated by different symbols. In total, 339 individual sources are monitored for flares. All sources are listed in Appendix A.

Since the catalog flux is averaged over longer observations and does not reflect the behavior during a flaring state, the extrapolation is done optimistically: Based on the catalog values, the flux normalization is taken at the upper end of the uncertainty range, and the spectral index is taken at the harder end of the uncertainty range. In addition, the flux is scaled by a factor of 10 in order to simulate a flare.

Aside from the Fermi source catalogs, the source lists are extended using sources found in the TeVCat, a catalog of blazars observed at very high energy gamma-rays [151]. It contains sources whose spectral energy distribution peaks at TeV energies, towards which Fermi-LAT's sensitivity decreases. Hence, these sources are not all classified as being time-variable in the Fermi catalogs, but since their extremely energetic nature may provide a suitable environment for neutrino production they are added to the source lists.

Eventually, the selection yields 179 sources for MAGIC, 190 sources for VERITAS, and 139 sources for H.E.S.S.. Accounting for the sources common to several lists, 339 individual sources are monitored. A complete list is given in Appendix A.

6.1.3 Alert Threshold

After the definition of the analysis and the source lists, the threshold for triggering an alert shall be set.

One output of the time-dependent analysis is the test statistic, where larger values indicate a more signal-like cluster. A toy simulation using the same data scrambling approach from previous sensitivity calulations (Sec. 5.3) is used to estimate the distribution of the test statistic in a background-only scenario. From this distribution, the p-value (Eq. 5.12) corresponding to a given observation is derived.

In the following, two different definitions of the significance level are used:

- The *pre-trial* p-value is defined as the probability of observing the given value (or higher) for the test statistic (Eq. 5.10) from an online trigger in a background-only scenario. The pre-trial test statistic distribution is obtained as follows: A hypothetical source location is chosen. Archival data is scrambled, a random event close to the source (i.e. having $w_i \geq 1$) is chosen which is supposed to trigger the online analysis. The test statistic obtained for that trigger is used to build a PDF.

  There is no intrinsic time scale in this construction, except for T_{max}, hence this significance parameter is not affected by the overall time period for which the program is operated. As such, it is a suitable quantity to define the alert threshold in a real-time analysis.

- The *post-trial* p-value is defined as the probability of finding the given test statistic (or higher) as the overall best result in one year of background-only data. The post-trial test statistic distribution is obtained as follows: A hypothetical source location is chosen. Archival data is scrambled and a random period of 365 days is scanned for the best fit (i.e. the highest test statistic) from that source in that year. This best test statistic found is used to build the PDF.

  This construction accounts for the trials due to operating the experiment for one year. Since the time scale of one year is larger than $2 \cdot T_{max}$, the first and last trial in the scan are uncorrelated. Therefore, the analysis of a longer data period simply incurs an additional trial factor proportional to the number of years, i.e. the scaling factor for the exposure.

  In an offline analysis, where a certain period of data is scanned for the overall best flare, this kind of trial correction is used to obtain the final significance level of a quoted result.

The distribution of the test statistic can vary at different declinations, due to the varying background event rate and properties of the events, such as the energy and the angular resolution. In Fig. 6.4a the right-cumulative distributions, i.e. the survival functions, of the test statistic are shown for the pre- and post-trial constructions at three exemplary declinations. In practice, the distribution is sampled at 39 individual, evenly spaced, declinations.

Also the functional relation between pre- and post-trial significances depends on the declination, as is shown in Fig. 6.4b. The blue band shows the most extreme relation found over all declinations, while the blue line indicates the behavior at the horizon as an example. No simple and unique analytic model could be found which

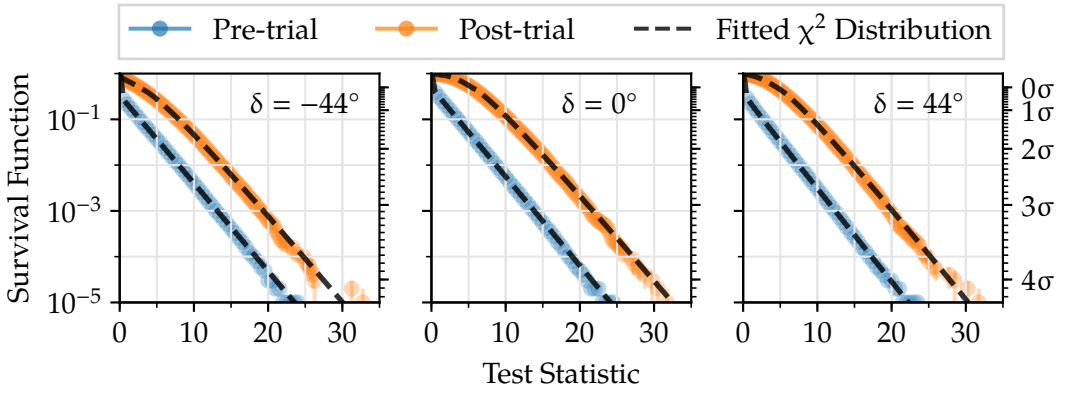

(a) Examples of test statistic distribution at different declinations.

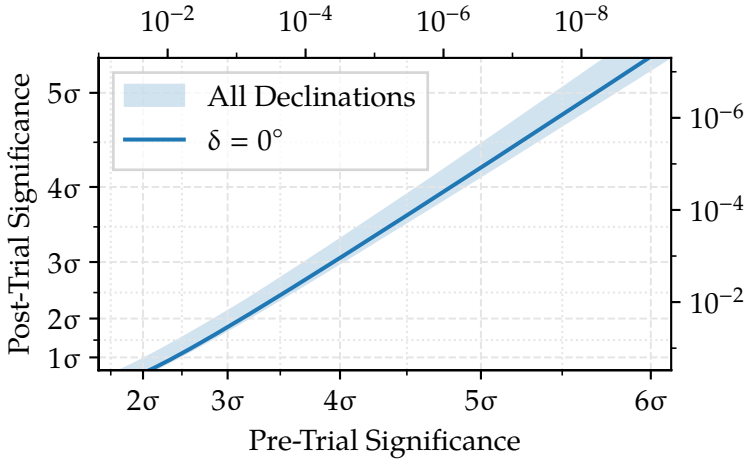

(b) Relation between pre-trial and post-trial significance levels.

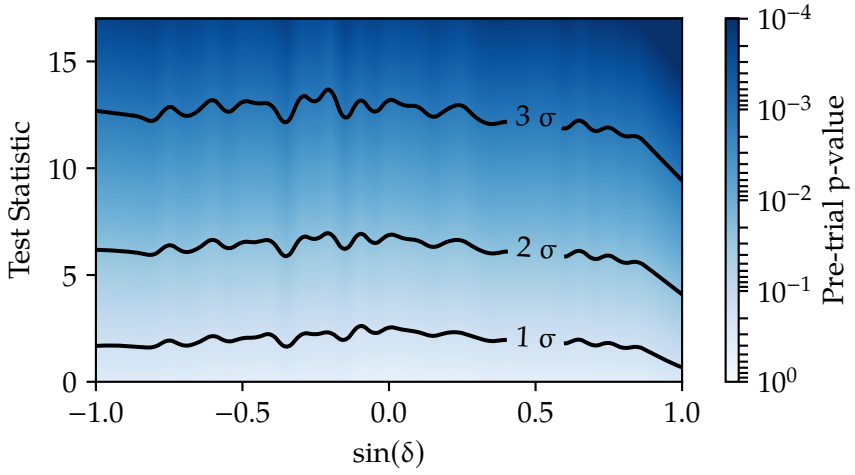

(c) Test statistic distribution for all declinations.

Figure 6.4: Test statistic distribution in a background-only scenario. The pre-trial distribution is used in the online monitoring by comparing it to a pre-defined threshold. The post-trial distribution provides the overall significance after scanning one year of data for the best result, e.g. in an offline analysis.

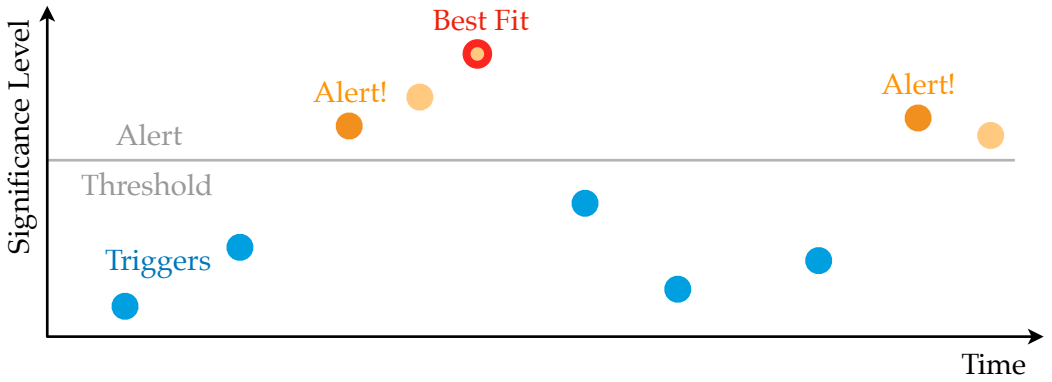

Figure 6.5: Sketch of triggers and alerts in a real-time analysis: Every incoming event triggers the analysis (blue) and its significance is compared to the threshold. The first time that threshold is crossed, an *online* alert is issued (dark orange). Subsequent triggers, which also yield an above-threshold result, do not qualify as an independent alert (bright orange). A flare might continue to build up and reach its peak significance after the initial alert. This global best fit (red) is typically the outcome of an *offline* analysis.

describes the correlations between the tested time windows, hence the use of the toy simulations. Eventually, Fig. 6.4c displays the relation between the test statistic and the pre-trial p-value for the entire sky, with linear interpolation between the simulated declinations.

Before examining the expected alert rate, the meaning of an alert must be clarified. A sketch of the outcome of the online analysis is shown in Fig. 6.5.

- Every incoming event close to a source, i.e. with $w_i \geq 1$, triggers the analysis (blue dots). Most triggers will yield a result below the significance threshold.
- Once that threshold is crossed, an alert is sent out (dark orange dots). Crossing the threshold requires the previous trigger having been below the threshold and the current trigger being above the threshold.
- Should an alert be followed by further above-threshold triggers, they are considered belonging to the on-going flare (bright orange dots). In this case, no new alert is emitted for now. This conservative decision preserves blindness with respect to the time period following the trigger blind. The data can be used in later in an blind follow-up analysis.
- At some point the most-significant cluster of events will be recorded (red circle), typically following an earlier alert. Offline analyses scanning a fixed time period typically yield this kind of result.

The pre-trial significance is computed for alert candidates. It should be interpreted carefully, as it is a tool to normalize declination-dependent effects. An alert is emitted

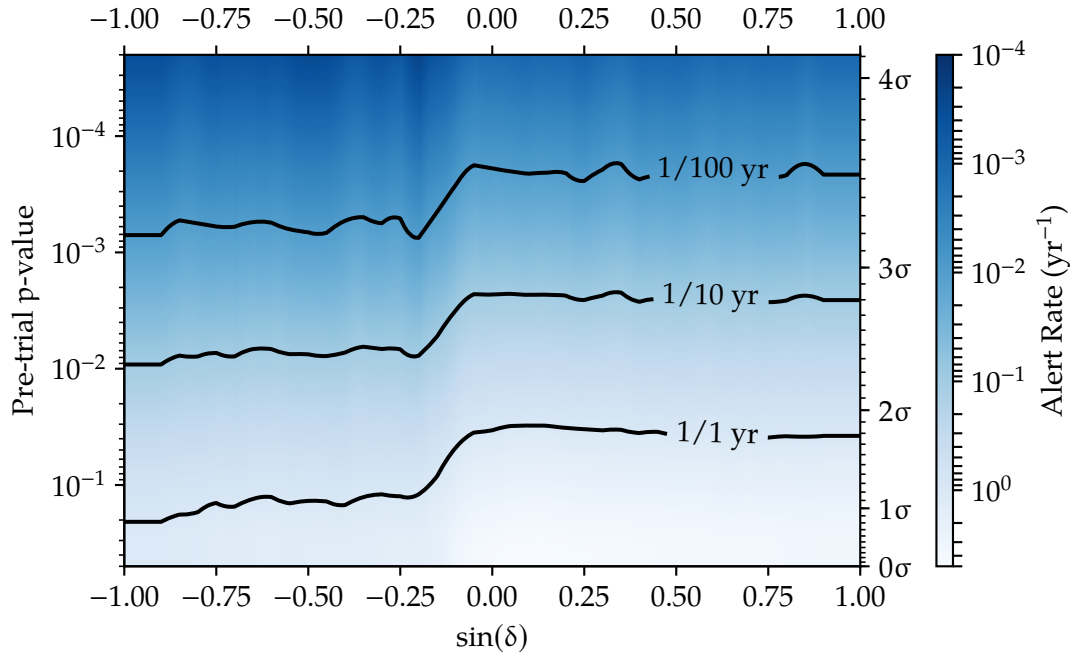

Figure 6.6: Expected rate of alerts for monitored sources as a function of the alert threshold. The alert threshold is given by the pre-trial p-value.

as soon as the threshold is crossed, therefore the significance levels attributed to the alerts are expected to be just above the threshold. In comparison, offline searches report the significance at the flare maximum, and account for the trial factor for searching a certain time period.

In order to determine the expected alert rate for one year of operation, the online analysis is applied to scrambled data. The timescale of one year corresponds to the scale on which IACTs plan their observations through a competitive selection of targets. Different declinations are scanned and a pre-trial significance is assigned to each trigger. Then, triggers fulfilling the above definition of an alert are counted. The number of expected alerts per year is shown in Fig. 6.6 as a function of declination.

The shape of the distribution largely follows the event rate of the online event filter, which is larger in the northern sky ($\delta > 0$) than in the southern sky. As the sensitivity of IceCube is better with respect to sources in the northern sky, this behavior of the alert rate is useful for targeting more-promising sources in the northern sky.

Combining Fig. 6.6 with the previously defined source lists yields a prediction of the rate of alerts emitted towards each telescope.

In Fig. 6.7a the general relation between the alert rate, the alert threshold, and the number of monitored sources is shown. It is averaged over the northern sky, where the alert rate almost independent of the exact declination of the sources. For the three particular source lists considered here, the explicit alert rates are shown in Fig. 6.7b. The figure also contains the rate of test alerts, which is explained in the next section.

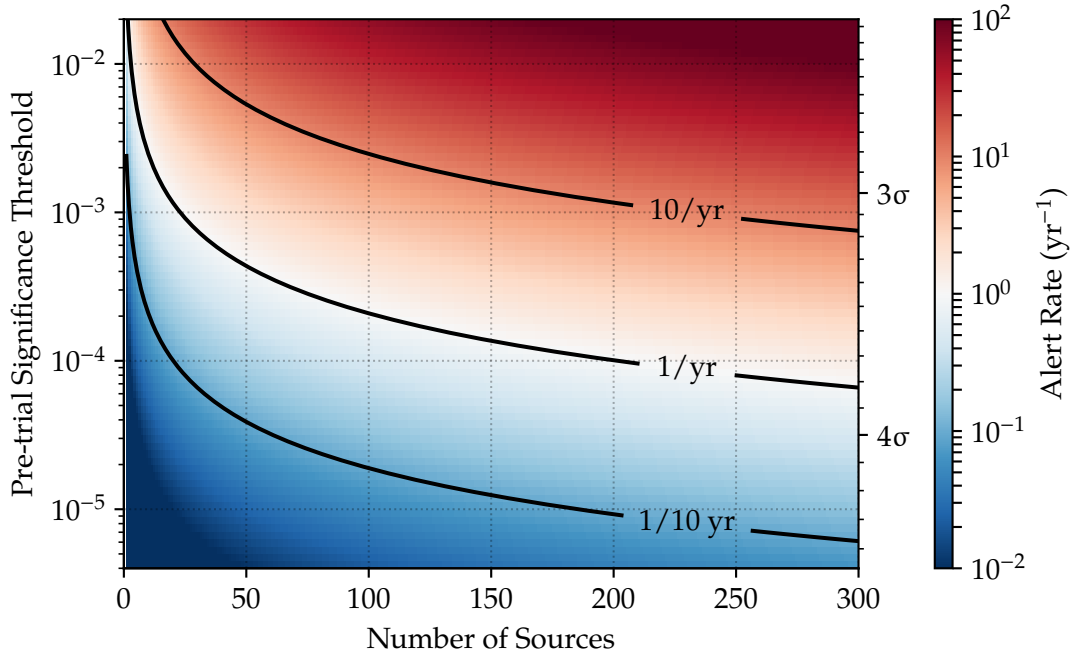

(a) Alert rate as a function of the pre-trial significance threshold for monitored sources in the northern sky. The rates in the southern sky are approximately five times lower.

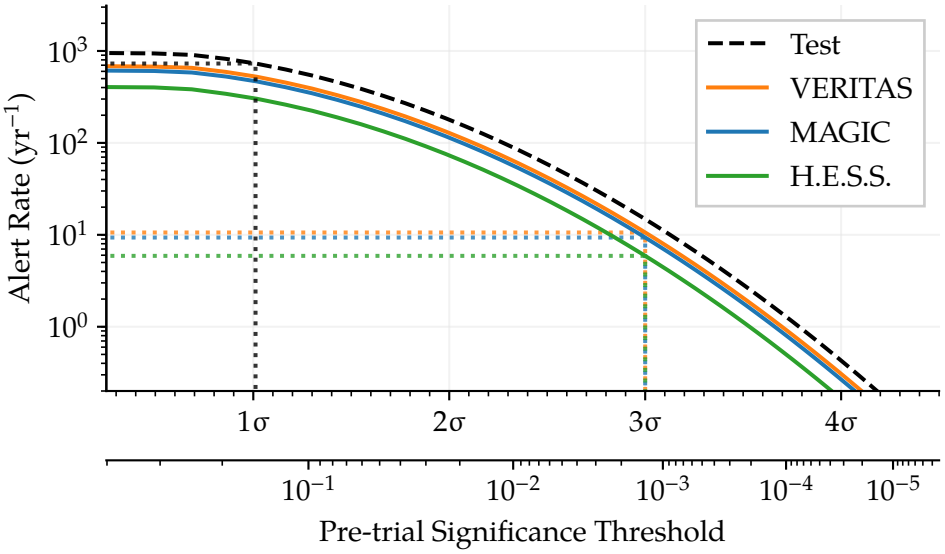

(b) Alert rates for actual source lists. Dotted lines indicate the chosen alert thresholds and the resulting alert rates.

Figure 6.7: Alert rate for monitored sources. While the upper figure is generally applicable for a list of monitored sources, the lower figure displays the rate specifically for the chosen source lists. The MAGIC (VERITAS; HESS) lists comprise 179 (190; 139)sources.

Only a certain number of alerts can be followed up, which is limited by the observation time granted by the telescope and its duty cycle. This limitation governs the desired alert rate and thus the significance threshold.

IACTs achieve their best performance in dark, moon-less conditions, which make up 1500 h per year. Observations in the presence of moonlight is possible, with reduced sensitivity [152]. Weather and maintenance reduce the time during which optimal sensitivity can be achieved to 1000 h, or 10% of a year. Therefore, in order to obtain at least one successful follow-up observation per year, a rate of one alert per month is desirable.

Choosing a significance threshold of 3σ, approximately 10 alerts for each MAGIC and VERITAS, and 6 alerts for H.E.S.S., are expected.

Each alert contains information about the source candidate, the significance level (from Fig. 6.4c), and the flare time window. It also contains the false alert rate (from Fig. 6.7a), i.e. the rate of alerts that is expected from a source at the same declination with at least the given significance level. This information is included with the alert to allow the partner telescope to judge the importance of the alert and reconcile it with its usual observation schedule.

With this alert threshold set, the median number of events required to trigger an alert is shown in Fig. 6.9a for different flare time scales. The corresponding flux, integrated over the flare duration, can be found in Fig 6.9b. This curve follows the general sensitivity curve shown in Fig. 5.12. Depending on the declination, as little as three events on an hourly to daily time scale can be sufficient to trigger an alert.

For a follow-up observation to be useful, an alert should be generated while the flare is going on. A study of when an alert is triggered on average is depicted in Fig. 6.8. A comparison of this work's trigger time to that of the previous iteration has shown that the improvements made in this work yield an alert $\approx 20\%$ earlier in an ongoing flare. The improved sensitivity allows more timely triggers, while covering a wider range of possible flare times.

Test Alerts

In addition to the real alerts, a test alert system is added. Observing the rate of these test alerts allows to monitor the entire analysis chain, from the event selection at the South Pole, over the transmission, up to the analysis and alert code. In order to overcome statistical fluctuations, a large number (300) of locations is chosen, equally distributed on the sky.

Unnecessary unblinding of data is avoided by running the analysis on a scrambled data set. It is created by shifting azimuth and right ascension by one event. Due to the high event rate of one event per five minutes and the events being largely atmospheric background, the effect of this scrambling method is equivalent to randomizing the right ascension. It destroys any potential signal, but preserves the correlation between the observed variables [97]. It also preserves a time structure introduced by possible malfunctions.

The scrambling method is constructed in order to create a persistent, blinded

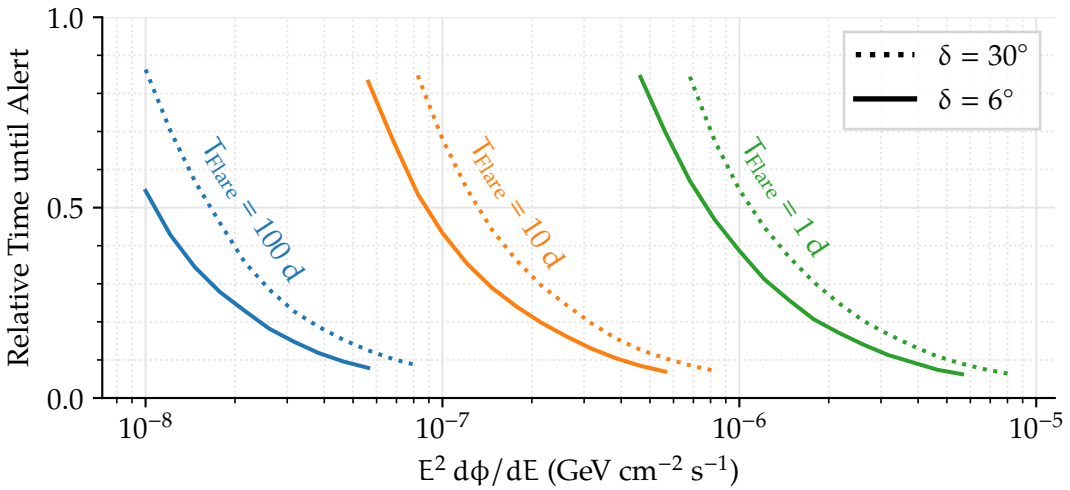

Figure 6.8: Average time until an alert is sent. Three different flare durations are simulated over a range of fluxes. The vertical axis shows at which point the alert threshold is crossed during the flare, relative to the total flare time window (i.e. 0 is the beginning, 1 is the end of the flare).

representation of the data. When a new event arrives, this event's coordinates will be scrambled but the previous events' scrambled state will remain, producing a consistent stream of scrambled events. It is necessary since subsequent, tested analysis time windows overlap and are correlated. A simple randomly shuffling of the right ascension coordinate would destroy that time correlation and distort the alert rate.

As can be seen in Fig. 6.7b, a test alert threshold of 1σ yields a rate of ≈ 700 test alerts per year, corresponding to two test alerts per day.

6.2 Online Unbiased Search for Neutrino Clusters

In addition to monitoring known gamma-ray emitters for neutrino flares, the flare search method can be extended to scan the entire sky.

This removes the bias of the source lists and may reveal sources which have not been considered for time-dependent neutrino emission. It can also target sources which have not been observed in gamma-rays (e.g. due to being obscured [153]), or transient phenomena. The large number of possible source locations, and the correspondingly large trial factor, lower the sensitivity of the all-sky search, compared to the dedicated source monitoring. Therefore, both analyses can legitimately coexist and are worth to operating in parallel.

Lacking a source list, every incoming event is treated as a potential trigger and the area around that event needs to be searched for an excess.

The likelihood space comprises many local extrema in the sky and the box-shaped time profile introduces a non-smooth behavior in the time domain. In turn, a gradient-

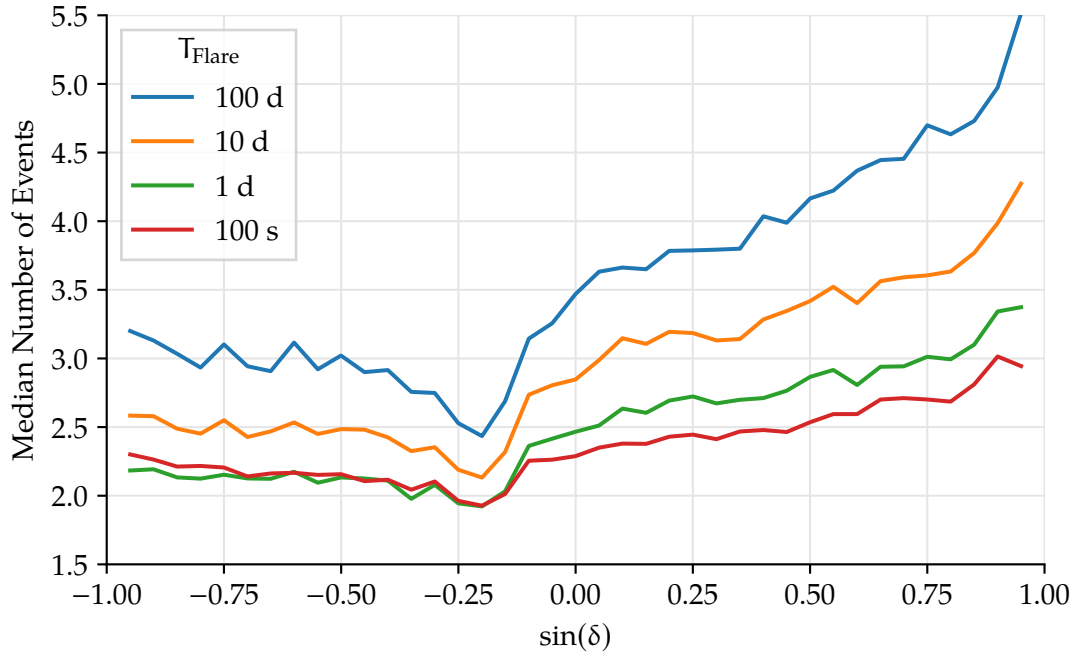

(a) Median number of events necessary to trigger an alert with a significance level of 3σ.

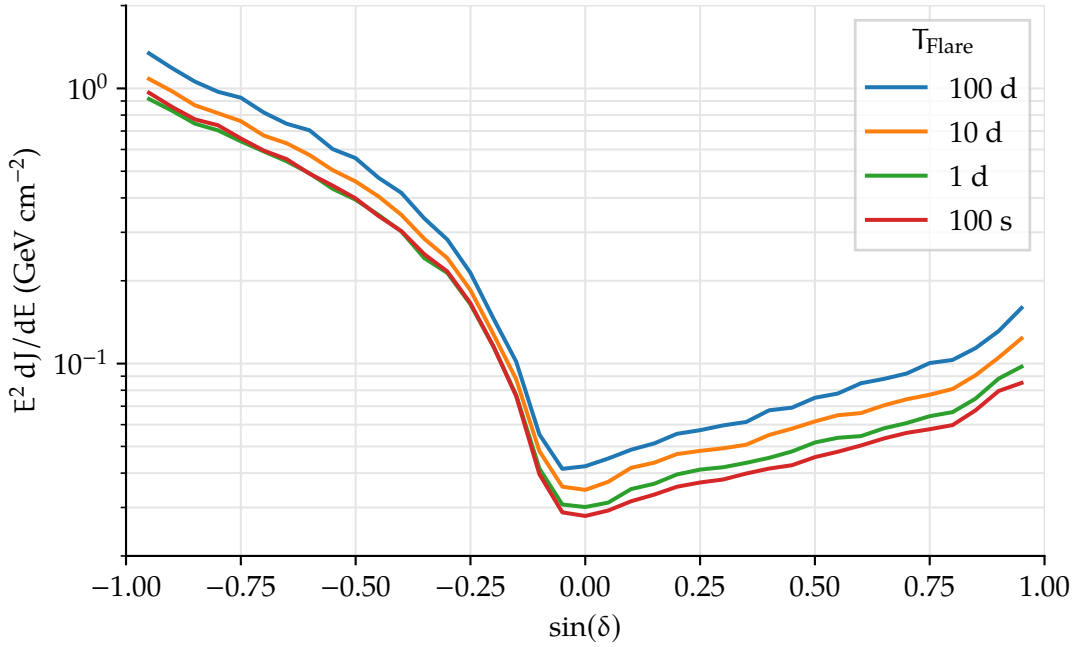

(b) Median fluence necessary to trigger an alert with a significance level of 3σ.

Figure 6.9: Thresholds to trigger an alert from a monitored source. The shown flux will trigger an alert in 50% of the cases.

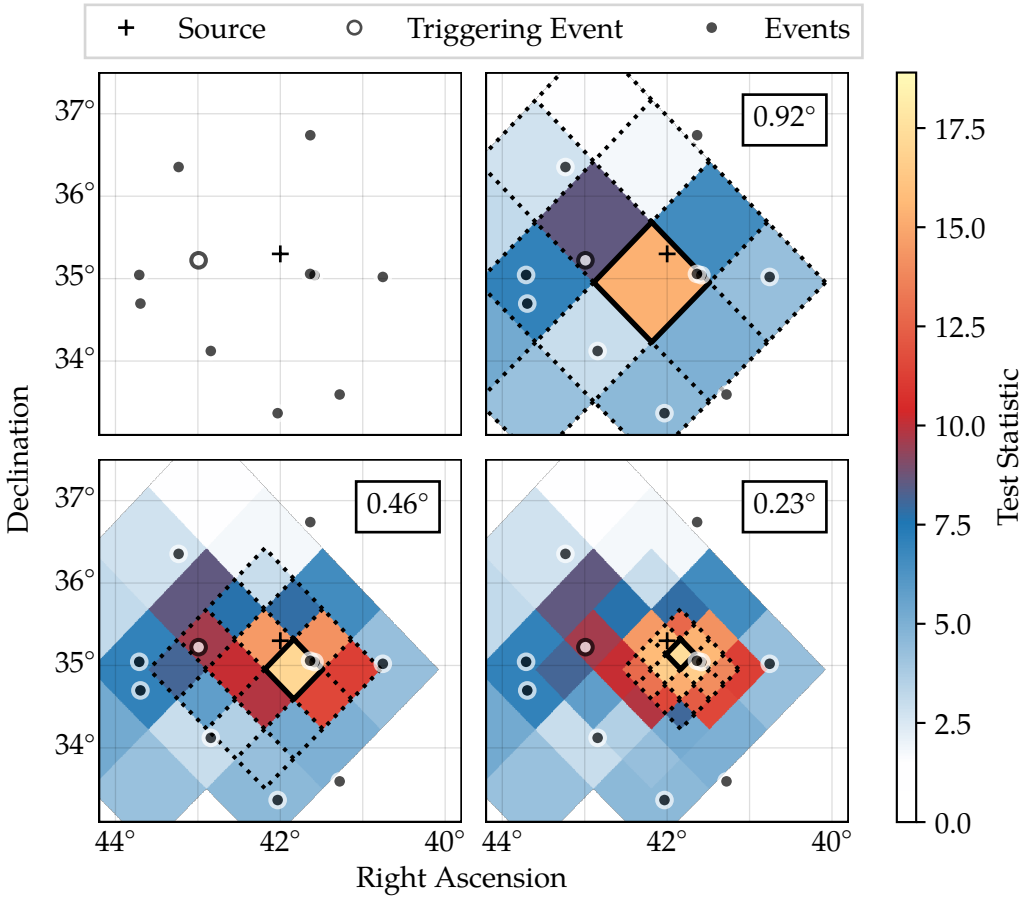

Figure 6.10: Sketch of the all-sky scan method. Figures are centered on the location of the simulated source. Dotted lines indicate which pixels were scanned in each iteration. The grid spacing is given in the top right. A solid line marks the pixel with the best test statistic.

descent minimizer works reliably to determine the flux and spectrum for a fixed source location and time window, but is not suitable here. Instead, an iterative fit of the flare direction is implemented, which wraps the time-clustering scan with a directional scan.

The Hierarchical Equal Area isoLatitude Pixelization (HEALPix[1]) software, along with the Python wrapper "healpy", provide efficient means for dividing a sphere (i.e. the sky) into bins of equal area [154, 155]. Each bin's center is treated as a source hypothesis, to which the previously implemented time clustering algorithm can be applied.

In order to keep the computational effort manageable, the search starts on a coarse

[1] `http://healpix.sourceforge.net`

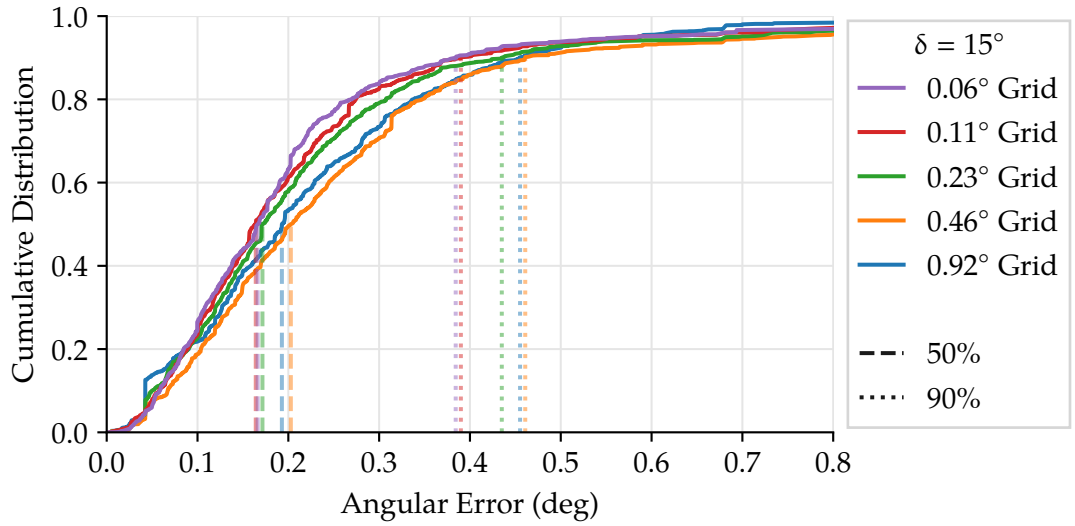

(a) Distribution of angular errors for different grid spacings. Simulated flares comprised 5 events over 10 days. The grid search started with a grid spacing of 0.92° and was iteratively refined to the labeled grid spacing.

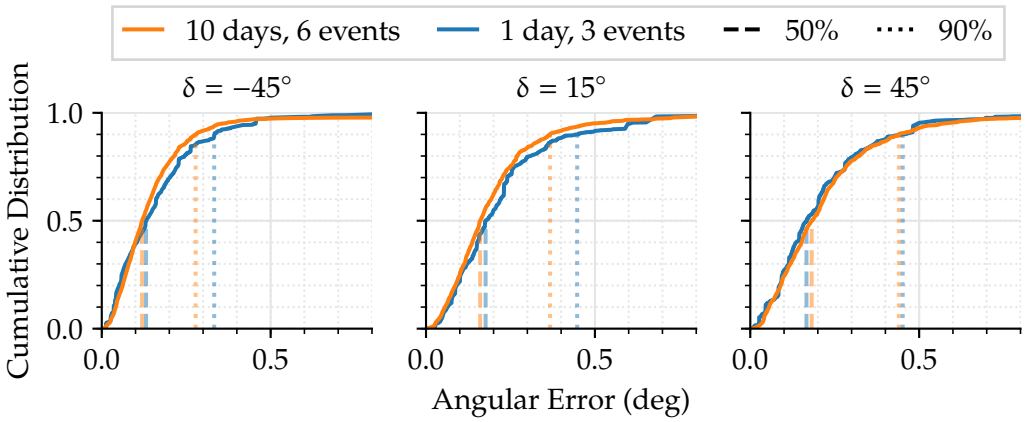

(b) Angular error of alerts using the final configuration. Two different flare durations and strengths were simulated. Only flares which would have crossed the online alert threshold are shown.

Figure 6.11: Angular error of the all-sky flare search. The angular error is defined as the distance between the location of the simulated flare and the best fit localization.

grid, using a grid spacing of 0.92°. Only those grid points are considered, at which the most recent event contributes an event weight $w_i \geq 1$. Since the event weight is dominated by the spatial term, the scanned area scales with the angular uncertainty of the event. Again, to constrain the runtime, the search is limited to a radius of 2 degrees. As a result, grid points which are substantially influenced by the triggering event are tested, and directions which are unlikely to be correlated with the triggering event are ignored.

Having found the most-significant pixel, the bin size is halved and the previously most-significant pixel is split into sub-pixels. The test statistic is evaluated again on each sub-pixels. This process is repeated until the target grid size is reached. The algorithm is illustrated in Fig. 6.10, using scrambled data and a few simulated signal events.

A toy simulation was performed in order to optimize the pixelization, simulating a neutrino flare at a known location and recording the distance between the true and the most-significant location as a function of the grid spacing. Figure 6.11a shows that no significant improvement is seen for a spacing smaller than 0.1°, which is consistent with the angular error of the best-reconstructed events.

Using the final configuration and alert threshold, the point spread function has been tested at different decliations. Results are shown in Fig. 6.11b, indicating that the best resolution is achieved in the southern sky, where events are more energetic and larger photon statistics allow for a more accurate pointing compared to the northern sky. In general, the localization error is around 0.2° on average, and the 90-percentile is better than 0.5°. The results are almost independent of the signal strength, provided that the signal is strong enough to cross the alert threshold. Hence, the pointing of any significant clustering will already be limited by the resolution of the experiment. Nevertheless, the median angular error is better than than for the majority of single events, which only achieve a comparable resolution at the highest neutrino energies, as shown in Fig. 3.7. The individual events contributing to a cluster are TeV events with a median pointing uncertainty of $\approx 0.6°$ or greater.

6.2.1 Alert Threshold

Similar to the source monitoring in the previous section, the test statistic found by the scanning algorithm is converted to a significance level. As before, a pre-trial p-value is defined as the probability of observing the given test statistic, or a larger one, from a random trigger under the background-only hypothesis. Compared to the source monitoring, the test statistic distribution is shaped differently. Since the algorithm does not just optimize the time window, but also the location, it tends to find larger test statistic values.

A toy simulation using the scrambling approach (Sec. 5.3) creates random realizations the data under the background-only hypothesis. After picking a random event as the trigger, the pixel scan yields a test statistic. Testing triggers on the entire sky eventually yields the test statistic distribution as a function of declination, as shown in Fig. 6.12. Compared to the earlier distribution for the case of fixed source locations

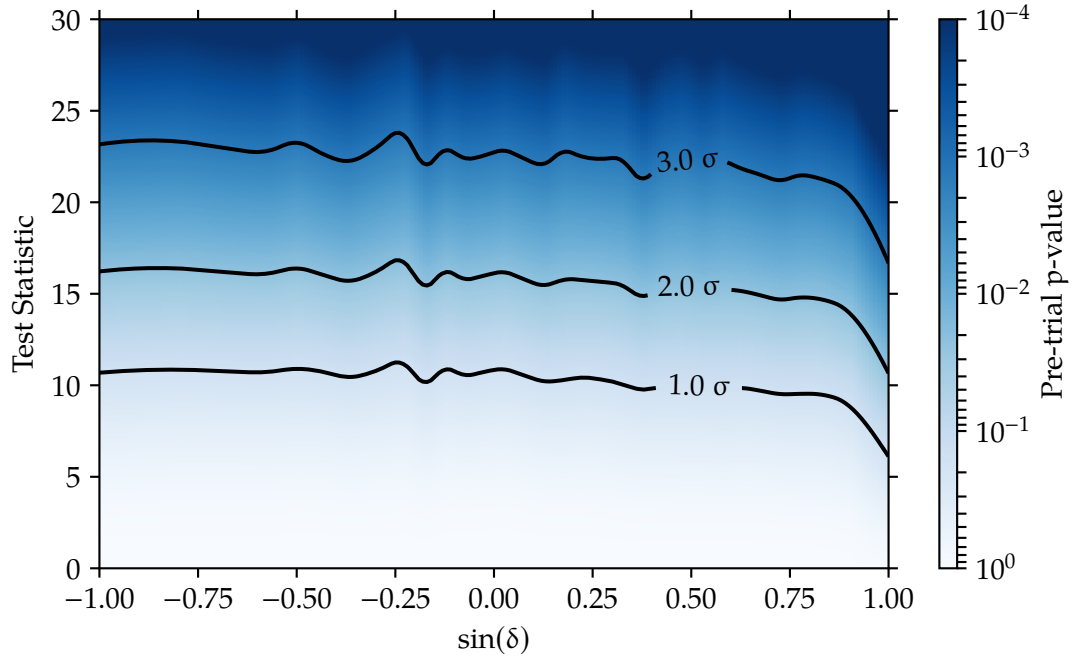

Figure 6.12: Test statistic distribution for the all-sky scan as a function of declination. The distribution is sampled from a toy simulation of the online analysis and binned in sin(δ). In each bin, the distribution is normalized, then a linear interpolation is employed to cover the entire sky.

(Fig. 6.4c), the shift towards larger test statistic values is obvious.

Figure 6.12 is used to assign the pre-trial significance level after the sky around a triggering event has been scanned. This value is used to define the alert threshold. As before, there is no intrinsic time scale concerning the length of the analyzed data sample, and no account for the number of pixels scanned.

However, due to the vastness of the sky, testing every possible direction for a cluster always tends to find a random aggregation of background events with a seemingly high significance level. The celestial sphere comprises $\approx$ 41,253 deg^2. Given an optimistic angular extension of at most 0.5°, a typical neutrino cluster would cover an area of $\approx$ 0.8 deg^2. Thus, an all-sky scan would test approximately 51,566 independent hypotheses in the sky for a source. In a simple approximation the Bonferroni correction multiplies the pre-trial p-value with a a trial factor equalling the number of independent, tested hypotheses [145]. Thus, a pre-trial significance level of 5σ, corrected for the number of hypotheses, yields a post-trial significance of $\approx$ 2.2σ [145]. Conversely, retaining a discovery at the 5σ level requires a pre-trial significance of 6.8σ.

In practice, an analytic expression of the trial factor is not available and the post-trial significance level of the best fit result is derived using toy simulations, which will be discussed in the next section. The discussion however highlights that such a search,

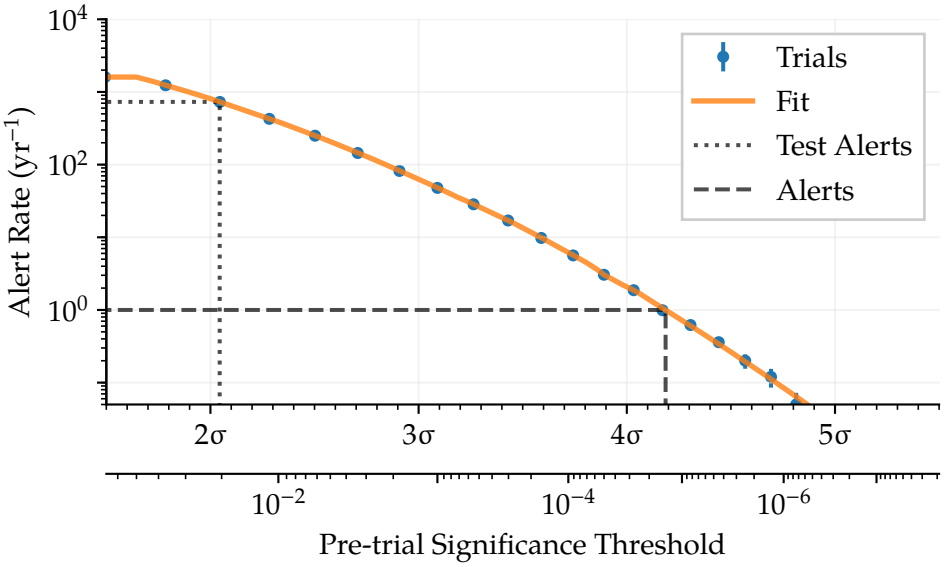

Figure 6.13: Expected alert rate for the online all-sky scan, derived from a toy simulation. The alert threshold is configured in order to achieve a target alert rate of one alert per year.

unconstrained in space and time, is likely to pick up a background overfluctuation. Thus, the alert threshold is set quite high in order to yield a background alert rate of one alert per year. The expected alert rate is shown in Fig. 6.13. An alert threshold of a pre-trial significance level of roughly $1.26 \cdot 10^{-5}$ is chosen.

The same method for generating test alerts, which is used for the source monitoring (Sec. 6.1.3), is also employed here to create on average two test alerts per day.

6.3 Results from Archival Data

The previously described alert system was turned on in March 2019. Archival data recorded with the complete 86-string IceCube detector is available going back to May 2011.

In the past, occasional updates to the online calibration and filtering have required the adjustment of event selections for different data taking seasons. As the experiment matured, such adjustments have become much less frequent. Therefore, the IceCube collaboration has decided to reprocess its historical data using the most-recent calibration and filtering configuration. As a result, it is possible to select the events from the online filter developed for this work, as if the filter had been running since 2011. This yields a homogenous data sample with uniform properties, starting in May 2011 and seamlessly transitioning to the current online setup.

Such a sample facilitates searches for time-dependent point sources and allows scanning $\approx$ 8 years uninterruptedly. In contrast, previous scans had to treat the different data taking periods individually, challenging the detection of flares at the transition between different periods.

In the following, this long-term data sample is scanned in order to test the analyses and determine which alerts would have been generated if the system had already been running the past.

The analysed data sample consists of all available, good runs. In principle, the definition of "good" should follow the criteria described in Sec. 3.6, which are used for the online data quality monitoring. However, it was not possible to retrieve a consistent record of the trigger rate over last 8 years, which is a required input for the online detector monitoring. Therefore, a different scheme is employed, which has been developed for offline point source searches [44]. For each run, the median event rate in a window of ±5 days is calculated. If the event rate of the run is within ±5% of that running median rate, the run is considered good for the analysis. It may be rejected when e.g. only a part of the strings were taking data. This estimation is performed on the second-to-last event selection level, where the event rate is large enough (6 Hz) to keep statistical errors small. An overview of the uptime is presented in Fig. 6.14.

There are gaps between the good runs: most of them are of the order of a minute, since the detector used to be power-cycled every 8 hours. In 15 cases, gaps larger than 24 hours were found and investigated concerning their cause: 10 gaps with a total of 262.6 hours were caused by commissioning and calibration work, five additional gaps of 131.4 hours in total are due to missing data in the reprocessed data sample. In the past, raw waveforms were stored on tapes and shipped once a year from the South Pole to Madison, WI. During reprocessing, it was discovered that several tapes were missing, or had been damaged or degraded to a degree, where both the original and the backup tapes had become unreadable. In addition, many smaller gaps are caused by maintenance and calibration work.

Eventually, the final dataset comprises a good uptime of 2756 days, which corresponds to 96.6% of the total, possible uptime.

For archival studies, where computational constraints are weaker than for online analyses, the best available reconstructions can be applied to events. Enabling additional modifications in the directional reconstruction of SplineMPE (Sec. 3.4.1) adds terms related to detector noise and stochastic energy losses by muons to the likelihood. In addition, the angular error estimation using the Paraboloid method (Sec. 3.4.2) can be applied to all events. However, as can be seen in Fig. 6.15, these best offline reconstructions improve the point source discovery potential by less than 10%, compared to the online reconstruction. Therefore, the following results are obtained using the online sample.

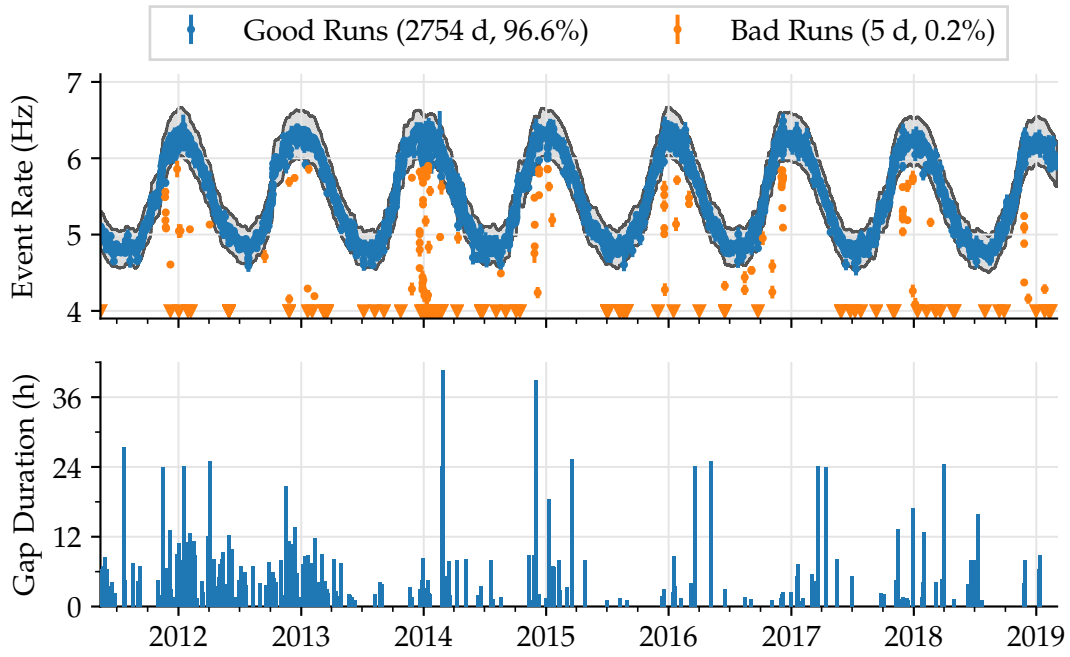

Figure 6.14: Uptime of the data sample for the archival analysis. The upper panel shows the runs, which were considered good for this analysis (blue), and those that were rejected due to their anomalous event rate (orange). Not shown are times, where the data was interrupted for maintenance or calibration. The lower panel shows the gaps between the (good) runs in the final data sample.

Source Monitoring

The online source monitoring algorithm has been applied to the archival dataset in the same way as if it was run online. A complete list of the alerts is given in Appendix B.

The averaged archival alert rate of 10 alerts/year for MAGIC, 9.5 alerts/year for VERITAS, and 5.5 alerts/year for H.E.S.S., is consistent with the expectation of Fig. 6.7b.

As explained in Sec. 6.1.3, the alert only indicates the point in time when the alert threshold was crossed first. Looking in hindsight at this archival data sample, it is more interesting to see how the flare candidate evolved following the alert. Therefore, the most-significant flare window in all of the 339 individual sources is presented.

The most significant flare was found from the direction of 1ES 0347-121. This a BL Lac-type object at the coordinates of $\alpha = 57.35°, \delta = -11.98°$ with a redshift of $z = 0.188$.

The properties of the flare are summarized in Fig. 6.16. An alert would have been triggered on Dec. 31, 2014 at 22:24, based on two nearby events recorded during 111 minutes. Two additional events were observed during the following five hours. In

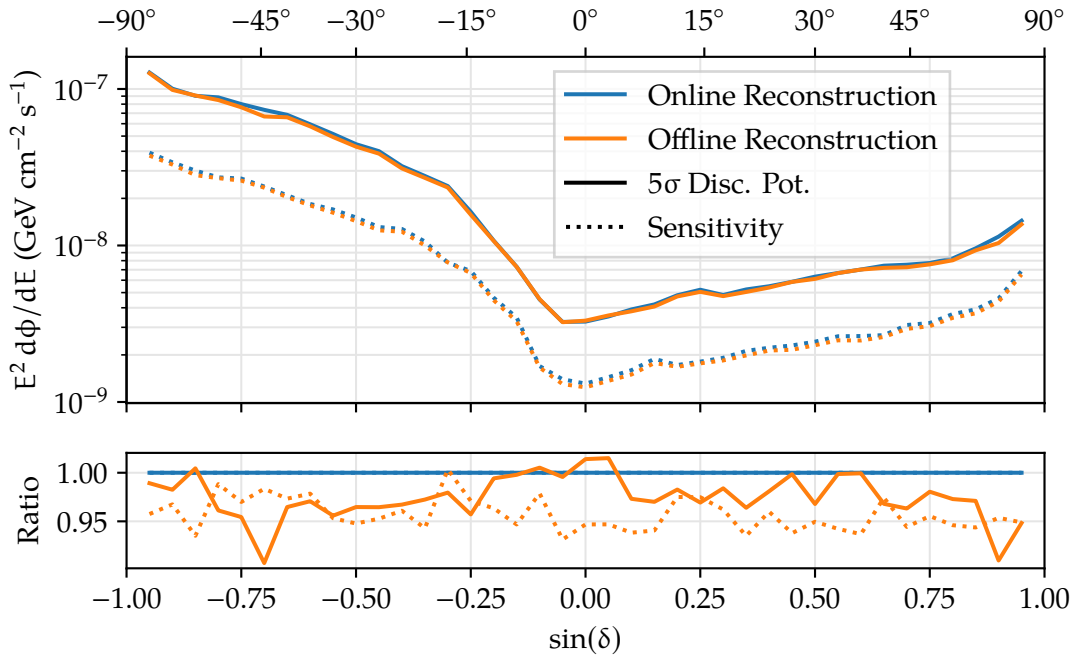

Figure 6.15: Time-integrated sensitivity using one year of data. Events selected by the online filter were reconstructed with the configuration used online at the South Pole, and, for comparison, also reconstructed with the much slower settings used in offline analyses.

total, the best fit time window comprised four events in roughly 7 hours.

Features of the events, such as localization and energy, as well as the duration of the time window, are encoded in the test statistic Λ. Under the background hypothesis, a value of Λ at least as large as the one observed, is found only once per $1.5 \cdot 10^6$ simulated triggers, corresponding to a pre-trial p-value (Sec. 6.1.3) of $6.7 \cdot 10^{-7}$. Accounting for the total analyzed time period of ≈ 7.5 years and the 339 tested source locations, the post-trial significance level is $2.4 \cdot 10^{-2}$, equivalent to 2σ.

Unfortunately, during the time window of 7 h, good data is only available for 5.4 h. This relative uptime of 78 % is unusually low for IceCube and related to the flare spanning the boundary of the calendar years 2014 and 2015. Unable to deal with the year roll-over, the IceCube data acquisition system requires a restart at the beginning of a new year. In 2015, this was done only 1.5 h later, causing the timestamps of hits between 00:00 and 01:30 to be unreliable, thus preventing the analysis of the events from that period.

Observations of the source during the time of the flare are not publically available in very high energy gamma-rays. However, Fermi-LAT has been monitoring the entire sky for several years and provides a lightcurve in gamma-rays with energies between 100 MeV and 10 GeV. The Fermi All-sky Variability Analysis (FAVA) is a photometric analysis, which estimates the variability of the flux observed in two energy bands

Start Date	2014-12-31 20:32
Start MJD	57022.85620
End Date	2015-01-01 03:28
End MJD	57023.14487
Duration	6.9 h
Uptime	5.4 h (77.8 %)
Test Statistic Λ	31.77
Fitted n_s	3.93
Fitted γ	-2.47
Pre-trial p-value	$6.74 \cdot 10^{-7}$ (4.83σ)
Post-trial p-value	$2.36 \cdot 10^{-2}$ (1.99σ)

(a) Results of the best-fit time window.

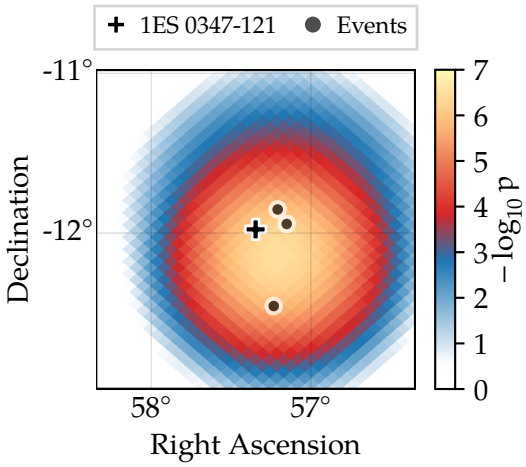

(b) Skymap during the best-fit time window.

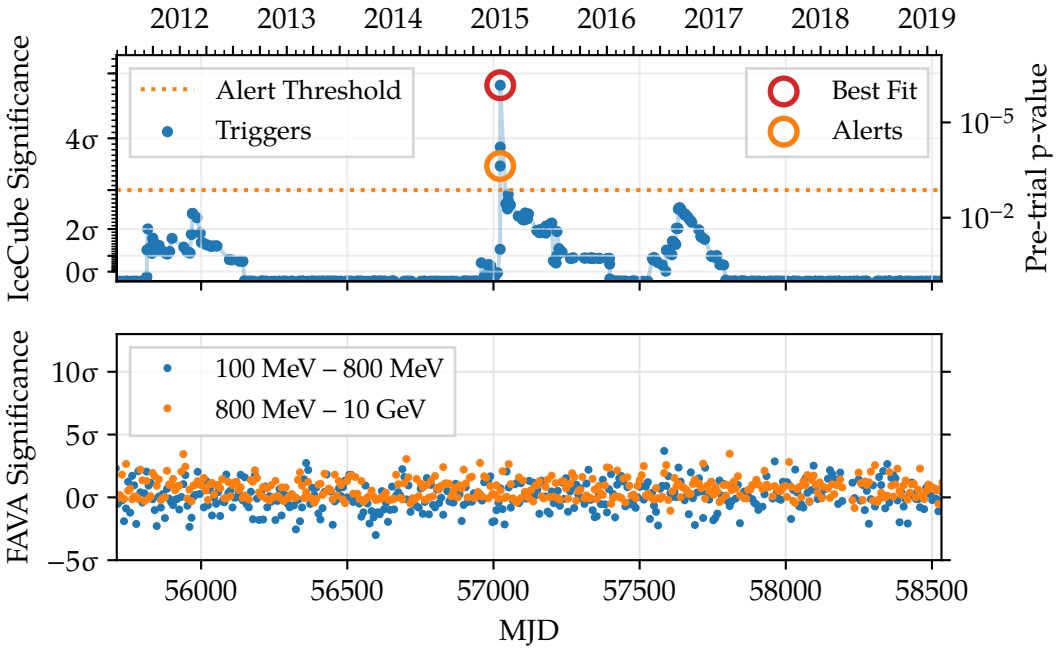

(c) Neutrino curve at the source location, showing the time evolution of the neutrino significance at the source location. The significance level at each neutrino trigger is shown in the upper panel. An alert would have been sent 17 hours prior to the best fit. The lightcurve from the Fermi All-sky Variability Analysis (FAVA) is shown underneath.

Figure 6.16: Results for 1ES 0347-121, which yielded the most-significant flare among all monitored sources. While an overview of the time evolution during the analyzed 7.5-year period is presented in (c), the table (a) and and skymap (b) focus on the most-significant time window.

in a bin around the source. The number of observed photons is binned weekly and compared to the average over the entire operating period of the satellite. This deviation, expressed as a significance assuming Poisson statistics, is shown below the neutrino lightcurve in Fig. 6.16c. No activity is seen around the time of the neutrino flare.

All-sky Flare Search

The online all-sky scanning algorithm has been applied to the archival dataset in the same way as if it was run online. The results are shown in the skymap and table of Fig. 6.17.

Eight alerts would have been generated, half of them in the northern sky and half of them in the southern sky. This alert rate is consistent with the expectations of Fig. 6.13.

As discussed for the source monitoring, more interesting than the time of the alert is what happened afterwards. Therefore, the overall most-significant result, which was found following the alert in 2013, will be discussed.

The properties of the best flare are summarized in Fig. 6.18. An alert would have been issued on Feb. 06, 2013 at 21:14, based on 9 nearby events recorded during 8.6 days. Two additional events were observed during the following 17 hours. In total, the best fit time window comprised 11 events in 9.4 days.

Features of the events, such as localization and energy, as well as the duration of the time window, are encoded in the test statistic Λ. Under the background hypothesis, a value of Λ at least as large as the one observed, is found only once per $2.1 \cdot 10^6$ simulated triggers, corresponding to a pre-trial p-value (Sec. 6.2.1) of $4.7 \cdot 10^{-7}$.

Although this result is unlikely to be found at a random trigger event under the background hypothesis, it becomes more likely when considering the number of triggers and the size of the data sample.

In order to obtain the trial-corrected p-value, the all-sky scan was applied to 100 scrambled representations of the data under the background hypothesis (Sec. 5.3). Each scan was run over 1 year of livetime of the scrambled data, and the p-value of the hottest spot was recorded. In Fig. 6.19, the right-cumulative distribution (the survival function) of the best pre-trial p-value is shown. In 4% of simulated trials, the hottest spot was more significant than the observed result.

Since the simulated period of 1 year is long compared to the largest allowed flare duration of 180 days, the first and last trigger on each simulated event sample are uncorrelated. Therefore, the p-value resulting from Fig. 6.19 is multiplied with 7.5, to account for the number of years which were actually analyzed. Eventually, the post-trial significance level is 32%.

In the lower panel of Fig. 6.18c, the neutrino triggers at this spot are shown in comparison to the gamma-ray lightcurves from the FAVA analysis. Some activity can be seen in the 100–800 MeV band during the year surrounding the alert. Similar activity appears during the year 2018, without correlated activity in neutrinos. Three potential counterparts were found within a search radius of 1 degree. The blazar

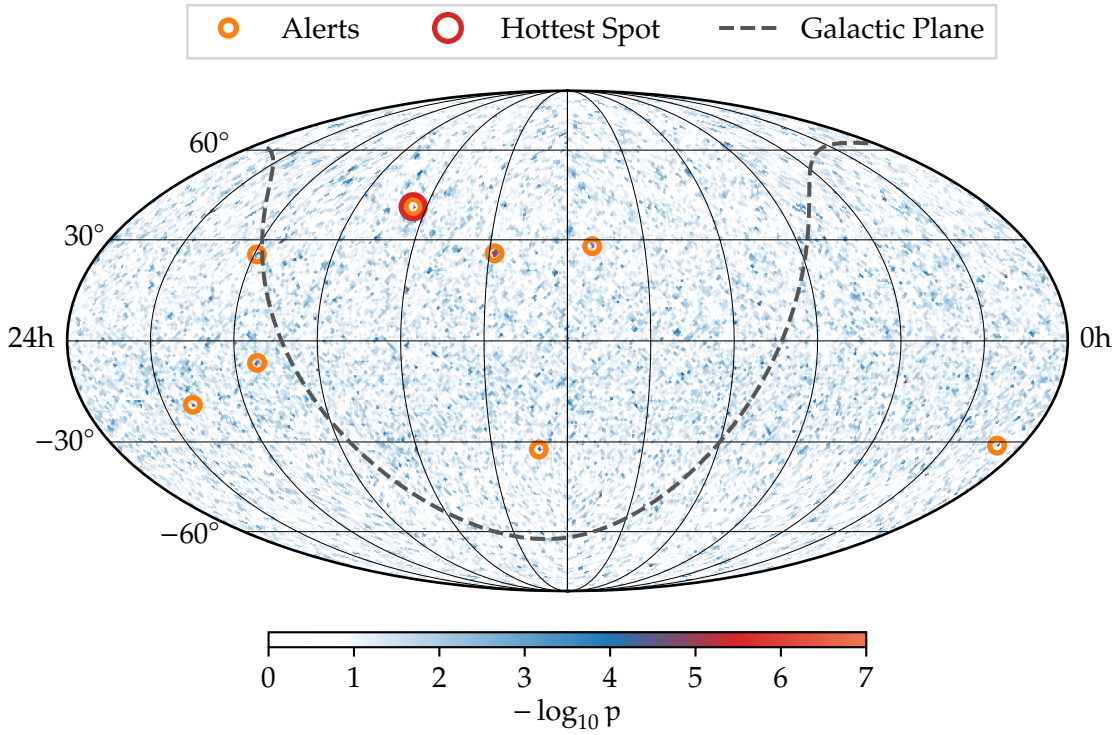

(a) Skymap of the time-dependent all-sky scan. The colored map shows the best local p-value in each pixel. Orange circles indicate the location of archival alerts. The overall most-significant spot is circled in red.

α	δ	Time Window		Λ	n_s	γ	p
170.3°	28.0°	2012-07-27 22:00	2012-10-26 14:23	39.4	12.2	-2.1	$6.5 \cdot 10^{-7}$
245.7°	40.4°	2013-02-06 21:14	2013-02-15 12:47	34.7	9.1	-2.7	$2.9 \cdot 10^{-6}$
292.1°	-6.4°	2014-02-10 06:04	2014-03-23 19:19	33.0	10.7	-2.3	$1.2 \cdot 10^{-5}$
191.4°	-32.4°	2014-05-19 23:20	2014-05-20 10:30	33.3	3.0	-2.0	$1.2 \cdot 10^{-5}$
9.8°	-31.1°	2015-07-13 18:06	2015-07-13 19:04	35.4	3.0	-4.0	$5.1 \cdot 10^{-6}$
299.0°	25.5°	2015-12-16 01:01	2015-12-28 06:24	33.1	12.9	-3.9	$9.8 \cdot 10^{-6}$
319.4°	-18.8°	2017-03-21 09:15	2017-04-10 20:15	34.1	7.6	-3.9	$6.2 \cdot 10^{-6}$
207.9°	25.9°	2017-05-15 13:59	2017-07-17 19:37	36.0	7.6	-1.7	$2.7 \cdot 10^{-6}$

(b) Properties of the alerts found in the archival dataset.

Figure 6.17: Results from all-sky scan of archival data. The figure shows the best-fit result in each pixel, overlaid with the location of the archival alerts. Details on each alert are given in the table below.

Start Date	2013-02-06 21:14
Start MJD	56329.88514
End Date	2013-02-16 05:57
End MJD	56339.24820
Duration	9.4 days
Uptime	8.5 days (91.2 %)
Test Statistic Λ	38.40
Fitted n_s	10.67
Fitted γ	-2.72
Pre-trial p-value	$4.7 \cdot 10^{-7}$ (4.9σ)
Post-trial p-value	$3.2 \cdot 10^{-1}$ (0.5σ)

(a) Results of the best fit.

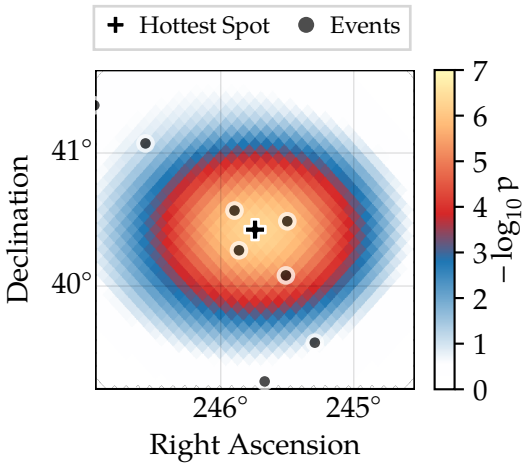

(b) Skymap during the best-fit time window.

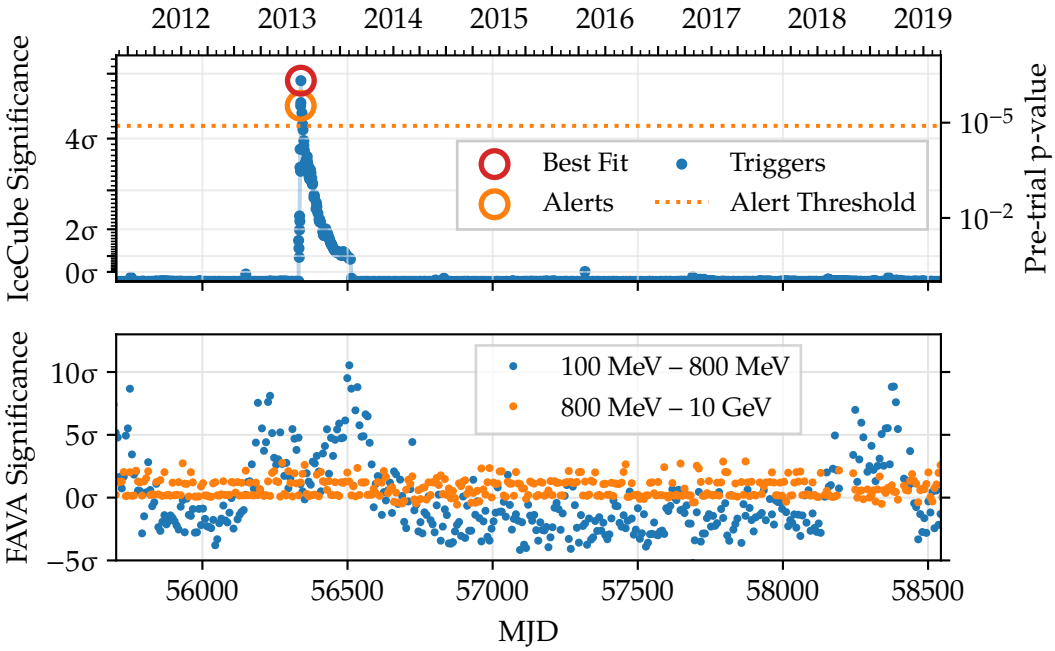

(c) Neutrino curve at the location of the hottest spot, showing the neutrino significance level over time in the upper panel. An alert would have been sent 17 hours prior to the best fit. The lightcurve from the Fermi All-sky Variability Analysis is shown underneath.

Figure 6.18: Properties of the hottest spot found in the all-sky scan over 7.5 years of data. While an overview of the time evolution is presented in the (c), the table (a) and and skymap (b) focus on the most-significant time window.

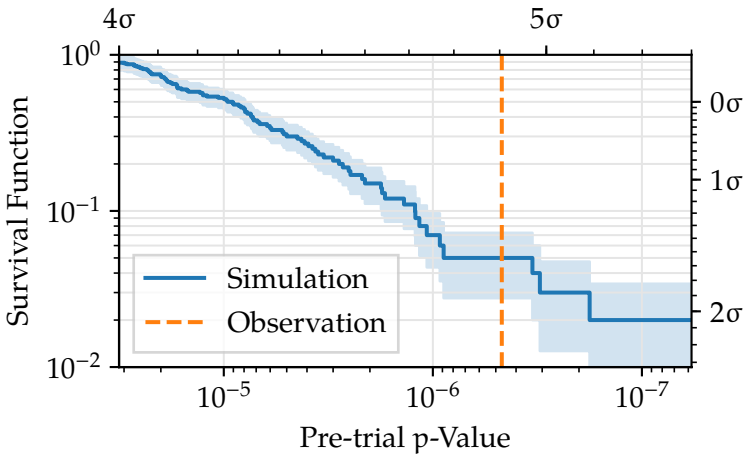

Figure 6.19: Distribution of the post-trial significance for the hottest spot found in the all-sky scan. The vertical axis indicates how often the hottest spot was found above a certain pre-trial p-value, when scanning 1 year of data under the background hypothesis. The vertical line marks the best flare found in the scan of 7.5 years archival data.

"7C 162329.50+410025.00" ($z = 0.030$), the type-II supernova "iPTF 13bld" ($z = 0.0331$) which exploded 100 days after the neutrino flare, and the type-1a supernova "SN 2013ec" ($z = 0.081$) which exploded 4 months before the neutrino flare. It is possible that emission from all three candidates appear in the FAVA lightcurve. FAVA only coarsely accounts for per-event properties, such as the per-event point spread function. A follow-up analysis of the data from Fermi-LAT using a likelihood method is necessary to disentangle the contributions from each candidate and help to provide a clearer picture, but is beyond the scope of this thesis.

6.4 Selection of Most-Energetic Track-Like Events

The online event selection provides a sample of through-going muon tracks, most of which have their origin in cosmic-ray induced air showers. While the previous sections have identified a potential signal by searching for clusters of events, this section aims at identifying single events, which have a high probability of being of astrophysical origin.

Past measurements of the diffuse astrophysical flux provide an estimate for the energy spectrum and normalization of that flux. It was found that the most-energetic muons clearly stand out from the atmospheric background, and allow constraining the parameters of the astrophysical flux. In the following, this knowledge is turned into an online analysis: Assuming the measured parameters of the atmospheric (background) and astrophysical (signal) fluxes, the most energetic, and therefore most signal-like, events will be selected from the online event stream and published immediately. In the absence of a point source discovery, and due to many possible classes of potential sources, the goal is to alert the global multi-messenger community and obtain follow-up observations by telescopes observing different electromagnetic wavelengths.

The IceCube collaboration already operates a similar scheme since 2015, when it launched two public alert streams [96]:

- The High-Energy Starting Events (HESE) use a veto technique in order to reject atmospheric background, and select only events with an interaction vertex inside the detector. Although this greatly improves the purity of events, the event rate suffers from the very small fiducial interaction volume. In addition, the events typically exhibit a large shower from the hadronic cascade at the interaction vertex, and the track of a muon leaving the detector. As the online reconstructions operate under the hypothesis of pure muons, the angular resolution of those events is worse than that of actual through-going tracks.

  The expected event rate used to be 4/year, but was reduced to 1/year in 2019 in an effort to reduce the number of falsely identified and/or poorly reconstructed events [156].

- The Extreme High-Energy (EHE) event selection features a relatively simple cut on the quality of the directional reconstruction and the total observed charge.

  By selecting only the brightest events, it is effectively selecting the most-energetic ones. The resulting rate of alerts is 6/year.

In both cases, the fraction of signal events among the alerts is expected to be 50%.

In the following, the online event selection developed in Sec. 4.4 will be used to select additional, very energetic events. By aiming for through-going muon tracks it exploits a much larger fiducial volume than the selection of starting events. In addition, the use of a BDT-based event selection provides a more efficient event selection, as judges the events by looking at more than the one parameter used by the

EHE alerts. Furthermore, the use of a more accurate muon energy proxy will increase the efficiency and allow to set a lower threshold for the alerts.

In order to quantify the fraction of signal events contained in a given sub-sample of events, a variable called "signalness" is defined as follows:

$$\text{Signalness}(\hat{x}) = \frac{N_S(x > \hat{x})}{N_B(x > \hat{x}) + N_S(x > \hat{x})}\,, \tag{6.1}$$

where $\hat{x}$ is an observable of a given event; and N_S and N_B denote the expected number of events with a value of x at least as extreme as $\hat{x}$ under the signal and background hypotheses, respectively. In short, it provides a measure for the fraction of signal events above a given choice of cut.

Eventually, two classes of alerts are desired:

- The "golden" selection: Events from a subsample with a signalness of at least 50% will be made public immediately and recommended for automated follow-up observations.
- The "bronze" selection[2]: Events from a subsample with a signalness of at least 30% will also be published automatically, but are recommended for discretionary follow-up observations, as observation time permits.

As before,x the identification of those events distinguishes the northern sky ($\theta \geq 82°$) and the southern sky ($\theta < 82°$) in order to account for the different classes of backgrounds.

Northern Sky

At the final level of the online GFU event selection, the events from the northern sky largely comprise through-going muon tracks. Due to the softer energy spectrum of atmospheric neutrinos ($\sim E^{-3.7}$) compared to the diffuse astrophysical flux ($\sim E^{-2.19}$), the chance of an event being of astrophysical origin increase with energy. Hence, a straight energy cut should suffice to identify the most signal-like events.

The neutrino interactions are likely to take place outside of the detector, then the resulting muon will traverse the detector and decay outside of it. From the observed section of the track, only the muon energy at the detector can be reconstructed as described in Sec. 3.4.3, and provides a lower bound on the neutrino energy. For an efficient selection, the chosen energy estimator should provide the best resolution. As shown in Fig. 3.8, in the region above 100 TeV the TruncatedEnergy method yields the best online estimate.

Relating the true muon energy at the detector to the energy estimate, as shown in Fig. 6.20, it is also evident that the absolute energy is well calibrated. However, the event sample is contaminated by a small fraction of events with a large estimated energy, but small true energy (shown with an orange box). The origins of these events is twofold:

[2]The "silver" branding is reserved for future real-time alerts from shower-like events.

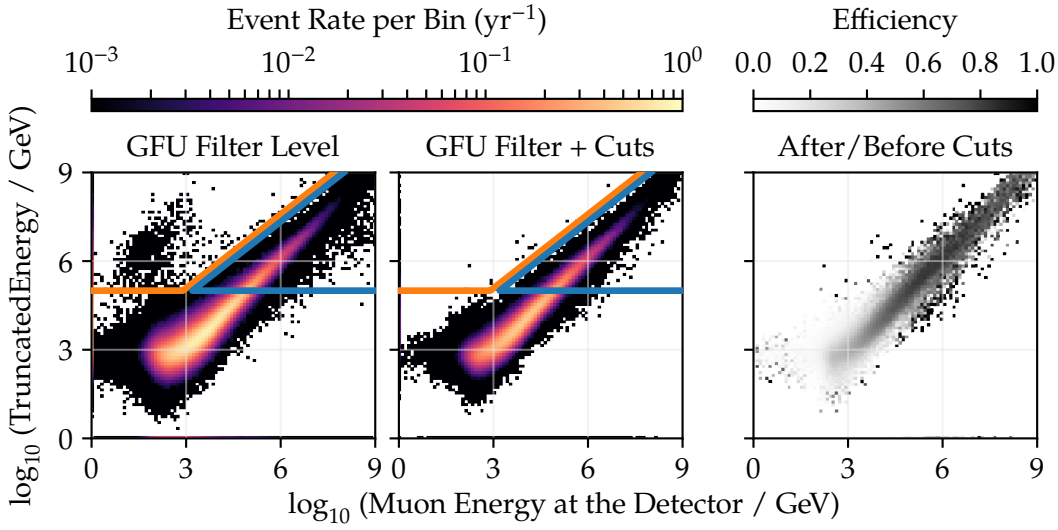

Figure 6.20: Relation between the muon energy proxy (TruncatedEnergy) and the true muon energy upon entering the detector for up-going events passing the GFU filter. While the energy resolution for most events is very reasonable (blue box), a poor energy estimate is assigned to a small fraction of events (orange box). Cuts on the BDT score and the track length remove the events with poor energy estimates, while efficiently retaining the well-reconstructed events.

- The energy estimator relies on the hypothesis of muon tracks. Therefore, a reliable directional reconstruction is crucial for a reliable energy estimate. Mis-identified, shower-like events are assigned very high energy estimates and would survive an energy cut, causing undesirable, automatic alerts.

  Since the BDT was trained to select well-reconstructed events, a tighter cut on the BDT score (above 0.1) rejects events with worse directional and energy reconstruction.

- Muon tracks which pass close to the detector can still be reasonably well reconstructed in terms of their direction, even when the reconstructed track does not intersect with the detector. The energy reconstruction however was found to be very unreliable for this class of events, and the energy was generally overestimated.

  Requiring the reconstructed track to intersect the detector rejects these events.

The effect of the two cuts is visible when comparing the two panels of Fig. 6.20. The amount of events above 100 TeV with a mis-reconstructed muon energy (orange box) has been reduced to 0.03%.

With the choice of an energy estimator, and the precuts, the final alert threshold

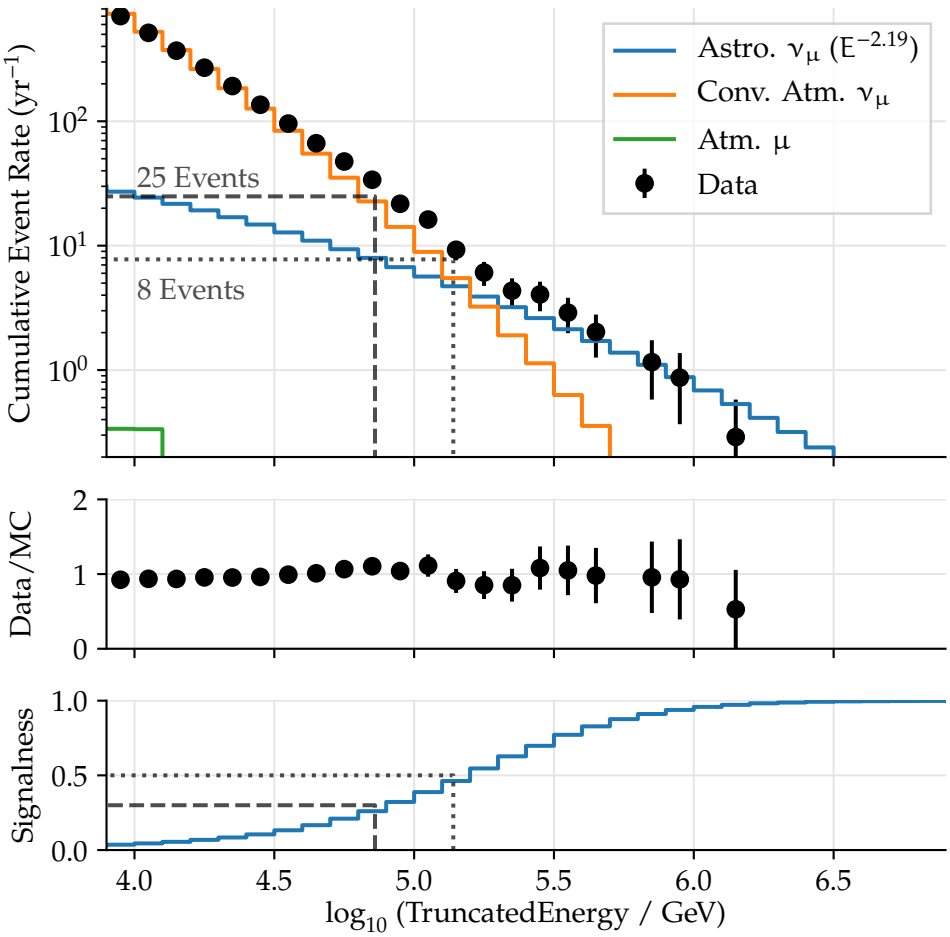

Figure 6.21: Distribution of the energy proxy in the northern sky. The left cumulative distribution shows the yearly rate of events, which would survive an energy cut. The two proposed cuts yield 25 and 8 events, with a signalness of 30% and 50%, respectively.

can be set, as shown in Fig. 6.21. The expected atmospheric contribution follows the conventional atmospheric flux model [13], where a simple power-law is assumed for the astrophysical signal. The parameters of each model were set according to the recent fit of the diffuse astrophysical flux [15]. At around 100 TeV, the atmospheric and astrophysical contributions cross, defining a signal- and a background-dominated region.

The signalness is also shown as a function of declination in Fig. 6.22. Only a slight dependency on the declination is observed towards the horizon, hence the cut is simply kept one dimensional and two possible energy cuts are determined:

- Events with a muon energy proxy above 74 TeV: For this class of events, 24.2 events are expected per year with a signal content of 30%.

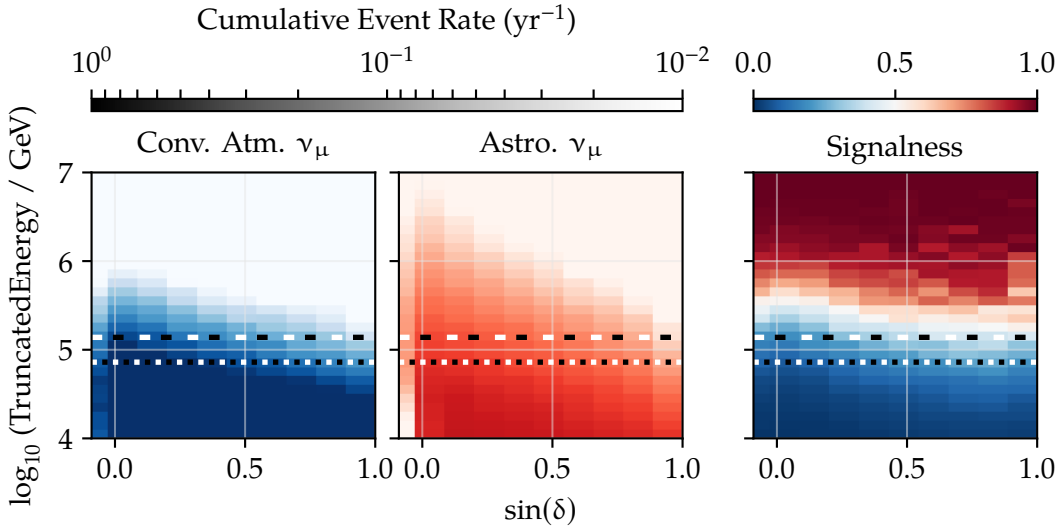

Figure 6.22: Cumulative distribution of the energy proxy for the atmospheric background (left) and the astrophysical signal (center) as a function of declination. The resulting signalness is shown in the right panel. Two proposed cuts are drawn with horizontal lines, yielding a signalness of 30% (dotted) and 50% (dashed).

- Events with a muon energy proxy above 139 TeV. For this class of events, 7.7 events are expected per year with a signal content of 50%.

A detailed breakdown in terms of the expected number of signal and background events is given later in Tab. 6.1. The surviving events are found to be well resolved, with a median angular resolution of 0.2°. 90% of events are reconstructed within 0.7° of the true direction. This resolution is comparable to the current EHE alerts.

The effective area of the event selection is depicted in Fig. 6.23 for both proposed selections. In comparison to the current online EHE alert selection, the effective area is more than doubled for neutrino energies between 100 TeV and 1 PeV.

The improvement can be explained by the energy resolution of the TruncatedEnergy estimator used in this work. The EHE alert selection relies on a cut on the observed charge in the detector, which also provides a poor proxy for the muon energy: It does not take into account the local properties of the ice, with increased absorption in the upper half of the detector and very clear ice in the lower half. It also does not take into account the geometry of the event, such as the relation between the deposited energy and the length of the track observed in the detector. Therefore, the resolution of this estimator is worse than that of TruncatedEnergy and a tight cut is required suppress background at the cost of signal efficiency. The better muon energy proxy in this work allows relaxing the cut while keeping the same level of background, yielding a final alert rate that is about twice as high as that of the online EHE alert selection.

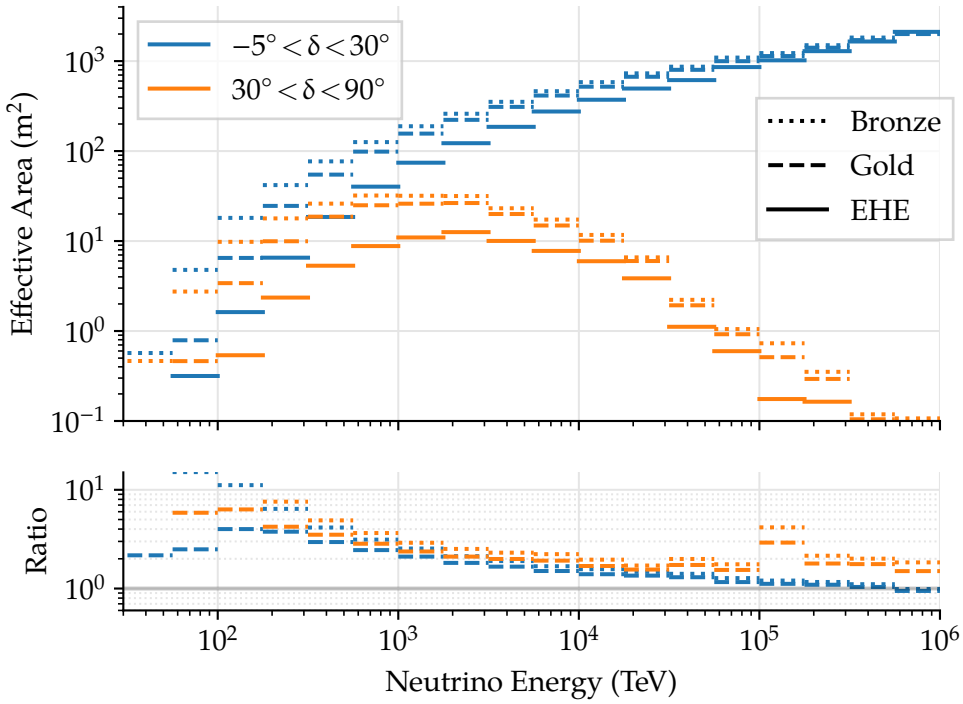

Figure 6.23: Effective area for high-energy muon alerts in the northern sky. Colors distinguish different declination bands. The bronze and golden selections refer to a signalness of 30% and 50%, respectively. For comparison, the ratio between this work and the current EHE online alert selection is illustrated in the lower panel.

Investigation of the events found in both selections confirmed that the EHE alert selection chooses events with a large track length in the bottom half of the detector.

Southern sky

In this part of the sky the background comprises largely muons and muon bundles from cosmic-ray induced air showers. The BDT is already trained to to distinguish those from the single, high energetic signal events and allows to select events which are well-reconstructed.

Still, the atmospheric background is much larger than a potential atmospheric signal. Compared to the northern sky, two main differences arise here:

- The energy estimators work under the hypothesis of a single muon. Multiple low-energetic muons and muon bundles are interpreted by the estimator as a single high-energetic event.

  Algorithms like TruncatedEnergy and MuEX aim to estimate the energy from the constant Cherenkov emission and ignore the stochastic energy losses. However,

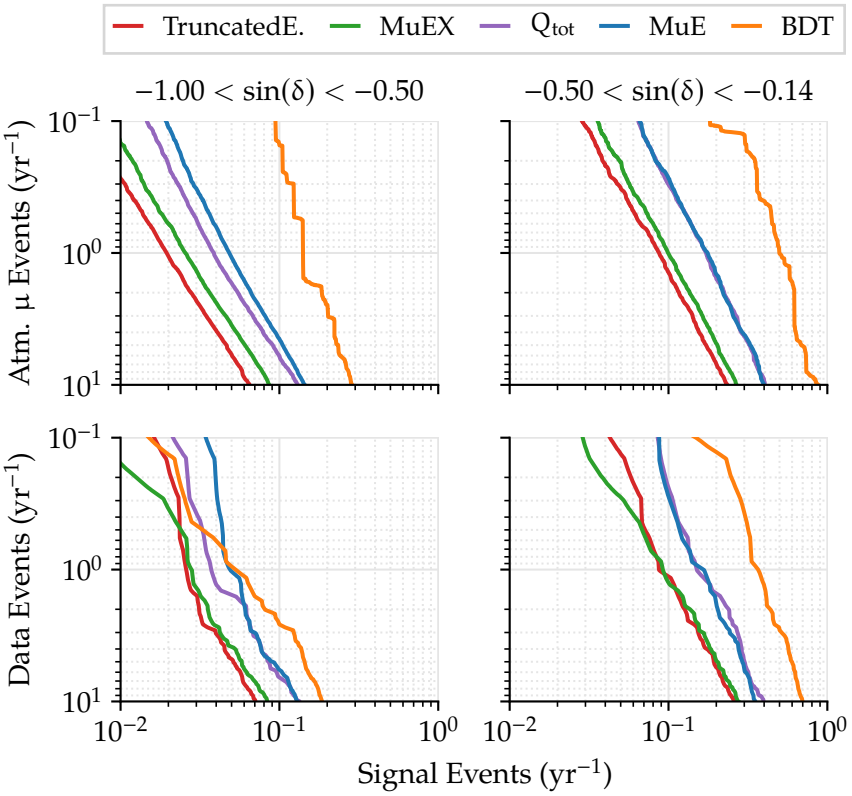

Figure 6.24: Comparison of cut variables in the southern sky. Cuts on different energy estimators, as well as the BDT score, are scanned and the surviving rate of events is shown. Signal efficiency is shown on the horizontal axis. Background rejection is shown on the vertical axis, estimated from simulation (upper panels), and with respect to data (lower panels).

the stochastic losses are a distinguishing feature of truly high-energetic muons. Therefore these advanced estimators, that work well in the northern sky, are not the best discriminator here.

- A measurement of the diffuse astrophysical flux, along with a parametrization of the atmospheric neutrino flux, has been performed using through-going muons in the northern sky.

  A comparable measurement is not yet available for the southern sky. Thus, agreement between data and simulation is worse, hindering an accurate assessment of the signalness of an event sample.

Several energy proxy variables are available for further cuts. In order to determine, which one provides the most efficient separation of signal and background, they were compared with respect to their ability to reduce the atmospheric background (as well as the total data rate), while retaining as many high energy signal events as possible.

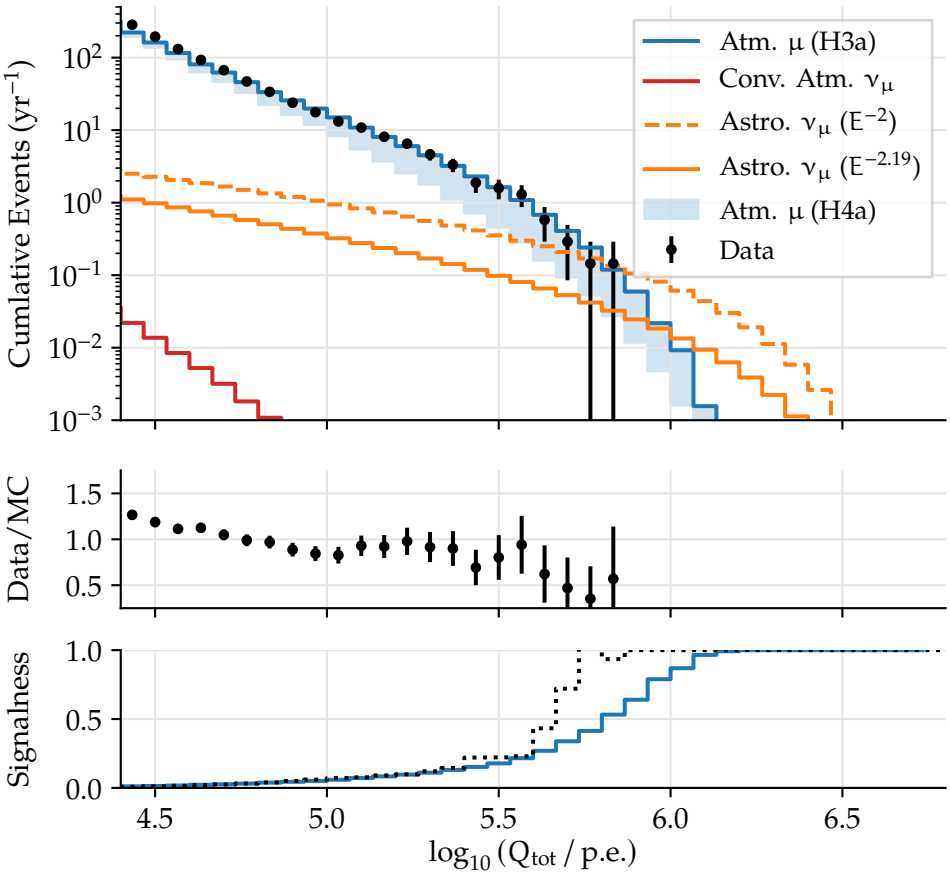

Figure 6.25: Left-cumulative distribution showing the yearly rate of events. Astrophysical signal is estimated for two different spectra. Atmospheric background is shown for two cosmic-ray composition models, with the shaded band indicating the difference between them.

A scan of possible cut values is depicted in Fig. 6.24, where the background rejection is shown versus signal efficiency when scanning through the possible range of cuts. While the BDT score appears to be the most efficient one to cut on, the total deposited charge (Q_{tot}) provides better agreement between data and simulation and is chosen for the selection. Note, that it is used only to select the most-energetic events, not for the eventual determination of the muon energy. TruncatedEnergy provides the best energy resolution, under the assumption that the event comprises a single muon.

The distribution of the the energy proxy is shown in Fig. 6.25. A uniform treatment of the detector is achieved by excluding the DeepCore DOMs from the calculation of the total charge Q_{tot}. Uncertainties in the cosmic ray flux modelling, in particular in the composition cause a discrepancy in the agreement between data and simulation. Using data to estimate the background is hindered by the very low event counts

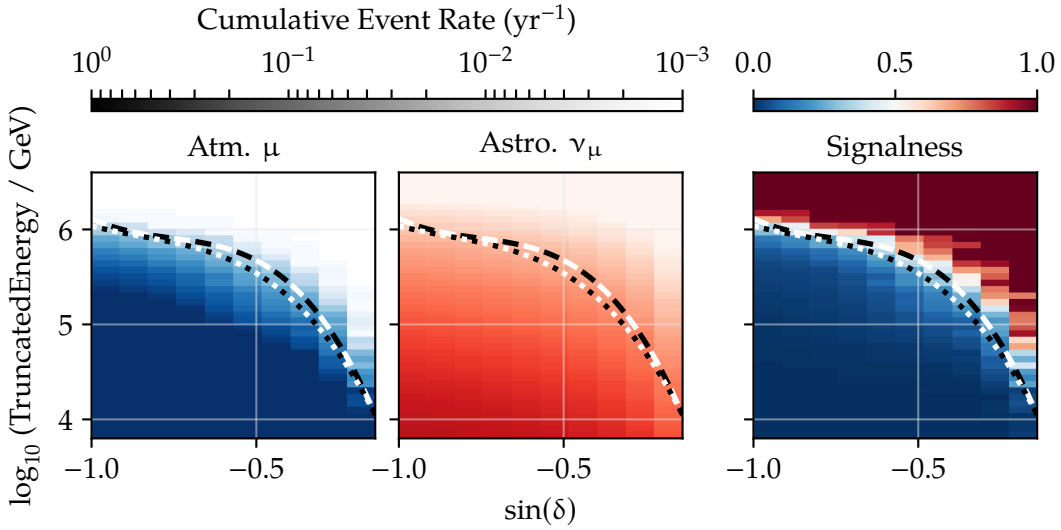

Figure 6.26: Cumulative distribution of the cut variable as a function of declination for the atmospheric background (left) and the astrophysical signal (center). The resulting signalness is shown in the right panel. Two proposed cuts are drawn, yielding a signalness of 30% (dotted) and 50% (dashed).

at these energies. Therefore, the following approach is chosen for a conservative definition of the cut:

- The background simulation is weighted to a model which assumes a mixed extra-galactic component with an all iron composition at the highest energies (H3a, [132]).

  For comparison, a model with an all proton composition at the highest energies, predicting fewer background events, is also shown (H4a, [132]).

- The signal is estimated from the a power-law with a spectral index of -2.19, which was measured in the northern sky [15].

As the event rates are depending on the declination, a two-dimensional cut is defined in six declination bins, chosen for an equal number of events in each bin. The declination-dependent distribution, as well as the signalness, are shown in Fig. 6.26. As was done for the northern sky, two cuts are proposed and parametrized as a polynomial. The bronze cut achieves a signalness of 30% and is given by

$$\log_{10} Q_{\text{tot}} \geq -2.23928 \sin^3\delta - 7.34434 \sin^2\delta - 7.94114 \sin\delta + 3.12003 \,, \tag{6.2}$$

while the golden cut yields a signalness of 50% and is given by

$$\log_{10} Q_{\text{tot}} \geq -4.06580 \sin^3\delta - 10.60906 \sin^2\delta - 9.61048 \sin\delta + 3.01219 \,. \tag{6.3}$$

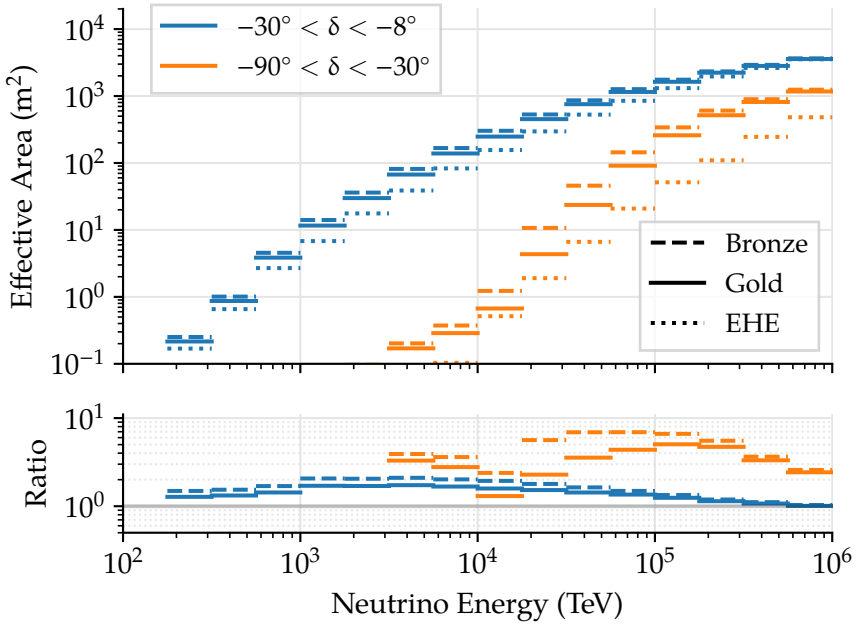

Figure 6.27: Effective area for high-energy muon alerts in the northern sky. Colors distinguish different declination bands. Solid (dashed) lines correspond to the gold (bronze) cuts proposed in this work, which achieve a signalness of 50% (30%). The dotted line shows the effective area of the EHE alerts. The ratio between this work and the EHE alerts is illustrated in the lower panel.

The surviving events have a median angular error between 0.2° above a declination of -30°, and 0.3° in the case of more vertical events. A detailed breakdown is given in Tab. 6.2. In comparison to the current EHE online alerts, the selection of downgoing events presented in this work yields events with much smaller directional reconstruction errors.

In addition to the resolution, the neutrino effective area is improved as well, as shown in Fig. 6.27. At all declinations, the effective area is larger than that of the current EHE online alerts. Although both selections are selecting events based on their total charge, the previous BDT-based selection stage of the GFU filter adds an additional level of background rejection and eventually allows a more efficient cut.

Expected Alert Rate and Overlap with other Channels

Using the archival sample of GFU-filtered events from May 2011 until March 2019 allows estimating the average yearly alert rate. It is shown in Table 6.1 and compared to the expectations from simulation, which agree well with the observation.

In addition to the average alert rate, the archival data sample is also suitable for checking the overlap with the other selections. Three event selections are considered

	Signalness	Data	$E^{-2.19}$	E^{-2}	Atm. ν_μ	Atm. μ
Northern Sky	30%	24.2	7.2	10.1	16.8	0.0
	50%	7.7	4.4	6.8	4.4	0.0
Southern Sky	30%	1.4	0.3	0.9	0.03	0.9
	50%	0.2	0.3	0.7	0.02	0.4

Table 6.1: Expected alert rates from the selection of high-energy muons. All numbers are given in events per year. The expected signal is shown for different spectral indices.

for comparison: the online alerts from High-Energy Starting Events (HESE), the Extreme High Energy (EHE) events, and the most-energetic events from the diffuse flux measurement [15, 39].

- Charged-current muon-neutrino interactions from the HESE sample are expected to only partially overlap with this work.

  In the northern sky, the effective area for starting events is much smaller than for the through-going events of this work. In the southern sky, the HESE selection targets lower energetic events (i.e. starting around 60 TeV), where it can achieve good purity through the veto method.

  Events can only trigger both the HESE selection and the selection of this work with energies above 100 TeV and an interaction vertex inside the detector, which leaves very little phase space for overlap.

  Only 9 out of 22 HESE candidates pass the GFU online event selection. Out of those 9 events, only one event passes both sets of alert cuts. The remaining events are in fact found either below the energy threshold of the online filter in general, or below the alert threshold.

  In conclusion, the two alert streams are fairly disjunct.

- The EHE alert selection is expected to be a subset of this work.

  The energy threshold of this work is lower and the effective area is larger. Therefore, well-reconstructed, very energetic events should appear in both

		This Work		EHE Alerts	
		50%	90%	50%	90%
Northern Sky	$-5^\circ < \delta < 90^\circ$	0.2°	0.7°	0.2°	0.7°
Southern Sky	$-30^\circ < \delta < -5^\circ$	0.2°	0.7°	0.4°	1.5°
	$-90^\circ < \delta < -30^\circ$	0.3°	2.6°	1.0°	3.5°

Table 6.2: Angular error of the selected high-energy muons. Assuming a signal flux $\propto E^{-2.19}$, the reconstructed direction is at most this far from the true direction for 50% (90%) of events.

selections.

In fact, all 23 EHE alert events appear in the GFU event sample (including IC-170922A which is discussed in Sec. 6.6). Of those, 10 events would pass the golden cuts. An additional 9 events would pass the bronze cuts. The energy estimation used in this work assigns a lower energy to those events than the estimate used for the EHE alerts, hence they are assigned to the class of lower signalness.

Finally, four events in the southern sky do not pass the proposed set of cuts. All of them are corner-clipping events, with low energy estimates and BDT scores close to the selection threshold. They are not outstanding events, with little evidence for being of astrophysical origin.

- Following the measurement of the diffuse flux, the properties of events from that selection with energy estimates exceeding 200 TeV have already been published [15, 39].

  Since this work follows the offline diffuse event selection, a large overlap is also expected here.

  Indeed, 19 out of 24 inspected events pass the bronze alert cut. Five events are rejected by the pre-cuts: In four cases, the track is reconstructed outside of the detector, and in one case, the event is a corner-clipping event with a topology similar to a cascade and hence is assigned a low BDT score.

The overlap between the different selections is visualized in Fig. 6.28, where colored circles indicate the events from the golden and bronze selections. Black dots denote those events which were already part of the HESE or EHE alert selections, or among the most-energetic events in the event selection used for the diffuse flux measurement.

The complete list of events, which would have triggered alerts if the system had been running in the past, can be found in Appendix C. That table also indicates for each event whether it was previously found in another selection.

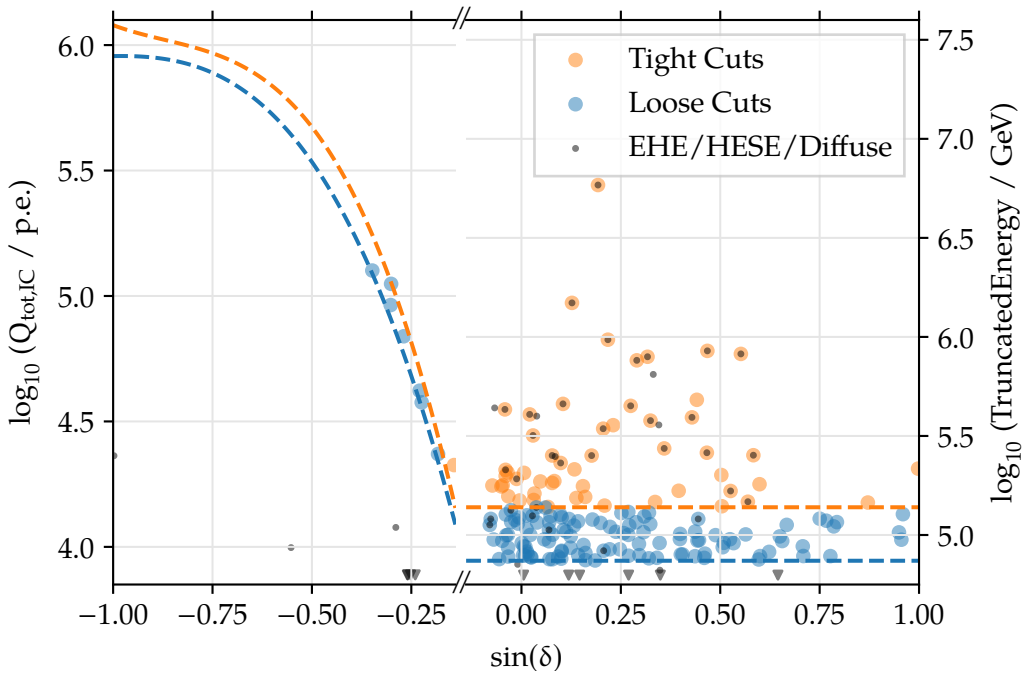

Figure 6.28: Events from different high-energy event selections, observed between May 2011 and May 2018. Events in the southern sky (left) are drawn with respect to their total charge, events in the northern sky (right) are drawn with respect to the muon energy proxy.

6.5 Offline Analysis of Flares from 1ES 1959+650

The content of this chapter has previously been published in the proceedings of the 35th International Cosmic Ray Conference (ICRC2017) [157]. The author is the corresponding author for the article and carried out the two time-dependent analyses.

The blazar 1ES 1959+650 is a high-frequency peaked BL Lac object, located at $\alpha = 299.943°$, $\delta = 65.145°$, at a redshift of $z = 0.047$ [158]. The jet of that active galactic nucleus points towards earth. Its spectral energy distribution exhibits two broad humps, one in the UV–X-ray regime and and one in the GeV–TeV energy range, and no emission lines.

It has been established as an emitter of very high energy (VHE) gamma-rays [159, 160], whose gamma-ray emission was found to be variable. The most notable flaring episode was recorded around June 4, 2002: During a multi-wavelength observation campaign a gamma-ray flare was observed by the Whipple telescope [159, 161], without an accompanying increase in X-ray emission [162] Several emission models were proposed to describe this "orphan" gamma ray flare. A simple synchrotron self-compton model was found to under-predict the observed radio and optical fluxes [162]. Hadronic models, such as the "mirror model", were developed as an alternative and predict a correlated neutrino flux for this event [163].

A search for neutrino events correlated with the flare was performed on the data from the AMANDA neutrino telescope [164, 165]. In a time window of 66 days around the time of the flare, three neutrino events were found from the direction of

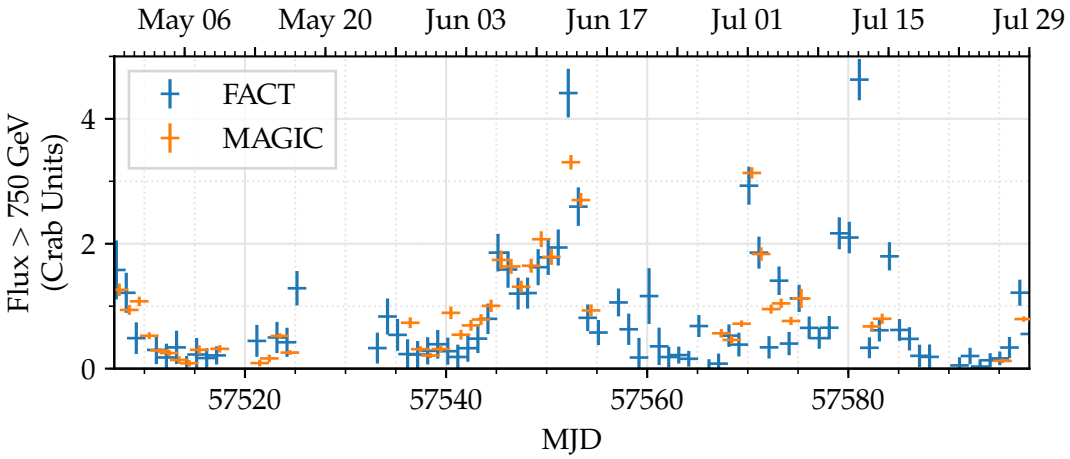

Figure 6.29: Integrated gamma-ray flux above 750 GeV from 1ES 1959+650 as observed by the FACT and MAGIC telescopes between May and July 2016. The error bars account for statistical and systematical uncertainties. Observations from the same night are plotted slightly offset to keep overlapping data points discernible. (Published in [157])

the blazar. One of those events was observed 7 hours earlier than the gamma-ray telescope observation yielding the highest observed flux of the orphan flare. Yet, no reliable estimate of the significance could be determined as the hypothesis was not defined a-priori.

Following the flaring episode in 2002, 1ES1959+650 has remained in a quiescent state in gamma rays [166, 167]. In terms of neutrino observations, of all source locations that were examined in the time-integrated analysis of 7 years of IceCube data, 1ES 1959+650 appeared as the most-significant one. With a pre-trial p-value of 1.8%, and a p-value of 54% after accounting for the number of tested sources, no significant deviation from the background expectation was found between 2007 and 2014 [44].

Now, increased gamma ray activity has been observed between April and July 2016. with gamma-ray flux levels of the order of the 2002 flare [168]. This new flaring episode provided another, rare opportunity to investigate a direct connection between the neutrino and VHE gamma ray emission in 1ES 1959+650, which will be investigated in the following.

Very High Energy Gamma-ray Observations

In an effort to obtain a most complete lightcurve observations from the FACT and MAGIC telescopes will be combined for this analysis.

The First G-APD Cherenkov Telescope (FACT), is located next to the two MAGIC telescopes at 2200 m a.s.l. on the Canary Island of La Palma. The name derives from its novel camera design which is based on a particular type of silicon photomultiplier, the Geiger-mode Avalanche Photo Diode (G-APD) [169]. Silicon photomultipliers do not degrade when exposed to bright light, making them a suitable tool for maximizing the telescope's duty cycle and minimizing the moon-time related gaps in the gamma-ray light curve. Thus, FACT observations cover a large fraction of the flaring period [170], well complementing the observations from the MAGIC telescopes.

The MAGIC telescopes are a system of two 17 m Cherenkov telescopes, which are also located on La Palma. Their large, combined mirror area allows for observations of gamma-rays starting at energies of 50 GeV. In addition, rejection of hadronic background benefits from the stereoscopic observations.

1ES 1959+650 has been observed by both experiments between April and July, 2016, in moon-less nights and during moon time, and with zenith angles ranging from 35 to 52 degrees. The interesting flaring episode, which is analyzed here, took place between April 29 and July 26, 2016, spanning 89 days.

Both collaborations analyzed their observations and evaluated the integrated gamma-ray flux above 750 GeV. In both cases, similar systematic errors were considered, such as zenith dependent effects, ambient light conditions, energy spectrum dependent systematics and atmospheric conditions, such as transmissivity and the Calima. Eventually, this facilitates the combination of the lightcurves as in Fig. 6.29. The flaring behavior is well visible, with the most extreme flares reaching more than four times the flux level of the quiescent state. On those nights, during which both

telescopes observed the source the results agree well within their uncertainties. While MAGIC results have smaller uncertainties, FACT provides additional coverage in time.

Analysis Outline

Concerning neutrino data, three analyses are performed in the following:

- A time-integrated analysis of the entire time window. This analysis is most agnostic with respect to the time structure of the potential signal. Aside from the fixed beginning and end of the time window, it is independent of the gamma-ray data.

- A time-dependent analysis, utilizing the time-clustering method presented in Sec. 5.2. A potential burst of neutrinos is assumed to be clustered in time, superimposed on a uniform distribution of background events. Also this method is independent of the gamma-ray data.

- A time-dependent search for a neutrino signal correlated with the gamma-ray flares. Here, neutrino events are weighted using the gamma-ray lightcurve, testing a direct correlation between both fluxes.

Several neutrino event samples were available. The online event selection running at the time was the predecessor of the one developed in Ch. 4.4 of this work. As the entire analysis was carried out after the gamma-ray flare was over, time was not a pressing concern and offline event selections were available as well: the selection developed for the 7-year point-source search [44], and the selection developed for the measurement of the diffuse astrophysical flux [122]. All selections were compared in terms of their point source discovery potential at the declination of the source.

Best sensitivity and discovery potential was achieved using the diffuse selection which was chosen for the final analysis. Its discovery potential was between 10% and 20% better (depending on the flare duration) compared to point source selection, and between 20% and 40% better compared to the online selection at that time. If the analysis was carried out today, the online selection could provide a discovery potential comparable to that of offline event selections, as compared in Fig. 5.12. Additional data processing would not be necessary, shortening the time to be spent for the analysis.

Time-Integrated Analysis

This analysis is very similar to the time-integrated approach described in Sec. 5. Since the total analyzed time period is rather short, the average background event rate $\langle n_b \rangle$ can be estimated from off-time data (i.e. the same period in the previous year) and

fixed in the likelihood [131]. Thus, the test statistic Λ of Eq. 5.4 is modified to:

$$\Lambda(n_s, \gamma) = -n_s + \sum_i^{\text{events}} \log\left[\frac{n_s}{\langle n_b \rangle} \frac{\mathcal{S}_i(\gamma)}{\mathcal{B}_i}\right]. \tag{6.4}$$

The number of signal-like events n_s and the spectral index γ are free parameters in the fit, and the signal and background probability densities, $\mathcal{S}_i$ and $\mathcal{B}_i$, remain as defined in Eq. 5.1 and 5.2.

Then, the analysis proceeds as explained in Sec. 5.

Time-Dependent Analysis

For the time-dependent analysis, the time-clustering method from Sec. 5.2 is used.

A free parameter in offline analyses is the choice of the largest allowed time window T_{max}. For this particular scenario, i.e. this event selection, and the relatively short analysis period of 89 days, the discovery potential of the time-clustering search is worse than that of the time-integrated search for flares longer than 3 weeks. Therefore, the largest allowed time window of the time-clustering search was limited to 21 days.

Correlation with Gamma-Ray Lightcurve

While the two previous analyses focused solely on neutrinos, this analysis tests for a direct correlation between the gamma ray and neutrino emission.

It follows the time-integrated method presented in Sec. 5, but extends the per-event signal and background PDFs, Eqn. 5.1 and 5.2, with an additional PDF in the time domain, which is constructed from the gamma-ray observations. For this purpose, data from both experiments are combined.

After the flaring state became evident, both telescopes observed 1ES 1959+650 on a regular basis. For 45 out of the 89 nights considered here, MAGIC provides precise measurements of the flux in VHE gamma rays [168]. Poor visibility conditions or strong moonlight cause gaps in between the observations. FACT, however, is better suited to operate in conditions of ambient light due to its technical design, and can thus provide measurements for 80 nights [170], adding 36 (MAGIC has one night not included in the FACT data) nights of coverage next to the MAGIC observations. In addition, the FACT telescope is dedicated to monitoring a small number of selected TeV blazars, and therefore fewer science targets compete for observation time [171].

In order to fully utilize their respective strengths and obtain the largest possible coverage of the source behavior over time, the data from both experiments is combined as follows: If on a given night the source has only been observed by one instrument, that measurement is used. On nights where both instruments did provide data, the measured fluxes have been averaged, weighted by their respective errors. As the observations are only possible for a few hours at night-time, the lightcurve has been binned in one day intervals lasting from noon on one day to noon on the next day. This approach strives to balance a conservative extrapolation of the gamma ray flux

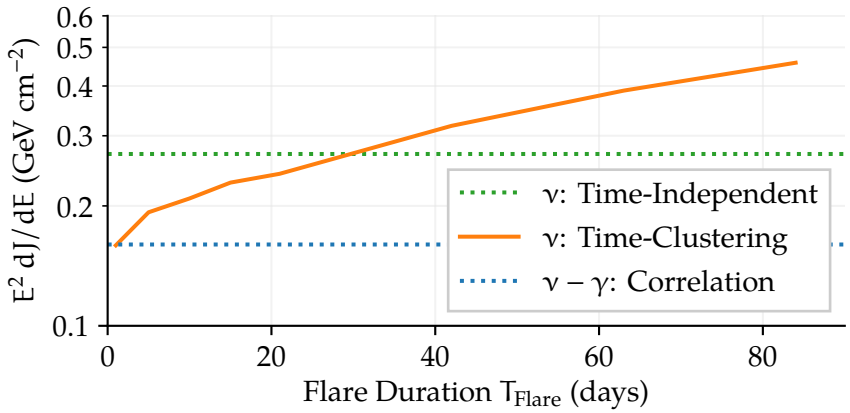

Figure 6.30: Discovery potential of the three analyses: The time-integrated test is independent of the arrival times of the neutrinos. The sensitivity of the time-clustering method depends on the length of the most-significant flare, which is shown on the horizontal axis. The time-correlation test assumes a neutrino signal following the gamma ray lightcurve, yet it is shown in this plot for comparison. (Published in [157])

with a possible time delay between the arrival of neutrinos and gamma rays. In case that no observations were taken on a given night, the surrounding bin is excluded from the analysis. On such nights, no statements on the activity of the source can be made in good conscience, as the observed strong flaring typically varies on the timescale of a day. In any case, both a significant flare of neutrinos on an excluded day, as well as a large time delay between the emission of gamma rays and multiple neutrinos would be covered by the two previous analyses, which rely only on the neutrino data.

Figure 6.30 compares the discovery potential for the three analyses. In general, if single flares in neutrinos with a duration of less than 30 days could be resolved, the time-clustering analysis would be the most sensitive one, whereas for longer time-scales the time-integrated test is more sensitive. The correlation test is very sensitive, if the neutrinos were to follow the gamma ray light curve. Thus, the analyses are complementary as they test different time scales and emission scenarios.

Results

The analyses have been applied to the 89-day time window from April 29th to July 26th, 2016. Figure 6.31 shows the location of events, which influence the likelihood analyses due to their proximity to the source. Three events are spatially compatible with the location of 1ES 1959+650 within their respective 1σ error circles, yet they are poorly localized with an uncertainty larger than two degrees.

As the majority of events is well compatible with the background expectation, a test statistic of zero was obtained from the time-integrated test at the position of the

source. A scan of the test statistic in the vicinity of the source is shown in the right panel of Fig. 6.31. No spatial clustering is visible near the source.

Figure 6.32 shows the arrival times and the event weights over time. The time-clustering test is bound to decide on one most signal-like cluster. It selected a time window of 3.3 hours around the most-energetic event in the sample. There are two events in this time window and the fit results yield a signal strength of $n_s = 2$ and a spectral index of $\gamma = -1.4$. Such an outcome is expected from background with a p-value of 37%. For this particular day, no gamma-ray observations are available and the state of the source is not known. Observations from the Fermi-LAT telescope do not show an increased gamma-ray flux on that day. However, the high-frequency

Best-fit cluster in 2016	
Start Date	May, 18 01:07:57
End Date	May, 18 04:27:56
Λ	5.09
n_s	1.96
γ	-1.40
p	37%

(a) Properties of the best-fit cluster.

Analysis	$E^2 dJ/dE$ (GeV cm^{-2})
May, 2008 – May, 2015	
Time-integrated [44]	$2.27 \cdot 10^{-1}$
May – July, 2016	
Time-integrated	$1.01 \cdot 10^{-1}$
Time-dependent	$1.06 \cdot 10^{-1}$
$\nu - \gamma$ correlation	$1.00 \cdot 10^{-1}$

(b) Upper limits at 90% confidence level.

Table 6.3: Analysis results. Details on the best-fit cluster from the time-clustering analysis are given on the left. Upper limits on the fluence during the analyzed period of 89 days assuming a spectral index of -2, are given on the right and compared to an earlier analysis of a non-flaring period.

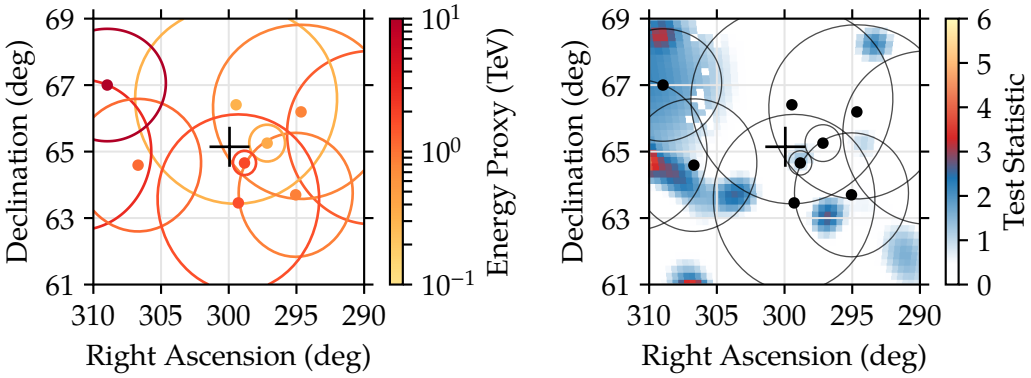

Figure 6.31: Skymap of the 10 highest weighted events in equatorial coordinates. Event locations are shown with a dot; circles indicate the 1σ uncertainty. A black cross marks the location of 1ES 1959+650. Left: The color scale indicates the muon energy proxy. Right: Events are superimposed onto a scan of the test statistic of the time-integrated analysis.

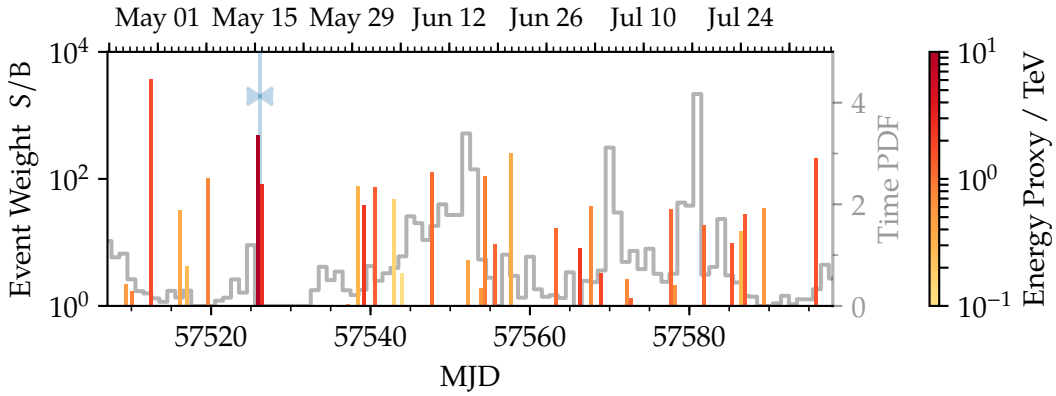

Figure 6.32: Neutrinos from 1ES 1959+650 over time. Bar heights indicate the event weights, i.e. the product of spatial and energy weight, assuming a spectrum $\propto E^{-2}$. The color of the bars indicates the muon energy proxy. In the background, the time PDF used in the correlation test is drawn in grey. A blue bar highlights the location of the most-significant cluster.

peak of the spectral energy distribution of that blazar is located above the energy range to which Fermi-LAT is sensitive, hence the blazar's flaring activity in the VHE gamma-ray band may have been inaccessible to that instrument.

Finally, due to the absence of signal-like events on the days covered by gamma-ray observations the final neutrino–gamma correlation test also yields a test statistic of zero and is therefore most-compatible with background. Upper limits on the fluence in the analyzed time period are given in Tab. 6.3.

In summary, no significant excess has been observed in the direction of 1ES 1959+650, neither by integrating over the whole flaring episode, nor by testing for clusters on shorter time scales. Also, no indication for a neutrino flux correlated with the gamma ray flux was found.

A neutrino was found coincident with a gamma-ray flare during the previous, flaring episode from this source in 2002 when an orphan flare was observed. During the flaring episode of 2016, orphan behavior is not supported by the available X-ray data [172]. However, it cannot be excluded for June 13, the day of the strongest gamma-ray emission, where concurrent X-ray data is lacking.

After the flare in 2002 and the correlated neutrino detection in AMANDA, models were developed which attempt to predict possible neutrino fluxes in the light of strong VHE gamma-ray flares: Yet, even with an IceCube-sized detector, a stacking of 40 hours of similar orphan flares is required for a detection in the mirror model [163, 173]. Similarly, the recent spine-sheath model [174] predicts only 0.04 additional neutrino events on the days of the brightest flares, where the gamma ray flux levels reach 10-15 times that of the low state [167].

Eventually, further observations in all wavelengths of this and similar objects are necessary to properly constrain acceleration scenarios. In the context of the realtime

alert system of Sec. 6.1, continued monitoring for potential neutrinos from this source and subsequent, timely alerts to the partner observatories may help to create a larger dataset of simultaneous multi-messenger observations in the future.

6.6 Offline Analysis of TXS 0506+056

Parts of the content of this chapter have previously been published in two papers. Here, they are complemented with additional information and put in general context in the concluding discussion.
The first paper describes the neutrino trigger and the results of the following multi-wavelength observation campaign [19]. The estimation of the muon and neutrino energies were contributed by the author (Fig. S2 in that paper), making use of the simulation datasets which were processed for this thesis.
In addition, the real-time software framework, which was developed in the course of this work, was used to issue the alert. Furthermore, the author made the SplineMPE reconstruction, which is the best directional reconstruction used in the online filter of this work (Sec. 4.3) available to the EHE alerts.
The second paper follows up the high-energy neutrino trigger with a search for neutrino clusters from the same direction in IceCube's archival data [175]. The necessary data sample covering the time between 2015 and 2017 was obtained using the online filtering and processing algorithm developed in this thesis. The time-dependent analysis using the box time profile was performed by the author, using the method of Sec. 5.2, resulting in Fig. 1 and 2 in that paper.

The alert system for extreme high-energy (EHE) events has been operated by IceCube since 2015. Similar to the selection described in Sec. 6.4, it aims to select the most energetic, through-going muon tracks, as they have a large probability of being of astrophysical origin. Six alerts are expected per year, with four of them being astrophysical under the assumption of a flux $\propto E^{-2}$.

On September 22, 2017, a very energetic muon triggered such an EHE alert, which was published in an automated message to the Gamma-ray Coordinates Network (GCN) 43 s later. Once the set of pulses from the event was received as well, a refined reconstruction found the best-fit direction at a right ascension of $\alpha = 77.43°$ and a declination of $\delta = 5.72°$. Following detector status checks (Sec. 3.6), the updated direction was sent to the astronomical community in a GCN Circular message 4 h after the initial alert. A view of the event, which is referred to as IC-170922A in line with the naming scheme of IceCube alerts, is shown in Fig. 6.33.

The direction of the neutrino candidate is compatible with the blazar TXS 0506+056, which is located 0.1° away from the best-fit direction of the muon track. 18 observatories, involving over 1000 astrophysicists, around the world began follow-up observations in radio optical, and X-ray domains, as well as high-energy and very high-energy gamma-rays, delivering a comprehensive picture of the presumed counter-part over 15 decades in energy [19, Fig. 4]. Fermi-LAT found the blazar to be in an state of excited high-energy gamma-ray emission, which had begun in April 2017. Around the time of the alert, the flux reached over 4 times that of the quiescent state.

MAGIC started observing on September 24, but bad weather limited the the observations to 1 h, yielding an upper limit. Resuming on September 28, following 13 h of observations the MAGIC telescopes reported the detection of VHE gamma-

rays from the source reaching energies of up to 400 GeV [176]. A constant flux is incompatible with the light-curve observed in VHE gamma-rays at a p-value of 1.4%. The detection at a significance level of 6.2σ marks the first observation of a

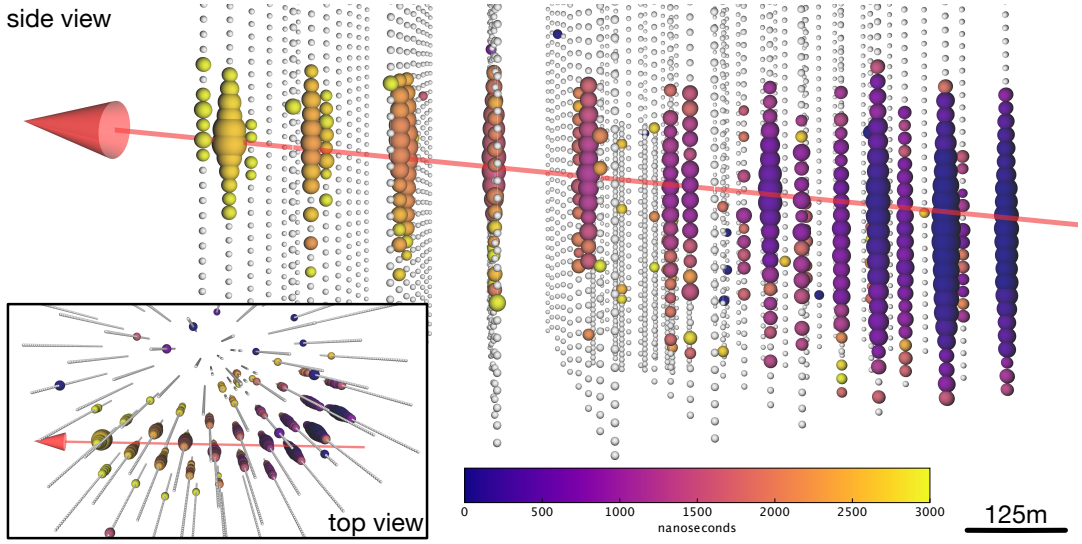

Figure 6.33: Event view of IC-170922A, with a top view given in the smaller panel. The color of a sphere marks the time at which the first hit was recorded, whereas the size of a sphere indicates the total observed charge in that DOM. A red arrow depicts the best-fit direction of the muon track (taken from [19]).

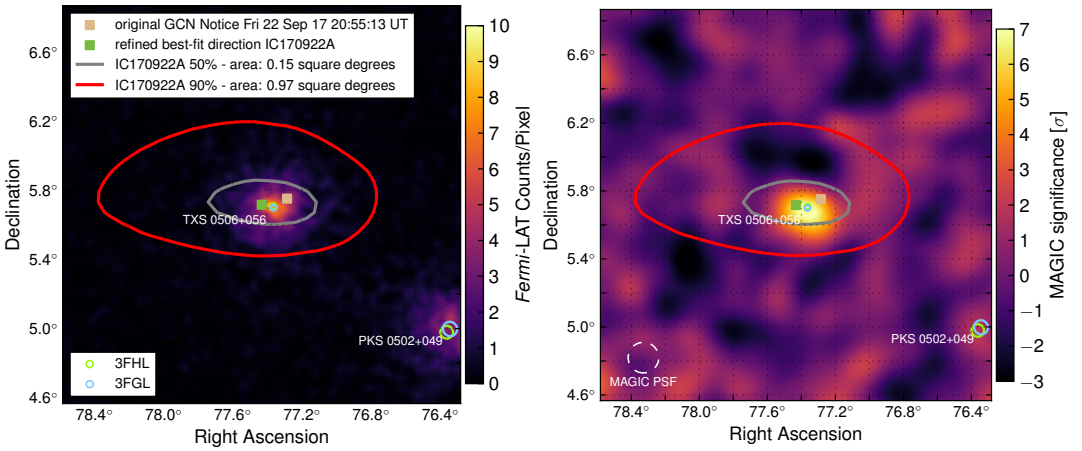

(a) Fermi-LAT

(b) MAGIC

Figure 6.34: Skymaps around the IC-170922A alert. The (very-)high energy gamma-ray sky is shown on the left (right). The best fit the neutrino direction, and its error contours are overlaid (taken from [19]).

counter-part to a high-energetic neutrino candidate in VHE gamma-rays. As shown in Fig. 6.34, the blazar TXS 0506+056 is the brightest object in the gamma-ray sky in the vicinity of the neutrino direction.

Several scenarios have been examined in order to quantify the chance coincidence probability of the event. In the first scenario, the neutrino flux is assumed proportional to the high-energy gamma-ray flux. The second model tests the hypothesis of the neutrino flux being correlated to the variations in the high-energy gamma-ray flux, while a third model relates the neutrino flux to the VHE gamma-ray flux. These tests were designed to cover different assumptions, regarding the neutrino being dominantly produced by the brightest (V)HE gamma-ray sources, or by the most variable, but not necessarily exceptionally bright, sources. All tests account for the look-elsewhere effect by considering also the previous 10 alerts sent since 2015, as well as 41 additional "would-have-been" alerts of the same type that were found in archival data prior to the deployment of the EHE alert channel. Eventually, all tests disfavor the hypothesis of a chance-coincidence at a significance level of 3σ.

While features such as the neutrino flux and energy spectrum cannot be estimated from a single event, any flux capable of producing a high-energetic event might produce additional lower-energetic events in the IceCube detector. A pre-defined IceCube analysis testing the point-source hypothesis in time windows of ± 1 days, and 30 days centered on the time of the alert, has been applied to the event selection developed in Sec. 4.4. An additional investigation of this source using archival IceCube data is presented later.

6.6.1 High-Energy Neutrino Trigger

The triggering event was part of the event selection developed in Sec. 4.4, and would have passed the high energy neutrino alert scheme from Sec. 6.4. Therefore, this event selection can be used to study the properties of that neutrino candidate.

Single events such as IC-170922A stand out due to their energy. Since it was a through-going track, a potential neutrino interaction could only take place outside of the detector. Thus, the neutrino energy can only be inferred from the muon energy reconstructed from the observed segment of the track. A view of the distribution of the muon energy proxy is given in Fig. 6.35, considering a declination band of $\pm 2^\circ$ around the event. An event at least as energetic as IC-170922A can be expected on average every two years. The figure shows the contributions to the events at this declination from the different neutrino flavors in astrophysical and atmospheric fluxes. The observed muon energy of ≈ 230 TeV is located just above the crossing of the atmospheric and astrophysical muon-neutrino fluxes. Using Eq. 6.1, a signalness of 57% can be assigned, meaning that the event is slightly more likely to originate from signal than from background.

If the event is assumed to be astrophysical, 97.9% of events of this energy or higher originate from muon-neutrinos, 1.6% from tau-neutrinos and 0.5% from electron-neutrino interactions.

Employing simulations of the neutrino flux, its passage through the earth and

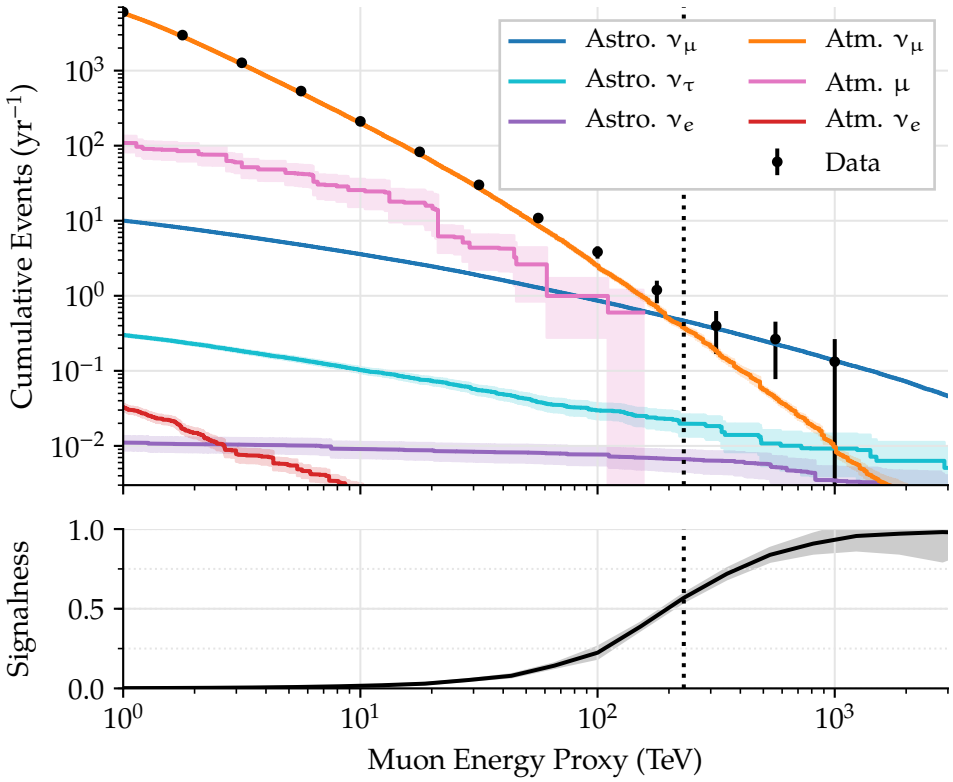

Figure 6.35: Right-cumulative distribution of the energy proxy (TruncatedEnergy) in band of ±2° around the declination of TXS 0506+056.
Colored lines denote the different contributions estimated from simulations, assuming an astrophysical diffuse flux $\propto E^{-2.19}$ [15], the conventional atmospheric neutrino flux constrained in previous analyses [13, 15], as well as atmospheric muons [132]. Shaded areas indicate statistical uncertainties of the simulations.
Signalness is the fraction of astrophysical events among the total flux.
A dotted black line marks the value of the energy proxy for the alert event.

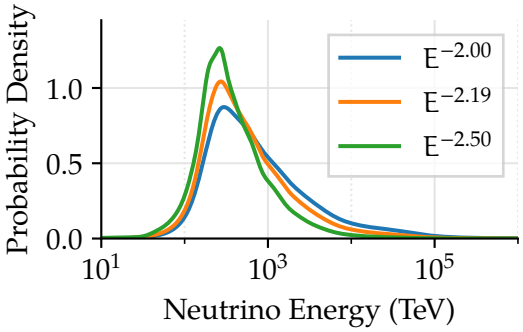

(a) Probability distribution for the neutrino energy of IC-170922A.

$d\Phi/dE$ $\propto$	Quantile 10%	50%	90%	Peak
$E^{-2.00}$	181	555	4,986	296
$E^{-2.19}$	162	423	2,735	274
$E^{-2.50}$	131	313	1,350	264

(b) Quantiles and most-probable (peak) neutrino energy in TeV.

Figure 6.36: Muon-neutrino energy estimation for IC-170922A. Probability distributions for different assumed power-law fluxes are shown on the left. Quantiles of the distribution are given in the table, along with the most-probable (peak) energy.

possible interaction points in the Antarctic glacier, an estimate of the original neutrino energy can be made. Such an estimation requires the assumption of the energy spectrum of the original neutrino flux, which cannot be made from a single event. Thus, the probability distribution in Fig. 6.36 is shown for a benchmark spectrum $\propto E^{-2.00}$, the diffuse through-going muon flux $\propto E^{-2.19}$ [15], and the softer spectrum derived from starting events $\propto E^{-2.50}$ [38]. While the most-probable energy is found between 260 and 300 TeV, the distribution is rather broad and asymmetric as indicated by the quantiles, which span over a decade in energy. On the lower end, it is constrained by the reconstructed muon energy, while the tail towards higher energies is caused by the unconstrained location of the neutrino interaction vertex.

6.6.2 Archival Search for Neutrino Flares

The intriguing coincidence of the high-energy neutrino alert and the blazar poses the question whether lower-energetic neutrinos have been induced at the same location at times different from the alert.

IceCube has taken data for several years, with changing detector configurations. For this search, data from May 2008, recorded with the 40-string configuration, up to February 2018 has been investigated. The event samples until May 2015 had previously been studied in earlier IceCube point-source searches [44, 81, 84, 177]. No offline event selection had been developed for the time between May 2015 and February 2018. However, the online event selection from Sec. 4.4 had been retroactively applied to the data from that time frame. For this analysis, it was supplemented by using the most accurate and most time-consuming settings for the directional reconstruction (SplineMPE, see Sec. 3.4.1), estimating the angular errors using the paraboloid method (Sec. 3.4.2).

First, the time-integrated analysis (Sec. 5) is applied to the entire period spanning

Name	Start	End	Reference
IC40	5 April 2008	20 May 2009	[81]
IC59	20 May 2009	31 May 2010	[177]
IC79	31 May 2010	13 May 2011	[177]
IC86a	13 May 2011	16 May 2012	[84]
IC86b	16 May 2012	18 May 2015	[44]
IC86c	18 May 2015	31 October 2017	This work

Table 6.4: Data periods used in the analysis. The number in the name denotes the number of active strings. IceCube was still under construction during the first three periods. The years with the full detector have been split due to changes in the calibration and event filtering.

9.5 years. Second, two time-dependent analysis are performed. The time-clustering method from Sec. 5.2 employs a box-shaped time profile. In addition, a Gaussian time profile is used by multiplying the signal and background PDFs (Eq. 5.1 and 5.2) with a normal distribution, whose location and width are free fit parameters.

All analyses test for the hypothesis of an excess of signal-like neutrinos near the source location, over the sole presence of random background events. Triggered by the high-energy muon alert, the presence of one event with a very large weight (dominated by the spatial PDF, Eq. 5.1) was known beforehand and an analysis would be guaranteed to give a significant result. The significance level would have to be corrected for the look-elsewhere effect by accounting for the possibility of performing the analysis anywhere else on the sky.

Therefore, the IC-170922A event is removed from the sample and the hypothesis to be tested is whether *additional* neutrino emission can be found independent of the high-energy trigger.

Since the time-dependent analysis codes cannot deal with the transition between different event selections, which feature individual signal and background behavior, the analyses are applied to each data period individually. All data samples are listed in Tab. 6.4. Eventually, the most-significant result will be selected, with a trial factor applied to account for the number of tested event samples. In addition, a trial factor of two would conservatively correct for the two different, albeit correlated, shapes of time profiles.

Results

Both time-dependent analyses detect an excess of events around December 2014 in the IC86b period. The fit results for this work, i.e. using the box-shaped time PDF, are summarized in Tab. 6.5 and are well compatible within their uncertainties.

Using the Gaussian time PDF, the most-significant time window is found centered on December 13, 2014 with a standard deviation of 110 days [175]. A more-extreme test statistic is only found for every 33,000-th randomized trial (Sec. 5.3), corresponding

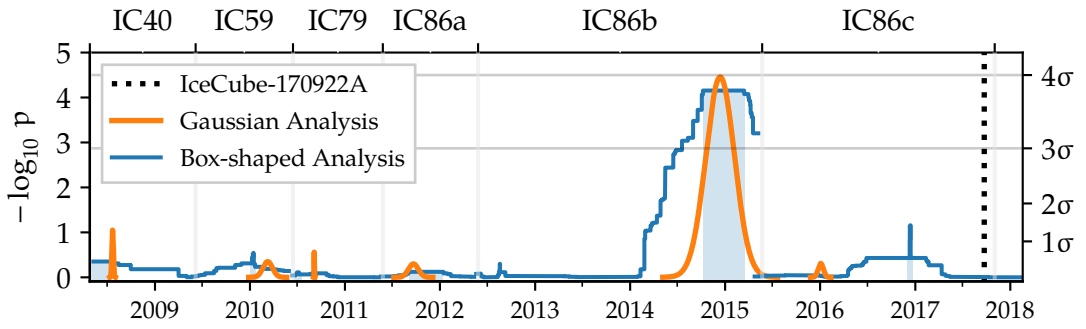

(a) Outline of all time-windows tested by the time-clustering search (blue) and their respective significance levels. Orange lines mark the most-significant result found in each period using the Gaussian-shaped time profile.

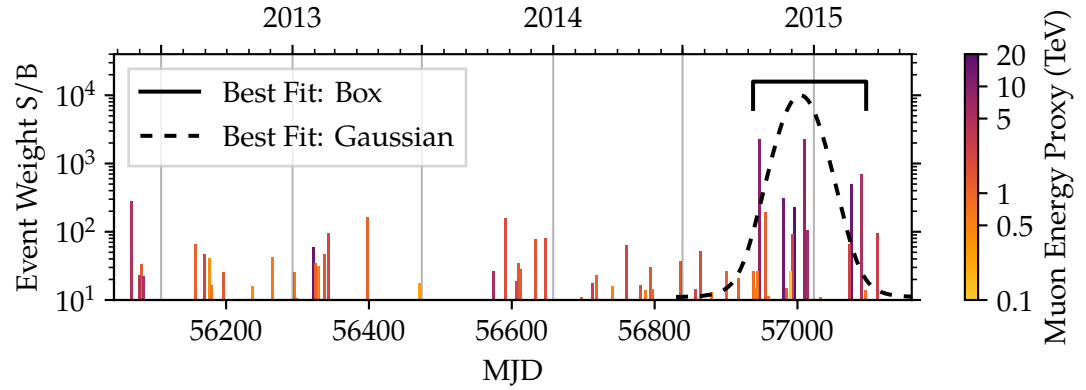

(b) Event weights (height of the bars) and energies (color of the bars) near the most-significant cluster, assuming a spectral index of −2.2.

Figure 6.37: Neutrino curves for the direction of TXS 0506+056. The significance level of the time-dependent tests is shown over time in the top panel. A zoomed view around the best-fit time window is given in the lower panel, where the weights of the events recorded over time are indicated by the height of the bars. Muon energies are indicated by the color of the bars (published in [175]).

to a p-value of $3 \cdot 10^{-5}$. Accounting for the entire period of 9.5 years which were analyzed besides the 3 years of IC86b (see Tab. 6.4), incurs a trial factor of 9.5/3 and consequently a p-value of $1 \cdot 10^{-4}$.

The best-fit box time window ranges from 56937.81 (October 7, 2014) to 57096.21 (March 15, 2015). It spans 158 days, which almost differs from the Gaussian result by $\sqrt{2}$, as is expected from toy simulations. Being centered 13 days later is compatible with the uncertainty of ±21 d on the time. With a p-value of $2 \cdot 10^{-4}$, the significance level of the analysis developed in this work is just slightly below that of the Gaussian one.

As defined before, the most-significant result, the one from the Gaussian analysis,

Data Period	n_s	γ	Duration	End Date	Λ	p	
IC40	1.0	-1.4	84.8 d	2008/07/19	4.6	44%	
IC59	2.9	-2.3	9.6 h	2010/10/13	8.5	29%	
IC79	2.6	-4.0	7.7 d	2010/07/08	2.5	77%	
IC86a	7.0	-2.8	130 d	2012/01/12	3.6	74%	
IC86b	14.4	-2.2	158 d	2015/03/05	30.3	$9 \cdot 10^{-5}$	3.8σ
IC86c	7.3	-3.3	1.4 d	2016/12/13	15.1	7%	

Table 6.5: Fit results for the different data periods obtained with the time-clustering analysis in this work. The significance in the last column only accounts for for the duration of the respective data period, not for the total duration of all tested data period.

is chosen and an additional trial factor of 2 is applied. This is a conservative choice, since both analyses are not independent, testing the same data for a similar time structur. Eventually, the significance level of the excess is 3.5σ.

No excess is found in any of the other time periods, in particular not in connection to the alert in 2017. The evolution of the significance level over time is shown in Fig. 6.37a. From the time-clustering analysis, the significance level of the most-significant of all tested time windows at each point in time is drawn. For comparison, also the best-fit Gaussian is shown for each time period. Both analyses are expected to agree in the presence of a strong, signal-like excess, as is the case in 2014/15. In the absence of a signal, the analyses pick up random, insignificant fluctuations of the background.

Since both time-dependent analyses yielded similar results, the following will focus on the results of the time-clustering test for clarity.

The best-fit time window consists of 13 ± 5 events, which clearly stand out as a cluster in Fig. 6.37b, where the event weights are shown over time. Converting the number of events into a flux, assuming the fitted spectral index, and integrating over the flare duration yields a fluence of

$$dJ/dE = 2.1 \cdot 10^{-8} \cdot (E/100\,\mathrm{TeV})^{-2.2}\ \mathrm{TeV}^{-1}\,\mathrm{cm}^{-2}\ . \tag{6.5}$$

Combined uncertainty on the fluence and the spectral index are determined from the likelihood scan in Fig. 6.38a.

The cluster is well-localized in space, as can be seen in Fig. 6.38b. TXS 0506+056 is the only known high-energy gamma-ray source in the excess. The second closest source, the blazar PKS 0502+049, is two degrees away and already outside the range of the figure.

From the time-integrated analysis over the whole 9.5 year period, a p-value of 2.3σ is found when the alert event is excluded. Events from the 2014/15 flare drive the fit results and yield comparable parameters for the number of signal-like events and the spectrum. Yet, the significance level is lower, since the time-integrated analysis cannot isolate the flaring period among the remaining background.

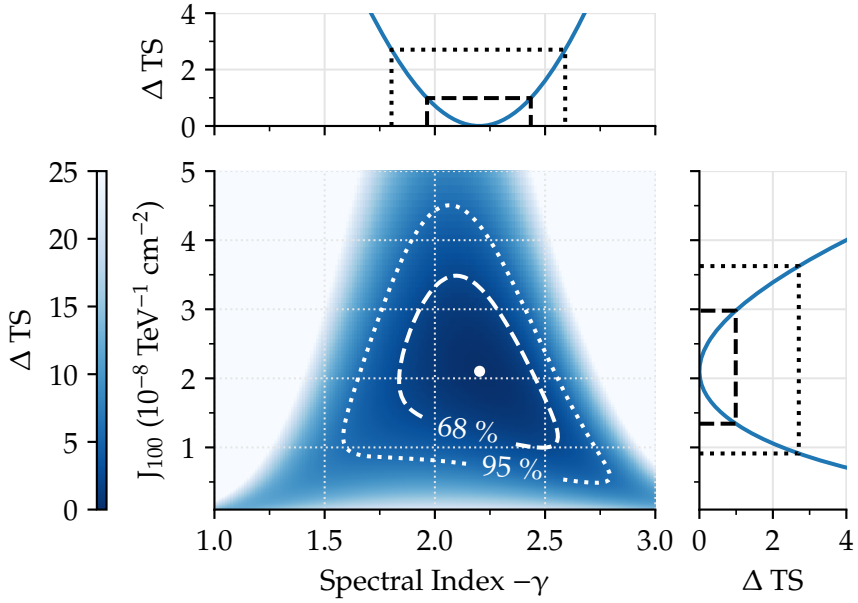

(a) Likelihood scan for this work. With the time window fixed to the best-fit period, n_s and γ are the only free parameters. J_{100} denotes the fluence normalization at 100 TeV. The smaller panels above and to the right depict the profile likelihood in one dimension. Dashed (dotted) contours mark the 68% (95%) statistical uncertainties, assuming Wilks' theorem.

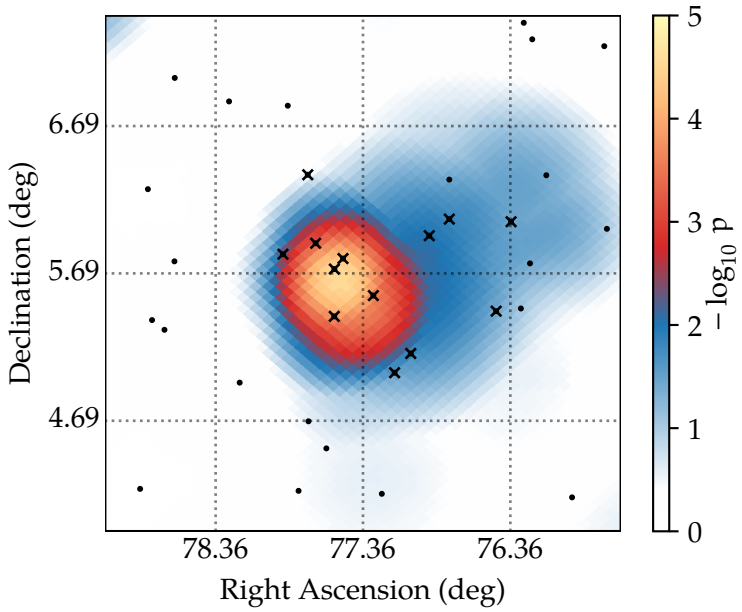

(b) Skymap centered on the location of TXS 0506+056, for the analysis developed in this work. Events recorded during the best-fit period of 158 days are drawn as dots, with crosses marking the 13 highest-weighted events. The color shows the best local p-value found at each pixel.

Figure 6.38: Scan of the likelihood space during the most-significant time window, and a scan of the sky surrounding the source location.

Discussion of the Result

The cluster of neutrinos found in 2014 did not trigger the astronomical community and multi-wavelength coverage is sparse. Contemporaneous observations in gamma-rays are available from Fermi-LAT. No significant change in flux or spectrum emerges during the 2014/15 flaring period [178].

Including the IC-170922A triggering event in the analysis did not yield a significant cluster at the time of the alert, as it is a single event and not accompanied by additional lower-energetic events close in time and space.

A significance level of 3.5σ indicates evidence, but a discovery of a neutrino source cannot be claimed. Yet, the analysis was performed in a blind fashion and the statistical result relies only on few, generic assumptions in terms of a power-law spectrum and the shape of the time profile.

Both Fig. 6.37b and 6.38b show that the number of well-localized events as well as their energies contribute to the significance. Less than 6 events are expected in a bin of 1° around the source due to background, while this analysis fits 14 signal-like events. Such a large number of events allows for a robust determination of an energy spectrum $\propto E^{-2.2}$, which is much harder than the atmospheric background $\propto E^{-3.7}$ and further supports the signal interpretation.

At the given declination, the central 1σ interval of energies in which IceCube is most sensitive to neutrinos ranges from 32 TeV to 3.6 PeV. The observed muon-neutrino fluence integrated over that range, along with the measured redshift of $z = 0.337 \pm 0.001$, yields an isotropic neutrino luminosity of $1.2 \cdot 10^{47}\,\mathrm{erg\,s^{-1}}$, averaged over 158 days. This is more than four times larger than the isotropic gamma-ray luminosity of $0.28 \cdot 10^{47}\,\mathrm{erg\,s^{-1}}$, integrated over Fermi-LAT observations between 100 MeV and 100 GeV. If neutrinos and photons were produced in the same $p\gamma$-interactions, the lower observed luminosity in gamma-rays could be caused by photons or having at energies lower than those observable by Fermi-LAT, or being absorbed near the source [179].

The averaged neutrino flux determined from the time-integrated analysis averaged over 9.5 years of $E^2 d\phi/dE = 7.4 \cdot 10^{-10}\,\mathrm{GeV\,cm^{-2}\,s^{-1}}$, which yielded 13 signal-like events in the analysis of 9.5 years, convolved with the effective area of the online EHE alert selection would actually deliver approximately one EHE alert in the same time frame.

While the correlation is intriguing, it cannot resolve the nature of the neutrino sky. Previous correlation searches between known gamma-ray blazars and neutrinos limits the contribution from blazars to the astrophysical neutrino flux to 30% [180]. In terms of theoretical models lepto-hadronic models of electrons and protons in a fast inner jet spine, surrounded by a slow-moving sheath of external photons, can consistently interpret the observations of 2017 [181]. In turn, this case may provide evidence for proton acceleration in the jets of AGN. Reconciling the observations of 2018 with the neutrino flare of 2014 is however more challenging. Lepto-hadronic models are constrained by the X-ray and high-energy gamma-ray emission, but can only justify 2 signal neutrinos in the absence of gamma-ray flares. Five neutrino events

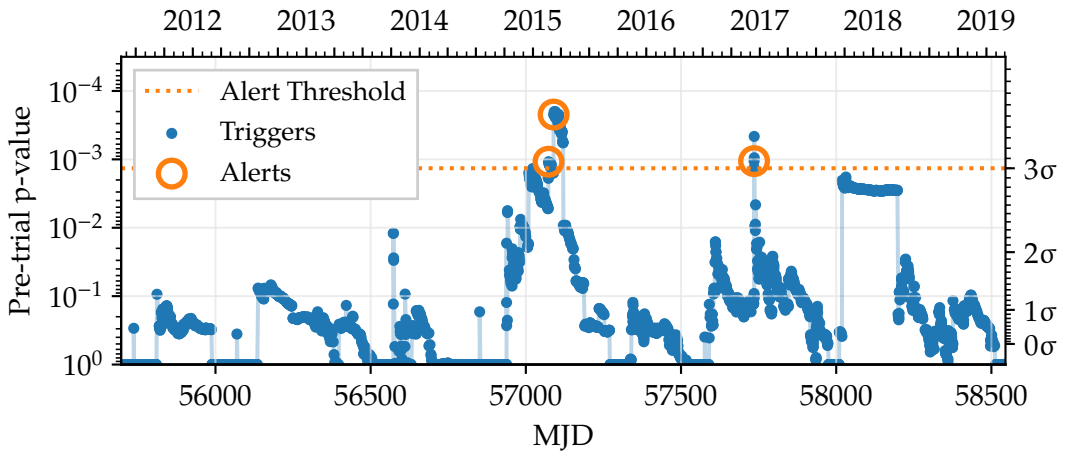

Figure 6.39: Alert triggers for TXS 0506+056. If the online source monitoring had been running in the past, follow-up observatories would have been notified three times (orange circles).

are possible within the constraints imposed by the X-ray flux, but would require an optical thickness at high-energy gamma-rays, which is incompatible with the spectrum observed by Fermi-LAT [182].

Nevertheless, TXS 0506+056 is among the 50 brightest objects in the third catalog of AGN detected by Fermi-LAT [183]. A determination of the redshift only took place in the wake of the IC-170922A alert, and places TXS 0506+056 as one of the most luminous objects up to that distance [184]. In addition, its location just below the horizon is essentially in the sweet-spot of IceCube's point-source sensitivity (see. Fig. 5.12). The sensitivity towards more northern sources suffers from absorption of high-energetic neutrinos in the Earth, and atmospheric muons limit the sensitivity in the southern sky. If the sensitivity was indeed just reaching to the level the brightest sources, those sources would be expected to show up as over-fluctuations in the declination band of TXS 0506+056.

Considering the result of applying the online all-sky scan developed in this work to archival data (Sec. 6.3), the flare at the location of TXS 0506+056 was only 15th most-significant spot in the sky. As such, it would not have triggered an alert from the online all-sky scan, which is also follows from the significance of 3.5σ. It is therefore not a very interesting spot per se, but rather intriguing due the correlation between TXS 0506+056 and IC-170922A.

Lacking a measured redshift, TXS 0506+056 was not previously included in the catalog of online-monitored sources, which has now changed. Applying the online alert scheme (Sec. 6.1) to archival data (Sec. 6.3) allows to test whether an alert would have been triggered for the archival flare. All triggering events and alerts are shown in Fig. 6.39. Indeed, the system would have triggered at least twice during the 2014/15 flaring period, and at an unrelated point in 2016. As the high-energy neutrino in 2017 was not accompanied by lower-energetic events, it did not reach the alert threshold in

this search.

Technical obstacles described in Sec. 6.3 render a few runs unavailable to the archival online event sample. In particular, these gaps during the period of the 2014/15 flare cause two signal-like events from the original analysis to be missing in the archival sample. Nevertheless, the two alerts which would have been triggered during the flare highlight the potential of the real-time source monitoring and its ability to trigger the necessary multi-wavelength observations in the future.

7 Summary

When the work on this thesis began, the recent breakthroughs in the field of multi-messenger astronomy and astrophysics could not have been anticipated.

Although the origin of cosmic rays is still unclear, the discovery of gravitational waves in September 2015, as well as the detection of gravitational waves coincident with a gamma-ray burst from a binary system of merging neutron stars in September 2017, mark two breakthrough discoveries of the recent years. In addition, the observation of very-high energy gamma-ray flares from the blazar TXS 0506+056 in coincidence with a high-energetic neutrino from IceCube, as well as the independent evidence for an extra-galactic source of high-energetic neutrinos, which was found in this work, pave the way for future revelations. Successful observations of those events with different messenger particles and in in different wavelengths confirm and emphasize the potential of real-time astronomy and the value of contemporary observations.

Tools developed in the course of this work have contributed to this success. The real-time event selection, which has been deployed at the South Pole in 2017, boosts the instantaneous point-source sensitivity to that of dedicated former offline analyses. It is not just used in the applications demonstrated in this thesis, but has now become a standard tool in IceCube, whenever a rapid investigation and follow-up of externally observed phenomena is needed. It is also used in automated searches, e.g. in collaboration with the LIGO and VIRGO observatories. The software tools that were developed along with the analysis, but designed to be more universally applicable, enabled the IC-170922A alert that gave rise to the observations of TXS 0506+056.

Furthermore, the enhanced event selection doubles the rate of alerts like IC-170922A, and improves the angular resolution of events from the southern sky by a factor of two. It has been turned on in May 2019 and improves the chances for future observations to eventually discover the sources of neutrinos and cosmic rays.

Similary, the sensitivity of the online monitoring of source candidates has been improved on all time-scales. It is complemented by a new search for neutrino flares from sources which are not yet monitored. The upgraded source monitoring and the new all-sky analysis are in operation since March 2019.

Meanwhile, the search for neutrino emission from 1ES 1959+650 came up empty. In comparison to the earlier study of this source with the AMANDA experiment, this time the presence of a contemporaneous orphan gamma-ray flare could not be established, due to a lack of multi-messenger observations. Continued monitoring of this source with the online system has the potential to change this situation in the future.

Finally, the analysis of TXS 0506+056 provided additional, independent evidence

for a neutrino source. While this does not conclusively unravel the origin of the cosmic rays, it provides strong motivation to continue and expand the efforts of multi-messenger astronomy and the assembly of contemporaneous multi-wavelength data. Continuing efforts in this direction will eventually complete the picture of astrophysical accelerators.

Future experiments can boost that effort. In terms of gamma-ray observations, the future Cherenkov Telescope Array (CTA) will greatly improve the observational capabilities for sources of very high-energy gamma-rays, allowing more timely follow-up and providing a denser sample of observations.

On the neutrino side of things, IceCube has now collected over 10 years of data. Accumulating additional data will only weakly benefit the time-integrated sensitivity. If its sensitivity is scratching the flux of the brightest sources, and the sources are indeed exhibit strong time variability, the important quantity is the instantaneous sensitivity, which does not improve by simply operating the experiment for more years. Progress requires novel analysis techniques and additional input, such as better calibration and ice models, which may be obtained from the first phase of the IceCube Upgrade in the next years. Reconstruction techniques which benefit from improved understanding of the detector and the detection medium would improve the pointing accuracy and give rise to better point-source sensitivity. Alternatively, an expanded detector, will increase the rate with which astrophysical neutrinos are detected, although the design and deployment require patience for the next one or two decades.

A List of Monitored Sources

Name	α (°)	δ (°)	Fermi Name	MAGIC	VERITAS	H.E.S.S.
S5 1803+784	270.13	78.462	3FGL J1800.5+7827	•		
S5 2007+77	301.31	77.881	3FGL J2005.2+7752	•		
6C B163030.4+771303	247.26	77.127	3FHL J1629.0+7707	•		
RX J0805.4+7534	121.35	75.582	3FGL J0805.4+7534	•	•	
S5 1027+74	157.82	74.711	3FHL J1031.2+7442	•		
S5 0716+71	110.47	71.342	3FHL J0721.8+7120	•	•	
TXS 0149+710	28.36	71.252	3FGL J0153.4+7114		•	
S5 1217+71	185.07	71.093	3FGL J1220.2+7105	•		
Markarian 180	174.13	70.153	3FHL J1136.5+7009	•	•	
S4 1749+70	267.17	70.097	3FGL J1748.6+7005	•		
3C 371	271.68	69.818	3FGL J1806.7+6949	•	•	
TXS 1700+685	255.05	68.485	3FGL J1700.1+6829	•		
4C +67.04	17.55	68.095	3FHL J0110.1+6806		•	
1ES 0502+675	77.00	67.620	3FHL J0508.0+6737	•	•	
RX J1136.5+6737	174.13	67.618	3FHL J1136.4+6737	•	•	
S4 1849+67	282.34	67.094	3FHL J1849.3+6705	•		
S4 0954+65	149.69	65.565	3FHL J0958.7+6533	•	•	
1ES 1959+650	300.02	65.154	3FGL J2000.0+6509	•	•	
GB6 J0814+6431	123.68	64.480	3FGL J0814.7+6428	•		
MS 1229.2+6430	187.88	64.238	3FGL J1231.5+6414		•	
1RXS J042523.0+632016	66.30	63.288	3FGL J0425.2+6319		•	
1RXS J192649.5+615445	291.71	61.912	3FHL J1926.9+6154		•	
NVSS J094022+614825	145.09	61.807	3FHL J0940.5+6149		•	
GB6 J1542+6129	235.74	61.499	3FGL J1542.9+6129		•	
1RXS J013106.4+612035	22.78	61.343	3FHL J0131.1+6120		•	
LSI +61_303	40.13	61.229	3FGL J0240.5+6113		•	
TXS 0354+599	59.71	60.040	3FGL J0358.8+6002	•		
1ES 0033+595	8.97	59.834	3FHL J0035.9+5950		•	
RGB J0710+591	107.62	59.142	3FHL J0710.4+5908	•	•	
TXS 1148+592	177.85	58.988	3FGL J1151.4+5858		•	
TXS 0059+581	15.70	58.425	3FGL J0102.8+5825	•		
PG 1246+586	192.08	58.341	3FHL J1248.3+5820		•	
1RXS J013748.0+581422	24.46	58.236	3FGL J0137.8+5813		•	

Name	α (°)	δ (°)	Fermi Name	MAGIC	VERITAS	H.E.S.S.
SBS 0812+578	124.09	57.653	3FHL J0816.4+5739		•	
GB6 J0047+5657	11.77	56.971	3FGL J0047.0+5658	•		
4C +56.27	276.06	56.833	3FGL J1824.2+5649	•		
RBS 1409	219.24	56.657	3FHL J1436.9+5639		•	
TXS 1055+567	164.66	56.468	3FHL J1058.6+5628	•	•	
TXS 1557+565	239.74	56.418	3FGL J1558.9+5625	•		
TXS 1902+556	285.80	55.677	3FHL J1903.2+5540		•	
4C +55.17	149.41	55.383	3FGL J0957.6+5523		•	
GB6 J0742+5444	115.65	54.735	3FHL J0742.5+5444	•		
NVSS J234753+543627	356.97	54.608	3FGL J2347.9+5436		•	
OQ 530	214.98	54.419	3FGL J1419.9+5425	•		
1RXS J182925.7+540255	277.35	54.050	3FGL J1829.4+5402		•	
1RXS J010325.9+533721	15.86	53.620	3FGL J0103.4+5336		•	
GB6 J0601+5315	90.50	53.267	3FHL J0602.0+5316		•	
S4 1250+53	193.30	53.020	3FGL J1253.2+5300		•	
1ES 2037+521	309.85	52.331	3FHL J2039.4+5219		•	
1ES 0806+524	122.46	52.310	3FHL J0809.8+5218	•	•	
GB6 J0148+5202	27.08	52.035	3FHL J0148.2+5201		•	
1ES 2344+514	356.76	51.708	3FGL J2347.0+5142	•	•	
RFC J0248+5131	42.16	51.536	3FHL J0248.6+5132		•	
SBS 0846+513	132.49	51.142	3FHL J0849.9+5108	•		
1ES 1028+511	157.83	50.893	3FHL J1031.3+5053		•	
GB6 J0712+5033	108.19	50.545	3FHL J0712.7+5032	•		
NVSS J000922+503028	2.34	50.508	3FHL J0009.4+5030		•	
1ES 1727+502	262.09	50.222	3FHL J1728.3+5013	•	•	
GB6 J0937+5008	144.45	50.145	3FGL J0937.7+5008	•		
SBS 1646+499	251.87	49.837	3FGL J1647.4+4950	•		
RGB J2056+496	314.18	49.669	3FHL J2056.7+4940		•	
OM 484	178.35	49.536	3FGL J1153.4+4932	•		
1ES 1011+496	153.77	49.435	3FHL J1015.0+4926	•	•	
NVSS J030727+491510	46.86	49.253	3FHL J0307.4+4916		•	
3C 380	277.41	48.749	3FGL J1829.6+4844	•		
RX J1415.5+4830	213.91	48.515	3FHL J1415.6+4830	•		
GB 1310+487	198.16	48.478	3FHL J1312.6+4828	•		
GB6 J1838+4802	279.70	48.043	3FGL J1838.8+4802		•	
OC 457	24.26	47.876	3FGL J0137.0+4752	•		
TXS 0603+476	91.85	47.663	3FHL J0607.4+4739		•	
4C +47.44	249.43	47.264	3FGL J1637.7+4715	•		
MG4 J000800+4712	2.00	47.202	3FHL J0007.9+4711		•	
7C 2010+4619	303.02	46.482	3FHL J2012.0+4629		•	

Name	α (°)	δ (°)	Fermi Name	MAGIC	VERITAS	H.E.S.S.
4C +45.08	79.37	45.668	3FGL J0517.4+4540	•		
B3 0650+453	103.60	45.247	3FGL J0654.4+4514	•		
GB6 J0128+4439	22.13	44.507	3FGL J0128.5+4430	•		
NVSS J224753+441317	341.97	44.221	3FGL J2247.8+4413		•	
MAGIC J2001+435	300.31	43.884	3FHL J2001.2+4353		•	
B3 1747+433	267.25	43.364	3FHL J1748.9+4321		•	
B3 1307+433	197.36	43.085	3FHL J1309.4+4305		•	
3C 66A	35.67	43.034	3FHL J0222.6+4302	•	•	
H 1426+428	217.14	42.672	3FHL J1428.5+4240	•	•	
S4 0814+42	124.56	42.399	3FGL J0818.2+4223	•	•	
BL Lacertae	330.69	42.276	3FHL J2202.7+4216	•	•	
RBS 0970	170.20	42.203	3FHL J1120.8+4212		•	
1ES 2321+419	350.98	42.184	3FGL J2323.9+4211	•	•	
B3 1518+423	230.09	42.154	3FGL J1520.3+4209	•		
RBS 1040	177.64	41.911	3FHL J1150.5+4154		•	
4C +41.11	65.98	41.834	3FHL J0423.8+4149		•	
NGC 1275	49.96	41.512	3FHL J0319.8+4130	•	•	
B3 0609+413	93.21	41.377	3FHL J0612.8+4122		•	
IC 310	49.17	41.335	3FHL J0316.6+4120	•	•	
Cygnus X	307.17	41.170	3FGL J2028.6+4110		•	
MG4 J225201+4030	343.00	40.516	3FGL J2251.9+4031		•	
RX J1100.3+4019	165.09	40.324	3FHL J1100.3+4020		•	
3C 345	250.75	39.849	3FGL J1642.9+3950	•		
B3 0045+395	11.98	39.816	3FHL J0047.9+3947		•	
Markarian 501	253.47	39.758	3FHL J1653.8+3945	•	•	•
RGB J0136+391	24.14	39.100	3FHL J0136.5+3906		•	
B2 1732+38A	263.61	38.975	3FHL J1734.4+3858	•		
GB6 J0342+3858	55.57	38.959	3FGL J0342.2+3857	•		
B2 0557+38	90.26	38.641	3FHL J0601.0+3837		•	
B3 2247+381	342.53	38.433	3FGL J2250.1+3825	•	•	
S4 0003+38	1.61	38.418	3FGL J0006.4+3825	•		
Markarian 421	166.12	38.205	3FHL J1104.4+3812	•	•	•
NVSS J232914+375414	352.31	37.904	3FGL J2329.2+3754		•	
GB6 J0706+3744	106.63	37.743	3FHL J0706.5+3744		•	
B2 1504+37	226.52	37.543	3FHL J1506.0+3732	•		
RX J1249.8+3708	192.44	37.130	3FHL J1249.8+3708		•	
1RXS J230437.1+370506	346.15	37.085	3FGL J2304.6+3704		•	
Ton 116	190.80	36.462	3FHL J1243.2+3627		•	
MG2 J190411+3627	286.05	36.450	3FHL J1904.1+3627		•	
MG2 J112758+3620	171.96	36.308	3FGL J1127.8+3618	•		

Name	α (°)	δ (°)	Fermi Name	MAGIC	VERITAS	H.E.S.S.
B2 2125+35	321.93	36.218	3FHL J2127.7+3612		•	
S3 0218+35	35.29	35.938	3FHL J0221.1+3556	•	•	•
B2 0806+35	122.41	34.927	3FGL J0809.6+3456		•	
1RXS J234332.5+343957	355.89	34.668	3FHL J2343.6+3439		•	
GB6 J0043+3426	10.97	34.423	3FHL J0043.8+3425	•		•
1ES 0120+340	20.79	34.347	3FHL J0123.0+3422		•	
B2 2114+33	319.06	33.656	3FHL J2116.2+3339		•	
Ton 1015	137.65	33.490	3FGL J0910.5+3329		•	
B2 0619+33	95.72	33.436	3FGL J0622.9+3326		•	
B2 0716+33	109.85	33.130	3FHL J0719.4+3307	•		•
OP 313	197.66	32.370	3FGL J1310.6+3222	•		•
RX J1841.7+3218	280.45	32.311	3FGL J1841.7+3218		•	
B2 1846+32A	282.13	32.299	3FHL J1848.5+3217	•		•
RX J1754.1+3212	268.55	32.206	3FGL J1754.1+3212		•	
4C +31.03	18.24	32.147	3FHL J0112.9+3208	•		•
NVSS J230022+313703	345.10	31.618	3FHL J2300.3+3136		•	
RX J1702.6+3115	255.66	31.262	3FGL J1702.6+3116		•	
NVSS J020344+304238	30.96	30.748	3FHL J0203.8+3044	•		•
B2 1348+30B	207.70	30.599	3FGL J1350.8+3035	•		•
RX J1531.9+3016	233.01	30.275	3FHL J1531.9+3016		•	
1ES 1218+304	185.34	30.177	3FGL J1221.3+3010	•	•	•
1ES 1215+303	184.48	30.115	3FHL J1217.9+3006	•	•	•
RBS 0042	4.62	29.792	3FGL J0018.4+2947		•	
Ton 0396	138.97	29.557	3FGL J0915.8+2933		•	
NVSS J205350+292314	313.46	29.387	3FHL J2053.8+2922		•	
TXS 0330+291	53.45	29.275	3FHL J0333.7+2916		•	
Ton 599	179.88	29.237	3FHL J1159.5+2914	•	•	•
GB6 J1001+2911	150.25	29.226	3FGL J1001.0+2913	•		•
MG2 J180948+2910	272.44	29.172	3FGL J1809.7+2909		•	
MG3 J184126+2910	280.34	29.161	3FHL J1841.3+2909		•	
MG2 J043337+2905	68.41	29.096	3FHL J0433.6+2905	•		•
1RXS J191053.2+285622	287.75	28.944	3FGL J1910.8+2855		•	
B2 1229+29	187.94	28.793	3FHL J1231.7+2847	•	•	•
B2 2234+28A	339.08	28.489	3FGL J2236.3+2829	•		•
NVSS J192502+281542	291.26	28.262	3FHL J1925.0+2815		•	
MG2 J110606+2812	166.49	28.237	3FGL J1105.9+2814	•		
W Comae	185.38	28.232	3FHL J1221.5+2813	•	•	•
TXS 0141+268	26.14	27.084	3FHL J0144.5+2705		•	
RX J0620.6+2644	95.17	26.725	3FHL J0620.6+2645		•	
1RXS J013427.2+263846	23.62	26.645	3FHL J0134.4+2638		•	

Name	α (°)	δ (°)	Fermi Name	MAGIC	VERITAS	H.E.S.S.
1E 1415.6+2557	214.49	25.724	3FHL J1418.0+2543		•	
RX J0115.7+2519	18.94	25.331	3FHL J0115.8+2519		•	
ON 246	187.58	25.326	3FGL J1230.3+2519	•	•	•
OK 290	149.15	25.266	3FGL J0956.6+2515	•		
1ES 0647+250	102.69	25.050	3FHL J0650.7+2503	•	•	
PKS 1441+25	220.98	25.044	3FHL J1443.9+2502	•	•	•
MS 1221.8+2452	186.11	24.607	3FHL J1224.4+2436	•	•	•
MG2 J130304+2434	195.75	24.595	3FGL J1303.0+2435	•		•
MG2 J204208+2426	310.53	24.448	3FGL J2042.1+2428		•	
S3 0745+24	117.09	24.024	3FGL J0748.3+2401	•		•
TXS 1312+240	198.68	23.807	3FHL J1314.7+2349		•	
PKS 1424+240	216.75	23.800	3FGL J1427.0+2347		•	
MG3 J032201+2336	50.50	23.603	3FHL J0322.0+2336		•	
RX J0908.9+2311	137.27	23.167	3FGL J0909.0+2310	•		•
S2 0109+22	18.03	22.755	3FHL J0112.1+2245	•	•	•
MS 1458.8+2249	225.25	22.640	3FHL J1500.9+2238	•	•	•
TXS 1318+225	200.27	22.263	3FGL J1321.0+2215	•		
Crab Pulsar	83.63	22.015	3FGL J0534.5+2201	•	•	•
GB6 J0045+2127	11.33	21.461	3FHL J0045.3+2127		•	
4C +21.35	186.23	21.382	3FHL J1224.9+2122	•	•	•
HESS J1943+213	295.98	21.306	3FHL J1943.9+2117		•	
VER J0521+211	80.44	21.213	3FHL J0521.7+2112	•	•	•
1RXS J065033.9+205603	102.63	20.934	3FGL J0650.5+2055		•	
NVSS J173605+203301	264.02	20.550	3FHL J1736.0+2032		•	
RGB J2243+203	340.98	20.351	3FHL J2243.9+2020		•	
1ES 0229+200	38.22	20.273	3FGL J0232.8+2016	•	•	•
RBS 0958	169.27	20.233	3FGL J1117.0+2014	•	•	•
OJ 287	133.71	20.100	3FHL J0854.8+2006	•	•	•
3C 264	176.27	19.606	3FHL J1145.0+1935		•	
RX J2030.8+1935	307.74	19.604	3FHL J2031.0+1936		•	
MG2 J071354+1934	108.50	19.559	3FGL J0713.9+1933	•		
1ES 1741+196	266.00	19.546	3FGL J1743.9+1934	•	•	
RBS 0413	49.97	18.754	3FHL J0319.8+1845	•	•	•
RX J2156.0+1818	329.01	18.310	3FGL J2156.0+1818		•	
MG1 J120953+1809	182.47	18.178	3FGL J1209.8+1810	•		•
PKS 0507+17	77.52	18.009	3FHL J0510.0+1800	•	•	•
PKS 1717+177	259.81	17.758	3FHL J1719.2+1745	•	•	•
OX 169	325.90	17.709	3FHL J2143.5+1742	•		•
PKS 0735+17	114.54	17.698	3FGL J0738.1+1741	•	•	•
AO 0235+164	39.67	16.627	3FHL J0238.6+1637	•		•

Name	α (°)	δ (°)	Fermi Name	MAGIC	VERITAS	H.E.S.S.
3C 454.3	343.49	16.148	3FHL J2253.9+1608	•		•
NVSS J184425+154646	281.11	15.779	3FHL J1844.4+1547		•	
GB6 J0515+1527	78.95	15.455	3FHL J0515.8+1528		•	
RX J0648.7+1516	102.19	15.270	3FHL J0648.7+1517	•	•	
WISE J154824.39+14570	237.10	14.951	3FHL J1548.4+1456		•	
RGB J2313+147	348.50	14.754	3FHL J2314.0+1445	•	•	•
87GB 195252.4+135009	298.80	13.954	3FGL J1955.1+1357	•		•
GB6 J0114+1325	18.72	13.434	3FGL J0114.8+1326	•		•
PKS B1413+135	214.01	13.426	3FGL J1416.0+1325	•		•
3C 207	130.21	13.253	3FGL J0840.8+1315	•		
RX J0338.4+1302	54.62	13.038	3FHL J0338.5+1302		•	
NVSS J060015+124344	90.06	12.729	3FHL J0600.3+1245		•	
OI 280	117.67	12.539	3FGL J0750.6+1232	•		
M 87	187.70	12.398	3FHL J1230.8+1223	•	•	•
3FHL J2115.2+1218	318.81	12.310	3FHL J2115.2+1218		•	
PKS 1725+123	262.00	12.289	3FGL J1728.0+1217	•		•
GB6 J0045+1217	11.43	12.287	3FGL J0045.7+1217		•	
1ES 1440+122	220.70	12.011	3FHL J1442.8+1200	•	•	
H 1722+119	261.27	11.871	3FHL J1725.0+1152		•	
RBS 0723	131.80	11.564	3FHL J0847.2+1134	•	•	
PG 1553+113	238.93	11.190	3FHL J1555.7+1111	•	•	•
MG1 J160340+1106	240.95	11.108	3FGL J1603.7+1106	•		•
PKS 2032+107	308.88	10.946	3FHL J2035.5+1056	•		•
MG1 J021114+1051	32.81	10.859	3FHL J0211.2+1051	•	•	•
RX J0159.5+1047	29.89	10.785	3FHL J0159.5+1047		•	
1RXS J194246.3+103339	295.70	10.557	3FHL J1942.7+1033		•	
PKS 0306+102	47.26	10.498	3FGL J0309.0+1029	•		
TXS 1720+102	260.69	10.243	3FGL J1722.7+1014	•		•
PKS 0754+100	119.27	9.947	3FGL J0757.0+0956	•	•	•
OT 081	267.88	9.658	3FGL J1751.5+0939	•	•	•
RX J1931.1+0937	292.79	9.618	3FHL J1931.1+0937		•	
1RXS J194934.1+090655	297.39	9.115	3FHL J1949.5+0906		•	
GB6 J0316+0904	49.06	9.090	3FHL J0316.2+0905	•	•	•
MG1 J181841+0903	274.66	9.061	3FGL J1818.6+0903	•		•
ZS 0214+083	34.28	8.605	3FHL J0217.1+0836	•		•
GB6 J0154+0823	28.51	8.398	3FHL J0154.0+0823		•	
1RXS J154604.6+081912	236.52	8.320	3FHL J1546.1+0818		•	
PMN J1506+0814	226.69	8.219	3FHL J1506.7+0813	•	•	•
PKS 0256+075	44.88	7.777	3FGL J0259.5+0746	•		•
GB6 J0100+0745	15.09	7.764	3FHL J0100.3+0746		•	

Name	α (°)	δ (°)	Fermi Name	MAGIC	VERITAS	H.E.S.S.
TXS 2331+073	353.54	7.541	3FGL J2334.1+0732	•		•
1RXS J193320.3+072616	293.33	7.439	3FHL J1933.3+0726		•	
TXS 1827+062	277.54	6.292	3FGL J1830.1+0617	•		•
PMN J1440+0610	220.25	6.181	3FGL J1440.9+0610	•		•
HESS J0632+057	98.25	5.800	3FHL J0632.7+0550		•	
TXS 0506+056	77.36	5.693	3FGL J0509.4+0541	•	•	•
PKS 0502+049	76.36	4.979	3FHL J0505.4+0458	•		
CGCG 050-083	235.89	4.872	3FHL J1543.6+0452		•	
PKS 0829+046	127.96	4.496	3FHL J0831.8+0429	•		•
PKS 1725+044	262.15	4.478	3FGL J1728.5+0428	•		•
MG1 J050533+0415	76.39	4.265	3FHL J0505.5+0415		•	
NGC 1218	47.11	4.111	3FHL J0308.4+0408		•	
PMN J0721+0406	110.36	4.074	3FGL J0721.4+0404	•		
GB6 J0024+0349	6.11	3.843	3FGL J0024.4+0350	•		•
NVSS J181118+034113	272.83	3.687	3FHL J1811.3+0341		•	
3FHL J0706.1+0247	106.53	2.790	3FHL J0706.1+0247		•	
PKS 1546+027	237.37	2.631	3FGL J1549.4+0237	•		•
1H 0323+022	51.56	2.421	3FGL J0326.2+0225		•	
RGB J0152+017	28.14	1.778	3FHL J0152.6+0147	•	•	•
PKS 0736+017	114.83	1.628	3FHL J0739.3+0137	•	•	•
4C +01.28	164.63	1.564	3FGL J1058.5+0133	•		•
PKS 0310+013	48.19	1.561	3FGL J0312.7+0133	•		•
1ES 0414+009	64.22	1.089	3FHL J0416.8+0105	•	•	•
PKS 0422+00	66.18	0.595	3FGL J0424.7+0035	•		•
1RXS J002200.9+000659	5.50	0.116	3FHL J0022.0+0006		•	
1RXS J115404.9-001008	178.52	-0.169	3FHL J1154.1-0010		•	
PKS 0440-00	70.66	-0.299	3FGL J0442.6-0017	•		•
PKS 1215-002	184.51	-0.497	3FGL J1218.0-0029	•		•
PMN J2014-0047	303.61	-0.798	3FHL J2014.4-0047	•		•
PKS 0420-01	65.83	-1.342	3FHL J0423.3-0120	•		•
PKS 0336-01	54.88	-1.768	3FHL J0339.5-0146	•		•
PMN J1028-0237	157.14	-2.584	3FGL J1028.5-0235	•		
NVSS J060915-024754	92.31	-2.798	3FHL J0609.2-0247		•	
TXS 2106-030	317.19	-2.843	3FGL J2108.6-0250		•	
TXS 0800-034	120.80	-3.599	3FHL J0803.2-0336		•	
NVSS J152048-034850	230.20	-3.814	3FGL J1520.8-0348		•	
PKS B1310-041	198.22	-4.403	3FGL J1312.8-0424	•		
PMN J0017-0512	4.40	-5.205	3FGL J0017.6-0512	•		•
3C 279	194.04	-5.795	3FHL J1256.1-0547	•		•
1RXS J120417.0-070959	181.07	-7.169	3FHL J1204.2-0709		•	

Name	α (°)	δ (°)	Fermi Name	MAGIC	VERITAS	H.E.S.S.
1RXS J081917.6-075620	124.82	-7.941	3FHL J0819.4-0756		•	
PKS 0605-08	92.01	-8.589	3FGL J0608.0-0835	•		•
PMN J0953-0840	148.26	-8.672	3FHL J0953.0-0840		•	
PMN J2016-0903	304.10	-9.084	3FGL J2016.4-0905	•		•
PKS 1510-089	228.21	-9.108	3FHL J1512.8-0906	•	•	•
PKS 0048-09	12.67	-9.485	3FGL J0050.6-0929	•		•
PKS 0139-09	25.37	-9.485	3FGL J0141.4-0929	•		•
TXS 0053-098	14.10	-9.617	3FHL J0056.3-0936	•	•	•
PKS 1352-104	208.75	-10.738	3FGL J1355.0-1044	•		•
1RXS J022314.6-111741	35.81	-11.294	3FHL J0223.0-1119		•	
TXS 1951-115	298.70	-11.377	3FGL J1954.8-1122	•		•
PKS 1346-112	207.41	-11.560	3FGL J1349.6-1133	•		•
PKS 0113-118	19.01	-11.579	3FGL J0116.0-1134	•		•
PMN J1256-1146	194.07	-11.777	3FHL J1256.2-1146		•	
1ES 0347-121	57.35	-11.977	3FHL J0349.3-1159	•		•
PMN J0850-1213	132.52	-12.239	3FHL J0850.0-1214	•		•
TXS 0637-128	100.03	-12.888	3FGL J0640.0-1252		•	
PKS 1730-13	263.25	-13.069	3FHL J1733.0-1304	•		•
PKS 0403-13	61.40	-13.123	3FGL J0405.5-1307	•		•
PMN J0816-1311	124.11	-13.198	3FHL J0816.4-1311		•	
TXS 0938-133	145.24	-13.618	3FGL J0940.9-1337	•		•
PKS 2233-148	339.15	-14.551	3FHL J2236.5-1433	•		•
PKS 2155-152	329.52	-15.032	3FGL J2158.0-1501	•		•
PMN J2345-1555	356.30	-15.915	3FHL J2345.1-1554	•		•
PKS 2345-16	357.00	-16.511	3FHL J2347.9-1630	•		•
1RXS J102658.5-174905	156.73	-17.840	3FGL J1026.9-1750	•		•
PKS 1958-179	300.26	-17.845	3FGL J2001.0-1750	•		•
SHBL J001355.9-18540	3.47	-18.891	3FGL J0013.9-1853	•		•
KUV 00311-1938	8.39	-19.359	3FHL J0033.5-1921	•		•
1H 1914-194	289.44	-19.366	3FHL J1917.7-1921	•		•
PKS 0925-203	142.00	-20.620	3FGL J0927.9-2037	•		•
PKS 0338-214	55.14	-21.322	3FGL J0340.5-2119			•
PMN J1159-2142	179.82	-21.684	3FGL J1159.2-2141			•
PKS 1004-217	151.70	-21.985	3FGL J1006.7-2159			•
PKS 1156-221	179.83	-22.440	3FGL J1159.3-2226			•
PKS 0823-223	126.50	-22.505	3FGL J0825.9-2230			•
1ES 1101-232	165.91	-23.492	3FGL J1103.5-2329			•
PKS 0301-243	45.87	-24.123	3FGL J0303.4-2407			•
AP Lib	229.42	-24.372	3FGL J1517.6-2422			•
NGC 253	11.89	-25.288	3FGL J0047.5-2516			•

Name	α (°)	δ (°)	Fermi Name	MAGIC	VERITAS	H.E.S.S.
PKS 1244-255	191.69	-25.791	3FGL J1246.7-2547			•
PMN J0622-2605	95.61	-26.115	3FGL J0622.4-2606			•
PMN J2250-2806	342.68	-28.116	3FGL J2250.7-2806			•
Galactic Centre	266.42	-29.008	3FHL J1745.6-2900	•		•
PKS B1921-293	291.22	-29.235	3FGL J1924.8-2914			•
PKS 1034-293	159.27	-29.583	3FGL J1037.0-2934			•
PKS 2155-304	329.72	-30.227	3FGL J2158.8-3013			•
H 2356-309	359.78	-30.628	3FHL J2359.1-3038			•
1RXS J101015.9-311909	152.57	-31.340	3FGL J1010.2-3120			•
PKS 0548-322	87.67	-32.271	3FGL J0550.6-3217			•
PKS 2220-351	335.59	-35.012	3FGL J2222.3-3500			•
PKS 0625-35	96.78	-35.488	3FGL J0627.0-3529			•
PMN J1125-3556	171.38	-35.970	3FGL J1125.5-3558			•
PKS 0521-36	80.74	-36.471	3FGL J0522.9-3628			•
NVSS J223708-392137	339.29	-39.361	3FGL J2237.1-3921			•
1ES 2322-409	351.18	-40.683	3FHL J2324.7-4040			•
1ES 1312-423	198.76	-42.614	3FHL J1315.0-4237			•
Centaurus A	201.37	-43.019	3FHL J1325.5-4300			•
PKS 0447-439	72.36	-43.836	3FGL J0449.4-4350			•
PKS 0537-441	84.71	-44.086	3FGL J0538.8-4405			•
PKS 2322-482	351.36	-47.975	3FGL J2325.4-4758			•
PKS 2005-489	302.35	-48.828	3FGL J2009.3-4849			•
PKS 2326-502	352.33	-49.923	3FGL J2329.3-4955			•
PKS 0903-57	136.22	-57.571	3FGL J0904.8-5734			•
PKS 0235-618	39.20	-61.600	3FGL J0236.7-6136			•
PKS 1057-79	164.63	-80.051	3FGL J1058.5-8003			•

Table A.1: List of sources monitored by the online flare search (Sec. 6.1).

B List of Archival Alerts

	Source Name	MJD	Duration	n_s	γ	$-\log_{10} p$	MAGIC	VERITAS	H.E.S.S.
2011	MG2 J110606+2812	55696.0	4.7 h	2.8	-2.3	2.9	•		
	RBS 0970	55713.0	22.2 m	3.0	-2.2	4.5		•	
	TXS 1902+556	55759.7	10.4 d	7.1	-4.0	2.9		•	
	Mrk 180	55773.6	44.6 d	4.5	-1.3	3.1	•	•	
	Mrk 180	55788.4	59.5 d	5.7	-1.5	3.4	•	•	
	ZS 0214+083	55806.2	5.3 d	6.2	-2.3	2.9	•		
	Mrk 180	55818.1	89.1 d	6.4	-1.6	3.1	•	•	
	ZS 0214+083	55837.7	36.8 d	8.4	-2.4	2.9	•		•
	TXS 1312+240	55854.5	21.4 h	6.3	-4.0	2.9		•	
	PKS 0422+00	55884.3	31.6 d	10.9	-3.1	3.1	•		•
	S5 1027+74	55918.3	13.3 h	4.8	-3.6	3.8	•		
2012	87GB 195252.4+135009	55961.8	45.5 d	14.8	-3.4	3.1	•		•
	RBS 0413	55962.0	3.8 d	5.9	-4.0	3.0	•	•	•
	RBS 0413	55967.2	9.0 d	8.3	-4.0	3.1	•	•	•
	TXS 1055+567	56053.6	16.8 d	9.3	-3.7	3.2	•	•	
	TXS 1055+567	56060.0	23.2 d	10.0	-3.7	2.9	•	•	
	TXS 1055+567	56087.9	51.0 d	13.7	-3.9	2.9	•	•	
	RX J0908.9+2311	56091.5	2.4 h	3.0	-3.0	3.5	•		•
	TXS 1055+567	56099.6	62.8 d	14.1	-3.8	3.0	•	•	
	PKS 0537-441	56159.2	23.3 m	2.0	-2.3	3.2			•
	PKS 1424+240	56182.2	79.5 d	14.5	-3.0	2.9		•	
	MAGIC J2001+435	56185.7	14.1 m	2.0	-1.9	2.9		•	
	PKS 1424+240	56186.1	83.4 d	14.8	-3.0	2.9		•	
	GB6 J0342+3858	56212.4	22.1 d	12.2	-3.1	3.2	•		
	1ES 1741+196	56289.2	146.8 d	14.0	-3.4	2.9	•		
2013	SBS 0812+578	56324.3	165.2 d	14.0	-3.6	3.0		•	
	S3 0218+35	56340.0	178.6 d	18.4	-4.0	3.1	•	•	•
	PKS 1725+123	56406.0	2.9 d	7.1	-2.6	3.5	•		•
	3C 380	56488.2	74.5 d	13.9	-3.8	2.9	•		
	3C 380	56496.2	82.5 d	14.2	-3.8	3.0	•		

	Source Name	MJD	Duration	n_s	γ	$-\log_{10} p$	MAGIC	VERITAS	H.E.S.S.
	SBS 1646+499	56617.8	3.0 h	3.9	-2.0	3.4	•		
	GB6 J0154+0823	56657.2	79.3 d	19.6	-3.0	3.1		•	
2014	GB6 J0154+0823	56661.2	83.2 d	19.1	-3.0	2.9		•	
	GB6 J0154+0823	56688.1	110.1 d	21.3	-2.7	3.4		•	
	1RXS J081917.6-075620	56694.3	8.8 h	2.0	-1.4	3.1		•	
	GB6 J0154+0823	56701.7	123.7 d	20.4	-2.8	2.9		•	
	GB6 J0154+0823	56711.2	133.2 d	21.0	-2.8	3.0		•	
	SBS 1646+499	56721.8	151.4 d	17.2	-3.1	2.9	•		
	MG4 J225201+4030	56729.1	19.4 d	5.6	-2.2	2.9		•	
	MG4 J225201+4030	56741.5	31.8 d	7.5	-2.5	2.9		•	
	PKS 1717+177	56751.8	26.7 d	10.3	-2.9	3.1	•	•	•
	PKS 1717+177	56755.5	30.4 d	11.0	-2.9	3.1	•	•	•
	RX J1702.6+3115	56803.0	90.1 d	14.0	-4.0	3.0		•	
	CGCG 050-083	56883.7	14.4 h	3.9	-2.5	3.0		•	
	B3 2247+381	56885.1	1.5 h	3.0	-2.4	3.1	•	•	
	CGCG 050-083	56885.2	2.1 d	5.6	-2.5	3.4		•	
	1ES 0347-121	57022.9	1.9 h	2.0	-2.3	3.6	•		•
2015	CGCG 050-083	57039.9	2.7 d	5.8	-4.0	3.2		•	
	TXS 0506+056	57073.0	145.2 d	10.2	-2.2	3.0	•	•	•
	1ES 1440+122	57076.8	8.1 d	8.9	-4.0	3.0	•	•	
	1ES 1440+122	57080.5	11.8 d	10.1	-4.0	3.2	•	•	
	TXS 0506+056	57084.1	156.3 d	10.3	-2.2	2.9	•		•
	TXS 0506+056	57089.4	161.7 d	12.0	-2.2	3.7	•	•	•
	B2 0619+33	57137.5	55.3 d	8.7	-3.2	2.9		•	
	OC 457	57160.0	1.3 d	2.9	-2.8	2.9	•		
	B2 0619+33	57167.5	85.3 d	10.9	-3.3	2.9		•	
	B2 0619+33	57175.7	93.6 d	11.3	-3.2	2.9		•	
	B2 0619+33	57195.3	113.2 d	12.5	-3.6	2.9		•	
	1RXS J193320.3+072616	57196.3	2.1 d	6.1	-2.8	3.2		•	
	B2 0619+33	57197.3	115.1 d	12.7	-3.6	2.9		•	
	1ES 0414+009	57199.1	4.0 d	6.6	-2.6	3.0	•	•	•
	B2 0619+33	57202.4	120.2 d	12.8	-3.3	2.9		•	
	B2 0619+33	57208.5	126.3 d	13.6	-3.2	3.0		•	
	OQ 530	57294.0	27.6 m	3.0	-2.0	3.2	•		
	RGB J2243+203	57308.9	130.5 d	17.5	-3.3	3.1		•	
	PKS 2005-489	57310.6	67.8 d	3.7	-4.0	2.9			•
	RGB J2243+203	57321.0	142.7 d	17.4	-3.3	2.9		•	
	RGB J2243+203	57332.6	154.2 d	19.5	-3.3	3.6		•	

	Source Name	MJD	Duration	n_s	γ	$-\log_{10} p$	MAGIC	VERITAS	H.E.S.S.
2016	1RXS J013748.0+581422	57334.6	2.0 d	4.8	-2.4	2.9		•	
	S4 1849+67	57342.3	12.7 h	3.9	-3.1	3.5	•		
	MG1 J050533+0415	57346.1	3.2 d	7.3	-4.0	2.9		•	
	RGB J2243+203	57368.1	176.5 d	17.7	-3.2	2.9		•	
	RGB J2243+203	57371.4	179.7 d	18.2	-3.2	3.0		•	
	RGB J2243+203	57386.5	122.8 d	15.1	-3.2	2.9		•	
	RGB J2243+203	57390.2	126.5 d	15.3	-3.1	3.0		•	
	RGB J2243+203	57393.2	129.5 d	15.3	-3.1	2.9		•	
	GB6 J0937+5008	57394.5	36.8 m	3.0	-3.2	3.2	•		
	RGB J2243+203	57413.3	149.6 d	15.7	-3.0	2.9		•	
	NVSS J173605+203301	57436.7	17.4 d	11.7	-3.2	2.9		•	
	6C B163030.4+771303	57458.1	2.4 h	3.0	-3.3	3.3	•		
	RBS 1040	57473.1	11.8 d	4.1	-1.4	3.2		•	
	H 2356-309	57514.7	32.8 d	5.3	-2.3	3.0			•
	1ES 0806+524	57515.5	25.3 d	2.9	-1.2	3.8	•	•	
	H 2356-309	57531.9	50.0 d	5.9	-2.3	3.3			•
	H 2356-309	57556.5	81.1 d	6.8	-2.3	3.4			•
	PKS 1725+044	57564.5	1.1 h	3.0	-4.0	3.5	•		•
	1ES 1215+303	57565.6	15.7 d	9.1	-3.8	3.4	•	•	•
	1ES 1218+304	57566.1	5.6 d	7.0	-4.0	3.1	•	•	•
	S4 1250+53	57631.6	38.1 d	8.6	-2.8	2.9		•	
	NVSS J205350+292314	57635.2	7.6 h	3.9	-4.0	3.1		•	
	NVSS J205350+292314	57638.3	3.3 d	5.7	-3.3	2.9		•	
	Mrk 421	57667.3	7.1 h	3.9	-3.9	3.0	•	•	•
	GB6 J1542+6129	57707.8	152.9 d	9.5	-2.5	2.9		•	
	1RXS J013106.4+612035	57709.8	35.4 d	8.5	-4.0	3.0		•	
	GB6 J1542+6129	57712.1	157.2 d	9.7	-2.5	2.9		•	
	SBS 1646+499	57715.9	5.0 h	2.9	-1.6	3.0	•		
	SBS 1646+499	57716.5	19.4 h	4.3	-2.1	3.5	•		
	GB6 J1542+6129	57717.8	162.9 d	9.6	-2.5	2.9		•	
	1RXS J013106.4+612035	57718.8	44.3 d	9.0	-4.0	3.0		•	
	GB6 J1542+6129	57726.7	171.8 d	10.0	-2.5	2.9		•	
	B2 1732+38A	57727.0	71.0 d	9.6	-2.3	2.9	•		
	M 87	57730.0	3.9 m	3.0	-2.8	4.0	•	•	•
	TXS 0506+056	57735.4	1.1 d	6.2	-3.3	3.0	•	•	•
	GB6 J1542+6129	57735.4	177.9 d	10.7	-2.5	3.0		•	
	GB6 J0154+0823	57738.7	68.1 d	4.0	-1.7	3.4		•	
	GB6 J1542+6129	57761.1	142.4 d	8.9	-2.4	2.9		•	

	Source Name	MJD	Duration	n_s	γ	$-\log_{10} p$	MAGIC	VERITAS	H.E.S.S.
2017	1RXS J013106.4+612035	57769.6	95.1 d	11.1	-3.9	3.0		•	
	1RXS J013106.4+612035	57778.6	104.1 d	11.8	-3.9	3.0		•	
	GB6 J1542+6129	57800.4	171.1 d	10.6	-2.5	3.1		•	
	1RXS J013106.4+612035	57801.3	126.9 d	13.1	-3.9	3.0		•	
	87GB 195252.4+135009	57811.0	2.5 h	3.0	-2.3	3.2	•		•
	GB6 J0045+2127	57830.2	13.6 d	10.1	-4.0	2.9		•	
	GB6 J0045+2127	57831.4	14.8 d	11.4	-4.0	3.6		•	
	1RXS J013106.4+612035	57836.1	161.6 d	14.1	-3.9	2.9		•	
	OI 280	57842.6	2.2 d	5.8	-4.0	3.5	•		
	1RXS J013106.4+612035	57843.8	169.4 d	15.1	-3.8	3.1		•	
	PKS 1215-002	57860.1	5.3 d	7.1	-3.6	3.5	•		•
	PMN J1028-0237	57904.0	4.7 d	5.9	-4.0	2.9	•		
	1ES 0229+200	57922.6	134.8 d	16.4	-4.0	2.9	•		
	1ES 0229+200	57922.7	92.4 d	14.1	-4.0	2.9		•	•
	1ES 0229+200	57925.7	137.8 d	16.9	-4.0	2.9	•	•	•
	NVSS J232914+375414	57927.4	2.9 d	7.9	-4.0	3.0		•	
	NVSS J232914+375414	57930.5	6.0 d	9.7	-3.5	3.6		•	
	GB6 J0515+1527	57936.3	110.4 d	19.8	-3.3	3.0		•	
	MS 1221.8+2452	57947.4	3.1 d	5.6	-3.1	3.3	•	•	•
	1ES 0414+009	57950.0	3.6 d	7.0	-3.2	2.9	•	•	•
	GB6 J0045+2127	58001.2	173.8 d	10.0	-2.1	2.9		•	
	OC 457	58036.5	72.5 d	14.6	-3.1	3.3	•		
	PKS 0139-09	58042.2	2.7 d	3.8	-3.9	3.0	•		•
	1ES 1011+496	58053.9	19.0 h	3.9	-2.0	3.7	•	•	
	OC 457	58087.1	123.1 d	15.9	-3.3	3.1	•		
	RX J1702.6+3115	58092.9	13.8 h	5.2	-2.7	3.4		•	
	RX J1702.6+3115	58095.2	2.9 d	6.4	-2.7	3.0		•	
	RX J1702.6+3115	58096.3	5.9 d	7.5	-2.7	3.7		•	
	PKS 0139-09	58104.2	94.9 d	6.8	-3.9	3.0	•		•
	1RXS J234332.5+343957	58113.5	92.0 d	13.6	-4.0	3.0		•	
2018	PKS 0139-09	58125.7	116.5 d	7.2	-3.9	2.9	•		•
	VER J0521+211	58131.5	29.0 d	9.7	-2.5	3.0	•	•	•
	VER J0521+211	58138.1	35.6 d	10.5	-2.6	2.9	•		
	VER J0521+211	58148.9	46.4 d	11.1	-2.5	3.2	•	•	•
	PKS 0139-09	58157.2	148.0 d	7.7	-3.9	3.0	•		•
	PKS 0605-08	58163.4	23.8 d	6.3	-3.2	3.6	•		•
	TXS 1902+556	58299.7	56.3 d	11.6	-3.1	2.9		•	
	TXS 1902+556	58307.9	64.5 d	12.7	-3.1	3.0		•	
	4C +31.03	58328.2	9.4 d	4.0	-1.8	3.1	•		•

	Source Name	MJD	Duration	n_s	γ	$-\log_{10} p$	MAGIC	VERITAS	H.E.S.S.
	OX 169	58348.3	1.9 d	6.5	-2.9	3.4	•		•
	PKS 1034-293	58350.0	167.5 d	6.8	-4.0	3.8			•
	OX 169	58352.2	5.8 d	7.2	-3.2	3.2	•		•
	4C +45.08	58472.7	23.4 h	5.6	-3.5	2.9	•		
	GB6 J0937+5008	58475.8	153.5 d	14.6	-2.7	2.9	•		
2019	GB6 J0937+5008	58506.5	175.2 d	15.6	-2.8	3.0	•		
2019	1RXS J192649.5+615445	58526.6	32.8 m	3.0	-3.9	3.4		•	

Table B.1: List of alerts from the monitored sources, which were found by scanning the archival data sample from May 2011 to March 2019. These alerts would have been sent out, if the current system had been running in the past. "MJD" lists the time of the alert trigger, while "Duration" shows how far the fitted time window extends from the given "MJD" into the past. n_s and γ are the fit results for the number of signal-like events and the spectral index. p is the pre-trial significance level.

C List of High Energy Muons

	Run	Event	MJD	α (deg)	δ (deg)	$\sigma_{50\%}$ (deg)	$\sigma_{90\%}$ (deg)	$\hat{E}_\mu$ (TeV)	E_ν^{peak} (TeV)	Signalness (%)	Referenced in EHE	Diffuse	HESE
2011	118178	17334444	55695.1	136.9	-1.9	0.5	1.3	157	187	51 %			
	118309	46569873	55722.4	272.9	35.7	0.3	0.9	253	294	75 %		•	
	118631	36844560	55806.1	9.7	7.7	0.2	0.5	215	243	61 %			
	118660	61529737	55811.8	196.6	9.2	0.2	0.5	156	186	51 %			
	119136	66932419	55911.3	36.8	18.5	0.5	1.3	794	891	95 %		•	
2012	119739	41603205	55987.8	238.1	18.9	0.2	0.5	378	433	82 %	•		
	120157	59255331	56063.0	198.8	31.7	0.3	0.7	167	194	61 %		•	
	120535	24248640	56146.2	330.0	1.7	0.2	0.5	318	373	74 %		•	
	120680	12284754	56186.3	182.5	3.8	0.3	0.9	139	174	44 %			
	120798	20915945	56211.8	205.3	-2.4	0.2	0.5	431	481	84 %	•	•	
	120860	64513030	56226.6	170.2	27.9	0.2	0.6	850	961	93 %		•	
2013	121769	40349510	56319.3	353.4	-2.0	0.3	0.7	207	235	61 %			
	122604	17469985	56470.1	93.0	16.9	0.3	0.8	762	851	94 %		•	•
	123107	8144529	56579.9	33.3	10.2	0.2	0.5	252	293	67 %		•	
	123281	52248792	56620.1	285.7	19.6	0.2	0.5	147	180	55 %			
2014	123620	47444787	56658.4	191.5	-2.9	0.2	0.6	176	200	56 %			
	123762	72626160	56666.5	293.3	33.5	0.2	0.5	821	924	93 %	•	•	
	124547	66087371	56757.1	162.1	86.0	6.2	16.0	216	246	63 %			
	124852	74171655	56817.6	106.1	1.2	0.2	0.6	406	459	82 %		•	
	124861	32863663	56819.2	110.1	11.1	0.2	0.5	5,846	5,960	>99 %	•	•	
	125001	73159253	56843.7	25.7	2.7	0.4	1.1	186	212	56 %			
	125349	12316485	56927.2	51.0	-0.3	0.5	1.3	149	182	48 %			

	Run	Event	MJD	α (deg)	δ (deg)	$\sigma_{50\%}$ (deg)	$\sigma_{90\%}$ (deg)	$\hat{E}_{\mu}$ (TeV)	E_{ν}^{peak} (TeV)	Signalness (%)	Referenced in EHE	Diffuse	HESE
2015	125968	61389842	57049.5	100.4	4.4	0.2	0.5	252	293	66 %		•	
	126370	61611641	57157.9	91.7	11.9	0.3	0.9	344	401	77 %		•	
	126620	19175993	57217.9	326.0	25.4	0.2	0.6	393	447	84 %		•	
	126718	53509959	57246.8	328.7	6.0	0.2	0.5	459	509	83 %	•	•	
	126798	67205547	57265.2	54.8	34.7	0.2	0.5	147	180	58 %	•		
	126812	38566267	57269.8	133.9	27.8	0.2	0.5	260	304	74 %		•	
	126863	14025085	57284.2	279.7	30.2	0.3	0.7	201	228	67 %			
	126989	59479399	57312.7	197.3	21.0	0.8	2.1	274	323	76 %		•	
	127112	69211097	57340.9	76.3	12.6	0.3	0.9	968	1,090	95 %		•	
	127154	9907321	57348.5	262.1	-2.3	0.2	0.5	213	242	62 %	•		
2016	127357	17650073	57391.4	78.1	4.7	0.4	1.0	187	212	56 %			
	127603	48070937	57443.9	312.2	60.6	0.3	0.7	146	179	58 %			
	127742	55820225	57478.6	151.3	15.9	0.2	0.5	449	498	85 %		•	
	128311	26552458	57606.5	122.6	-0.7	0.2	0.5	192	218	58 %	•		
	128547	14557367	57655.7	240.5	1.8	1.0	2.6	150	182	48 %			
	128567	21044380	57662.4	191.7	36.8	0.4	1.0	180	205	64 %			
	128606	54200591	57673.6	189.4	-8.2	0.3	0.9	684	759	25 %			
	128755	32356079	57709.3	78.3	1.9	0.4	0.9	162	191	51 %			

	Run	Event	MJD	α (deg)	δ (deg)	$\sigma_{50\%}$ (deg)	$\sigma_{90\%}$ (deg)	$\hat{E}_\mu$ (TeV)	E_ν^{peak} (TeV)	Signalness (%)	Referenced in EHE	Diffuse	HESE
2017	129020	20626582	57758.1	311.6	7.9	0.5	1.2	154	185	49 %			
	129506	49650572	57887.3	226.7	30.3	0.2	0.5	140	175	56 %			
	129677	55886338	57930.5	281.0	8.9	0.3	0.7	176	201	55 %			
	129701	49353375	57938.3	230.3	23.3	0.2	0.5	167	195	60 %			
	129777	67372962	57951.8	208.2	26.2	0.3	0.8	481	534	87 %			
	129855	33565191	57968.1	2.0	4.4	0.9	2.4	183	208	55 %			
	129878	40814378	57974.6	20.9	-2.3	0.2	0.5	199	226	60 %			
	129933	32926212	57989.6	41.7	12.1	0.7	1.8	141	175	49 %			
	130033	50579430	58018.9	77.3	5.7	0.2	0.5	231	264	63 %	•		
	130034	7858514	58019.0	173.1	-2.7	0.2	0.5	178	202	56 %			
	130214	17569642	58063.8	340.3	7.3	0.2	0.5	1,485	1,573	98 %	•		
2018	130588	44934051	58141.7	75.1	13.3	0.5	1.3	358	415	79 %			
	130912	76035104	58218.8	218.6	0.4	0.2	0.5	206	234	60 %			
	130932	35022693	58225.3	305.9	-4.2	0.2	0.5	178	202	58 %			
	131764	48222919	58442.7	26.5	13.0	1.0	2.6	158	188	54 %			
	131767	7377802	58442.9	323.4	49.4	1.1	2.9	138	174	57 %			
	131768	80926380	58443.6	132.0	32.9	0.4	1.0	184	208	64 %			
2019	132206	36575563	58528.7	228.1	-4.2	0.2	0.5	294	348	74 %			

Table C.1: High-energy muons found in the archival dataset which would have been selected for an automatic alert. The three right-most columns indicate whether the events have been previously identified in the extreme high-energy alert system ("EHE"), the high-energy starting event analysis or its alert system ("HESE"), or in the measurement of the diffuse astrophysical flux ("Diffuse", only until the beginning of 2016).

Bibliography

[1] D. Pacini. La Radiazione Penetrante alla Superficie ed in Seno alle Acque. *Il Nuovo Cimento*, 3, 93 (1912) (see p. 17)

[2] V. F. Hess. Über Beobachtungen der durchdringenden Strahlung bei sieben Freiballonfahrten. *Physikalische Zeitschrift*, 13, 1084 (1912) (see p. 17)

[3] M. Tanabashi et al. (Particle Data Group). Review of Particle Physics. *Phys. Rev. D*, 98, 030001 (2018) (see p. 18)

[4] K. Greisen. End to the Cosmic Ray Spectrum?, *Phys. Rev. Lett.* 16, 748 (1966) (see p. 18)

[5] G. T. Zatsepin and V. A. Kuzmin. Upper Limit of the Spectrum of Cosmic Rays. *JETP Lett.* 4, [Pisma Zh. Eksp. Teor. Fiz.4,114(1966)], 78 (1966) (see p. 18)

[6] J. Bellido (Pierre Auger). "Depth of Maximum of Air-shower Profiles at the Pierre Auger Observatory: Measurements above $10^{17.2}$ eV and Composition Implications", in 35th International Cosmic Ray Conference (ICRC): Busan, Korea (2017), p. 506 (see p. 19)

[7] D. Ikeda and W. Hanlon (Telescope Array). "Hybrid Measurement of the Energy Spectrum and Composition of Ultra-High Energy Cosmic Rays by the Telescope Array", in 35th International Cosmic Ray Conference (ICRC): Busan, Korea (2017), p. 515 (see p. 19)

[8] M. Aguilar et al. (AMS). Precision Measurement of the $(e^+ + e^-)$ Flux in Primary Cosmic Rays from 0.5 GeV to 1 TeV with the Alpha Magnetic Spectrometer on the International Space Station. *Phys. Rev. Lett.* 113, 221102 (2014) (see p. 19)

[9] W. Baade and F. Zwicky. Cosmic Rays from Super-novae. *Contributions from the Mount Wilson Observatory*, 3, 79 (1934) (see pp. 19, 24)

[10] M. Ackermann et al. (Fermi-LAT). Detection of the Characteristic Pion-Decay Signature in Supernova Remnants. *Science*, 339, 807 (2013) (see pp. 19, 24)

[11] A. Aab et al. (Pierre Auger). Observation of a Large-scale Anisotropy in the Arrival Directions of Cosmic Rays above 8×10^{18} eV. *Science*, 357, 1266 (2017) (see p. 19)

[12] A. Aab et al. (Pierre Auger). Measurement of the Cosmic Ray Spectrum above 4×10^{18} eV Using Inclined Events Detected with the Pierre Auger Observatory. *JCAP*, 1508, 049 (2015) (see p. 19)

[13] M. Honda, T. Kajita, K. Kasahara, S. Midorikawa, and T. Sanuki. Calculation of Atmospheric Neutrino Flux using the Interaction Model Calibrated with Atmospheric Muon Data. *Phys. Rev.* D75, 043006 (2007) (see pp. 20, 72, 97, 98, 136, 157)

[14] A. Bhattacharya, R. Enberg, M. H. Reno, I. Sarcevic, and A. Stasto. Perturbative Charm Production and the Prompt Atmospheric Neutrino Flux in Light of RHIC and LHC. *JHEP*, 06, 110 (2015) (see pp. 20, 98)

[15] C. Haack and C. Wiebusch (IceCube). "A Measurement of the Diffuse Astrophysical Muon Neutrino Flux Using Eight Years of IceCube Data", in 35th International Cosmic Ray Conference (ICRC): Busan, Korea (2017), p. 1005 (see pp. 20, 85, 96–98, 136, 141, 143, 144, 157, 158)

[16] E. Fermi. On the Origin of the Cosmic Radiation. *Phys. Rev.* 75, 1169 (1949) (see pp. 20, 24)

[17] P. M. Bauleo and J. R. Martino. The Dawn of the Particle Astronomy Era in Ultra-high-energy Cosmic Rays. *Nature*, 458, 847 (2009) (see p. 21)

[18] C. M. Urry and P. Padovani. Unified Schemes for Radio-loud Active Galactic Nuclei. *Publ. Astron. Soc. Pac.* 107, 803 (1995) (see p. 22)

[19] M. G. Aartsen et al. (IceCube, Fermi-LAT, MAGIC, AGILE, ASAS-SN, HAWC, H.E.S.S., INTEGRAL, Kanata, Kiso, Kapteyn, Liverpool Telescope, Subaru, Swift NuSTAR, VERITAS, VLA/17B-403). Multimessenger Observations of a Flaring Blazar Coincident with High-energy Neutrino IceCube-170922A. *Science*, 361, eaat1378 (2018) (see pp. 23, 154, 155)

[20] B. Pontecorvo. Mesonium and Antimesonium. *Soviet Journal of Experimental and Theoretical Physics*, 6, 429 (1958) (see p. 23)

[21] S. Sahu, A. F. Osorio Oliveros, and J. C. Sanabria. Hadronic-origin Orphan TeV Flare from 1ES 1959+650. *Phys. Rev.* D87, 103015 (2013) (see p. 23)

[22] R. M. Bionta et al. (IMB). Observation of a Neutrino Burst in Coincidence with Supernova SN 1987a in the Large Magellanic Cloud. *Phys. Rev. Lett.* 58, 1494 (1987) (see p. 24)

[23] K. Hirata et al. (Kamiokande-II). Observation of a Neutrino Burst from the Supernova SN 1987a. *Phys. Rev. Lett.* 58, 1490 (1987) (see p. 24)

[24] W. D. Arnett, J. N. Bahcall, R. P. Kirshner, and S. E. Woosley. Supernova 1987A. *Ann. Rev. Astron. Astrophys.* 27, 629 (1989) (see p. 24)

[25] M. Aglietta et al. Coincidences Among the Data Recorded by the Baksan, Kamioka and Mont Blanc Underground Neutrino Detectors, and by the Maryland and Rome Gravitational Wave Detectors During Supernova SN1987A. *Nuovo Cim.* C14, 171 (1991) (see p. 24)

[26] S. E. Woosley and J. S. Bloom. The Supernova Gamma-Ray Burst Connection. *Ann. Rev. Astron. Astrophys.* 44, 507 (2006) (see p. 24)

[27] B. P. Abbott et al. (LIGO Scientific, Virgo). GW170817: Observation of Gravitational Waves from a Binary Neutron Star Inspiral. *Phys. Rev. Lett.* 119, 161101 (2017) (see p. 24)

[28] M. Ackermann et al. (Fermi-LAT). The Fermi Large Area Telescope On Orbit: Event Classification, Instrument Response Functions, and Calibration. *Astrophys. J. Suppl.* 203, 4 (2012) (see p. 24)

[29] J. Aleksić et al. The Major Upgrade of the MAGIC Telescopes, Part I: The Hardware Improvements and the Commissioning of the System. *Astropart. Phys.* 72, 61 (2016) (see p. 24)

[30] J. Aleksić et al. The Major Upgrade of the MAGIC Telescopes, Part II: A Performance Study Using Observations of the Crab Nebula. *Astropart. Phys.* 72, 76 (2016) (see p. 24)

[31] J. Holder et al. "Status of the VERITAS Observatory", in 4th Heidelberg International Symposium on High-Energy Gamma Ray Astronomy: Heidelberg, Germany, Vol. 1085, 1 (2008), pp. 657–660 (see p. 24)

[32] M. de Naurois (H.E.S.S.). "H.E.S.S.-II - Gamma ray astronomy from 20 GeV to hundreds of TeV's", in 6th Roma International Workshop on Astroparticle Physics (RICAP): Rome, Italy, Vol. 136 (2016), p. 03001 (see p. 24)

[33] F. Aharonian et al. (H.E.S.S.). A Low Level of Extragalactic Background Light as Revealed by Gamma-rays from Blazars. *Nature*, 440, 1018 (2006) (see pp. 24, 110)

[34] A. Dominguez et al. Extragalactic Background Light Inferred from AEGIS Galaxy SED-type Fractions. *Mon. Not. Roy. Astron. Soc.* 410, 2556 (2011) (see pp. 24, 110)

[35] S. Abdollahi et al. (Fermi-LAT). A Gamma-ray Determination of the Universe's Star Formation History. *Science*, 362, 1031 (2018) (see p. 24)

[36] M. L. Ahnen et al. (MAGIC). Detection of Very High Energy Gamma-ray Emission from the Gravitationally-lensed Blazar QSO B0218+357 with the MAGIC Telescopes. *Astron. Astrophys.* 595, A98 (2016) (see pp. 24, 110)

[37] R. Enberg, M. H. Reno, and I. Sarcevic. Prompt Neutrino Fluxes from Atmospheric Charm. *Phys. Rev.* D78, 043005 (2008) (see p. 26)

[38] C. Kopper, W. Giang, and N. Kurahashi (IceCube). "Observation of Astrophysical Neutrinos in Four Years of IceCube Data", in 34th International Cosmic Ray Conference (ICRC): The Hague, The Netherlands (2015), p. 1081 (see pp. 26, 158)

[39] M. G. Aartsen et al. (IceCube). Observation and Characterization of a Cosmic Muon Neutrino Flux from the Northern Hemisphere using Six Years of IceCube data. *Astrophys. J.* 833, 3 (2016) (see pp. 26, 71, 72, 143, 144)

[40] J. Stettner (IceCube). "Measurement of the Diffuse Astrophysical Muon-Neutrino Spectrum with Ten Years of IceCube Data", in 36th International Cosmic Ray Conference (ICRC): Madison, WI (2019), p. 1017 (see pp. 25, 27)

[41] A. Schneider. "Characterization of the Astrophysical Diffuse Neutrino Flux with IceCube High-Energy Starting Events", in 36th International Cosmic Ray Conference (ICRC): Madison, WI (2019) (see p. 25)

[42] L. Fusco. "Study of the High-energy Neutrino Diffuse Flux with the ANTARES Neutrino Telescope", in 36th International Cosmic Ray Conference (ICRC): Madison, WI (2019), p. 891 (see p. 25)

[43] C. Kopper. "Observation of Astrophysical Neutrinos in Six Years of IceCube Data", in 35th International Cosmic Ray Conference (ICRC): Busan, Korea (2017), p. 981 (see pp. 26, 27)

[44] M. G. Aartsen et al. (IceCube). All-sky Search for Time-integrated Neutrino Emission from Astrophysical Sources with 7 yr of IceCube Data. *Astrophys. J.* 835, 151 (2017) (see pp. 26, 27, 44, 45, 71, 76, 96, 100, 103, 104, 125, 147, 148, 151, 158, 159)

[45] A. Christov, T. Montaruli, and T. Carver. "Time-dependent Point Source Searches with the IceCube Detector", in TeV Particle Astrophysics (TeVPA) (2016) (see p. 27)

[46] A. Albert et al. (ANTARES, IceCube). Joint Constraints on Galactic Diffuse Neutrino Emission from the ANTARES and IceCube Neutrino Telescopes. *Astrophys. J.* 868, L20 (2018) (see pp. 28, 89)

[47] J. Babson et al. (DUMAND). Cosmic Ray Muons in the Deep Ocean. *Phys. Rev.* D42, 3613 (1990) (see p. 29)

[48] I. A. Belolaptikov et al. (BAIKAL). The Baikal Underwater Neutrino Telescope: Design, Performance and First Results. *Astropart. Phys.* 7, 263 (1997) (see p. 29)

[49] M. Ageron et al. (ANTARES). ANTARES: The First Undersea Neutrino Telescope. *Nucl. Instrum. Meth.* A656, 11 (2011) (see p. 29)

[50] E. Andres et al. The AMANDA Neutrino Telescope: Principle of Operation and First Results. *Astropart. Phys.* 13, 1 (2000) (see p. 29)

[51] P. A. Cherenkov. Visible Emission of Clean Liquids by Action of γ Radiation. *Doklady Akademii nauk SSSR*, 451 (1934) (see pp. 29, 39, 45)

[52] M. G. Aartsen et al. (IceCube). The IceCube Neutrino Observatory: Instrumentation and Online Systems. *JINST*, 12, P03012 (2017) (see pp. 30, 34–36, 53)

[53] M. G. Aartsen et al. (IceCube). Measurement of the Cosmic-ray Energy Spectrum with IceTop-73. *Phys. Rev.* D88, 042004 (2013) (see p. 29)

[54] M. G. Aartsen et al. (IceCube). Measurement of South Pole ice transparency with the IceCube LED calibration system. *Nucl. Instrum. Meth.* A711, 73 (2013) (see p. 30)

[55] P. Askebjer et al. Optical properties of deep ice at the South Pole: Absorption. *Appl. Opt.* 36, 4168 (1997) (see p. 30)

[56] M. Ackermann et al. Optical Properties of Deep Glacial Ice at the South Pole. *J. Geophys. Res.* 111, D13203 (2006) (see pp. 30, 31)

[57] P. B. Price and K. Woschnagg. Role of group and phase velocity in high-energy neutrino observatories. *Astropart. Phys.* 15, 97 (2001) (see p. 30)

[58] J. Petit, J. Jouzel, D. Raynaud, et al. Climate and Atmospheric History of the Past 420,000 Years from the Vostok Ice Core, Antarctica. *Nature*, 429 (1999) (see p. 30)

[59] O. Watanabe et al. The Paleoclimate Record in the Ice Core from Dome Fuji Station, Antarctica. *Ann. Glaciol.* 176 (1999) (see p. 30)

[60] D. Chirkin (ICECUBE). "Evidence of Optical Anisotropy of the South Pole Ice", in 33rd International Cosmic Ray Conference (ICRC): Rio de Janeiro, Brasil (2013), p. 0580 (see p. 30)

[61] M. G. Aartsen et al. (IceCube). Search for Astrophysical Sources of Neutrinos Using Cascade Events in IceCube. *Astrophys. J.* 846, 136 (2017) (see p. 32)

[62] R. Abbasi et al. (IceCube). The IceCube Data Acquisition System: Signal Capture, Digitization, and Timestamping. *Nucl. Instrum. Meth.* A601, 294 (2009) (see p. 34)

[63] M. G. Aartsen et al. (IceCube). Energy Reconstruction Methods in the IceCube Neutrino Telescope. *JINST*, 9, P03009 (2014) (see pp. 34, 46, 47, 77)

[64] M. Zoll. A Search for Solar Dark Matter with the IceCube Neutrino Detector: Advances in Data Treatment and Analysis Technique. PhD thesis (Stockholms Universitet, 2016) (see p. 36)

[65] M. G. Aartsen et al. (IceCube). Evidence for High-Energy Extraterrestrial Neutrinos at the IceCube Detector. *Science*, 342, 1242856 (2013) (see pp. 38, 75)

[66] M. G. Aartsen et al. (IceCube). Observation of High-Energy Astrophysical Neutrinos in Three Years of IceCube Data. *Phys. Rev. Lett.* 113, 101101 (2014) (see pp. 38, 96)

[67] V. J. Stenger. *Track Fitting for DUMAND-II Octagon Array*, tech. rep. HDC-1-90 (University of Hawaii, 1990) (see p. 38)

[68] M. G. Aartsen et al. Improvement in Fast Particle Track Reconstruction with Robust Statistics. *Nucl. Instrum. Meth.* A736, 143 (2014) (see p. 39)

[69] J. Ahrens et al. (AMANDA). Muon Track Reconstruction and Data Selection Techniques in AMANDA. *Nucl. Instrum. Meth.* A524, 169 (2004) (see pp. 39, 40)

[70] D. Pandel. Bestimmung von Wasser- und Detektorparametern und Rekonstruktion von Myonen bis 100 TeV mit dem Baikal-Neutrinoteleskop NT-72. Diploma thesis (Humboldt-Universität zu Berlin, 1996) (see p. 40)

[71] J. Lundberg, P. Miocinovic, T. Burgess, J. Adams, S. Hundertmark, P. Desiati, K. Woschnagg, and P. Niessen. Light Tracking for Glaciers and Oceans: Scattering and Absorption in Heterogeneous Media with Photonics. *Nucl. Instrum. Meth.* A581, 619 (2007) (see p. 41)

[72] P. H. C. Eilers and B. D. Marx. Flexible Smoothing with B-Splines and Penalties. *Statistical Science*, 11, 89 (1996) (see p. 41)

[73] N. Whitehorn, J. van Santen, and S. Lafebre. Penalized Splines for Smooth Representation of High-dimensional Monte Carlo Datasets. *Comput. Phys. Commun.* 184, 2214 (2013) (see p. 41)

[74] M. Usner. Search for Astrophysical Tau-Neutrinos in Six Years of High-Energy Starting Events in the IceCube Detector. PhD thesis (Humboldt-Universität zu Berlin, 2018) (see p. 41)

[75] K. Schatto. Stacked Searches for High-Energy Neutrinos from Blazars with IceCube. PhD thesis (Johannes Gutenberg-Universität Mainz, 2014) (see pp. 41, 62)

[76] A. Kolmogorov. Sulla Determinazione Empirica di una Legge di Distribuzione. *Ist. Ital. Attuari.* 4, 83 (1933) (see p. 42)

[77] N. Smirnov. Table for Estimating the Goodness of Fit of Empirical Distributions. *The Annals of Mathematical Statistics*, 19, 279 (1948) (see p. 42)

[78] M. G. Aartsen et al. (IceCube). Observation of the Cosmic-ray Shadow of the Moon with IceCube. *Phys. Rev.* D89, 102004 (2014) (see p. 43)

[79] H. Cramér. *Mathematical Methods of Statistics*, Princeton Mathematical Series (Princeton Univ. Press, 1999) (see p. 43)

[80] C. Radhakrishna Rao. Information and the Accuracy Attainable in the Estimation of Statistical Parameters. *Bull. Calcutta Math. Soc.* 37, 81 (1945) (see p. 43)

[81] R. Abbasi et al. (IceCube). Time-integrated Searches for Point-like Sources of Neutrinos with the 40-String IceCube Detector. *Astrophys. J.* 732, 18 (2011) (see pp. 44, 158, 159)

[82] J. Lünemann. Suche nach Dunkler Materie in Galaxien und Galaxienhaufen mit dem Neutrinoteleskop IceCube. PhD thesis (Johannes Gutenberg-Universität Mainz, 2013) (see p. 44)

[83] T. Neunhöffer. Estimating the Angular Resolution of Tracks in Neutrino Telescopes Based on a Likelihood Analysis. *Astropart. Phys.* 25, 220 (2006) (see p. 44)

[84] M. G. Aartsen et al. (IceCube). Searches for Extended and Point-like Neutrino Sources with Four Years of IceCube Data. *Astrophys. J.* 796, 109 (2014) (see pp. 44, 96, 158, 159)

[85] B. Efron. Bootstrap Methods: Another Look at the Jackknife. *The Annals of Statistics*, 7, 1 (1979) (see p. 45)

[86] L. Rädel and C. Wiebusch. Calculation of the Cherenkov Light Yield from Electromagnetic Cascades in Ice with Geant4. *Astropart. Phys.* 44, 102 (2013) (see p. 45)

[87] J.-D. Zornoza and D. Chirkin (IceCube). "Muon Energy Reconstruction and Atmospheric Neutrino Spectrum Unfolding with the IceCube Detector", in 30th International Cosmic Ray Conference (ICRC): Mérida, Mexico, Vol. 5 (2007), pp. 1275–1278 (see p. 46)

[88] R. Abbasi et al. (IceCube). An Improved Method for Measuring Muon Energy Using the Truncated Mean of dE/dx. *Nucl. Instrum. Meth.* A703, 190 (2013) (see p. 46)

[89] A. Gazizov and M. P. Kowalski. ANIS: High Energy Neutrino Generator for Neutrino Telescopes. *Comput. Phys. Commun.* 172, 203 (2005) (see p. 47)

[90] A. M. Dziewonski and D. L. Anderson. Preliminary Reference Earth Model. *Physics of the Earth and Planetary Interiors*, 297 (1981) (see p. 48)

[91] D. Heck, J. Knapp, J. N. Capdevielle, G. Schatz, and T. Thouw. CORSIKA: A Monte Carlo Code to Simulate Extensive Air Showers. (1998) (see p. 48)

[92] D. A. Chirkin. Cosmic Ray Energy Spectrum Measurement with the Antarctic Muon and Neutrino Detector Array (AMANDA). PhD thesis (University of California, Berkeley, 2003) (see p. 48)

[93] D. Chirkin and W. Rhode. Muon Monte Carlo: A High-precision Tool for Muon Propagation through Matter. (2004) (see p. 48)

[94] J. H. Koehne, K. Frantzen, M. Schmitz, T. Fuchs, W. Rhode, D. Chirkin, and J. Becker Tjus. PROPOSAL: A Tool for Propagation of Charged Leptons. *Comput. Phys. Commun.* 184, 2070 (2013) (see p. 48)

[95] D. Chirkin (IceCube). "Photon Tracking with GPUs in IceCube", in 5th Very Large Volume Neutrino Telescope Workshop (VLVnT), Vol. A725 (2011), pp. 141–143 (see p. 48)

[96] M. G. Aartsen et al. (IceCube). The IceCube Realtime Alert System. *Astropart. Phys.* 92, 30 (2017) (see pp. 49–51, 54, 133)

[97] R. Franke. Design, Implementation and First Results of the Neutrino Triggered Target of Opportunity Program with the IceCube Neutrino Telescope. PhD thesis (Humboldt-Universität zu Berlin, 2014) (see pp. 49, 50, 58, 94, 117)

[98] S. Odrowski. High-Energy Neutrino Scan of the Galactic Plane. PhD thesis (Max-Planck-Institut für Kernphysik, Ruperto-Carola University of Heidelberg, Germany, 2012) (see p. 49)

[99] S. Tilav, P. Desiati, T. Kuwabara, D. Rocco, F. Rothmaier, M. Simmons, and H. Wissing (IceCube). "Atmospheric Variations as Observed by IceCube", in 31st International Cosmic Ray Conference (ICRC): Łódź, Poland (2009), p. 894 (see pp. 49, 92)

[100] M. Ackermann, E. Bernardini, N. Galante, F. Goebel, M. Hayashida, K. Satalecka, M. Tluczykont, and R. M. Wagner (IceCube, MAGIC). "Neutrino Triggered Target of Opportunity (NToO) Test Run with AMANDA-II and MAGIC", in 30th International Cosmic Ray Conference (ICRC): Mérida, Mexico, Vol. 3 (2007), pp. 1257–1260 (see pp. 51, 106)

[101] M. G. Aartsen et al. (IceCube and MAGIC and VERITAS). Very High-Energy Gamma-Ray Follow-Up Program Using Neutrino Triggers from IceCube. *JINST*, 11, P11009 (2016) (see pp. 51, 103, 104, 106, 107)

[102] M. G. Aartsen et al. (IceCube, PTF, Swift, Pan-STARRS1 Science Consortium). The Detection of a SN IIn in Optical Follow-up Observations of IceCube Neutrino Events. *Astrophys. J.* 811, 52 (2015) (see pp. 51, 58, 107)

[103] C. W. Akerlof et al. The ROTSE-III robotic telescope system. *Publ. Astron. Soc. Pac.* 115, 132 (2003) (see p. 51)

[104] N. M. Law et al. The Palomar Transient Factory: System Overview, Performance and First Results. *Publ. Astron. Soc. Pac.* 121, 1395 (2009) (see pp. 51, 107)

[105] N. Gehrels et al. (Swift Science). The Swift Gamma-Ray Burst Mission. *Astrophys. J.* 611, [Erratum: Astrophys. J.621,558(2005)], 1005 (2004) (see pp. 51, 107)

[106] T. Bray. *The JavaScript Object Notation (JSON) Data Interchange Format*, RFC 8259, Dec. 2017 (see p. 53)

[107] K. Maine, C. Devieux, and P. Swan. "Overview of IRIDIUM Satellite Network", in Proceedings of WESCON'95 (Dec. 1995), p. 483 (see p. 54)

[108] T. Valentic and R. Stehle. *First Applications of DoD Iridium RUDICS in the NSF Polar Programs*, Dec. 2008 (see p. 54)

[109] *ZeroMQ - Distributed Messaging* (see p. 54)

[110] R. Seaman et al. IVOA Recommendation: Sky Event Reporting Metadata Version 2.0. (2011) (see p. 54)

[111] M. G. Aartsen et al. (IceCube). Search for Sources of Astrophysical Neutrinos Using Seven Years of IceCube Cascade Events. *Astrophys. J.* 886, (2019) (see pp. 55, 59)

[112] D. Gora. "High-energy Gamma-ray Follow-up Program Using Neutrino Triggers from IceCube", in 34th International Cosmic Ray Conference (ICRC): The Hague, The Netherlands (2015), pp. 16–19 (see p. 58)

[113] M. Voge. Searches for Neutrinos from Supernovae Using Cherenkov In-Ice Detectors. PhD thesis (Humboldt-Universität zu Berlin, 2016) (see pp. 58, 59)

[114] J. Felde (IceCube). "Near Realtime Searches for Neutrinos from GRBs with IceCube", in 34th International Cosmic Ray Conference (ICRC): The Hague, The Netherlands, Vol. ICRC2015 (2015), p. 1089 (see p. 58)

[115] F. Bradascio. Segmented Muon Reconstruction. PhD thesis (Humboldt-Universität zu Berlin, in preparation) (see p. 62)

[116] M. Huennefeld (IceCube). "Deep Learning in Physics Exemplified by the Reconstruction of Muon-Neutrino Events in IceCube", in 35th International Cosmic Ray Conference (ICRC): Busan, Korea (2017), p. 1057 (see p. 65)

[117] F. Pedregosa et al. Scikit-learn: Machine Learning in Python. *Journal of Machine Learning Research*, 12, 2825 (2011) (see p. 66)

[118] G. C. Hill. "Bayesian Event Reconstruction and Background Rejection in Neutrino Detectors", in 27th International Cosmic Ray Conference (ICRC): Hamburg, Germany, Vol. 3 (2001), p. 1279 (see p. 68)

[119] T. R. DeYoung. Observation of Atmospheric Muon Neutrinos with AMANDA. PhD thesis (University of Wisconsin – Madison, 2001) (see p. 68)

[120] M. G. Aartsen et al. (IceCube). Search for Steady Point-like Sources in the Astrophysical Muon Neutrino Flux with 8 Years of IceCube Data. *Eur. Phys. J. C*, (2018) (see pp. 71, 85)

[121] M. G. Aartsen et al. (IceCube). Lowering IceCube's Energy Threshold for Point Source Searches in the Southern Sky. *Astrophys. J.* 824, L28 (2016) (see p. 75)

[122] M. G. Aartsen et al. (IceCube). Characterization of the Atmospheric Muon Flux in IceCube. *Astropart. Phys.* 78, 1 (2016) (see pp. 77, 78, 148)

[123] G. Punzi. "Sensitivity of Searches for New Signals and Its Optimization", in Statistical Problems in Particle Physics, Astrophysics and Cosmology (PHYSTAT2003): SLAC, Standford, CA (2003), pp. 79–83 (see p. 83)

[124] J. Braun, J. Dumm, F. De Palma, C. Finley, A. Karle, and T. Montaruli. Methods for Point Source Analysis in High Energy Neutrino Telescopes. *Astropart. Phys.* 29, 299 (2008) (see p. 87)

[125] R. H. Byrd, P. Lu, J. Nocedal, and C. Zhu. A Limited Memory Algorithm for Bound Constrained Optimization. *SIAM Journal on Scientific Computing*, 16, 1190 (1995) (see p. 88)

[126] C. Zhu, R. H. Byrd, and J. Nocedal. L-BFGS-B: Algorithm 778: L-BFGS-B, FORTRAN Routines for Large Scale Bound Constrained Optimization. *ACM Transactions on Mathematical Software*, 23, 550 (1997) (see p. 88)

[127] J. Braun, M. Baker, J. Dumm, C. Finley, A. Karle, and T. Montaruli. Time-dependent Point Source Search Methods in High Energy Neutrino Astronomy. *Astropart. Phys.* 33, 175 (2010) (see pp. 90, 91, 109)

[128] K. Satalecka, E. Bernardini, M. Ackermann, and M. Tluczykont (IceCube). "Cluster Search for Neutrino Flares from Pre-defined Directions", in 30th International Cosmic Ray Conference (ICRC): Mérida, Mexico, Vol. 5 (2007), pp. 1353–1356 (see p. 90)

[129] R. Abbasi et al. Time-dependent Searches for Point Sources of Neutrinos with the 40-string and 22-string Configurations of IceCube. *Astrophys. J.* 744, 1, 1 (2012) (see p. 92)

[130] S. S. Wilks. The Large-Sample Distribution of the Likelihood Ratio for Testing Composite Hypotheses. *Annals Math. Statist.* 9, 60 (1938) (see p. 93)

[131] M. G. Aartsen et al. (IceCube). Search for Prompt Neutrino Emission from Gamma-Ray Bursts with IceCube. *Astrophys. J.* 805, L5 (2015) (see pp. 96, 149)

[132] T. K. Gaisser. Spectrum of Cosmic-Ray Nucleons, Kaon Production, and the Atmospheric Muon Charge Ratio. *Astropart. Phys.* 35, 801 (2012) (see pp. 98, 141, 157)

[133] S. Müller (Pierre Auger). "Direct Measurement of the Muon Density in Air Showers with the Pierre Auger Observatory", in Ultra High Energy Cosmic Rays (UHECR2018): Paris, France, Vol. 210 (2018), p. 02013 (see p. 98)

[134] J. A. Bellido, R. W. Clay, N. N. Kalmykov, I. S. Karpikov, G. I. Rubtsov, S. V. Troitsky, and J. Ulrichs. Muon Content of Extensive Air Showers: Comparison of the Energy Spectra Obtained by the Sydney University Giant Air-shower Recorder and by the Pierre Auger Observatory. *Phys. Rev.* D98, 023014 (2018) (see p. 98)

[135] S. L. Glashow. Resonant Scattering of Antineutrinos. *Phys. Rev.* 118, 316 (1960) (see p. 101)

[136] L. Wolfenstein. Neutrino Oscillations in Matter. *Phys. Rev.* D17, 2369 (1978) (see p. 101)

[137] L. Wolfenstein. Neutrino Oscillations and Stellar Collapse. *Phys. Rev.* D20, 2634 (1979) (see p. 101)

[138] S. P. Mikheyev and A. Y. Smirnov. Resonance Amplification of Oscillations in Matter and Spectroscopy of Solar Neutrinos. *Sov. J. Nucl. Phys.* 42, 913 (1985) (see p. 101)

[139] T. Kintscher and A. Stasik. *Search for Counterpart to ANTARES Neutrino Detection with IceCube*, The Astronomer's Telegram #8097, 2015 (see p. 106)

[140] K. Meagher. "IceCube as a Neutrino Follow-up Observatory for Astronomical Transients", in 35th International Cosmic Ray Conference (ICRC): Busan, Korea (2017), p. 1007 (see p. 106)

[141] S. Adrian-Martinez et al. (ANTARES, IceCube, LIGO Scientific, Virgo). High-energy Neutrino Follow-up Search of Gravitational Wave Event GW150914 with ANTARES and IceCubea. *Phys. Rev.* D93, 122010 (2016) (see p. 106)

[142] B. P. Abbott et al. (LIGO Scientific, Virgo, Fermi GBM, INTEGRAL, IceCube, AstroSat Cadmium Zinc Telluride Imager Team, IPN, Insight-Hxmt, ANTARES, Swift, AGILE Team, 1M2H Team, Dark Energy Camera GW-EM, DES, DLT40, GRAWITA, Fermi-LAT, ATCA, ASKAP, Las Cumbres Observatory Group, OzGrav, DWF (Deeper Wider Faster Program), AST3, CAASTRO, VINROUGE, MASTER, J-GEM, GROWTH, JAGWAR, CaltechNRAO, TTU-NRAO, NuSTAR, Pan-STARRS, MAXI Team, TZAC Consortium, KU, Nordic Optical Telescope, ePESSTO, GROND, Texas Tech University, SALT Group, TOROS, BOOTES, MWA, CALET, IKI-GW Follow-up, H.E.S.S., LOFAR, LWA, HAWC, Pierre Auger, ALMA, Euro VLBI Team, Pi of Sky, Chandra Team at McGill University, DFN, ATLAS Telescopes, High Time Resolution Universe Survey, RIMAS, RATIR, SKA South Africa/MeerKAT). Multi-messenger Observations of a Binary Neutron Star Merger. *Astrophys. J.* 848, L12 (2017) (see p. 106)

[143] S. Countryman, A. Keivani, I. Bartos, Z. Marka, T. Kintscher, R. Corley, E. Blaufuss, C. Finley, and S. Marka. Low-Latency Algorithm for Multi-messenger Astrophysics (LLAMA) with Gravitational-Wave and High-Energy Neutrino Candidates. (2019) (see p. 106)

[144] M. Voge and A. Homeier. "Optical and X-ray Follow-up Programs of IceCube", in 33rd International Cosmic Ray Conference (ICRC): Rio de Janeiro, Brasil (2013) (see p. 107)

[145] C. E. Bonferroni. Teoria Statistica delle Classi e Calcolo delle Probabilità. *Publ. R. Istit. Super. Sci. Econ. Commerc. Firenze*, 8, 1 (1936) (see pp. 107, 123)

[146] M. G. Aartsen et al. (IceCube). Searches for Time Dependent Neutrino Sources with IceCube Data from 2008 to 2012. *Astrophys. J.* 807, 46 (2015) (see p. 109)

[147] F. Acero et al. (Fermi-LAT). Fermi Large Area Telescope Third Source Catalog. *Astrophys. J. Suppl.* 218, 23 (2015) (see p. 110)

[148] M. Ajello et al. (Fermi-LAT). 3FHL: The Third Catalog of Hard Fermi-LAT Sources. *Astrophys. J. Suppl.* 232, 18 (2017) (see p. 110)

[149] J. D. Scargle. Studies in Astronomical Time Series Analysis: 5. Bayesian Blocks, a New Method to Analyze Structure in Photon Counting Data. *Astrophys. J.* 504, 405 (1998) (see p. 110)

[150] J. D. Scargle, J. P. Norris, B. Jackson, and J. Chiang. Studies in Astronomical Time Series Analysis. 6. Bayesian Block Representations. *Astrophys. J.* 764, 167 (2013) (see p. 110)

[151] S. P. Wakely and D. Horan. "TeVCat: An Online Catalog for Very High Energy Gamma-Ray Astronomy", in 30th International Cosmic Ray Conference (ICRC): Mérida, Mexico, Vol. 3 (2007), pp. 1341–1344 (see p. 111)

[152] D. Guberman and P. Colin (MAGIC). "Performance of the MAGIC Telescopes under Moonlight", in 35th International Cosmic Ray Conference (ICRC): Busan, Korea (2017), p. 823 (see p. 117)

[153] K. Murase, D. Guetta, and M. Ahlers. Hidden Cosmic-Ray Accelerators as an Origin of TeV-PeV Cosmic Neutrinos. *Phys. Rev. Lett.* 116, 071101 (2016) (see p. 118)

[154] K. M. Gorski, E. Hivon, A. J. Banday, B. D. Wandelt, F. K. Hansen, M. Reinecke, and M. Bartelman. HEALPix - A Framework for High Resolution Discretization, and Fast Analysis of Data Distributed on the Sphere. *Astrophys. J.* 622, 759 (2005) (see p. 120)

[155] A. Zonca, L. Singer, D. Lenz, M. Reinecke, C. Rosset, E. Hivon, and K. Gorski. healpy: Equal Area Pixelization and Spherical Harmonics Transforms for Data on the Sphere in Python. *Journal of Open Source Software*, 4, 1298 (2019) (see p. 120)

[156] E. Blaufuss, T. Kintscher, L. Lu, and C. F. Tung. "The Next Generation of IceCube Real-time Neutrino Alerts", in 36th International Cosmic Ray Conference (ICRC): Madison, WI (2019), p. 1021 (see p. 133)

[157] T. Kintscher, K. Krings, D. Dorner, W. Bhattacharyya, and M. Takahashi (IceCube, FACT, MAGIC). "IceCube Search for Neutrinos from 1ES 1959+650: Completing the Picture", in 35th International Cosmic Ray Conference (ICRC): Busan, Korea (2017), p. 969 (see pp. 146, 150)

[158] J. F. Schachter et al. Ten New BL Lacertae Objects Discovered by an Efficient X-ray/Radio/Optical Technique. *Astrophys. J.* 412, 541 (1993) (see p. 146)

[159] J. Holder et al. (VERITAS). Detection of TeV Gamma-rays from the BL Lacertae Object 1ES 1959+650 with the Whipple 10-meter Telescope. *Astrophys. J.* 583, L9 (2003) (see p. 146)

[160] T. Nishiyama et al. "Detection of a New TeV Gamma-Ray Source of BL Lac Object 1ES 1959+650", in 26th International Cosmic Ray Conference (ICRC): Salt Lake City, UT, Vol. 3 (1999), p. 370 (see p. 146)

[161] M. K. Daniel et al. (VERITAS). Spectrum of Very High Energy Gamma-rays from the Blazar 1ES1959+650 During Flaring Activity in 2002. *Astrophys. J.* 621, 181 (2005) (see p. 146)

[162] H. Krawczynski et al. Multiwavelength Observations of Strong Flares from the TeV-Blazar 1ES 1959+650. *Astrophys. J.* 601, 151 (2004) (see p. 146)

[163] M. Böttcher. A Hadronic Synchrotron Mirror Model for the Orphan TeV Flare in 1ES 1959+650. *Astrophys. J.* 621, [Erratum: *Astrophys. J.* 641, 1233 (2006)], 176 (2005) (see pp. 146, 152)

[164] M. Ackermann. Searches for Signals from Cosmic Point-like Sources of High Energy Neutrinos in 5 Years of AMANDA-II Data. PhD thesis (Humboldt-Universität zu Berlin, 2006) (see p. 146)

[165] F. Halzen and D. Hooper. High Energy Neutrinos from the TeV Blazar 1ES 1959+650. *Astropart. Phys.* 23, 537 (2005) (see p. 146)

[166] E. Aliu et al. (VERITAS). Multiwavelength Observations and Modeling of 1ES 1959+650 in a Low Flux State. *Astrophys. J.* 775, 3 (2013) (see p. 147)

[167] K. Satalecka et al. (MAGIC). Monitoring of Bright Blazars with MAGIC in the 2007/2008 Season. *AIP Conf. Proc.* 1112, 223 (2009) (see pp. 147, 152)

[168] *The Astronomer's Telegram*, 9010, 9139, 9148, 9203, 9239, (2016) (see pp. 147, 149)

[169] A. Biland et al. Calibration and performance of the photon sensor response of FACT – The First G-APD Cherenkov telescope. *JINST*, 9, P10012 (2014) (see p. 147)

[170] D. Dorner et al. (FACT). "FACT - Time-Resolved Blazar SEDs", in 35th International Cosmic Ray Conference (ICRC): Busan, Korea (2017), p. 608 (see pp. 147, 149)

[171] D. Dorner et al. "FACT - Highlights from more than Five Years of Unbiased Monitoring at TeV Energies", in 35th International Cosmic Ray Conference (ICRC): Busan, Korea, Vol. ICRC2017 (2018), p. 609 (see p. 149)

[172] M. C. Stroh and A. D. Falcone. Swift X-ray Telescope Monitoring of Fermi-LAT Gamma Ray Sources of Interest. *Astrophys. J. Suppl.* 207, 28 (2013) (see p. 152)

[173] A. Reimer, M. Bottcher, and S. Postnikov. Neutrino Emission in the Hadronic Synchrotron Mirror Model: The Orphan TeV Flare from 1ES 1959+650. *Astrophys. J.* 630, 186 (2005) (see p. 152)

[174] C. Righi, F. Tavecchio, and D. Guetta. High-energy Emitting BL Lacs and High-energy Neutrinos - Prospects for the Direct Association with IceCube and KM3NeT. *Astron. Astrophys.* 598, A36 (2017) (see p. 152)

[175] M. G. Aartsen et al. (IceCube). Neutrino Emission from the Direction of the Blazar TXS 0506+056 prior to the IceCube-170922A Alert. *Science*, 361, 147 (2018) (see pp. 154, 159, 160)

[176] R. Mirzoyan. *First-time Detection of VHE Gamma-rays by MAGIC from a Direction Consistent with the Recent EHE Neutrino Event IceCube-170922A*, The Astronomer's Telegram #10817, 2017 (see p. 155)

[177] M. G. Aartsen et al. (IceCube). Search for Time-independent Neutrino Emission from Astrophysical Sources with 3 yr of IceCube Data. *Astrophys. J.* 779, 132 (2013) (see pp. 158, 159)

[178] P. Padovani, P. Giommi, E. Resconi, T. Glauch, B. Arsioli, N. Sahakyan, and M. Huber. Dissecting the Region Around IceCube-170922A: The Blazar TXS 0506+056 as the First Cosmic Neutrino Source. *Mon. Not. Roy. Astron. Soc.* 480, 192 (2018) (see p. 163)

[179] F. Halzen, A. Kheirandish, T. Weisgarber, and S. P. Wakely. On the Neutrino Flares from the Direction of TXS 0506+056. *Astrophys. J.* 874, L9 (2019) (see p. 163)

[180] M. G. Aartsen et al. (IceCube). The contribution of Fermi-2LAC blazars to the diffuse TeV-PeV neutrino flux. *Astrophys. J.* 835, 45 (2017) (see p. 163)

[181] S. Ansoldi et al. (MAGIC). The Blazar TXS 0506+056 Associated with a High-energy Neutrino: Insights into Extragalactic Jets and Cosmic Ray Acceleration. *Astrophys. J. Lett.* [Astrophys. J.863,L10(2018)] (2018) (see p. 163)

[182] X. Rodrigues, S. Gao, A. Fedynitch, A. Palladino, and W. Winter. Models for the Historical Flare of TXS 0506+056. *Astrophys. J.* 874, L29 (2019) (see p. 164)

[183] M. Ackermann et al. (Fermi-LAT). The Third Catalog of Active Galactic Nuclei Detected by the Fermi Large Area Telescope. *Astrophys. J.* 810, 14 (2015) (see p. 164)

[184] S. Paiano, R. Falomo, A. Treves, and R. Scarpa. The Redshift of the BL Lac Object TXS 0506+056. *Astrophys. J.* 854, L32 (2018) (see p. 164)

Acknowledgements

This work would not have been possible without the support of many people.

First of all, I would like to thank Elisa Bernardini for introducing the to this exciting field and giving me the opportunity to participate. You granted me the freedom to explore the potential of this topic, and always contributed many ideas and inspiring and encouraging discussions. I am very grateful for the invitation to Padova, which allowed me to finish this work eventually! There I would also like to thank Manuela Mallamaci for helping me navigate the Italian institutions and providing such a welcoming environment during my stay.

Also, thanks to Elisa and Manuela for proof-reading the thesis!

At DESY, I would like to thank all the people who made life and work in the office more enjoyable. In particular thanks to Konstancja Satalecka, for her saintly patience when listening to my grievances and providing an optimistic outlook, the chocolate in your office.

Thanks to Jakob van Santen for his constant readiness to help, unending insights, and especially for guiding me through the IceCube software landscape when I had just started this work. Furthermore, I want to thank all former and newer students and post-docs who made the point-source office, lunch discussions and the lakeside hangout enjoyable and fun. Thanks to Emanuel Jacobi, for getting me started on the event filtering. Alexander Stasik, thanks for all the help and enduring my rookie questions, the discussions with you really facilitated my transition to this new field. Marcel Usner for sharing insights and the Thanks to David, Hape, Juan Pablo and Meike for the fun trip to Chicago after the Collaboration meeting.

Furthermore, this work would would not have been possible without the IceCube collaboration. Especially I want to thank Erik Blaufuss for the great collaboration on all the real-time related topics over these years. Furthermore, almost all IceCube members deserve some credit for their ingenuity, scientific integrity, and fantastic tools and results on which this work is built.

Equally important are my friends – thank you for showing interest in the work that I did, and being always available for fun and relaxing times unrelated to physics, even though I surely wasn't always easy to deal with during stressful times. Last but not least, I want to thank for my family for their continuous support through the years!

Selbstständigkeitserklärung

Ich erkläre, dass ich die Dissertation selbständig und nur unter Verwendung der von mir gemäß § 7 Abs. 3 der Promotionsordnung der Mathematisch-Naturwissenschaftlichen Fakultät, veröffentlicht im Amtlichen Mitteilungsblatt der Humboldt-Universität zu Berlin Nr. 42/2018 am 11.07.2018, angegebenen Hilfsmittel angefertigt habe.

Berlin, den 18.11.2019,

(Unterschrift)

Ich erkläre, dass die von mir in der Universitätsbibliothek abgegebene schriftliche und elektronische Version der Dissertationsschrift mit der angenommenen Dissertation übereinstimmt.

Ich habe nur die Mängel beseitigt und die Auflagen erfüllt, die mir bei der Verteidigung mitgeteilt wurden und deren Erfüllung der Vorsitzende der Promotionskommission bestätigt hat.